High Aspect Ratio Lithographic Imaging at Ultra-high Numerical Apertures: Evanescent Interference Lithography with Resonant Reflector Underlayers

Prateek Mehrotra

B.E. (Hons. I)

A thesis is presented for the degree of

Doctor of Philosophy

in

Electrical and Electronic Engineering

at the

University of Canterbury,

Christchurch, New Zealand.

June 2012

Dedicated to my parents, Kishore and Mamta.

Abstract

A near-field technique known as evanescent interferometric lithography allows for high resolution imaging. However its primary limitation is that the image exponentially decays within the photoresist due to physical limits. This thesis aims to overcome this limitation and presents a method to considerably enhance the depth of focus of images created using evanescent interferometric lithography by using a material underlay beneath the photoresist.

A key enabler of this is the understanding that evanescent fields couple to surface states and operating within proximity of a resonance, the strength of the coupling allows for considerable energy extraction from the incident beam and redistribution of this energy in a photoresist cavity. This led to the analysis of the Fresnel equations, which suggested that such coupling was in fact the result of an enhanced reflectance that takes place at boundaries of carefully chosen materials. While it is known that metals and lossy dielectrics result in surface plasmon polaritons (SPP) and surface exciton polaritons (SEP) as conventional solutions to the Fresnel reflection equations for the TM polarization of light, there is no such naturally occurring surface state that allows evanescent wave enhancement with the TE polarization of light. Further investigation of the Fresnel reflection equations revealed both for TM and TE that in fact another solution exists that is but unconventional to enhance the reflectivity. This solution requires that one of the media have a negative loss. This is a new type of surface resonance that requires that one of the media be a gain medium; not one in the optical pumped sense but one that would naturally supply energy to a wave to make it grow. This new surface resonance is also a key result of this thesis. Clearly, however this is only a hypothetical solution as a real gain medium would violate the conservation of energy.

However, as it is only the reflectance of this gain medium that is useful for evanescent wave enhancement, in fact a multilayered stack consisting of naturally occurring materials is one way to achieve the desired reflectivity. This would of course be only an emulation of the reflectivity aspect of the gain medium. This multilayered stack is then an effective gain medium for the reflectivity purposes when imaging is carried out at a particular *NA* at a particular wavelength. This proposal is also a key idea of this thesis. At λ = 193 nm, this method was used to propose a feasible design to image high resolution structures, *NA* = 1.85 at an aspect ratio of ~3.2.

To experimentally demonstrate the enhancements, a new type of solid immersion test bed, the solid immersion Lloyd's mirror interference lithography test-bed was constructed. High quality line and space patterns with a half-pitch of 55.5 nm were created using λ = 405 nm, corresponding to a *NA* of 1.824, that

is well in the evanescent regime of light. Image depths of 33-40 nm were seen. Next, the evanescent image was coupled to an effective gain medium made up of a thin layer of hafnium oxide (HfO) upon silicon dioxide (SiO_2). This resulted in a considerable depth enhancement, and 105 nm tall structures were imaged.

The work in this thesis details the construction of the solid immersion lithography test-bed, describes the implementation of the modeling tools, details the theory and analysis required to achieve the relevant solutions and understanding of the physical mechanism and finally experimentally demonstrates an enhancement that allows evanescent interferometric lithography beyond conventional limits.

Acknowledgements

Through my PhD I feel privileged to have 'tasted' a portion of very exciting science and I feel satisfied with the challenges that I have overcome in the past two and a half years. I am grateful to the process because it has allowed me to rebuild several aspects of my mental self and hence accomplish the goal I had set out for myself when I began this degree. None of it would however be possible if I was not lucky enough to be surrounded by some very special people. I describe a few of them here, who have helped me considerably through this journey and also made it memorable and adventurous.

I consider myself very fortunate to have had Professor Richard Blaikie as my PhD supervisor. Richard's leadership skills, guidance and friendly encouraging attitude have allowed me to work hard and take pride in my work. Like several of his other students, I too see Richard as a mentor and am extremely grateful to him for always being there to resolve problems that I have come across. I find this partly lies in his ability to see the big picture while keeping in mind the necessary details, an approach which I constantly remind myself to take. Richard's professionalism and dedication to his students is worthy of great praise. Richard's leadership, positivity and far sightedness is missed here at the University of Canterbury as he is now based at the University of Otago, yet he has taken out a considerable portion out of his busy schedule to remotely supervise me through several experiments and the proof-reading of my thesis in an unbelievably short time frame. I am extremely grateful to Richard and I wish him and his family all the best in Otago.

I am also very thankful to Dr. Trey Holzwarth, an ex-post-doctoral fellow at the University of Canterbury for his awesome mentoring while he was here and for his encouragement, support and advice during my PhD and also prior to my job interview. Trey has a very unique ability to figure out how things tick, he learns well from all his experiences and he is always more than happy to impart this knowledge to others around him when they seek advice. It was also very nice to have had stimulating discussions with Trey regarding various matters while he was in New Zealand. The Christchurch earthquake meant that Trey's stay in NZ was cut a few months shorter than planned. Trey has also been a great mentor and a good friend, and he takes good care of his friends! I wish him, his wife and their newly born all the best.

I am extremely grateful to Mr. David Healey for helping me with the design and construction of the prism cage for the solid immersion interference lithography system. Dave has gone beyond what was needed and provided innovative input into the design of the cage and the backing plates. Without Dave's design, I

would not have any experimental results. Dave takes great pride in his work and aims to achieve the best in it, this is greatly appreciated. I wish him the best of luck with his recovery from the surgery.

I also consider myself extremely lucky to have had the opportunity to work with Dr. Chris A. Mack, Gentleman Scientist, Lithoguru who was in New Zealand for approximately two months in 2011. Chris has been able to take my existing PhD work and discover further insights, making the solutions considerably more attractive. A lot of this work is presented in Chapter 6. I am grateful to Chris and thank him for his mentoring and also for his encouragement, advice and support.

I am also thankful to Miss Rebekah Hunt, MacDiarmid institute administrator, for her constant support and assistance in various activities that I was involved in and taking care of things that I would not have a clue how to deal with, such as equipment ordering, conference registration, flight bookings and accommodation to name a few. This dedication to her job is greatly respected and appreciated.

Dr. Lakshman DeSilva helped with the deposition of Hafnium Oxide coatings, despite erratic behavior of the sputterer and I am really thankful to him for his persistence as otherwise none of the experiments demonstrating the core principle in Chapter 7 of this thesis would be possible.

I would like to thank the UC doctoral scholarship, the MacDiarmid Institute for Advanced Materials and Nanotechnology for continued funding, Dr. Maan Alkaisi, my co-supervisor for being supportive and encouraging at all times, Helen Devereux and Gary Turner for taking good care of the Nanolab facility, without which there would be no practical aspect to my thesis, the University of Canterbury, for taking such good care of its students despite the severe disruption caused by the earthquake, Pieter Kikstra, Mike Shurety and Florin Predan for helping me significantly with computer issues, and Jac Woudberg for helping me in the workshop. I am also grateful to my colleagues and friends John Foulkes, Ciaran Moore, Mikkel Scholer, Steve Weddell, Jannah Ibrahim, David Kim, Senthuran Sivasubramanium, Lynn Murray, Robert Heinhold, Steve Banerjee and Volker Nock for making my PhD a very fun journey. I wish Ciaran and Mikkel and their wives all the best as they begin an exciting new life with their newly borns!

Lastly but by no means the least, I am eternally grateful to my parents, Kishore and Mamta to whom I owe everything that is good in me. I would have been completely aimless and scattered, not knowing what lessons life has tried to teach me, had it not been for your careful nurturing, your dedication to cater to your child's best interests and putting them before your own at all times, your unconditional love, your tutelage of proper work ethics, life's experiences, the importance of an education and your constant drive to see your children excel. Thanks for everything, your constant support, encouragement and confidence in all my endeavors has allowed me to reach this far and complete this thesis.

Table of Contents

List of Figures

List of Tables

Chapter 1. Introduction

1.1 History & Overview

On December the 16th, 1947, William Shockley, John Bardeen and Walter Brattain, successfully built the first transistor in AT&T's Bell Labs for which the trio were awarded the 1956 Nobel prize in Physics [1]. This was known as a point contact transistor (see Figure 1-1), an early form of the bipolar junction transistor (BJT) that was well over 2 cm tall and made up of germanium, plastic and gold. It allowed current amplification at a wide range of frequencies and was the first working solid state amplifier [2].

Prior to this, the thermionic triode (an electronic vacuum tube) had been responsible for propelling the electronics age forward. However this was large, slow and power hungry and a paradigm shift was necessary [3]. The invention of the solid state transistor sparked an era that has resulted in an exponential increase in the progress of human technology. Six and a half decades later, the progress is strong but the spirit and drive to meet the continually increasing demands for computation are even stronger.

Of course, the potential benefits of this technology were only reaped after the invention of the integrated circuit (IC) by the US Army General Jack Kilby for which he was also awarded the Nobel Prize albeit much later in 2000 [4-5]. Robert Noyce, co-founder of Intel is also credited with the invention of the IC [4]. The semiconductor industry that was then spawned is responsible for the continuous drive to improve microarchitectures, further miniaturize features and fit an increasing number of transistors on an IC as this has allowed significant improvements in speed, cost and efficiency and hence affordable computational power wherever needed. The necessity for such computational power is omnipresent in today's world. In some cases it is a cheaper alternative, for instance the clichéd but spot-on example of the use of a microcontroller in modern toasters. In other cases such as the use of a state of the art microprocessor in cellphones or smartphones, such power at the palm of one's hand has allowed people to communicate with the world and schedule their tasks in a much easier manner.

The engineering discipline behind much of this progress is known as lithography. The semiconductor industry has historically used optical lithography to reduce the feature sizes used in the manufacture of ICs by a factor of 2 every 4 to 6 years [6]. The industry, however, has maintained the doubling of the number of transistors on a chip every 18 months; this growth is commonly referred to as Moore's law

(see. Figure 1-2), named after Gordon Moore, co-founder of the Intel Corporation along with Robert E. Noyce, who had predicted such a growth in an article published in Electronics Magazine on April 19th 1965 [7].

(a)

(b)

Figure 1-1 – First successful transistor - point contact transistor (a) Replica [8] (b) Close-up view [9]

By far the most important feature to reduce is the pitch of a repeating pattern of lines and spaces, since this determines the packing density of transistors in the circuit, and thus the cost and capability of the device. As an example, the Metal Oxide Semiconductor Field Effect Transistor (MOSFET) [10-11] is now the most common transistor used in both digital and analogue electronics, the basic principle for

which was first patented in 1925 by physicist Julius Edgar Lilienfeld [3, 12-14]. The pitch of the gate lines determined by lithography is the principal factor that controls how many MOSFETs can be manufactured per unit area of silicon real estate.

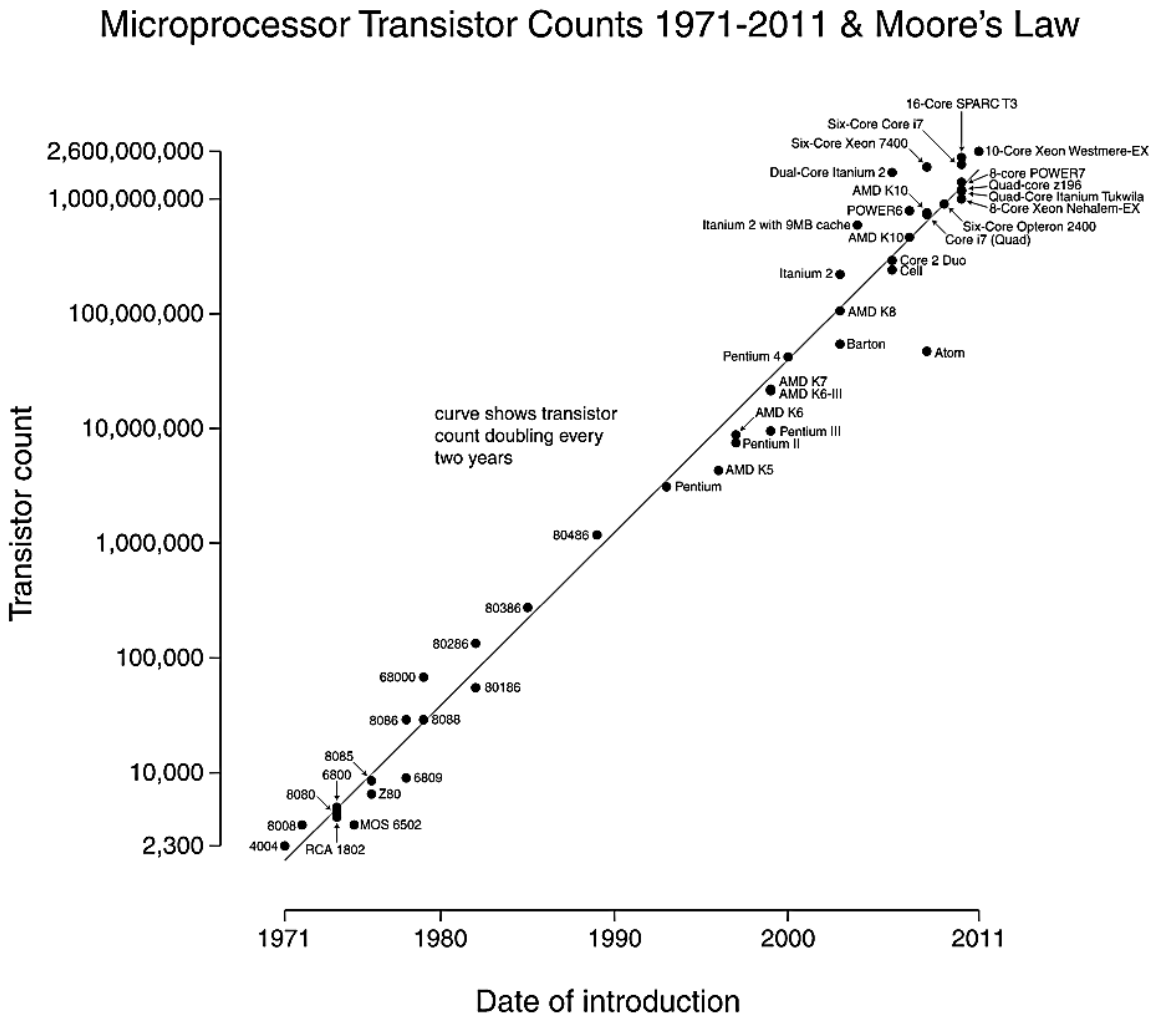

Figure 1-2 – Moore's Law & Microprocessor transistor count (logarithmic scale) vs. date of introduction [15]

The line width of the conduction channel in a state of the art MOSFET is presently 32 nm [16]; this is also known as the node size. In April 2012, Intel released its next generation IvyBridge with a node size of only 22 nm (Figure 1-3) [17-18]. Since the mid-1970s, projection optical lithography has been used to form these patterns, however in 2010, it was the first time that Intel deployed immersion lithography to achieve the 32 nm sized feature [19]. In immersion lithography, the light travels down through a system of lenses and then a layer of water before making contact with the imaging stack on the wafer. This ensures that the high spatial frequencies to a certain extent that carry information regarding the finer features on a shadow mask are prevented from decaying [20].

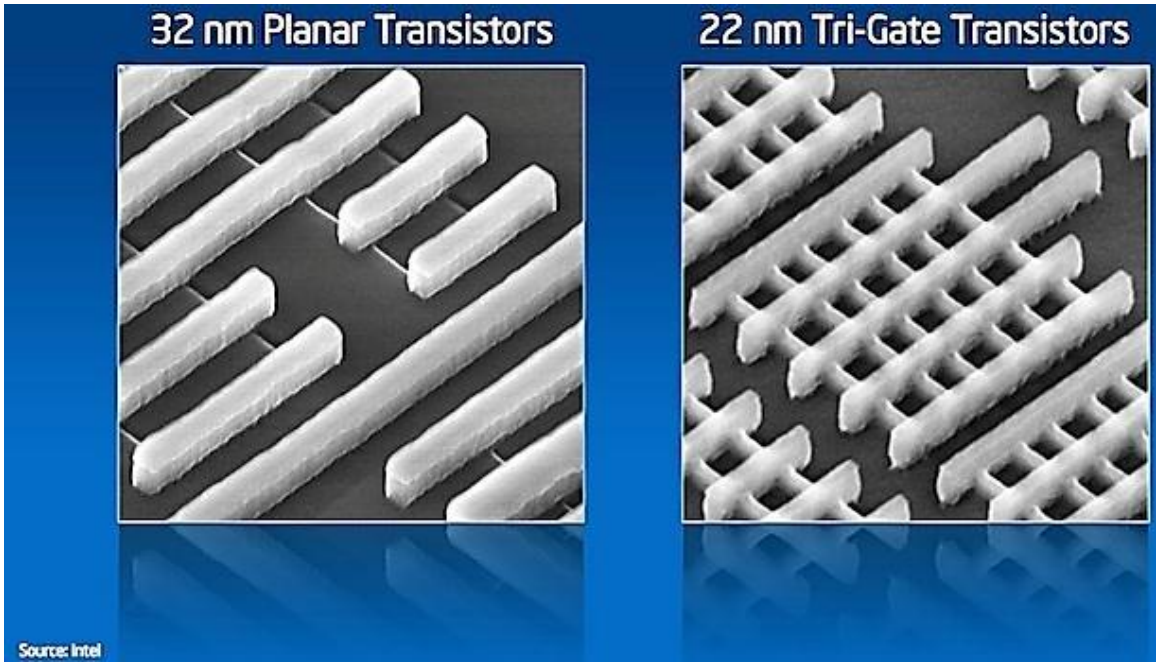

Figure 1-3 – (a) 32 nm Planar transistors on the Intel SandyBridge processor sold up until April 2012 (b) 22 nm Tri-Gate (aka 3D) transistors for the new Intel IvyBridge processor for better current control announced 23 April 2012 [21]

The industry has so far successfully tackled challenges that present themselves when attempts were made to further reduce size of features on an IC. Hence, if it is desired to progress through time at least at a pace at which we have for the past 40 years, then research in this field is vital.

It is believed that for a new technology to be marketable, three things are necessary;

Performance & quality of the results - This includes the feature resolution, line edge roughness (LER), pattern placement. In all a high quality factor is necessary

Cost - This is an economic factor. Moore's law is about lowering the cost per function. The goal is to integrate cheaper inexpensive components onto one piece of silicon to build a cheaper product. If the economic factor cannot be catered for, the product cannot be marketed.

Timing - The semiconductor industry is perhaps the fastest growing industry. It marches to Moore's law and if the right technology is not ready at the right time, regardless of all of the other factors listed above, the technology will not be marketable.

Moore's law has made several transitions. In the beginning, the primary goal was to scale up, i.e. add more transistors onto a chip. Over time, the goal shifted to being able to scaling down and shrinking down of feature sizes and hence transistors so that chip were faster and smaller.

It is predicted that Moore's law will make another transition in the near future. This will revolve around integration of multiple features on the same chip such as silicon photonics, microelectromechanical systems (MEMS), actuators, sensors, 3D integration of memory and microprocessors onto one chip. This is likely to replace scaling up and scaling down. Hence, innovation in the semiconductor industry is not over, by a long shot! [22]

1.2 Thesis Outline

This thesis presents research and experimentation dealing with scaling down, using a near-field optical lithography technique known as evanescent interference lithography. The technique allows achievement of considerably higher resolution (relative to wavelength) for repeating line and space patterns than those achieved by the industry's methods; however it also results in an image that is exponentially attenuated (evanescent) in the photosensitive medium (photoresist) thus making pattern transfer extremely difficult or even impossible. The thesis demonstrates via theory and successful experiments that coupling to the evanescent image via a carefully designed underlay beneath the photoresist allows energy to be extracted from the source beam and redistributed in the resist. This results in a pattern with a high aspect ratio. The end result is an extremely high resolution pattern of repeating lines and space that have a sufficiently high aspect ratio (or higher than necessary) to allow pattern transfer and thereby make this technique attractive to the semiconductor industry, but perhaps more so at this stage to fellow researchers involved in a similar area of work.

The remainder of this thesis is structured as follows. The background given in Chapter 2 introduces the reader to optical lithography and alternative technologies that are being worked on to act as replacements or additions to existing technology or even satisfy research curiosities that might one day allow the developed ideas to be used in the industry in one manner or the other. Ideas relating to the subject matter of the thesis work are also discussed including an in depth discussion of lithography using evanescent waves, that are capable of allowing extremely high resolutions.

Chapter 3 describes in detail the creation and experimentation with a test-bed to allow evanescent interference lithography. Results are presented as both atomic force microscope and scanning electron microscope scans and demonstrate successful ultra-high numerical aperture (*NA*) resolution lithography.

Following this, Chapter 4 presents the simulation and modeling of an interference lithography simulator that was created to allow analysis and further development of the results from Chapter 3.

Chapter 5 introduces the reader to the idea of evanescent wave enhancement by analyzing the Fresnel reflection equations at the boundary of two media in detail. The ideas are then developed to describe the physical mechanism behind such enhancement.

Chapter 6 again presents considerable theory, this time presenting the limits of evanescent wave interference lithography imaging in a photosensitive medium for both the transverse electric and transverse magnetic polarization of light. Ideas are then developed using a variant of the effective medium theory to show how multi-layered underlay setups may be handed. A design proposal is presented to be used at λ = 193 nm for the TE polarized system to demonstrate the potential of such an idea in enhancing the image depth from 20 nm to 83 nm for a pattern half-pitch of 26 nm.

A similar significant enhancement is then experimentally demonstrated in Chapter 7 along with further analysis of optimization limits. Several cases are experimentally demonstrated here that describe the performance of the system when a non-ideal setup is used, when a badly designed setup is improved using resonance compensation and when a well-designed setup is used. The enhancements are demonstrated once again using both AFM and SEM scans.

Chapter 8 concludes the results of the thesis and presents some insight regarding the future of this work.

1.3 Publications & Presentations

There are two more journal publications planned in addition to the conference/journal articles listed below. Of these, one is to be a comprehensive paper containing the key idea and methodology from this thesis along with experiments encompassing aspects of Chapter 2, Chapter 3, Chapter 5 and Chapter 7. The second is to be a rigorous derivation and analysis of imaging with evanescent interference fields as is carried out in Chapter 6. The work will be authored by Mehrotra, P., C.A. Mack and R.J. Blaikie.

Finally, aspects of this thesis have been published or presented as follows (primary author or presenter in bold),

Publications in Journals/Conference proceedings

Mehrotra, P., C.W. Holzwarth, and R.J. Blaikie, *Solid-immersion Lloyd's Mirror as a Testbed for Plasmon-enhanced High-NA Lithography*, San Jose, CA, USA: 2011 *Proc. SPIE, 7970, 79701L, SPIE Advanced Lithography, Alternative Lithographic Technologies III*. Feb 27 – Mar 3, 2011 (conference, oral)

Mehrotra, P., C.W. Holzwarth, and R.J. Blaikie, *Solid-immersion Lloyd's mirror as a testbed for plasmon-enhanced ultrahigh numerical aperture lithography.* Journal of Micro-Nanolithography MEMS and MOEMS, 2011. **10**(3). (journal)

Mehrotra, P. and R.J. Blaikie, *Using Reflection Resonances to Improve Depth of Field for Imaging at Ultra-High Numerical Apertures*, Sydney, NSW, Australia: 2011 IEEE in *Internaltional Quantum Electronics Conference (IQEC), Optical Nanoscopy*. Aug 28 – Sept 1, 2011 (conference, oral)

Mehrotra, P., C.A. Mack, and R.J. Blaikie, *A solid immersion interference lithography system for imaging ultra-high numerical apertures with high-aspect ratios in photoresist using resonant enhancement from effective gain media*, San Jose, CA, USA: 2011 *Proc. SPIE, 8326, 83260Z, SPIE Advanced Lithography, Optical Microlithography XXV*. Feb 12 – 16, 2012 (conference, oral)

Oral Presentations (presenter in bold)

Mehrotra, P., C.W. Holzwarth, and R.J. Blaikie, "Ultra-high-NA imaging with plasmonics and SILMIL", Conference on Advanced Materials and Nanotechnology (AMN-5), Wellington, NZ, February, 2011

Mehrotra, P., C.W. Holzwarth, and R.J. Blaikie, "Ultra-high-NA imaging with plasmonics and SILMIL", SPIE Advanced Lithography, San Jose, California, USA, February, 2011

Mehrotra, P., and R.J. Blaikie, "Using Reflection Resonances to Improve Depth of Field for Imaging at Ultra-High Numerical Apertures", Internaltional Quantum Electronics Conference (IQEC), Sydney Convention Center, Sydney, NSW, Australia, August, 2011.

R.J. Blaikie, P. Mehrotra, C.A. Mack., "Nanoscale Lithographic Imaging using Surface Plasmons and other Resonant Reflection Phenomena", Internaltional Conference on Nanoscience and Nanotechnology, Perth, Western Australia, Australia, February, 2012.

Mehrotra, P., C.A. Mack, and R.J. Blaikie, "A solid immersion interference lithography system for imaging ultra-high numerical apertures with high-aspect ratios in photoresist using resonant enhancement from effective gain media", SPIE Advanced Lithography, San Jose, California, USA, February, 2012

Mehrotra, P., C.A. Mack, and **R.J. Blaikie**, "Super-tall structures with Evanescent Interference Lithography using Resonant Reflection Phenomena", The 56th International Conference on Electron, Ion and Photon Beam technology and Nanofabrication, Waikoloa, Hawaii, USA, June, 2012

Poster Presentation

Mehrotra, P., C.W. Holzwarth, and R.J. Blaikie, "Ultra-high-NA Imaging with Plasmonics & SILMIL", The 55th International Conference on Electron, Ion and Photon Beam technology and Nanofabrication, Las Vegas, Nevada, USA, June, 2011

Chapter 2. Background

The development of low-cost lithography techniques for patterning nanoscale features over macroscopic areas (square millimeters and upwards) is important for a number of applications. For chemistry or biology the deposition of materials or the growth of cells on nano-patterned surfaces is of increasing interest [23-25], and for physics or engineering the ability to fabricate new nanoscale electrical, optical and/or magnetic devices requires convenient lithography techniques. Even in the semiconductor industry, where the requirements on the resolution, precision and throughput of a lithography technique are extremely challenging and lead to requiring high-cost manufacturing tools, the availability of lower-cost nanolithography techniques for research and process development is advantageous [26-27].

2.1 Overview

The primary goal of this chapter is to highlight the importance of the optical near-field and introduce the relevant background material applicable to the subject matter presented later in the thesis. The conventional optical projection lithography is explored here and this is used to present the optical diffraction limit, a resolution limit that restricts the minimum feature size that may be easily patterned. A short review of alternative technologies is also presented to highlight that several of these aim to image by making use of the optical near-field.

The performance of some of these techniques has been extended through the use of the plasmonic surface states. The first of these is the superlensing phenomenon that utilizes a silver layer to allow enhanced transmission of a sub-wavelength image to the imaging media which is reviewed here. Another plasmonic phenomenon that is briefly explored here (and in detail in the thesis) is the use of a plasmonic reflector, where a reflective enhancement of the image is proposed.

To shed some light on the use of optical surface states and also imaging at a single spatial frequency, two further sections are dedicated to their review. Firstly, the use of optical surface states forms a significant portion of this thesis, hence two different surface states namely plasmonic and excitonic are explored with their descriptions and commonly used setups. This is followed by a detailed review of interference lithography, the technique used to explore surface-state enhanced imaging here and its extension in to

solid-immersion to create the desired sub-wavelength spatial frequency or evanescent order for super-high resolution imaging.

2.2 Optical Lithography

Optical lithography, also known as photolithography involves the use of a shadow mask made up of opaque and transparent features (or phase features) that define the building blocks needed to be imaged onto a photosensitive material for patterning of transistors and interconnects. For several years, the preferred method of lithography was contact or proximity optical lithography. However, mask contamination was a major issue here. For this reason, the trend shifted to the use of projection lithography, where an expanded laser beam is directed towards the mask. The diffracted light produced by the features on the mask are then refocused onto the optical imaging stack with the use of an objective lens. A very simplistic schematic for this is depicted in Figure 2-1. In reality, illumination is oblique and numerous optical elements are employed for various purposes. The objective lens depicted in Figure 2-1 is in practice also used to allow reduction imaging. This allows the image to be a reduced magnification depiction of the features on the mask, which is an advantage as it simplifies mask manufacturing [6].

However, the image formed is only an approximation that is made using Fourier optics [28]. This is referred to as a diffraction limited image, meaning that it does not convey the complete information from the object plane. This is not an issue if the necessary features are properly imaged and are sufficiently distinguishable, however it does place a limit on how small the features on the source may be. Let us investigate what this means and how it restricts the minimum achievable resolution with optical lithography.

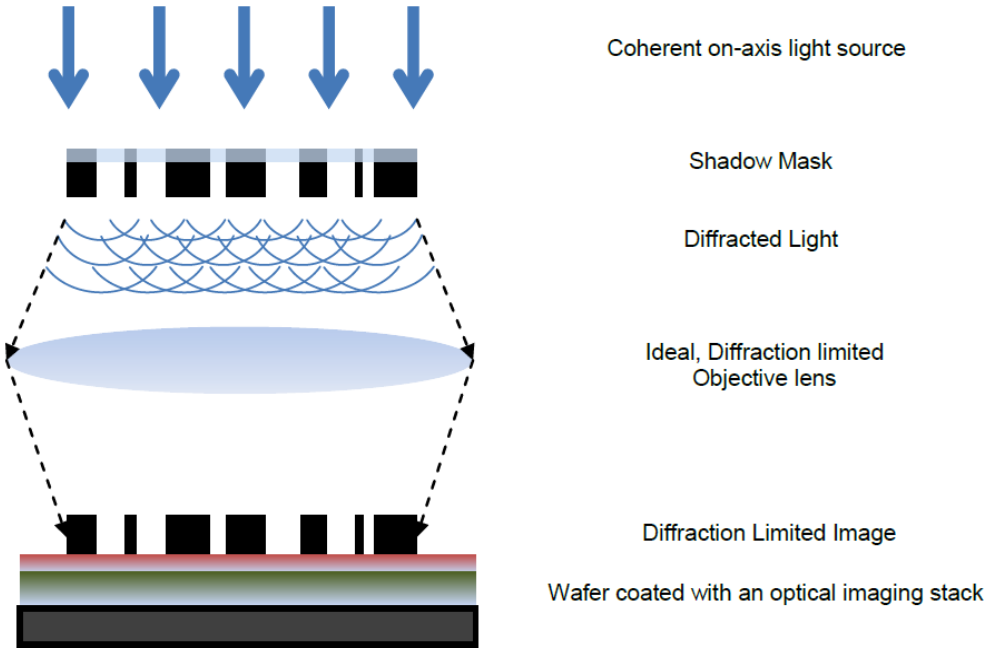

Figure 2-1 – Schematic of a simplistic on-axis coherently illuminated projection lithography system to demonstrate the creation of a diffraction limited image

2.2.1 The Diffraction Limit

Light diffracts as it passes through an object with opaque and transparent features. This creates a spectrum of spatial frequencies containing information about the dimensions of the features in the object plane. The smaller the feature size, the greater the resulting diffraction and hence a larger lens is necessary to capture the particular diffraction order for image reconstruction.

However, physical limits dictate what proportion of the information is available for image reconstruction in the far field in the Fraunhofer sense of the term 'far-field' [6, 28]. Consider objects comparable in size to the wavelength (λ) of the light and imagine that some objects are even smaller than half the wavelength of the light. This would result in diffraction past the 90^{O} angle, however this will not result in a propagating diffraction order. Instead, such a diffraction order decays exponentially from the source (and has a complex angle associated with it).

Under such circumstances, the best image may be formed by refocusing all of the propagating diffraction orders only or as many as can be captured. This is depicted using Figure 2-2, where a system has a light gathering ability such that the lens may capture a maximum diffraction order (or the largest propagating spatial frequency) that propagates at an angle θ_m from the source in a medium with refractive index n, then a value known as the numerical aperture NA may be defined as

$$NA = n \times sin(\theta_m) \tag{2.1}$$

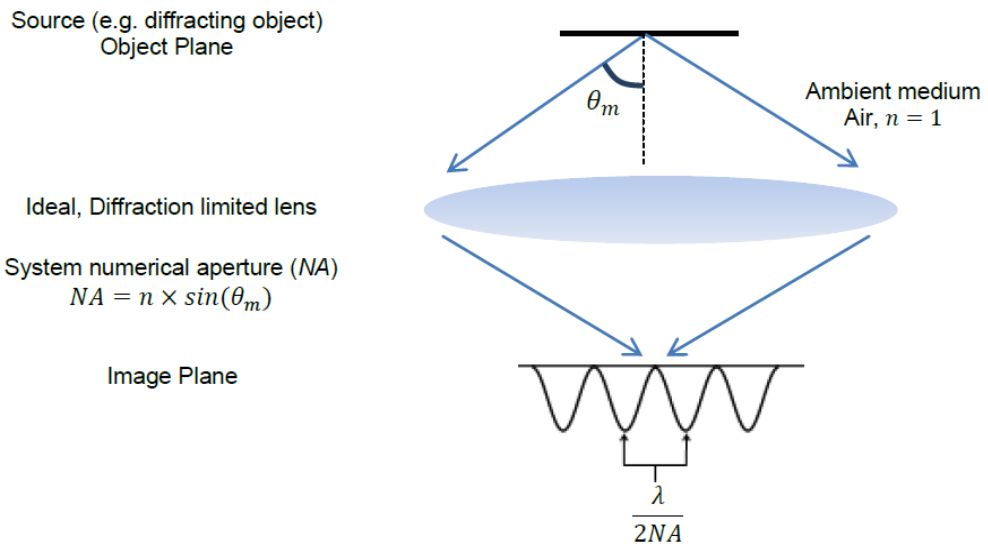

Figure 2-2 - Light gathering ability of the system defines a term known as the numerical aperture (*NA*). This is used to determine the best possible resolution that the system may achieve

The *NA* is also referred to as the optical size of a system and it indicates the largest spatial frequency that the system uses to create an image. Simple analysis of the superposition of the two interfering waves [6, 28] made up of the two maximal orders captured shows that for all these cases a standing-wave intensity profile is formed in the resist plane with period *p*,

$$p = \frac{\lambda}{2NA} \tag{2.2}$$

Note that a pattern with a smaller period (or pitch) may be created by increasing the refractive index *n* of the ambient medium, or by capturing a higher half angle θ_m closer to 90^O or by reducing the wavelength λ or by doing all three of these things. The half-pitch is then defined as half of the standing wave period, or $\lambda/(4NA)$ as given by (2.3) [6, 29]. Of course, several hurdles exist in an actual fabrication system, and the actual resolution limit *R*, defined as the minimum half-pitch of a pattern that can be resolved in a particular lithography system, is given as,

$$R = k_1 \frac{\lambda}{NA}, k_1 \geq 0.25, \tag{2.3}$$

where k_1 is some tooling factor for the particular lithography system [6]. In the semiconductor industry, every effort is made to minimize the factor k_1 such that it is close to 0.25. An example of a state of the art lithography system is the ASML TwinScan XT:1950i scanner that is a water immersion (immersion

lithography is discussed in a subsequent section) stepper which utilizes the industry standard argon fluoride (ArF) λ = 193 nm wavelength. It is designed to provide a maximal system *NA* of 1.35, for volume production of 300 mm wafers at the 32 nm node and beyond, and allows a throughput of ~ 140 wafers/hour (wph) [30-31].

Figure 2-3 – ASML TwinScan XT:1950i – A state of the art water immersion stepper for the sub-32 nm node, designed for a *NA* of 1.35 operating at the ArF, λ = 193 nm. It has a throughput of ~ 140 wafers/hour [30-31]

For $k_1 = 0.25$, equation (2.3) is known as Abbe's diffraction limit [6, 29]. It is also worthwhile mentioning that due to the sophistication of integrated circuits today, it is becoming increasingly easier to define features using successive steps each of which pattern a repeating set of lines and spaces followed by trimming away of the undesired features – the so called double patterning or multiple patterning techniques. This begs the question, what needs to be done to create an image that has a feature smaller than that given by Abbe's diffraction limit – to avoid the need for double patterning?

As mentioned above, when feature sizes smaller than the wavelength of light need to be imaged, a large proportion of the spatial frequency spectrum is non-propagating. This is in fact a state of light known as an evanescent wave that has the potential to provide higher resolutions that those given by (2.3). Evanescent spatial frequencies hold information regarding the sharpest (highest resolution) features in the object plane. Unfortunately evanescent fields are confined to the boundary between the object and ambient media and carry no energy away from the object plane. A wave that propagates in one medium may be evanescent in another. A simple example that most people are familiar with is the total internal reflection (TIR) that can take place at the boundary between a glass prism (n_2 = 1.5) and air (n_1 = 1), see Figure 2-4 for a schematic.

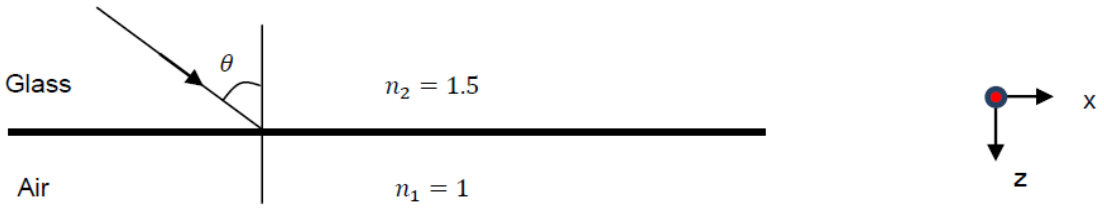

Figure 2-4 – Schematic of a simple glass-air boundary setup

TIR takes place when the *NA* is made to be greater than the refractive index of air. Hence, when the incident angle inside a glass prism at the glass-air boundary is $\theta \geq 42^O$, TIR takes place and Maxwell's equations dictate that an evanescent field must exist on the air side of the boundary. This may be explained by considering the wave number (measured in radians per metre). For a wave in free space its wave number is simply $k_0 = 2\pi/\lambda$. Within a medium of refractive index n, the wave number of the same wave (assume a uni-directional wave) now becomes $2\pi/(\lambda/n)$ or nk_0. Decomposing this value into its x and z constituent wave vectors i.e. k_x and k_z respectively, we have the relationship $n^2k_0^2 = k_x^2 + k_z^2$. Note, that for a particular uni-directional wave the value of k_x is the same in any media regardless of the refractive index of the media. This result is easily derived using Snell's law. The value of k_z however is dependent upon the refractive index of the particular media.

$$k_{z,1} = \sqrt{n_1^2k_0^2 - k_x^2}$$
$$k_{z,2} = \sqrt{n_2^2k_0^2 - k_x^2} \qquad (2.4)$$

Now consider in equation (2.4), the scenario where $n_1 = 1$ (air) and $k_x = k_0$. In this case the wave does not propagate away from the boundary into air and the incidence angle within the prism is exactly 42^O, resulting in $k_{z,1} = 0$ and $k_{z,2} = 1.12k_0$. If however, the incidence angle within the glass prism is greater

than 42^O (making $k_x > k_0$), then $k_{z,1}$ becomes imaginary and the field on the air side of boundary is known as an evanescent field, which decays in the direction normal to the interface, whereas on the glass side of the interface, the field is always in its propagating state.

Of course if the air was lossy, then the TIR would not be ideal. Similarly, if another glass slab was brought close to this boundary so that the air gap was less than a wavelength in size, then evanescent wave coupling would take place to the second glass slab, causing light to revert back to its propagating state in the second glass slab, an experiment that was first documented by Sir Isaac Newton himself and published in Opticks [32].

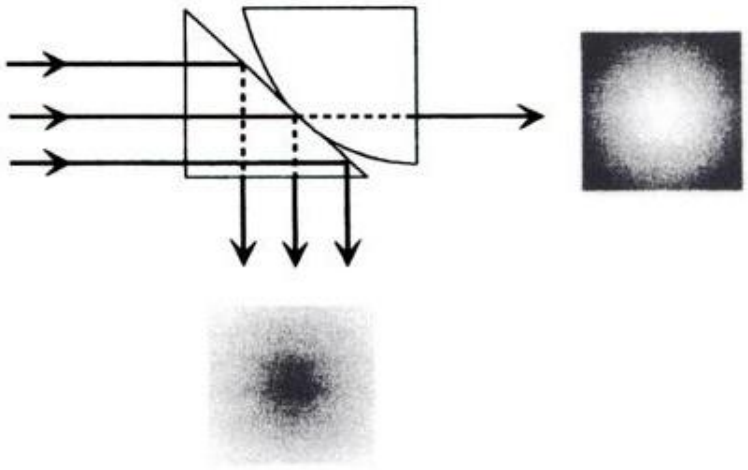

Figure 2-5 – Scheme of Newton's famous frustration of light experiment. A prism is illuminated in total internal reflection and a lens with a large radius of curvature is brought into contact with the prism. Along the axis of the incident beam, a luminous area larger than the point of contact is observed – Reprinted from [33]

Opticks is considered as one of the greatest works of science in history. Newton documents here the discovery of the so called Newton rings and frustration of evanescent waves, see Figure 2-5 for the scheme of this experiment. By adding a loss or bringing another glass slab close to the primary glass slab, one can 'frustrate' the evanescent field into propagation, allowing it to carry energy away from the boundary. This is so because the presence of another slab now changes the boundary conditions under which Maxwell's equations have to be solved. The latter case, where the addition of a loss frustrates the evanescent field is also explainable and the reader may refer to both Zhou et. al. [34] and Mehrotra et. al. [35] who explain this in different ways. We present our analysis of this interesting phenomenon in a later section dealing with evanescent field frustration within an absorbing medium.

Perhaps then, there is a way to utilize the evanescent components of light to create higher resolution images, by taking further advantage of this frustration. Before exploring this, let us investigate existing

research in alternative technologies, some of which take advantage of the optical near-field and some which do not. This should be help to set the scene for what is presented in the later chapters of this thesis.

2.3 Alternative Technologies

Intense research has been and is being carried on in readying alternative techniques to UV projection lithography. Extreme Ultra-violet (EUV) systems operating at λ = 13.5 nm are extensively pursued [36-41], but are expensive to run, offer a lower throughput than present systems, require greater maintenance and require high vacuums and reflective lensing due to the high absorption of most materials available at that wavelength. Their future availability is still in doubt.

Alternative non-optical techniques are also being pursued, *e.g.*, there is a considerable amount of literature available for the massively parallel electron beam lithography tool called MAPPER which is being developed to allow higher resolutions and a higher throughput [42-47]. Similarly, the directed self-assembly of block copolymers for nano-lithography has also garnished considerable research attention from universities and industry [48-52].

Other optical techniques are also being pursued that aim to pattern by beating the diffraction limit as opposed to reducing the wavelength and increase the *NA*. One such technique is Absorbance Modulation Optical Lithography (AMOL), [53-59] which has attracted considerable attention. It is an innovative optical technique that is in many ways a lithographic analogue of Stimulated Emission Depletion (STED) Microscopy [60-61]. AMOL proposes the replacement of a normal metal mask of a lithography system with a absorbance modulation layer (AML) that is in intimate contact with the underlying resist. The competition of two incident wavelengths of light each of which change the refractive index and extinction coefficient of the AML allows the creation of an adaptive absorbance mask (see Figure 2-6).

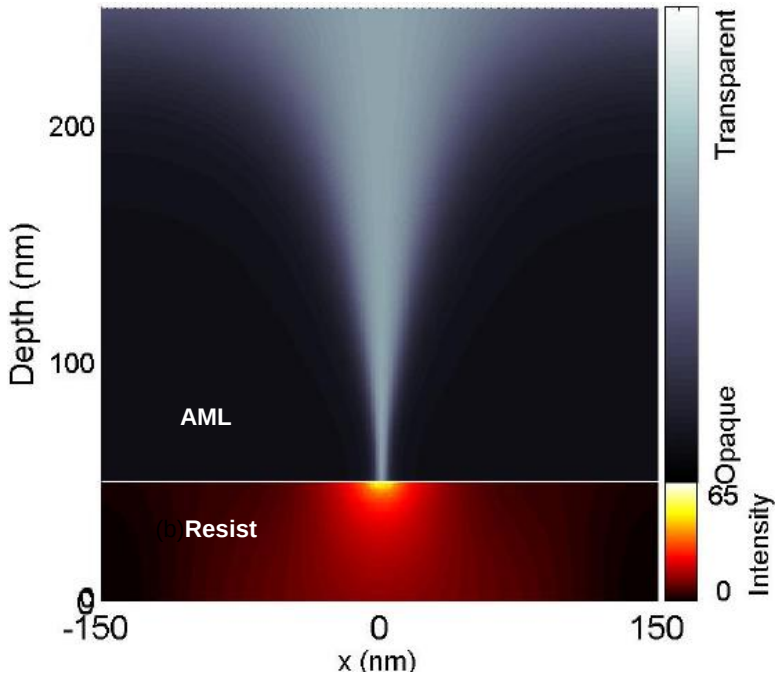

Figure 2-6 – Absorption modulated optical lithography with 2 different wavelengths. One wavelength is spatially modulated using an interference pattern, while the other forms a plane wave. Together this results in a transparent to opaque gradient in the absorbance modulated layer (AML). The image in the resist is then through a sub-diffraction aperture. – Reprinted from [62]

While one wavelength acts to create transparency, the other creates opacity in the AML. The intensity ratio of the competing wavelengths allows the creation of an artificial aperture through which the imaging wavelength is guided outwards in a more desirable manner than it would otherwise through a real aperture.

Several of the alternative optical technologies have been geared towards making use of the optical near-field, e.g. AMOL as described above. The Evanescent Near Field Optical Lithography (ENFOL) technique was created by a team at the University of Canterbury, New Zealand in 1999 [63-65] is also one that taps into the potential of imaging using the optical near-field. This is described further here, as it provides motivation for much of the work presented in this thesis.

Plasmonics has also been looked to for solutions to beating the diffraction limit ever since the classical paper by Sir John Pendry [66] was published and the superlens was experimentally demonstrated by two groups independently; Fang *et al*.[67-70] and Melville & Blaikie [71-80]. This is also discussed in some detail as the method was essentially used to extend performance of the ENFOL system mentioned in the previous paragraph.

2.4 ENFOL & Superlenses

Contact lithography, while simple, does not allow imaging of sub-diffraction limited features. This is because parts of the photoresist may still relatively be in the far-field of the mask where only propagating waves are captured. Imaging at higher resolutions using contact lithography would require intimate contact between the mask and the resist layers over a large area so that near-field exposures may take place. However, the extent of intimate contact required for near-field exposure is in the order of tens of nanometers and this is clearly not achievable over large areas due to the rigidity of mask plates that are commonly used in contact lithography. This is where Evanescent Near Field Optical Lithography (ENFOL) [63-65, 81] steps in.

ENFOL is a near-field lithography technique developed by a team at the University of Canterbury, New Zealand in 1999 (see Figure 2-7). It is a simple yet extremely effective extension of contact lithography that allows the mask pattern to be transferred directly to the photoresist. The difference here is that the mask material is in fact made up of a substrate that readily conforms under pressure, thus allowing intimate contact to be achieved between the mask and the resist.

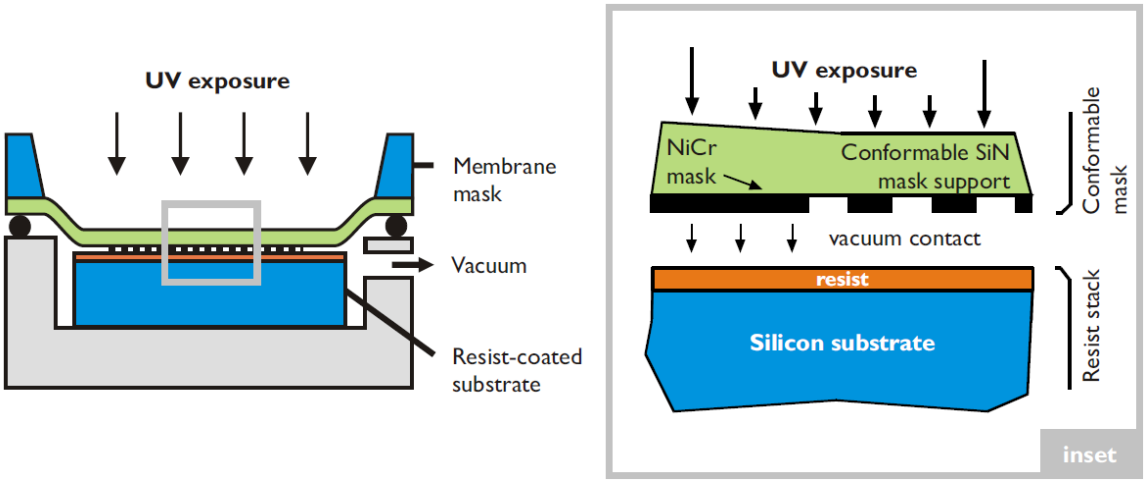

Figure 2-7 – Experimental setup for evanescent near-field optical lithography (ENFOL). Intimate contact lithography is achieved by taking advantage of a conformable membrane mask and a vacuum – reprinted from [82]

Once this is achieved, even the sub-diffraction limited features are imaged just as easily. ENFOL has received considerable attention in the past 13 years and was also used by Canon Inc. [83] to demonstrate 32 nm lines using light with a wavelength of 365 nm, this corresponds to a λ/11.4 feature size (see Figure 2-8).

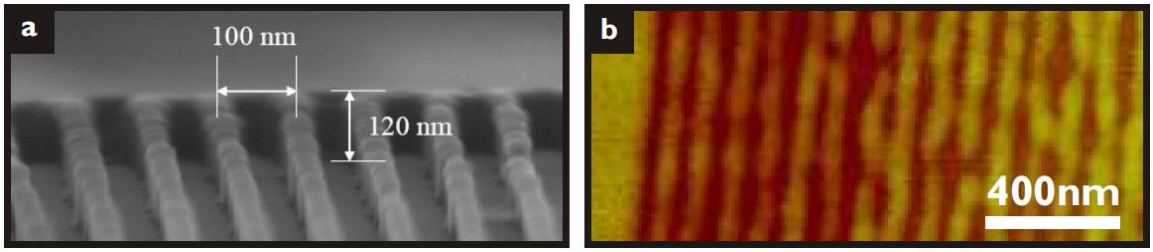

Figure 2-8 – Performance demonstration of the ENFOL system (a) SEM scan of 30 nm features (100 nm pitch) with an image depth of 120 nm using 365 nm light patterned by Canon Inc. [83] using a SiN mask (b) AFM scan of 50 nm features on a 100 nm period exposed using 240 nm light produced by Matthew Arnold at the University of Canterbury – reprinted from [82]

2.4.1 Resolution limits for ENFOL

In short, ENFOL has no fundamental resolution limit. The depth of field scales with the feature size and enforces a practical limit for imaging due to the evanescent nature of light. This may be explained simply by first considering a source that emanates evanescent waves. If two different evanescent orders are considered, their decay rate may be compared and shown to be very different, thereby also making their respective depth of field very different. This is illustrated here using a simple diagram (see Figure 2-9). Consider again the example of a glass prism and air boundary (see section 2.2.1 and equation (2.4)). In the first scenario, assume that $k_x = 2k_0$ (Figure 2-9 (a)), this makes the wave evanescent with an imaginary wave number $k_z = i\sqrt{3}k_0$ in the direction normal to the interface. The intensity of the field drops to 40% of its initial amplitude at a depth $d = \ln(0.4)/(-2\sqrt{3}k_0)$, whereas if the evanescent spatial frequency were to be doubled so that $k_x = 4k_0$ (Figure 2-9 (b)), then $k_z = i\sqrt{15}k_0$ and at the same depth d, the field's intensity falls to below 13% of its initial value. This decay variation with respect to evanescence is directly responsible for a depth of field scaling in an imaging medium with ENFOL.

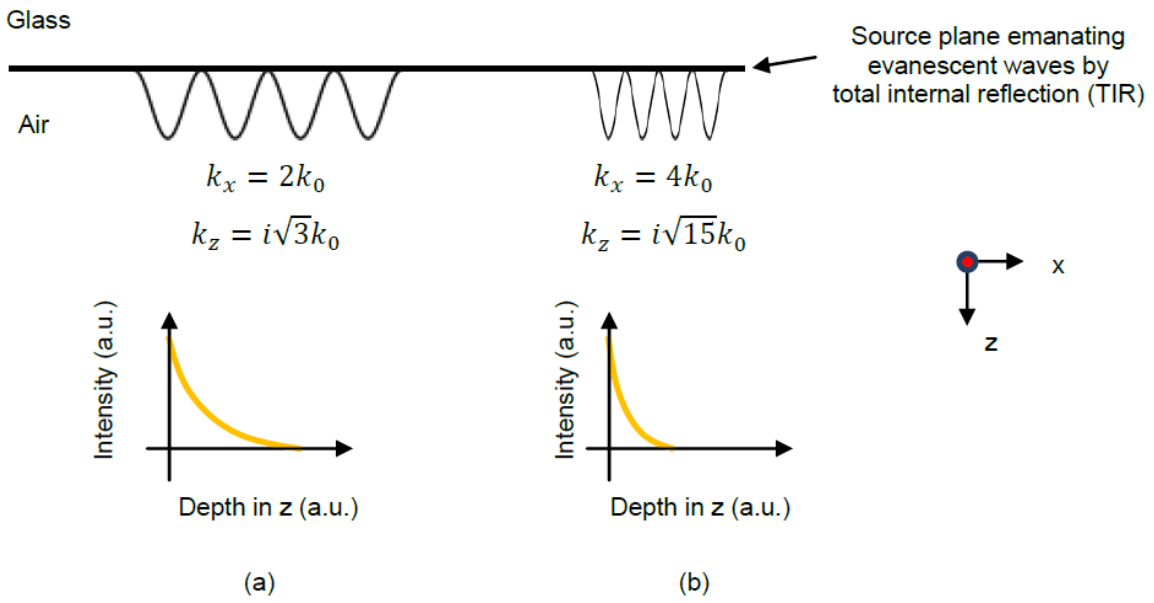

Figure 2-9 - Depth of field is essentially the intensity decay within the imaging medium, it is (a) lower for a lower evanescent spatial frequency and (b) higher for a higher evanescent spatial frequency

For this reason, the Canterbury group investigated how such evanescence could be countered by making use of a radical idea introduced in 2000, known as the superlens. But before the principle of operation of the superlens is described, let us briefly review how a perfect lens might work and what special media may be required to create such a device.

2.4.2 Superlens enhanced ENFOL

Negative Refraction and Perfect Lenses

The spatial spectrum from a sub-wavelength mask is dominated by evanescent waves and as ENFOL has shown, these may be imaged by bringing the imaging layer in intimate contact with the mask itself. This requires addressing issues such as mask contamination, and requiring mask defect testing and ultimately adds a cost (in monetary terms as well as time and effort) to the creation of masks more frequently than may otherwise be required if propagating images were being imaged. This raises the issue whether the decay of evanescent waves can in anyway be countered so that such intimate contact is non-degrading to the system.

It turns out that in 1968 Victor Veselago proposed that the use of a planar slab of material that had both a negative electrical permittivity and a negative magnetic permeability (known as a double negative material (DNG)) would also have a negative refractive index [84]. Approximately, three decades later in the year 2000, Sir John Pendry published a seminal paper [66] that suggested that such a material may in fact be used to create a perfect lens. Pendry showed that not only does a slab of negative refractive index

material allow refocusing of the propagating waves, it also in fact enhances the evanescent waves allowing the image to be perfectly refocused using a surface resonance. A schematic of how a perfect lens may be used to re-create an image is illustrated in Figure 2-10 [85].

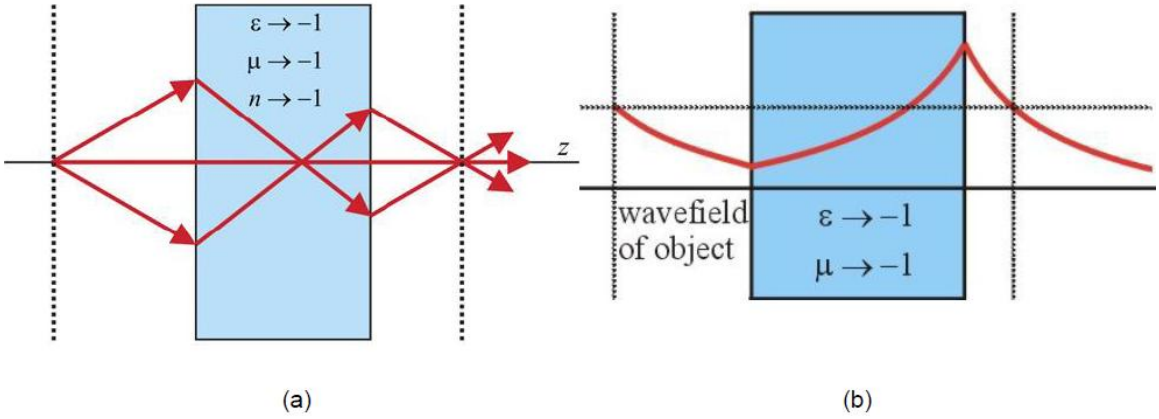

Figure 2-10 – A double negative slab exhibits negative refraction and evanescent wave enhancement (a) Focusing of propagating waves through negative refraction (b) Amplitude restoration of a decaying evanescent wave through surface resonant enhancement – Reprinted from [85]

A negative refractive index material requires that both the electrical permittivity and the magnetic permeability are simultaneously negative [84]. This allows the medium to bend light in the direction opposite to that which its positive refractive index counter-part does. While a negative index material does not naturally exist, the desired negative refracting effect may be obtained by fabricating structures of artificial atoms that are much smaller than the wavelength that is to be negatively refracted, i.e. in the order of $<< \lambda/10$. At microwave frequencies, these could consist of copper split ring resonators (SRR) and wires mounted on interlocked sheets of fiber glass, placed in regular arrays. The array of SRRs give the material an effectively negative permeability by mimicking a magnetic plasma, while the array of wires give the material a negative electrical permittivity by mimicking an electric plasma [86-88]. Such materials were first demonstrated by Smith et. al. [89] and Shelby et. al. [90] at a microwave frequency that has a wavelength of ~12 cm in free space.

In the optical frequency range, it is extremely rare to encounter materials that exhibit any magnetic coupling let alone exhibit a negative magnetic permeability. The fabrication of a negative index metamaterial at the optical frequencies i.e. 700 nm – 400 nm would require the artificial atoms to be smaller than 70 nm – 40 nm respectively, in addition requiring feature sizes that are even smaller. Unusual propagation behavior such as a reversal of phase and group velocities is exhibited in photonic crystals, however, negative propagation does not occur [91-93]. Hence, another approach is needed for the time being. This is where the silver superlens becomes an attractive option.

Silver Superlens

Metals in the visible frequency range do exhibit a negative electrical permittivity. Pendry also described in his paper that a metallic slab of silver can restore the amplitude of the higher order Fourier components (evanescent spatial frequencies) in order to recreate the image. Pendry's argument was that evanescent orders do not decay in phase, but only in amplitude and hence that these need to be amplified rather than phase corrected to achieve focusing. It was further highlighted that there is a link between the focusing action and the existence of well-defined surface plasmons.

This paper by Sir John Pendry attracted a considerable amount of interest from the research community and soon after two groups independently and simultaneously set out to and successfully demonstrated the silver superlens in the optical regime, Fang et al.[67-70] and Melville & Blaikie [72-80].

The working of a silver superlens is very interesting, as its operating principle is somewhat similar to that of a two pole band-pass filter from an electrical engineering analogy. In many ways, the silver superlens is an optical analogue of such a filter. For further information regarding the working of the silver superlens, the reader is directed to [94-95].

Let us not digress and highlight that Melville & Blaikie [71-80, 82] set out to use ENFOL once again as the imaging test-bed to demonstrate the performance of the silver superlens, which resulted in their work receiving considerable attention from the research community such as numerous citations and mentions [76, 96]. Schematics depicting a comparison between ENFOL and superlens-enhanced ENFOL setups are provided in Figure 2-11 below.

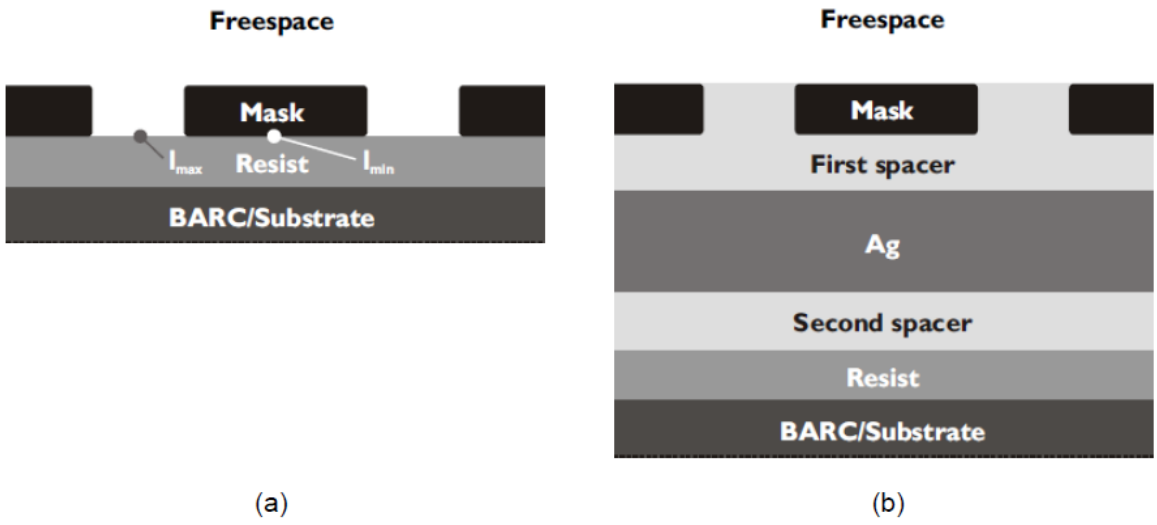

Figure 2-11 – Schematic layout for (a) ENFOL an (b) superlens enhanced ENFOL, cropped and reprinted from [82]

One of their results for imaging a sub wavelength grating mask is depicted in Figure 2-12 below for (a) conventional ENFOL and (b) superlens-enhanced ENFOL. The superlens-enhanced ENFOL is seen to have allowed far better imaging of the 170 nm sub-wavelength gratings than the ENFOL case, indicating a definite enhancement.

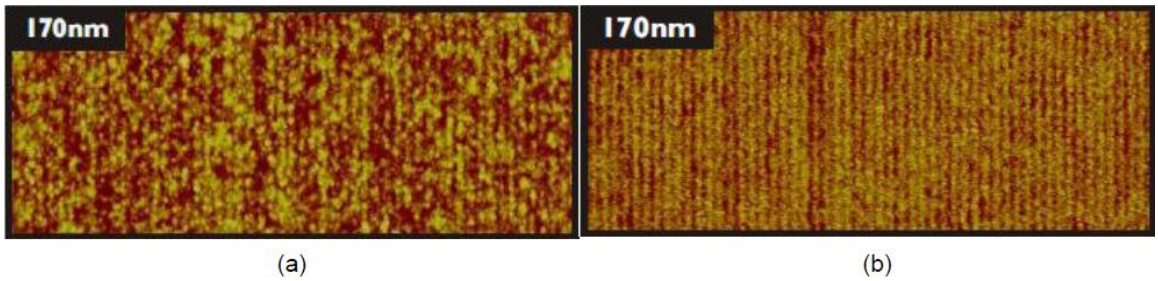

Figure 2-12 – AFM images of a 170 nm grating imaged with a 365-nm wavelength exposure through the 25nm/50nm/10nm PMMA/Ag/SiO_2 lensing stack (a) ENFOL (b) superlens enhanced ENFOL, reprinted from [82]

Of course, the evanescent wave curiosities did not end here. Following the success of the silver superlens adventure, another idea was proposed by Blaikie et. al. [97], regarding the possibility of how it might also be possible to enhance ENFOL by placing a metallic reflector below the imaging layer, when it was noted that the area above a superlens experienced an image enhancement. A more thorough investigation was later carried out by Arnold et. al. [98]. While originally termed surface plasmon enhanced contact lithography (SPECL), this is in fact an extension of ENFOL and so we refer to it here as plasmonic reflector-enhanced ENFOL.

2.4.3 Plasmonic Reflector-enhanced ENFOL

This is an interesting concept as conventional wisdom has thus far guided us to ensure a non-reflecting underlay. The rules of the game however may need to change if one wishes to image using evanescent and not propagating waves. Plasmonic reflector-enhanced ENFOL is depicted in Figure 2-13.

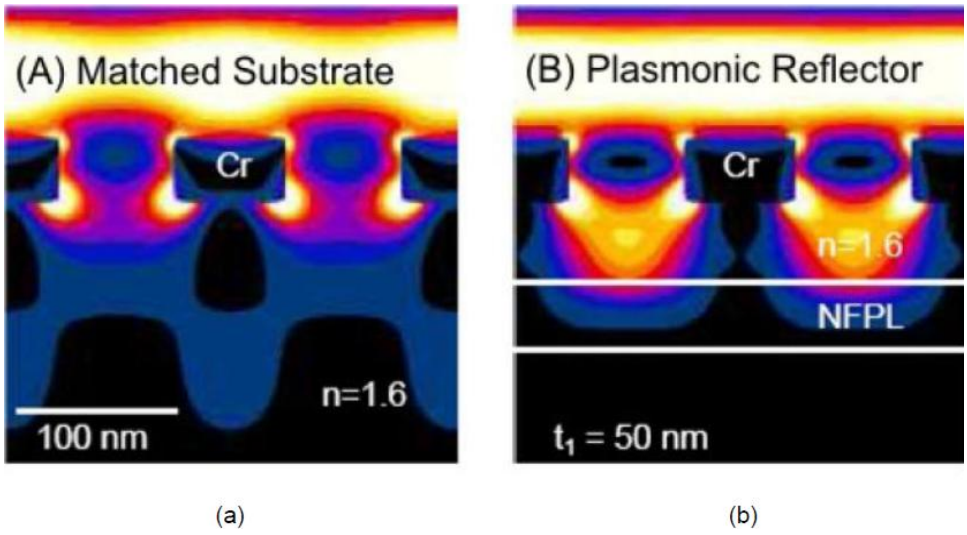

Figure 2-13 – Comparison of an ENFOL system with and without a near-field plasmonic layer (NFPL) demonstrating improved confinement in resist. Intensity profiles for 140 nm period Cr gratings illuminated at 365 nm with (a) an index matched substrate and (b) a silver NFPL. [97]

Arnold et. al. [98] concluded that a plasmonic slab would work as an approximate super-mirror and computed the reflector position and electrical permittivity to achieve optimum image uniformity. The paper also briefly investigates such a requirement for the scenario where only one evanescent spatial frequency is to be imaged using two beam imaging (aka evanescent interference lithography discussed in a subsequent section). A detailed review of how interference lithography may be used to create an image using only one spatial frequency is presented in a later section in this chapter.

This idea was further developed by us, and its inner workings were established; the theory developed once again highlights the link between evanescent wave enhancement and the presence of well-defined surface states. This theory formed a significant portion of another paper by Mehrotra et. al [35]. A large portion of the research presented in this thesis finds its roots in this idea and analyses what may be required of a reflector, theoretically and for practical feasibility if only one evanescent spatial frequency was being dealt with instead of the spectrum that ENFOL produces.

For this reason the next two sections presented here review surface states and lithography with a single ultra-high spatial frequency (aka. evanescent interference lithography). The applicability of surface states to the subject matter is presented in the following section. Two optical surface states are discussed. The first is a surface plasmon that has extensively been researched and cited numerous times in literature. The second is a surface exciton, a surface state that has received considerably little attention. Following that, a detailed review of conventional interference lithography followed by evanescent interference lithography is presented.

2.5 Surface States – Plasmonics & Excitonics

Plasmonics has been looked at to improve evanescent wave imaging as was illustrated with several examples in the last section. The core mechanism of operation there was however the presence of a surface state. A surface state is an electromagnetic state that exists at the interface of two media and is found only at the atom layers closest to the surface. The termination of the material, i.e. a surface causes a change in the electronic band structure that is contrastingly different from the bulk of material. This causes a weakened potential at the surface that allows new electronic states called surface states to form [99-100].

2.5.1 Surface Plasmon Polariton

A plasmon is a unit of a plasma oscillation. This is a quasiparticle that results from the quantization of plasma oscillations. The plasmon is a collective oscillation of the free electron gas density at optical frequencies. When coupled with a photon, it creates another quasiparticle known as the plasmon polariton. More information and in depth analysis of plasmonics and surface plasmons is available at [96, 101-102].

Plasmonics has always attracted considerable attention from researchers, and even more so in the past 2 decades. One of the drivers for these has been a classical letter in Nature by Ebbesen et. al. [103] that showed that the transmission through a thin metal film could in fact be enhanced by patterning it with a regular array of holes, a result so bizarre that it led the authors to believe they had made a mistake and retract their paper. Later it was proved that the result was in fact correct and the extraordinary phenomenon took place due to the ability of the plasmons to redistribute energy among spatial frequencies. The reader is encouraged to review related work by Ebbesen et. al., and Lezec et. al. and other researchers dealing with the effects of light passing through subwavelength metallic apertures both patterned and non-patterned [103-109].

On a slightly different note, plasmons may also be mimicked using structured surfaces; this was shown by Pendry et. al. [110]. Sir John Pendry is now also well known for the theoretical discovery that a thin film of silver would act as a superlens [66], this has been another driver in attracting research attention to plasmonics. A large portion of the work referenced in the above two paragraphs also suffices as excellent introductory material to plasmonics for a researcher new to this field.

The interface between a dielectric and a metal is capable of supporting a self-sustained oscillation known as a surface plasmon polariton (SPP). When the correct polarization of light is chosen such that there is a

component of the electric field that is normal to the interface (transverse magnetic (TM) polarization) and when the energy and spatial momentum of the incident wave vector matches that of the SPP, the oscillation is set in motion. Figure 2-14 illustrates such a process, whereby the excitation at a metal-dielectric surface has resulted in an SPP wave to travel in the direction of the *x* axis. Of considerable interest and relating to the subject matter presented in this thesis is the fact that there is enhancement and confinement of the fields to the interface, a characteristic of a surface state [111]. At an increasing distance, the fields decay exponentially into either media and are thus evanescent.

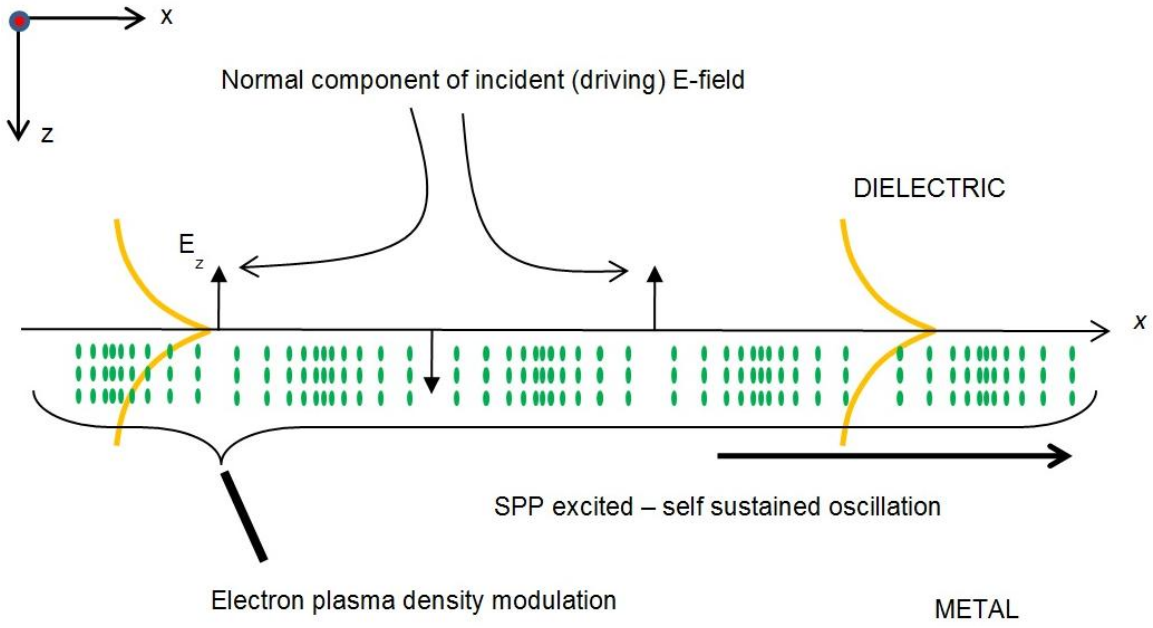

Figure 2-14 – A Surface Plasmon Polariton (SPP) excited at the interface of a metal and dielectric with enhanced and localized E-fields at the interface, and decay away from the interface

This is easily derivable by placing these demands when solving Maxwell's equations at such an interface [96]. The result of this derivation is a condition that needs to be satisfied that relates the requisite wave vector to the optical properties of the media.

$$k_x = \frac{2\pi}{\lambda}\frac{\varepsilon_{dielectric}\varepsilon_{metal}}{\varepsilon_{dielectric} + \varepsilon_{metal}} \qquad (2.5)$$

The requisite wave vector (2.5) for a surface state as such to exist may be excited by several means [101]. Firstly, it is required that the wave be evanescent in both media as this is the demand that was placed to derive (2.5). Hence, the *NA* of the wave is then higher than the refractive index of the dielectric media. For this reason, the SPP may not be excited through free-space coupling, because the maximum achievable *NA* in free space is 1 (at 90^{O} incidence angle). Clearly, another method is needed.

One of these methods is the use of inherent surface roughness at a metal layer boundary that acts to cause random re-scattering and result in several wave vectors, one of which will satisfy the requirement imposed by (2.5). Another method is the use of a diffraction grating that creates a more regular distribution of diffraction orders. Such a grating would then be tuned to also produce the diffraction order with the requisite wave vector. Lastly, the use of a prism coupled setup such as the one depicted in Figure 2-15 may also be used. The prism coupled setup may be implemented either as the Kretschmann configuration Figure 2-15 (a) or as the Otto configuration Figure 2-15 (b) [112]. Although, the principle of operation for both of these setups is the same, it is the latter of the two that has been utilized for the theory and experiments contained in this thesis, for reasons that will become clear as the imaging optical stack is introduced.

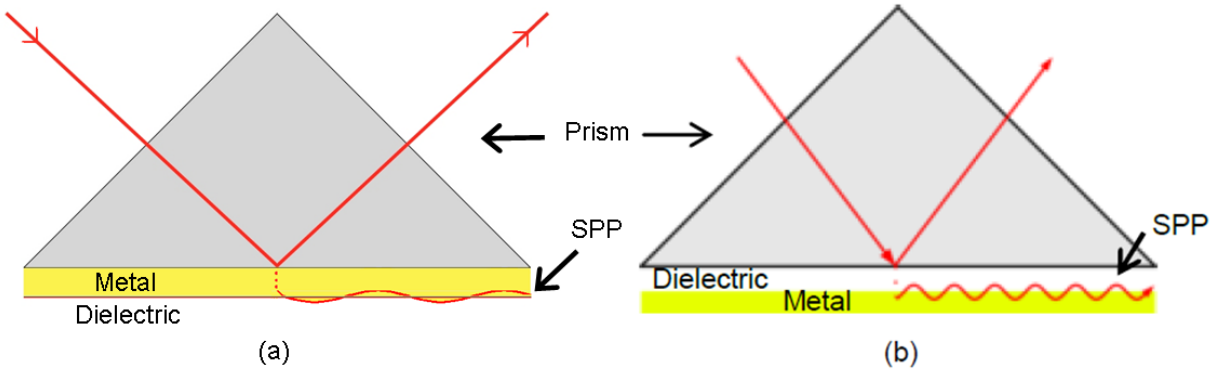

Figure 2-15 – Prism coupled setups to excite a Surface Plasmon Polariton (SPP) using the (a) Kretschmann configuration (b) Otto configuration (reprinted from [112] and modified)

The presence of a surface state is observed only when it acts to extract and redistribute energy. For example, while the interface of a lossless dielectric and a metal supports a surface state, the effect is invisible until a slight loss is introduced into either media. When this is done, a beam of light incident at and around the angle corresponding to the requisite wave vector is not fully reflected away. Instead, the reflection is attenuated, this is owing to the ability of the surface state to localize the electric fields and allow dissipation of energy in the lossy media. This is a near-field phenomenon that successfully results in energy extraction from the far-field and its redistribution in the near-field. The act of observation requires the introduction of loss into the system; however this act also changes the system slightly. The measurement of the reflected beam for various angles of incidence is a well-known experiment known as the attenuated total reflectance (ATR) experiment.

A common use of such a setup, particularly the Kretschmann configuration is in Surface Plasmon Resonance (SPR) sensors [112]. A typical SPR sensor is required to be able to sense the presence of a

molecule in a solution. This is achieved by first measuring an attenuated total reflectance (ATR) spectrum for the setup in the solution where there are no molecules present. At a particular angle, corresponding to the requisite wave vector for this setup, the reflection is severely attenuated as the SPP is excited. Following this, the Kretschmann setup is placed in the solution where the necessary molecules may be present. The setup is equipped with the required appendages to capture the molecule if it is present in the solution. If the molecules are captured, then the SPP is no longer excited at the same wave vector as it was before as the requisite criterion is now changed. The effective optical property of the dielectric now incorporates in some way the effects of both the original dielectric and the detected molecule. The shift in the resonant dip an ATR spectra allows the user to verify whether the molecule has been detected or not. This is illustrated using Figure 2-16.

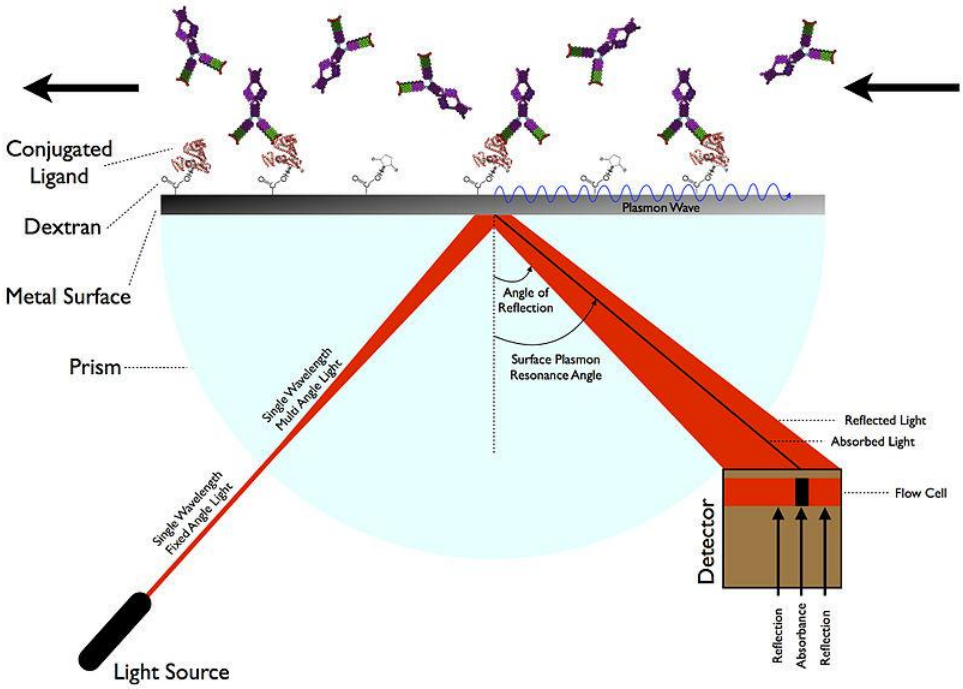

Figure 2-16 – Surface Plasmon Resonance sensor using the Kretschmann configuration [112]

2.5.2 Surface Exciton Polariton

Of relevance and interest to the thesis matter is the surface exciton polariton. This is another elementary excitation that propagates along the boundary between an outside dielectric medium and a crystal with Wannier-type excitons as the elementary bulk excitation. Considerable work was carried out by Lagois and Fisher [113-114] in the mid to late 1970s. Once again, its effects may be observed using the ATR method. Here, the excitation is not due to the contribution of free electrons, but due to the movement of the electron-hole pair at the terminated surface. Despite its similarities to the SPP, considerably little

literature exists on the SEP in recent times. Yang et. al. along with Bradberry and Sambles published several papers [111, 115-118] on this phenomenon in the early 1990's and successfully demonstrated the presence of the SEP at the interface of air and vanadium using a Kretschmann type prism coupled configuration. Yang et. al. also went on to describe the theory behind this surface state. It will be later shown in Chapter 5 that the interface of a low-loss dielectric such as photoresist and a high loss dielectric such as Molybdenum or Silicon also supports such a surface state and this may in fact be quite useful in evanescent wave enhancement.

In this section, two naturally occurring optical surface states were discussed, and some theory was presented to highlight their inner workings. Commonly used methods to couple to these were also discussed. In later chapters of the thesis, it will be shown how the use of surface states and evanescent interference lithography allows a considerable image enhancement allowing feasible patterning of regular lines and spaces. A novel "artificial" surface state using an effective gain medium (EGM), is also presented and analyzed in Chapters 6 and 7 as one of the novel contributions in this thesis. While the case study has been specifically directed towards the use of all dielectric media due to its ease of applicability by the industry and by other researchers, the use of various materials such as a combination of metals and lossy and lossless dielectrics is also possible to create a composite surface state that potentially provides an enhancement much greater than any naturally occurring surface state at very high *NA*s. This could be useful if one is able to create higher evanescent orders which may not be possible with a prism but for instance with a carefully designed sub-wavelength grating stack. In this thesis, interference lithography is used to create high evanescent order images. Hence, let us now conclude this chapter by reviewing interference lithography as this forms an essential portion of this thesis.

2.6 Interference Lithography

Interference lithography (IL) involves the interference of two coherent wavefronts to create a pattern of high and low intensity [119]. This can be achieved by a number of means of varying sophistication depending on the demands for resolution, spatial coherence and/or line-width control that are required [120-122], and multi-beam or multi-exposure techniques allow complex two- or three-dimensional patterns to be formed [123-129]. While high resolution interference lithography easily lends itself to the needs of data storage [130-132], where regular structures are patterned, it is not limited to this. For instance the project titled, gratings of regular arrays and trimmed exposures (GRATE) funded by DARPA was initiated to allow low-cost circuit manufacturing using IL [133]. Several other applications are presented in a subsequent sub-section dealing with IL.

The exciting aspect about this technology is that it allows the image to be made up of a single spatial frequency through simple two beam interference. While, this may at first seem limiting for the purpose of circuit fabrication, it is a very attractive option for researchers wishing to carry out experiments by limiting the system operation and analyses to a particular spatial frequency. As with solving any problem, this option thus allows the researcher to solve a bigger problem by first attacking a smaller chunk of the problem, dealing with a single spatial frequency.

On the other hand, as was mentioned earlier, the increasing complexity of circuits these days in fact requires step wise fabrication where individual steps consist of creating repeating lines and spaces followed by trimming away the patterns that are not needed. These steps are repeated several times and are known as a trim and expose methodology. An IL based technique seems adequate to satisfy the needs of this operation.

It is essential to mention before proceeding any further that IL requires a reasonable temporal coherence length (i.e. ideally a monochromatic source) and a sufficiently large coherence area to ensure that the image is free from beating effects. The latter requirement for a large coherence area may be easily achieved by employing a spatial filter in the optical path, hence the former (temporal coherence) requirement is more stringent of the two.

Figure 2-17 illustrates a simple schematic for IL carried out in air upon photoresist. The *NA* of the interference pattern is less than the refractive index of air. Two coherent plane waves with free-space wavelength λ_0 are brought together to interfere on a resist-coated substrate, at an angle θ relative to the surface normal. The waves can be brought together to interfere in air as depicted above or in a liquid- or solid medium as will be discussed in the next sub-section. The aim of research in IL is to be able to fabricate high resolution structures with high aspect ratios for large area patterning and several researchers have made their contributions to fulfilling either one or more of these requirements.

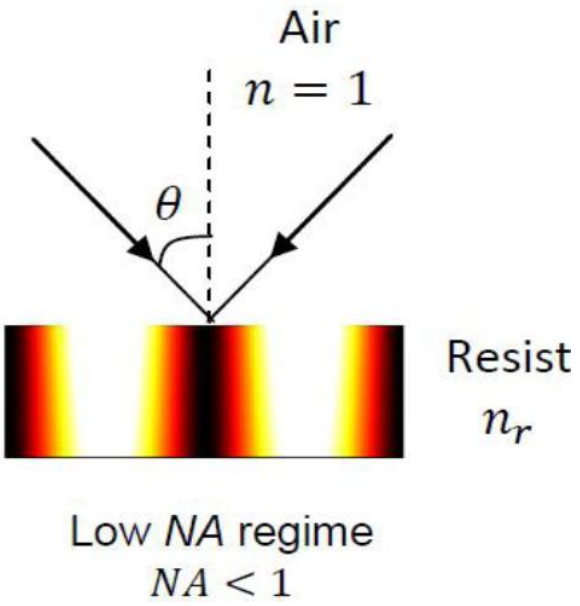

Figure 2-17 – Simple schematic representation of basic Interference Lithography carried out with air as the ambient medium

The simplest method to create an interference pattern is perhaps the Lloyd's mirror as depicted in the schematic of Figure 2-18. This was first described in 1834 and again in 1837 by Humphrey Lloyd [134].

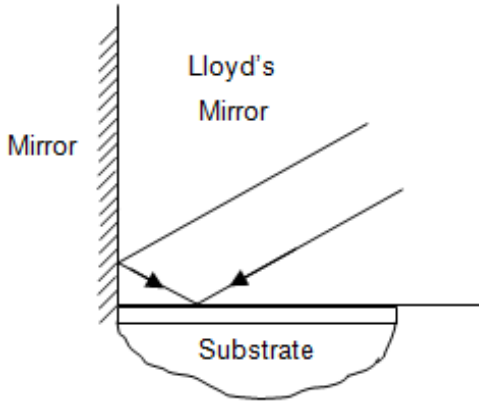

Figure 2-18 - Conventional Lloyd's mirror interference lithography system

A long coherence-length incident wave interferes with its reflected image; assuming the reflection is perfect, the image will form the ideal interference pattern. Since then, several advancements have taken place, though the principle of wave interference to create a pattern remains unchanged, and some of these are reviewed here.

2.6.1 Interference Lithography in the Low numerical aperture (*NA*) regime

MIT Nano-ruler

The MIT nano-ruler [135] is a tool to pattern nano-accurate gratings; it makes use of a method called scanning beam interference lithography system (SBIL) developed at the space nanotechnology laboratory (SNL) at the Massachusetts Institute of Technology (MIT). The SBIL has been designed to effectively draw out gratings over a large area with high precision. To achieve this however, the system incorporates digital signal processing and control theory. SBIL is a reasonably complex system that ensures interferometric accuracy by featuring a real time measurement and control of optical phase using heterodyne fringe detection, acousto-optic modulator phase locking and a high-speed digital signal processor (DSP) controller.

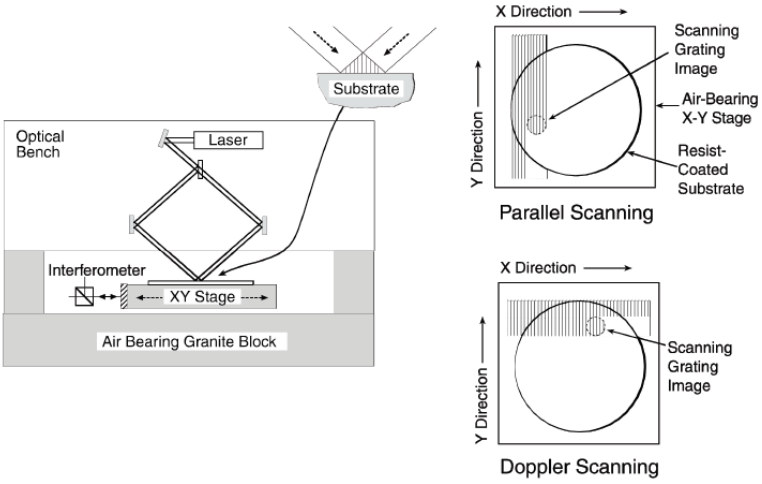

Figure 2-19 – Schematic of the scanning-beam-interference lithography (SBIL) system under development in the SNL. A pair of narrow, low-distortion beams overlap and interfere at the substrate, producing a small grating "image". The substrate is moved under the beams writing a large area grating. Tightly overlapped scans ensure a uniform dose. – Reprinted from [135]

A schematic of the SBIL is depicted in Figure 2-19 (note: control circuitry not depicted). The remarkable performance of this tool is evident in the reprint of Figure 2-20 that shows a person holding a 300 mm diameter silicon wafer that has been fully patterned with a 400 nm period grating.

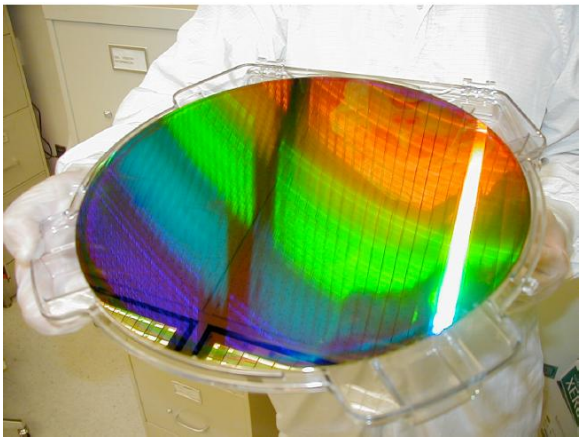

Figure 2-20 – A 300 mm-diameter silicon wafer patterned with a 400 nm-period grating by the Nanoruler. The grating is diffracting light from the overhead fluorescent bulbs. – Reprinted from [135]

Achromatic Intereference Lithography

Another technology developed at MIT, known as Achromatic Interference Lithography [136] tackles the issue regarding a low temporal coherence. A schematic is provided as a reprint in Figure 2-21. The goal of this technology is to compensate for the limited temporal coherence of a 193 nm ArF source. The method ensures that the printed grating period is dependent directly on the parent gratings utilized and is independent of the wavelength or coherence of the source. This ensures repeatability.

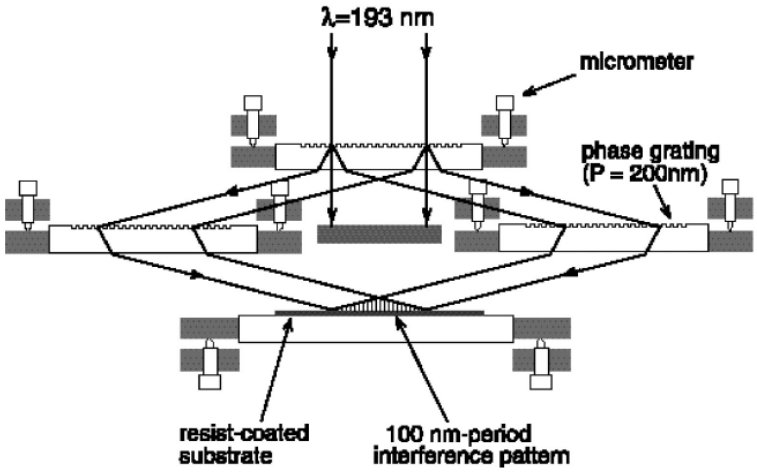

Figure 2-21 – Achromatic interferometric lithography (AIL) configuration employed to produce 100 nm-period gratings and grids – Reprinted from [136]

The results of this method are depicted again as a reprint in Figure 2-22, a 100 nm period grid is shown with 13 nm diameter posts etched into silicon.

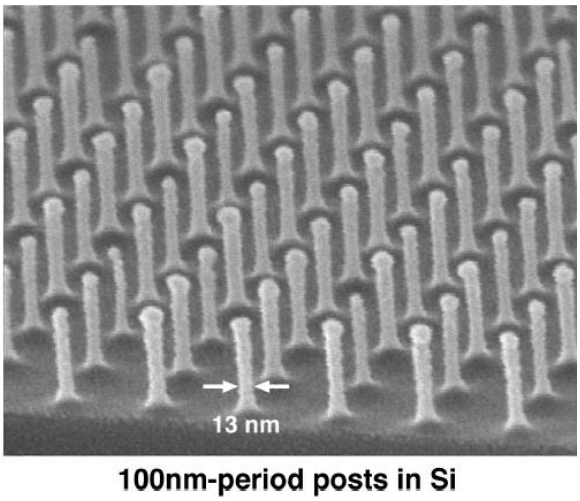

Figure 2-22 – Scanning electron micrograph of a 100 nm-period grid, exposed in PMMA on top of an antireflection coating, and transferred into Si by reactive ion etching

Further work is being pursued to allow sub-50 nm periods or 25 nm lines and spaces. Applications of this technology include patterned magnetic media, gratings for atom-beam interferometry, UV polarizers, and template self-assembly. This review is now continued and methods to extend the resolution capability of an interference lithography system are examined.

2.6.2 Interference Lithography in High and Ultra-high numerical aperture (*NA*) regimes (Immersion IL)

Let us go back to the problem of imaging structures with a lower pitch (period) than that given by (2.2). One may of course simply get around the problem by lowering the wavelength. There are several practical limits to lowering the wavelength, including the availability of sources, adequate photoresists and antireflection coatings, lens materials, and ultimately the absorbance of air as the wavelength drops below about 180 nm. Today, a wavelength of 193 nm (from an ArF excimer laser) is common, but lower wavelength systems have yet to be used in manufacturing.

It was briefly noted in section 2.2.1 that increasing the refractive index of the ambient medium would give the system a higher *NA*. This would allow the system to achieve a higher maximum resolution. Now recall Figure 2-1, consider the scenario where the ambient medium is a liquid (as opposed to air) that has a refractive index higher than 1. In such a case, the refractive angle of the waves that entering this fluid would be less (than it would be if the medium was air) due to Snell's law [6]. What is the advantage of this?

It is now possible to allow the mask to have smaller features (provided the correct sized objective lens is also used) so that the light may in fact refract at a larger angle within this fluid before it makes contact with the imaging stack and yet stay in the propagating regime (i.e. evanescence is prevented). Hence, this allows the system to have a considerably higher *NA*. Such a system is in fact utilized by the industry. The state of the art lithography system depicted in Figure 2-3 in fact makes use of a puddle of purified water ($n = 1.44$ at $\lambda = 193\,nm$) that is continually removed and replenished below the lens as wafers are processed and continually moved under this puddle. This allows the industry to carry out liquid immersion lithography at a *NA* of 1.35 [6]. Immersion lithography has been a major breakthrough in the semiconductor industry [30, 137-138]. Intel's 32 nm node was the first to utilize this technology [19].

Note, however that this *NA* is still lower than the refractive index of photoresist. One could also consider the use of a prism medium to generate a single high spatial frequency as opposed to using a mask and make use of a considerably higher refractive index fluid below the prism. Such as a prism would allow an even higher *NA*, one that may exceed the refractive index of the photoresist itself. This has of course been extensively considered in literature and is referred to as solid-immersion interference lithography. Figure 2-23 illustrates the high and ultra-high *NA* regimes where the *NA* is lower and higher than that of the resist respectively. In experimental setups, an immersion fluid is also used (omitted from Figure 2-23), to ensure that the image remains in its propagating state until it makes contact with the imaging stack.

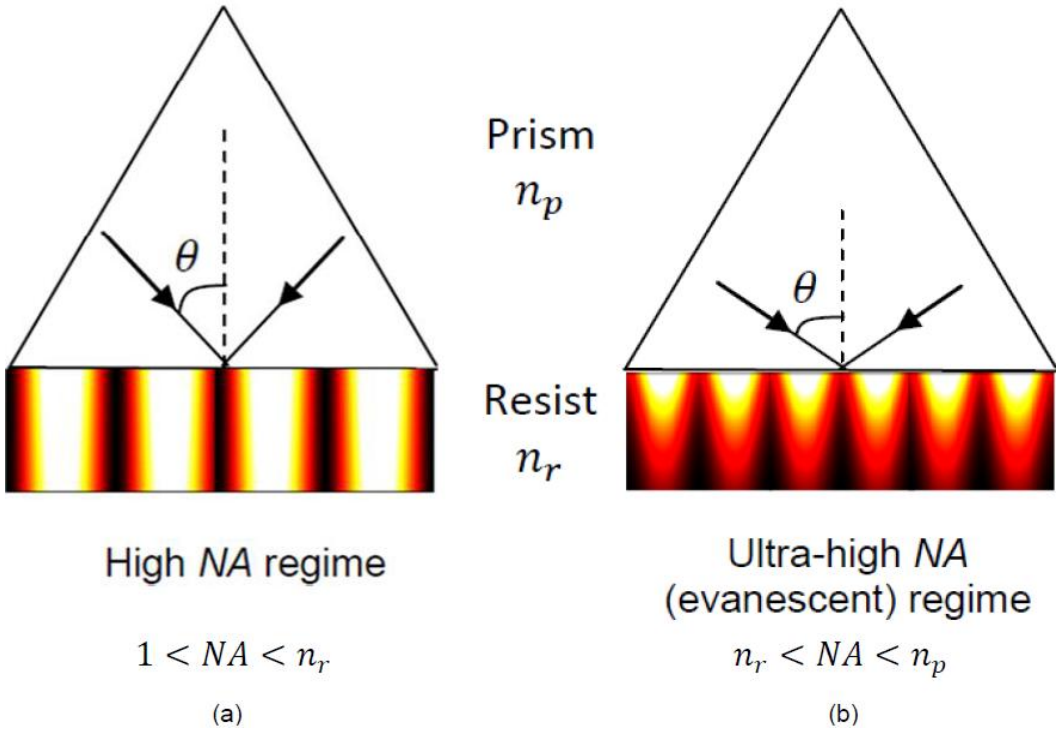

Figure 2-23 – Interference lithography, showing (a) high numerical aperture and (b) ultra-high numerical aperture (NA) configuration

The numerical aperture (*NA*) for such a system is now given by (2.6).

$$NA = n_p \times \sin\theta \tag{2.6}$$

Solid immersion IL also forms a significant portion of the work carried out in this thesis. While this allows a very high resolution image through interference of two counter propagating beams in the prism medium, it also causes almost complete total-internal-reflection at the surface of the resist, due to the index of the photoresist being lower than the *NA* that is being imaged. Once again, this results in an image that decays exponentially within the photoresist, an evanescent image. However, it is in this regime that the maximum-achievable resolution for the system will be achieved, as has been report for deep-UV imaging of 26 nm half-pitch features at 193 nm [139], corresponding *NA* = 1.85, the highest reported for immersion IL. Let us briefly review some of the literature around solid immersion interference lithography as is applicable to this thesis, before we proceed to a detailed analysis of evanescent interference lithography.

Solid Immersion Interference Lithography (Ultra-high numerical aperture (NA))

While there are other methods of creating and interfering evanescent waves such as by using carefully designed sub-wavelength gratings that produce the desired evanescent order [140-143], of considerable

relevance and interest to the thesis work is solid immersion interference lithography [34-35, 139, 144-148] as this presents a single spatial frequency as opposed to a spectrum. Solid immersion interference lithography systems have been created to work at $\lambda = 193$, such as NEMO [149], a tool by IBM that uses a quartz prism to image feature sizes below 30 nm.

Another example, worth special mention here is a popular and versatile research tool known as the Amphibian XIS™ [148]. It was created by Bruce Smith and colleagues at the Rochester Institute of Technology (RIT) and has been used to successfully demonstrate high and ultra-high *NA* interference lithography at a $\lambda = 193$ nm with a *NA* of 1.85 using a high index sapphire prism. More information on related work from this group is available at [34, 139, 146-148]. A schematic of the Amphibian XIS is presented in Figure 2-24 (reprinted from [139]). It operates by first using the necessary optics to achieve the required beam. Once again, the tool has been created in such a way that a source with a relatively poor coherence may be used. The coherence dependence on the source is removed by the use of a phase grating that splits an incident beam into multiple orders.

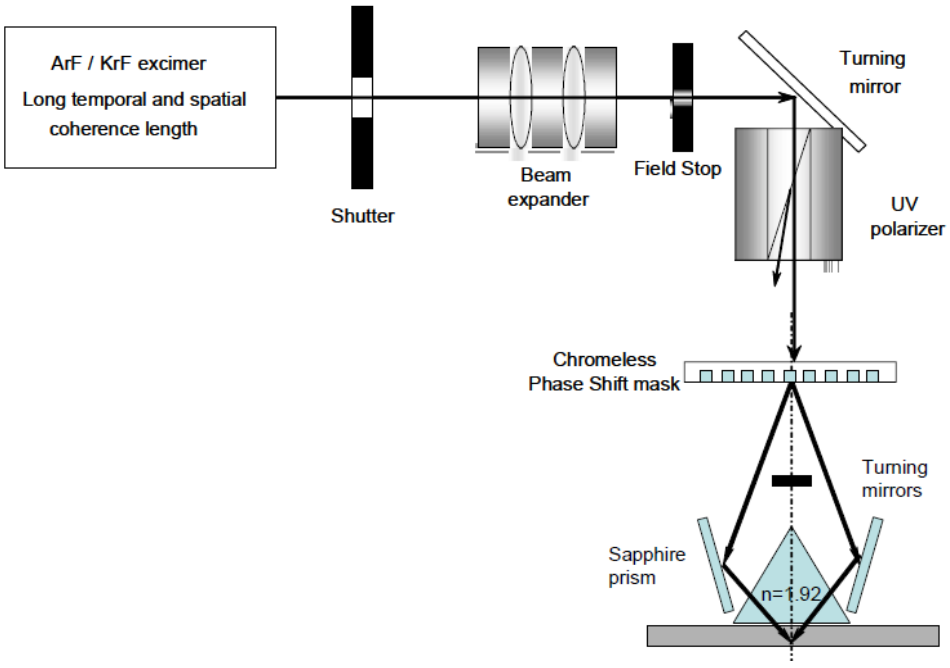

Figure 2-24 – Schematic of the sapphire imaging system used for solid immersion lithography (SIL) and evanescent wave lithography (EWL) – Reprinted from [139]

The +/- 1st orders (hence coherent) are then recaptured and interfered inside a sapphire prism using beam blocking optics. The *NA* is adjusted by simply adjusting the mirror angles. Figure 2-25 illustrates reprints from [139] that illustrate solid immersion IL using Amphibian at several *NA*s.

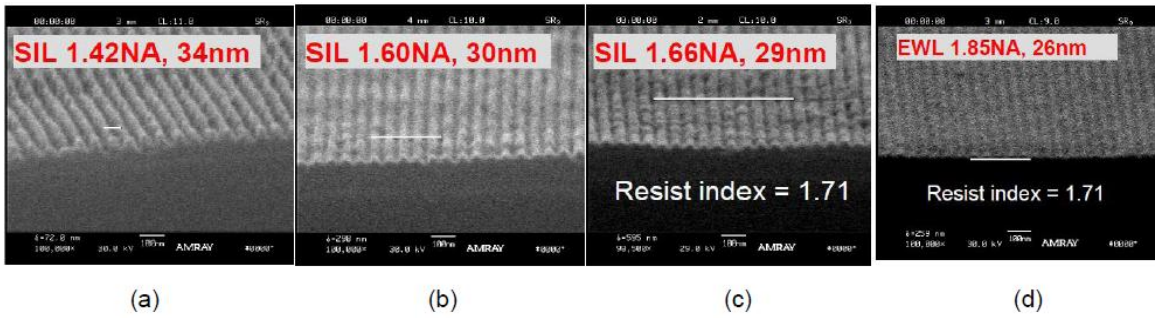

Figure 2-25 – Solid immersion lithography results using the sapphire imaging system in 78 nm photoresist (a) 1.42 *NA* for 34 nm half-pitch imaging (b) 1.60 *NA* for 30 nm half-pitch imaging (c) 1.66 *NA* for 29 nm half-pitch imaging (d) 1.85 *NA* – Propagating the evanescent field to image 26 nm half-pitch features.

Imaging is only possible within the resist due to frustration of the evanescent field back in to its propagating state [34]. This phenomenon has been rigorously analyzed by Zhou et. al. [34] to show that the effective index and extinction coefficient of the resist are in fact a function of the *NA* when operating in the evanescent regime, this is indeed a very interesting result and confirms why it is possible to create an image within the resist at greater than the critical angle.

It has recently also been reported that a scanning interference evanescent wave lithography (EWL) imaging head system is under construction [150] for large area patterning. The paper reports the use of the Amphibian^{TM} system that has been modified to act as an imaging head and float at a constant distance above the imaging media while EWL is carried out. This design of this system is a crucial area of research to pursue if the goal is to allow solid immersion interference lithography to become a competitive or alternative technology to conventional projection lithography. Moreover if this is combined with the technological framework and proposed design presented in this thesis, we believe that there is considerable potential for the technology to become extremely attractive to a wider audience of researchers.

Considerable research has also been carried out into the materials required for immersion lithography [151-156]. This has involved among several aspects, the investigation and comparison of various solid immersion prism materials such as garnets, oxides, fluorides, calcites and also liquid immersion materials other than water to be used as index matching liquids such as fluorocarbons, partially fluorinated organosiloxanes, hydrocarbons and of course the need to then also consider how higher index resists may be manufactured to support the image in its propagating state [157-166]. Let us conclude this section with a brief introduction of the solid immersion interference lithography system that has been implemented for this thesis.

Solid Immersion Lloyd's Mirror Interference Lithography (SILMIL)

Solid immersion Lloyd's mirror interference lithography (SILMIL) is a technique that was first proposed by us (Mehrotra et. al.) as an abstract to the SPIE Advanced Lithography 2011 conference [35, 167]. Incidentally, a similar technique was also proposed independently a few months later and successfully demonstrated by de Boor et al. [168] using an aluminum-coated Littrow prism and exposure with a 266 nm laser to pattern sub-50nm half-pitch gratings at *NA* = 1.30. This is illustrated in Figure 2-26, which is reprinted from [168].

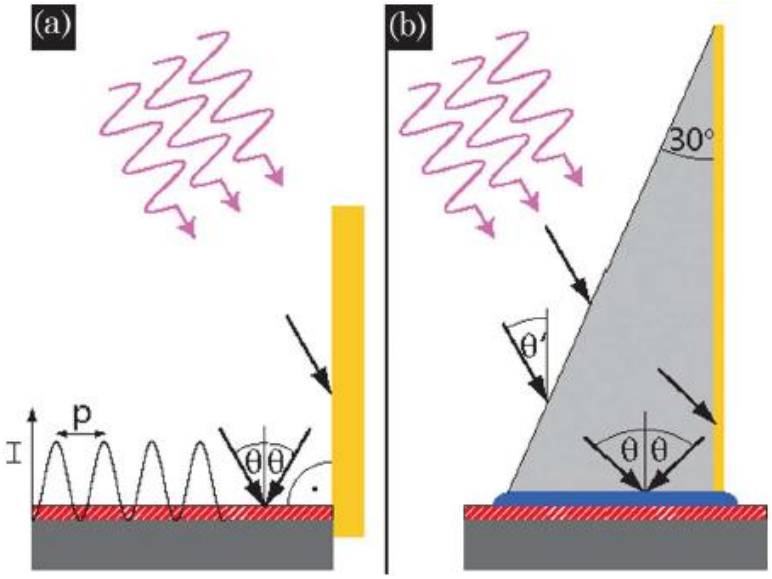

Figure 2-26 – (a) Standard Lloyd's mirror interferometer: a fraction of the light from an expanded laser beam reaches the sample directly, another fraction after reflection from a mirror (yellow), creating a sinusoidal intensity pattern across the sample. The substrate (dark gray) is coated with photoresist (red). (b) Immersion Lloyd's mirror interferometer: the laser light is directed onto a triangular prism at an angle θ' to the sample normal. Instead of by a separate mirror, the light is reflect by the metal coating (yellow) of the prism. The periodicity in (b) is smaller than that in (a) because of the refractive index of the prism. Total reflection at the bottom side of the prism is avoided by using an immersion liquid (blue). – Reprinted from [168]

The technique is extremely simple, yet quite powerful, but requires the use of a relatively higher temporally coherent source. It takes advantage of the geometry of a Lloyd's mirror and embeds it into a prism to allow solid immersion interference lithography. In our case, SILMIL also allows ultra-high-*NA* patterning. In this thesis, the SILMIL implementation utilizes the Yttrium Aluminum Garnet (YAG) material in a cuboid geometry as the high index lens material to conduct solid immersion IL. YAG fits the criteria outlined in [34] such as the need for low structural and intrinsic birefringence, low absorption and a high refractive index at the wavelength of choice and finally it is also desirable to have a sufficiently high durability. YAG satisfies all of these, and has a sufficiently high refractive index of $n = 1.856$ at

$\lambda = 405\,nm$, the wavelength of choice for solid immersion IL in this thesis. Chapter 3 is dedicated to the describing the construction and analyzing the performance of SILMIL.

This chapter concludes with an analysis of the behavior of electric fields at a point in the absorbing medium for the various polarizations of light and quantitatively shows how an evanescent field is frustrated in to imparting energy to the photosensitive medium, thereby allowing image formation.

2.7 Interference fields and Polarization – The good, the bad and the evanescent elliptical

2.7.1 Polarization and contrast in an ideal interference image

While choice of the right materials when designing an IL system is crucial, the polarization of light is equally important. Either the transverse magnetic (TM) or the transverse electric (TE) polarization of light or even an arbitrary polarization that is a mixture of these may be chosen. Figure 2-27 distinguishes between the TM and TE polarizations of light in a lossless medium, the red dot and cross indicate fields coming out of and going in to the page respectively.

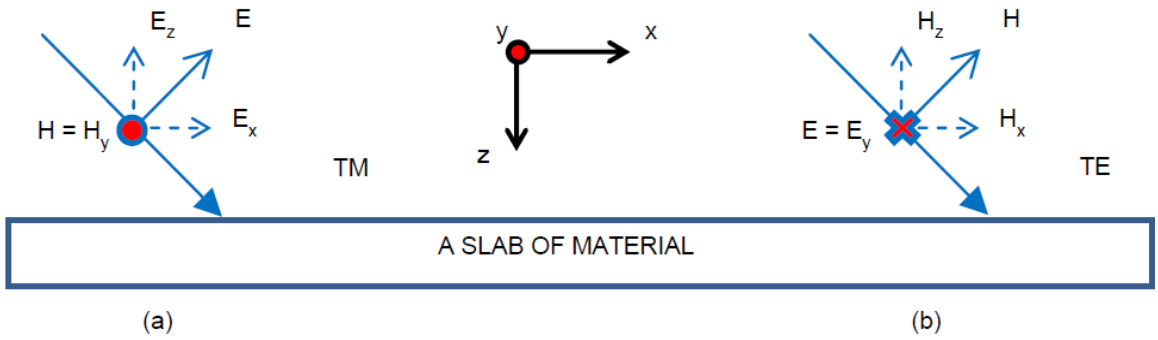

Figure 2-27 - The Transverse Magnetic (TM) and the Transverse Electric (TE) polarizations

With the TM polarization of light, the electric field *E* lies in the plane of incidence, while with TE, the electric field *E* is normal to the plane of incidence, where the plane of incidence is defined as a 2D plane parallel to this sheet of paper. This causes *E* to have two separate components when the light is TM polarized and only one when it is TE polarized. This distinction is of particular importance to us because the photoresist is sensitive to the *E* field of light only and hence the use of different polarizations results in very different interference patterns. Figure 2-28 illustrates the difference one might notice when interfering light of either the TM or the TE polarizations. The exact difference is dependent on the operating *NA*.

From Figure 2-28 (b), one may notice that an interference pattern made using the TE polarization of light has perfect nulls, i.e. anti-nodes that attain a value of 0. This is true for all *NA*s when using TE, as the standing waves are a result of the interference of the E_y component of the electric field. The peak to null ratio is ideally infinity, resulting in a high contrast image. Hence, the TE polarization is known as the 'good' polarization in lithography and is utilized by the semiconductor industry. For this reason, the TE polarization of light has been used for much of the experimental work in this thesis.

The SPP and SEP surface excitations described in the previous section naturally couple when the TM polarization of light is used, but not when the TE polarization of light is utilized. Hence, ways to couple surface states when the TE polarization of light is used would be ideal, one such scheme is developed in this thesis.

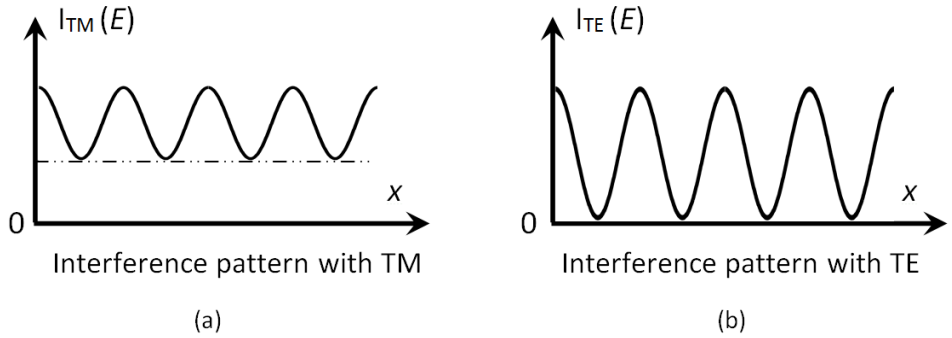

Figure 2-28 - Approximate interference pattern profiles formed with the (a) the transverse magnetic (TM) and (b) the transverse electric (TE) polarizations of light

An interference pattern made using the TM polarization of light does not have perfect nulls, see Figure 2-28 (a). In addition, a low contrast pattern is formed. These differences are attributed to the fact that the two electric field components namely E_x and E_z independently form standing waves in the x plane. Not surprisingly, the two standing waves are out of phase all of the time except at a certain angle at which there crests and nulls align. The simple sum of two sinusoids that are phase displaced gives us another sinusoid, however one that has a DC component associated with it. For our application, this is undesirable as it exposes the photoresist even at the location of the nulls of the interference pattern. This also causes a lower crest to null resulting in a low contrast image. For these reasons, the TM polarization is considered to be the 'bad' polarization in lithography.

2.7.2 Evanescent Fields

It is essential to point out that in Figure 2-27 and Figure 2-28, only propagating homogenous waves have been considered. A wave is considered to be homogenous when its planes of equal amplitude and equal

phase are parallel to each other. The cross product $E \times H$, of such a wave tells us the direction of propagation where the fields E and H are always perpendicular to the direction of propagation. Moreover, the electric and magnetic fields are always in time phase with each other and the same is true for their individual components.

Evanescent waves on the other hand are typical non-homogenous waves. Their planes of constant amplitude and phase are perpendicular or spatially 90^{O} with respect to one another and the presence of loss in the resist acts to reduce this angle only slightly. In a previous sub-section, evanescent interference lithography using solid immersion was mentioned. Here, the behavior of the electric fields of the TM and TE polarizations in the evanescent regimes is analyzed in detail.

Maxwell's equations allow us to relate the electric and magnetic fields of a wave. In the non-magnetic case, the following relationship exists,

$$\nabla \times \vec{\boldsymbol{H}} = \vec{J_f} + \frac{\partial \vec{\boldsymbol{D}}}{\partial t} \tag{2.7}$$

or simply

$$\nabla \times \vec{\boldsymbol{H}} = \varepsilon_0 \vec{\varepsilon_r} \frac{\partial \vec{\boldsymbol{E}}}{\partial t} \tag{2.8}$$

in the absence of a free current density. Note that, the horizontal arrows above fields and symbols indicate a complex value, whereas $\hat{\boldsymbol{x}}, \hat{\boldsymbol{y}}$ and $\hat{\boldsymbol{z}}$ represent unit vectors in the x, y and z directions respectively. Hence,

$$\vec{\varepsilon_r} = \varepsilon_r{}' + i\varepsilon_r{}'' \tag{2.9}$$

is the complex electrical permittivity of the medium. In our case, this medium is a lossy resist in which evanescent wave formation is to be understood. Let us first consider the TM case and define $\vec{\boldsymbol{H}} = \vec{\boldsymbol{H}}_y = \boldsymbol{A}e^{j(\vec{k_x}\hat{x} + \vec{k_z}\hat{z} - \omega t)}$, then (2.8) expands to,

$$-\frac{\partial \vec{H_y}}{\partial t}\hat{\boldsymbol{x}} + \frac{\partial \vec{H_y}}{\partial t}\hat{\boldsymbol{z}} = -\varepsilon_0 \vec{\varepsilon_r} j\omega(\vec{E_x}\hat{\boldsymbol{x}} + \vec{E_z}\hat{\boldsymbol{z}}) \tag{2.10}$$

This allows us to express the electric field components in terms of the magnetic field. Hence,

$$\vec{E_x} = \frac{\vec{k_z}}{\varepsilon_0 \vec{\varepsilon_r} \omega}\vec{H_y} = \frac{(k_{z,real} + ik_{z,imag})}{\varepsilon_0 \vec{\varepsilon_r} \omega}\vec{H_y} \tag{2.11}$$

$$\overrightarrow{E_z} = \frac{-k_x}{\varepsilon_0 \overrightarrow{\varepsilon_r} \omega} \overrightarrow{H_y}$$

Here, the assumption of a low-loss resist is first made, without loss of any generality so that the wave can be assumed to be purely evanescent, the lossy resist case is considered afterwards. This simplifies (2.11) to,

$$\overrightarrow{E_x} = \frac{\overrightarrow{k_z}}{\varepsilon_0 \varepsilon_r \omega} \overrightarrow{H_y} = \frac{i k_{z,imag}}{\varepsilon_0 \varepsilon_r \omega} \overrightarrow{H_y}$$
$$\overrightarrow{E_z} = \frac{-k_x}{\varepsilon_0 \varepsilon_r \omega} \overrightarrow{H_y} \qquad (2.12)$$

A key point to note here is that, omitting loss from the resist resulted in the removal of $k_{z,real}$ from the equations indicating that the loss acts to frustrate the evanescent wave into a propagating state and thereby allowing it to carry energy. This point will be further backed in the following analysis, but first we proceed as normal. Equation (2.12) tells us that the component $\overrightarrow{E_z}$ is in time phase with $\overrightarrow{H_y}$ (or almost if a slight loss is added to the resist). In contrast, it is 90^O out of time phase with $\overrightarrow{E_x}$, and both components have differing amplitudes. Figure 2-29 allows us to visualize this phenomenon in terms of phasors.

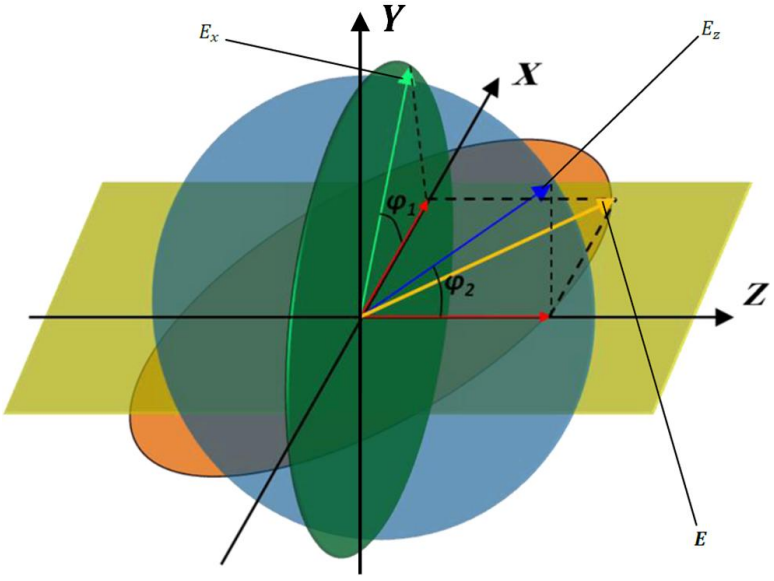

Figure 2-29 - Elliptically polarized evanescent field at a point in the absorbing imaging medium. The green and blue arrows represent phasors for the $\overrightarrow{E_x}$ and $\overrightarrow{E_z}$ fields, the paths of which are traced out by the respective green and blue circles. The net resulting electric field is a vector sum of the projection of the two phasors. This resulting field $\vec{E}$ is depicted using a yellow arrow and is seen to trace out an ellipse, thus explaining why such an evanescent field is elliptical in nature.

It depicts the $\overrightarrow{E_x}$ field as a phasor quantity, a green vector that rotates in the *x*-*y* plane, its path is traced out as a green circle. Similarly, the $\overrightarrow{E_z}$ field is also represented as a phasor quantity, a blue vector that rotates in the *y*-*z* plane and its path is traced out as a blue circle. Here, $\varphi_1$and φ_2 are the relative phases of $\overrightarrow{E_x}$ and $\overrightarrow{E_z}$ with respect to $\overrightarrow{H_y}$. The projections of these individual phasors onto the *x*-*z* plane depict the value of each field and are shown as red arrows. Then, the vector combination of the two projections (red arrows) creates a resultant field $\vec{\boldsymbol{E}}$ in the *x*-*z* plane, depicted using a yellow arrow. In time, we notice that the yellow arrow traces out an ellipse (orange ellipse) in the $x-z$ plane, thus showing us why such an evanescent field is said to be elliptically polarized. The $\overrightarrow{H_y}$ component is much simpler and oscillates in the *y* axis. One may write the complete electric field as

$$\vec{\boldsymbol{E}} = \overrightarrow{E_x}\hat{\boldsymbol{x}} + \overrightarrow{E_z}\hat{\boldsymbol{z}} \tag{2.13}$$

and use this to compute the time domain electric field intensity function at any given point as this is responsible for photochromic conversion in the photoresist.

$$\begin{aligned} \left|\vec{E}\right|^2 &= \frac{1}{2}\left(\left|\overrightarrow{E_x}\right|^2 + \left|\overrightarrow{E_z}\right|^2\right) + G\cos(2\omega t - \rho) \\ G &= \sqrt{\left(\frac{\left|\overrightarrow{E_x}\right|^2}{2}\right)^2 + \left(\frac{\left|\overrightarrow{E_z}\right|^2}{2}\right)^2 + \frac{1}{2}\left|\overrightarrow{E_x}\right|^2\left|\overrightarrow{E_z}\right|^2\cos\left(2(\varphi_1 - \varphi_2)\right)} \\ \rho &= tan^{-1}\left(\frac{-\left|\overrightarrow{E_x}\right|^2\sin(2\varphi_1) - \left|\overrightarrow{E_z}\right|^2\sin(2\varphi_2)}{\left|\overrightarrow{E_x}\right|^2\sin(2\varphi_1) + \left|\overrightarrow{E_z}\right|^2\sin(2\varphi_2)}\right) \end{aligned} \tag{2.14}$$

Equations (2.14) can be used to understand the electric field intensities in three distinct cases. Firstly, in the propagating regime with a low loss resist, assume $\varphi_1 = \varphi_2 = 0$. This results in,

$$\left|\vec{\boldsymbol{E}}\right|^2 = \frac{1}{2}\left(\left|\overrightarrow{E_x}\right|^2 + \left|\overrightarrow{E_z}\right|^2\right)(1 + \cos(2\omega t)) \tag{2.15}$$

Upon time averaging, the intensity takes a value of $I = \frac{1}{2}\left(\left|\overrightarrow{E_x}\right|^2 + \left|\overrightarrow{E_z}\right|^2\right)$. This is a linearly polarized wave, where the resultant electric field does not trace out a two dimensional shape in the *x*-*z* plane. Next, let us consider the evanescent regime and first assume a low loss resist, i.e. $\varphi_1 = 90^o, \varphi_2 = 0$, this gives an intensity,

$$\left|\vec{\boldsymbol{E}}\right|^2 = \frac{1}{2}\left|\overrightarrow{E_x}\right|^2\left(1 + cos(2\omega t)\right) + \frac{1}{2}\left|\overrightarrow{E_z}\right|^2(1 - cos(2\omega t)) \tag{2.16}$$

Note that if $E_x = E_z$, then (2.16) becomes a circularly polarized evanescent wave that has a constant intensity regardless of time, $I = \left|\overrightarrow{E_x}\right|^2 = \left|\overrightarrow{E_z}\right|^2$, i.e. the resultant electric field undergoes a phase change with time that causes it to trace out a circle in the *x*-*z* plane, however the magnitude of the resultant electric field remains uniform. Finally in the evanescent regime, there is also the case where an arbitrary phase difference exists between φ_1 and φ_2 due to the presence of loss in the resist. This is the general case, already covered by (2.14) and describes an elliptically polarized evanescent wave. The intensity upon time averaging is simply $I = \frac{1}{2}\left(\left|\overrightarrow{E_x}\right|^2 + \left|\overrightarrow{E_z}\right|^2\right)$. Once again, the resultant electric field undergoes a phase change with time, but it now traces out an ellipse in the *x*-*z* plane, the major and minor axes of which may not coincide with either the *x* or *z* axes.

In contrast, the TE case is much simpler as only one electric field component E_y exists and hence its intensity simply takes the time averaged value $I = \frac{1}{2}\left(\left|\overrightarrow{E_y}\right|^2\right)$. Whereas, it is now the H_x and H_z components that exhibit complex values. However, this does not matter to the analysis because as mentioned earlier, the photoresist is only sensitive to the electric field intensity.

In both cases, the cross product given by $\vec{E} \times \vec{H}$, a vector that changes direction, this is supportive of the fact that an evanescent wave has no particular direction and is simply bound to the interface of the media at which it was created.

With this summary of the evanescent field formation using TM and TE polarizations, one can appreciate the simplicity of imaging with the TE polarization. It must also be said that the expected evanescent interferometric images for the TM and TE polarizations will be much like those depicted in Figure 2-29, however the dosage is now a strongly attenuated function of resist depth due to the evanescent nature of the image.

2.7.3 Power Flow

This sub-section is completed by determining the power dissipation in the photoresist. This is computed as the negative divergence of the time-averaged Poynting vector or in the absence of free sources and magnetizing potentials [169] as,

$$Re\left\{-\nabla.\vec{\boldsymbol{S}}\right\} = Re\left\{-\nabla.\left(\vec{\boldsymbol{E}} \times \vec{\boldsymbol{H}}\right)\right\} = \omega\varepsilon_r{}'' I \qquad (2.17)$$

Hence, for a particular photoresist, we only need to consider the electric field intensity to determine the relative dosage. This result agrees with the fact that a loss-less resist cannot frustrate the evanescent wave

[34] and hence an image may not be created had there been no loss in the imaging medium. With this, the review of evanescent interference lithography is also concluded and a summary is provided below to highlight the issue that the work in this thesis aims to solve.

2.8 Summary

It has been the goal of this chapter to provide sufficient motivation and background material to highlight the importance of the study of the optical near-field. If one makes successful use of solid-immersion lithography using higher index immersion and lens materials, the next limiting refractive index would be that of the photoresist. Typical resists have a refractive index of 1.67 – 1.72 at the ArF wavelength. Thus, even using high-index materials above the resist, the *NA* would still be limited to about 1.6 or so. Going higher puts the imaging system into the evanescent regime as has been shown in this chapter, leading to images that are only practically useful for extremely thin resists making pattern transfer extremely difficult.

The chapter that follows directly, details the construction of a simple solid immersion interference lithography system that operates at λ = 405 nm. In later chapter theory is developed regarding evanescent wave imaging, this is applied in Chapter 7 to show that there is indeed another way to allow pattern transfer with evanescent interferometric images, by coupling onto them via special surface states, that behave in a similar manner to SPPs and SEPs on carefully designed media. This technique successfully demonstrates with experiments that it is in fact entirely possible to extend the ultimate limits of evanescent interferometric lithography and attract considerable research interest. For the $\lambda = 193\,nm$ case, a design is also proposed to achieve this for a very high resolution pattern.

Chapter 3. Evanescent Interference Lithography – Theory & Design of an Experimental test-bed

3.1 Introduction

Solid immersion interference lithography was described in the background section of this thesis. Here, the simple and cost-effective solid-immersion Lloyd's mirror interference lithography (SILMIL) technique is described for patterning periodic nanostructures at ultra-high numerical apertures (*NAs*) using a single long-coherence-length laser source, a mirror-coated prism and some other simple optical components. The technique was initially proposed by us (Mehrotra et. al.) as an abstract to the SPIE Advanced Lithography 2011 conference [35, 167]. It is however not without its limitations. Attempts have been made to critique and point out these limitations and address them. The setup has been designed as a research tool and not as a tool that is ready for use in a production facility. It is important to notify the researcher/reader that SILMIL is also not the prime focus of this thesis but deserves a large chapter in itself as it is a very important means to achieving an end result for the thesis. Chapter 7 describes that this desired end result is successfully achieved using SILMIL.

In this chapter a large body of work is first presented that was carried out to understand the SILMIL process. While low-NA patterns could be imaged with high fidelity, the higher-NA patterns were initially heavily degraded, exhibited low image depth, 'bumpy' resist profiles and severe pattern deformation. These degraded results are presented here anyway as they were useful in allowing the creation of a proper process flow. In addition, this first section also serves as an expanded summary of the experiment that the reader is likely to encounter in the subsequent sections of the thesis. First, two prism geometry types are compared in terms of their ability to cope with spurious reflections and in achieving a wide range of spatial periods. The demands of anti-reflection coatings on the prisms' surfaces to improve performance are also briefly discussed. Following this, the experimental techniques are described, and results are presented for two different prism types: a triangular fused-quartz prism (refractive index $n = 1.48$) capable of pattering over a very wide range of *NA*s, and a square yttrium aluminum garnet (YAG) prism

(n = 1.87 at λ = 325 nm) capable of producing sub-100 nm period structures at *NA*s of up to 1.85 (i.e. 44 nm half-pitch).

Following this, the SILMIL square prism setup is detailed for successful operation at λ = 405 nm at a case study numerical aperture (*NA*) of 1.824, now overcoming a lot of the hurdles that were faced with the preliminary setup. The section includes a break-up analysis of the system by providing such details on the components used as their design and or preparation, relative configuration, alignment, e.t.c. This is followed by a section presenting results of dosage variation using atomic force microscope (AFM) scans. The results are analyzed and aspects of it are critiqued. Large area AFM scans are also presented to give the reader a feel for the capability of SILMIL. Finally, some scanning electron microscopy (SEM) results are also presented for an optical stack that serve as a comparison with the enhanced results that are to follow in Chapter 7. With this, the chapter is summarized.

3.2 Solid Immersion Lloyd's Mirror Interference Lithography (SILMIL) Setup and Overview

Combining the concepts of a Lloyd's mirror with a solid-immersion IL system leads to the SILMIL technique as was described in Chapter 2. Figure 3-1 shows how a simple mirror-coated prism with a resist-coated sample mounted on one face can be configured for SILMIL, with the rotation of the prism/sample relative to the incident coherent laser beam being used to control the pitch of the interference pattern [35]. Of course, the refraction of the beam needs to be taken into account as the setup is rotated. Different prism types and geometries, with *NA*s as high as 1.85 are explored, which is well into the ultra-high *NA* regime. This is when the *NA* of the system exceeds the refractive index of the resist, n_r and the wave is evanescent in the resist media.

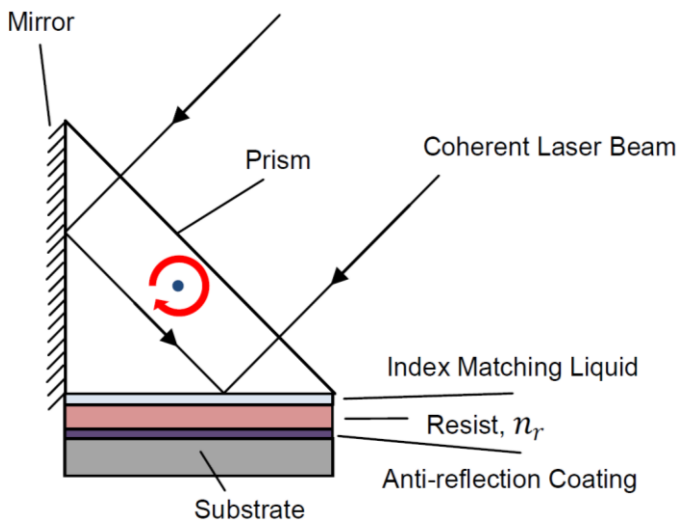

Figure 3-1 - Solid Immersion Lloyd's Mirror Interference Lithography (SILMIL) system. The prism and substrate holder is mounted on a rotational stage to vary the pitch of the patterns

The simplicity of the SILMIL system does not come without problems. Maintaining intimate contact between the prism and resist-coated substrate is an obvious problem, which can be overcome by the use of an appropriate index-matching liquid, or by design of a mechanical fixture and/or vacuum system for applying uniform pressure between sample and prism. Gap measurement with nanometer-level precision is possible, and has been demonstrated for solid-immersion IL [34, 139, 146-148, 150] by utilizing frustrated total-internal reflection as the sample and prism are brought into contact.

Spurious light scattering and reflections are other obvious problems caused by adding a prism to a Lloyd's mirror system. For grazing incidence, the mirror finish near the edges must be carefully controlled to minimize additive noise caused by scattering from these edges, and the incident beam shape must be controlled to avoid scattering from prism vertices. More seriously, spurious reflections from the air-prism interfaces (shown by the dashed line in Figure 3-2 for a triangular prism) will feed additional laser light back into the image region, with little or no control over its phase relative to the main interfering beams. This could be considered as constant background intensity, or an uncorrelated interference pattern in the case of multiple spurious reflections, severely reducing the fringe visibility of the main interference pattern.

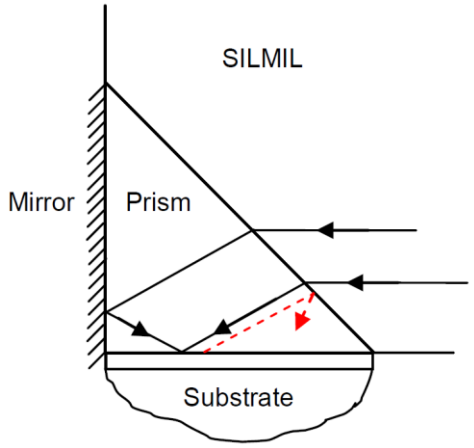

Figure 3-2 - Schematic diagram illustrating how spurious reflections (dashed, red) in a triangular-prism SILMIL arrangement can be redirected back towards the substrate.

An anti-reflection coating (ARC) on the incident surface of the prism will help to considerably reduce this issue. A multilayered ARC is conventionally used for a wide range of *NA*s to maximize performance range, but that will add considerably to the cost of the prism. Alternatively, two prisms may be coated with different single-layer ARCs for use at different angular ranges, allowing the lithographer to practically cover the complete range of *NA*s.

The other option is to reconsider the geometry of the prism such that the air-prism reflections are directed outward. This can be achieved using a square prism as opposed to a triangular one as illustrated in Figure 3-3.

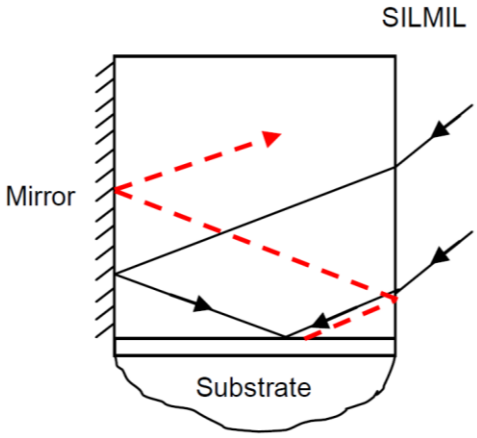

Figure 3-3 - Schematic diagram illustrating how spurious reflections, dashed lines are driven outward in SILMIL when a square prism is used.

A square or cuboid geometry in SILMIL drives the spurious reflections outward through the top surface, and with proper choice of prism dimensions multiple reflections from the prism-air interface can be

guaranteed before any such reflections are redirected back towards the substrate. This relaxes the specifications for any anti-reflection coatings that may be required on the prism, thereby reducing cost. For the experiments that follow, uncoated prisms have been successfully utilized.

A disadvantage of the square-prism SILMIL arrangement is that only a limited range of *NA*s are possible with illumination through the side face, with

$$n_p \sin\left(90° - \sin^{-1}\left(\frac{1}{n_p}\right)\right) < NA < n_p, \tag{3.1}$$

where n_p is the prism refractive index. This is compared with the triangular-prism arrangement in which *NA*s all the way from zero to n_p can be accessed with illumination through one face of the prism. To achieve lower *NA*s using the square geometry, the top surface can instead be the incident face, however in this case spurious *refraction* from the side face may cause problems.

In comparing the two different arrangements, the square geometry is best suited for high-*NA* and ultra-high-*NA* imaging, while the triangular geometry allows a wide range of *NA*s to be accessed by simple rotation of the prism/sample combination relative to the incident laser.

3.3 Initial technique & first experiments

Patterns were imaged using both the triangular-prism and square-prism SILMIL arrangements using two different prism materials for *NA*s from 0.1625 to 1.85, equaling the highest-reported *NA* for immersion IL. The initial experiments were carried out using a 50 mW HeCd laser (IK350-1RG, KIMMON Koha Co., Ltd.) with λ_0 = 325 nm and a coherence length of 30 cm. Commercial UV photoresist (AZ1518, Microchem Inc.) with a refractive index of 1.71 was used for imaging, which was spin-coated on top of a commercial bottom anti-reflection coating (BARC) material (BARLi-II 200,Clariant) on silicon substrates.

Two different SILMIL configurations were tested. Firstly, a 45° right-angled UV fused silica (UVFS) prism with n_p = 1.48 (PS611 ThorLabs Inc.) was coated with a 400-nm thick aluminum layer on one face using DC sputtering (Edwards Auto500 coating system) to test triangular-prism SILMIL (see Figure 3-1). An index matching liquid (FS06350, Cargille Labs Inc.) was used to prevent any air gaps from forming between the sample and prism.

The finer details of the setup itself are elaborated upon in the subsequent sections. For now, it should be sufficient to know that a cage was designed to contain the prism and allow for sample mounting. The cage was mounted on a rotational sample holder (PR01, ThorLabs Inc.) to allow for the *NA* to be easily varied.

The incident laser beam was passed through a spatial filter (KT110, ThorLabs Inc.) to achieve a cleaner wave front to be used for IL. In some cases a collimating lens was also used so that a plane wavefront could be used whilst keeping the beam size smaller than the size of the incident face of the prism, to prevent spurious reflections. With this arrangement exposure areas of up to 1 cm^2 were possible; fundamentally exposure area is only limited by the prism size and coherence length of the laser.

A second set of experiments were carried using a 25 mm square prism made from high-index Yttirum Aluminum Garnet (YAG) material (custom order, RedOptronics Inc.). This was supplied with a protected aluminum mirror on one face, with this face, and the one opposite and one adjacent face polished to a flatness of $\lambda/8$ at $\lambda_0 = 633$ nm (standard specification). The remaining faces were fine ground to provide diffuse scattering for any spuriously-reflected beams that may reach them after multiple internal reflections from the prim-air interfaces. The refractive index of the YAG prism material is $n_p = 1.88$ at $\lambda_0 = 325$ nm, which exceeds the resist index at the exposing wavelength, $n_r = 1.71$, thereby allowing ultra-high *NA* SILMIL to be tested. The YAG material is non-birefringent and has low absorbance and low index inhomogeneity at $\lambda_0 = 325$ nm, hence meets the requirements of a solid immersion system [34].

Exposures were performed in this square-prism system without the use of an index-matching fluid, as the appropriate high-index matching fluid that was tested (Series B, 1.70, Cargille, Labs Inc.) has high absorbance at 325 nm and was found to chemically attack the photoresist that was being used. However, by using moderate contact force in the sample-mounting cage apparatus intimate contact could be routinely achieved for small-area samples (5×5 mm^2).

Exposures were carried out for various times using a simple hand-timed shutter arrangement. Samples were rinsed in Toluene for 10 s post exposure and prior to development to wash away the index matching liquid (if used). The sample was blown dry with compressed nitrogen before the resist was developed in a 1.59% solution of tetra-methy ammonium hydroxide (AZ326 MIF developer diluted 2:1 with deionized water, AZ Electronic Materials) for 60 s. Samples were inspected optically using a light microscope equipped with a Normaski differential-interference contrast prism and lenses (Olympus BX-10), with which the presence of surface relief gratings with sub-visible-wavelength periods could be detected by their induced form birefringence. Samples displaying regions where good grating patterns were formed were subsequently characterized with atomic force microscopy (AFM) using tapping-mode imaging (AFM Model Dimension 3100, Digital Instruments Inc.).

3.4 Preliminary Results and Discussion: SILMIL at λ = 325 nm

3.4.1 Triangular-prism SILMIL

The UVFS prism was used to fabricate patterns with NAs ranging from 0.1625 to 1.39, corresponding to periods from 1 µm to 117 nm respectively. Figure 3-4 and Figure 3-5 illustrate the 1 µm and 117 nm patterns, with both plan-view and line-averaged cross-sections shown through each grating.

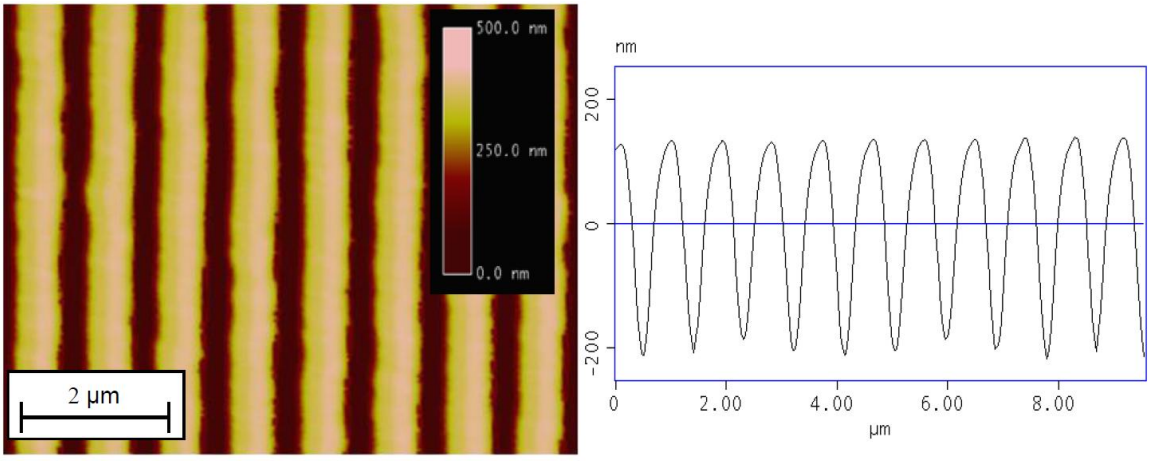

Figure 3-4 - 1 µm period IL pattern formed with a 45° UVFS prism: (a) representative image scan, (b) averaged cross-sectional profile

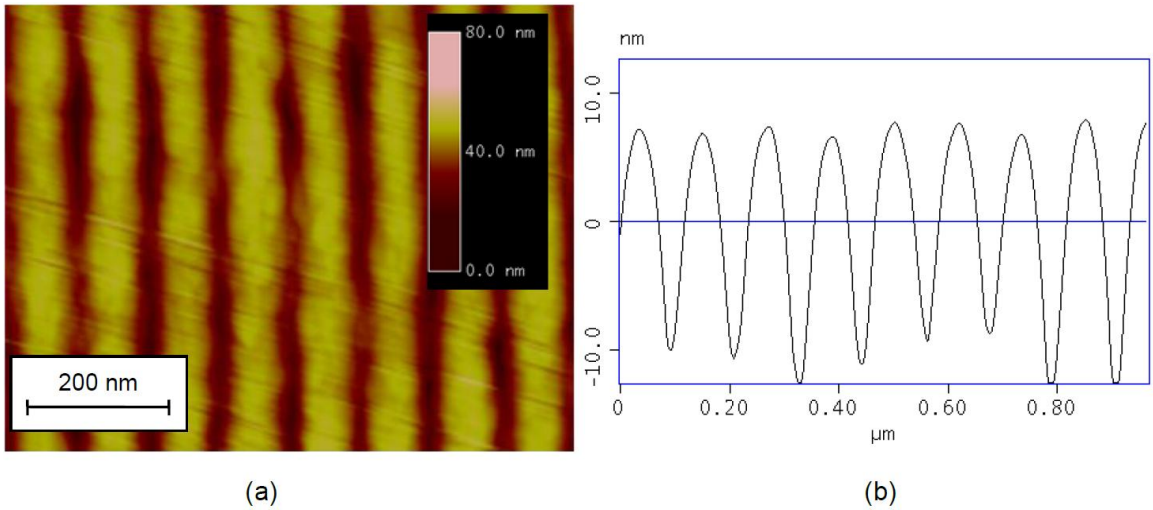

Figure 3-5 - 117 nm period IL with UVFS prism: (a) representative image scan, (b) averaged cross-sectional profile.

It is noted that the grating depth is much lower in the high-*NA* pattern (Figure 3-5). This is principally because the exposure time was reduced for this pattern compared with the exposure for forming the pattern of Figure 3-4; this was necessary in order to prevent the pattern being washed out completely from the additive noise that was observed in other samples, resulting from spurious scattering from the imperfect mirror edge and/or spurious back-reflections from the prism/air interface.

Some of the loss of image depth at higher *NA* is also attributed to the performance of the BARC that was used, which is designed to be effective only for low-*NA* imaging. Under high-*NA* conditions it will no longer act as a good absorber and will introduce significant, unwanted reflections back into the resist for the conditions under which the patterns of Figure 3-5 were exposed. Custom or multilayer BARC systems are possible to improve image depth under these conditions, but their inclusion and optimization were beyond the scope of this study.

3.4.2 Square-prism SILMIL

The use of square-prism SILMIL with the YAG prism resulted in a further reduction of the half-pitch, both due to inherently higher *NA*s from the higher prism index and the ability to access such conditions without spurious back-reflections from the prism reducing image contrast. Figure 3-6 shows a *NA*=1.625 (100 nm period) grating patterned using this setup. No index matching liquid was used, however hard contact was achieved by applying pressure through a backing screw. Similarly, the setup was also used to achieve its limit at a *NA* of 1.85 (88 nm period), giving a half-pitch of 44 nm or $\lambda_0/7.4$, shown in Figure 3-7. Note that a *NA* higher than the refractive index of the imaging media is achieved here, which is referred to as the ultra-high *NA* condition or EIL. In the square-prism SILMIL cases shown in Figure 3-6 and Figure 3-7 the image depth is reduced further than for the lower NA images of Figure 3-4 and Figure 3-5, but now the evanescent nature of the exposure will be a significant contributor.

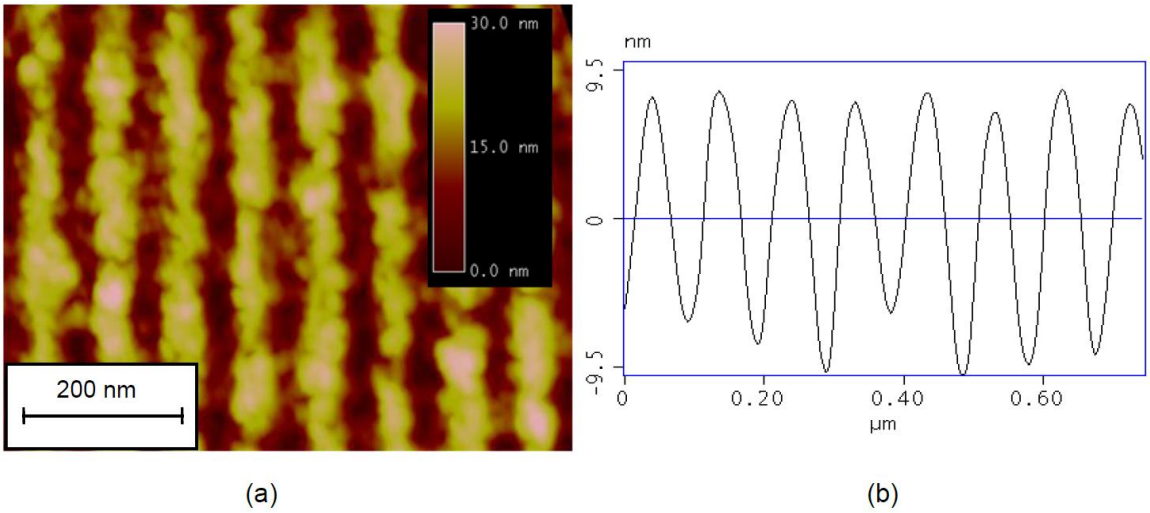

Figure 3-6 - 100-nm period IL with a YAG prism: (a) representative image scan (b) averaged cross-sectional profile.

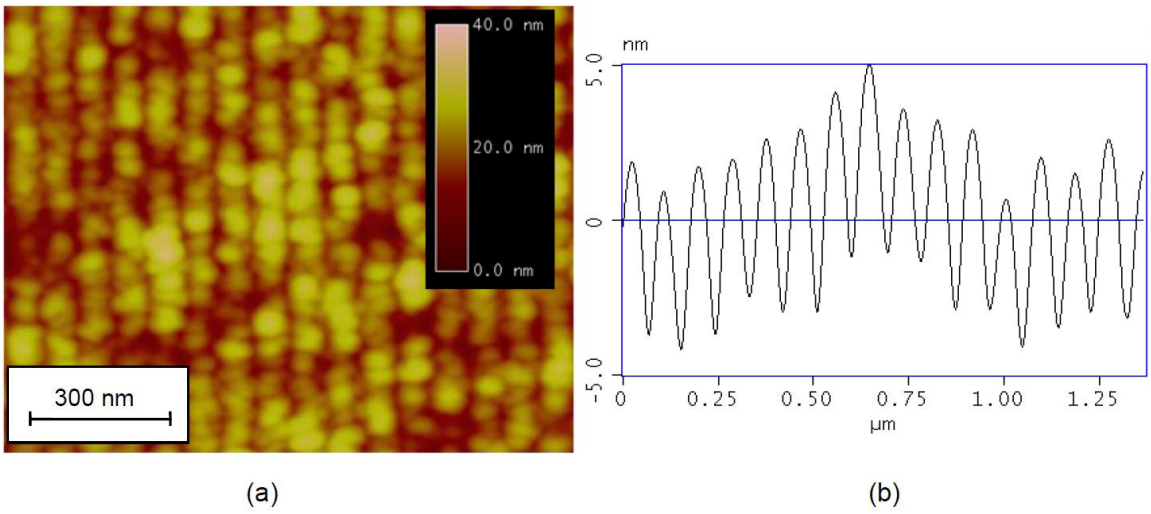

Figure 3-7 - 88-nm period IL with a YAG prism: (a) representative image scan (b) averaged cross-sectional profile.

The above meant to serve as a short summary of the initial experiments that were carried out in an attempt to learn more about what requires careful attention when SILMIL is carried out. It was clearly demonstrated through the above experiments that the image depth falls dramatically from ~300 nm to ~5nm as we go from the low *NA* (1µm pitch) regime to the ultra-high *NA* (88 nm pitch) regime. In the section that follows, the setup is presented in considerable detail and further attention is directed to improving the performance of SILMIL.

3.5 SILMIL Setup at λ = 405 nm

Clearly, the results of the previous section demonstrate that while an interference pattern may be imaged into photoresist, the quality of such patterns is heavily degraded if higher-*NA*s are imaged. In this section the process flow that another researcher may follow to image high quality patterns at ultra-high-*NA*s is detailed, this time using a longer-wavelength source at λ = 405 nm (for reasons described hereafter). The shortcomings of our previous work is listed here so the researcher knows about some of these common pitfalls in advance and how to avoid them.

One of the prime problems with the work outlined in the previous section was the lack of a non-absorbing (or weakly absorbing) index matching liquid (IML) at λ = 325 nm. An IML with a sufficiently high index as the prism and low absorption was not available at λ = 325 nm. The closest product was the Cargille Series B, 17000 but this was too absorptive at λ = 325 nm. However, the same product performed a lot better at λ = 405 nm despite having a lower refractive index of only 1.77 at this wavelength (as is described in this section). As a result, immense pressure was applied to the sample to achieve intimate contact at λ = 325 nm, in the previous section. In fact, the pressure was sufficiently high at several instances that the silicon substrate had succumbed to the stress. Secondly, such stress also caused a significant deformation of the resist profiles as is evident from both the atomic force microscope (AFM) scans and cross-sectional profiles. Finally, the IML was deposited directly on photoresist, which was then cleaned away with toluene after the exposure. The lack of a protection layer on the photoresist surface resulted in damage to the photoresist surface. When viewed under an AFM, this damage was visible as a drastic increase in the surface roughness of the photoresist when compared with a sample that was not wet with IML and/or toluene.

The high-*NA* experiments in the previous section that used a collimating lens also suffered from a severe lens misalignment due to the difference between the optical axes of the lens and the spatial filter. This was unaccounted for at the time of those experiments and meant that in several instances exposure was being carried out with severely non-uniform wave fronts. In this section, all of the above issues are addressed and resolved to demonstrate high-quality EIL.

3.5.1 System overview

Figure 3-8 once again illustrates a schematic of the square prism used for SILMIL. It is described in the subsequent sections how a setup such as this may be used to carry out high quality imaging at a ultra-high *NA*. The incident beam is interfered with an image of itself to create an interference pattern in an imaging

stack. Index matching liquid, photoresist and the substrate (silicon) make up the essential layers in this imaging stack.

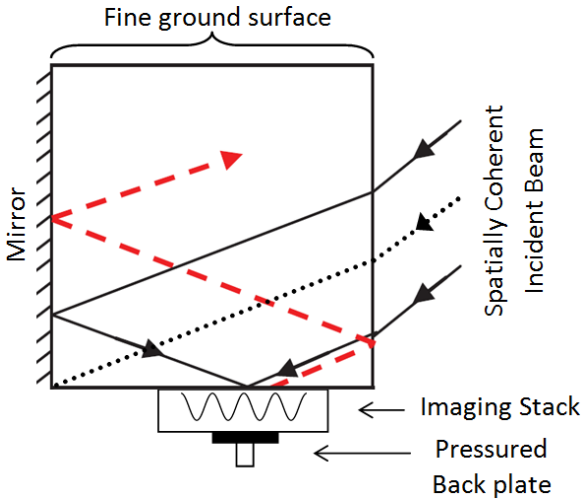

Figure 3-8 - Plan View of SILMIL basic operation

The AZ HiR 1075 was utilized as the photoresist as it is easily shipped to our lab facilities in New Zealand and it is designed for 200 nm sized features, this is 2.5 times smaller than the specification for the AZ1518 that was utilized in the previous section. Access to other photoresists that allowed better resolutions in the *i*-line was restricted. At the Massachusetts Institute of Technology (MIT) however, the PFi-88A2/PFi-88A8 *i*-line resists manufactured by Sumitomo Chemical Co. Japan are being used and 25 nm resolutions have been demonstrated using this through double patterning [125].

Although an anti-reflection coating (ARC) is not needed for high-*NA* EIL provided the resist is sufficiently thick, an ARC layer is used just because photoresist adheres better to it than it does to the bare silicon substrate. The simple prism geometry (cube) allows most spurious reflections (red dashed) to be driven out of the system reducing the amount of noise that is added to the imaging stack; this and other practical design and implementation issues have been resolved to allow for repeatable experiments to be performed with this system, as described in the following sub-sections.

The sub-sections that follow detail individual aspects such as the design, preparation and setup of each component that makes SILMIL possible. The laser and spatial filter setup is described, followed by schematics and illustrations detailing good beam and prism alignment. The design of the cage which accommodates the prism and allows for intimate contact between the optical stack and prism is also detailed. This is followed by information concerning the setup of the optical imaging stack.

3.5.2 Laser & spatial filtering

The use of certified laser safety glasses is strongly recommended for this particular setup. At λ = 405 nm an Ondax SureLock™ wavelength stabilized single mode, single frequency laser with a 40mW output and coherence length > 1 m was used. A coherence length of at least several centimeters is essential for the proper operation of SILMIL. The laser output is focused and a pinhole with an aperture size of 5µm (Thorlabs P5S) is used for filtering. The 5µm pinhole is mounted on a spatial filter (KT310/M, ThorLabs Inc.) and is used to filter the raw laser output, see schematic in Figure 3-9. Fine adjustment in the *x* and *y* axis is required to achieve maximal power output and this is expect to be a few milliwatts lower than the maximal rated laser output primarily due to path losses.

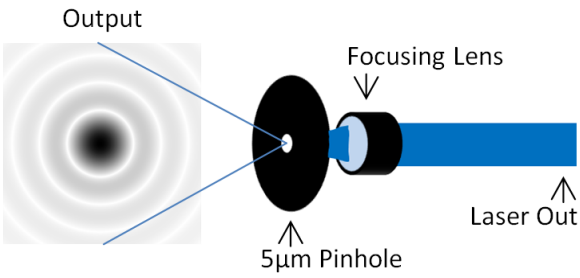

Figure 3-9 – Schema of spatial filtering of raw laser output using a 5µm pinhole. Mirror optics are not shown

The spatially filtered intensity profile is expected to be cylindrically symmetric and have the likeness of the output illustrated in Figure 3-9. This is an approximately Gaussian single-mode beam profile. For conventional Lloyd's mirror interferometric lithography, the single-mode beam output would be utilized at a certain distance away from the pinhole where it the power distribution along the wave front is near uniform and a plane wave approximation may be made. This is essential for proper IL. Alternatively, beam-shaping and collimating optics could also be employed to achieve a flat wave front.

For the design of the system that is discussed however, there is a prism in the optical path and care must be taken to prevent edge scattering of the plane waves due to the prism. One way this could be done is by employing beam blockers to ensure that the flat wave fronts are only incident upon prism face. Care must also be taken to ensure that the width of the wave front is such that any spurious reflections resulting inside of the prism are still driven outward without contributing noise to the image. As the title of the following sub-section suggests, a different approach was employed.

3.5.3 Exposure beam collimation & lens alignment

While the use of beam blockers would be ideal, this method was not used. Instead the output of the pinhole was collimated to the required spot size directly using a lens (LA4924-UV, Thorlabs Inc.). This allows for a higher intensity collimated beam and hence a shorter exposure time which allows for quicker data accumulation. As an example, a pseudo-dosage (to be discussed in a later section) of 2.5 mW-min at a *NA* of 1.824 requires a 38 seconds exposure with a 4mW beam (or power density 5.7mW/cm^2). In contrast, other researchers in our lab have carried out conventional IL successfully and require a power level of 0.12 mW at a distance of approximately 1.25 m away from the spatial filter where the wave fronts approximate a plane wave. In our case, using an intensity of ~0.12 mW would require an exposure time of approximately 21 minutes (or 33 times longer). This is considerably longer and unnecessary as will be evident from the results that are demonstrated later in this chapter.

The collimating lens must be chosen such that the collimated spot size is much less than the size of the prism face, once again to prevent contributed noise from any possible edge diffraction effects. It would be ideal to mount the collimating lens via an extension to the spatial filter itself. However, the optical axis of the spatial filter was misaligned with that of lens mount. Using an external mount provides all of the degrees of freedom necessary to compensate for this misalignment. The easiest way to achieve this was to mount the collimating lens on a precision kinematic mirror mount (KS1, Thorlabs Inc.) and attach to a switchable magnetic base (MB175, Thorlabs Inc.). Figure 3-10 shows a schematic and photograph of the various degrees of freedom now available.

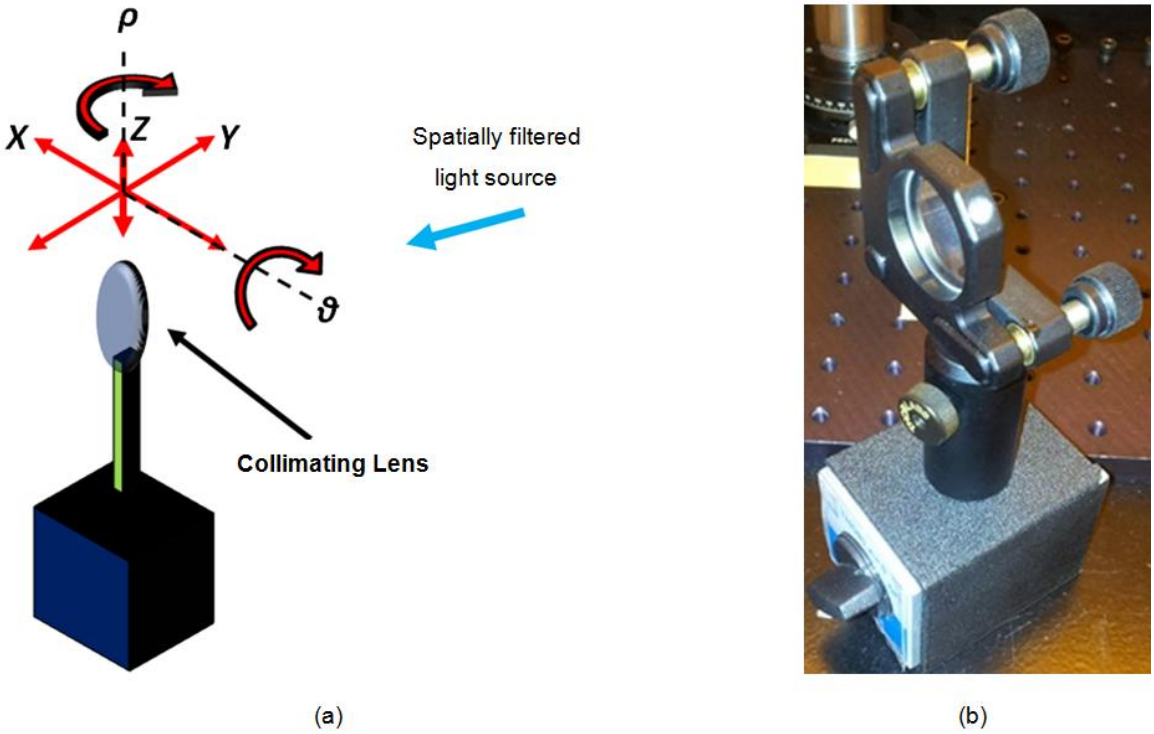

Figure 3-10 – Mounted collimating lens (a) Schematic showing multiple degrees of freedom (b) photograph of the mounted collimating lens

Proper collimation requires the following instructions to be executed in order.

1. The kinematic mount should be adjusted in the $\boldsymbol{\rho}$ and $\boldsymbol{\theta}$ axis to ensure that the optical axis of the collimating lens is parallel to the ground and the optical axis of the spatial filter setup. This of course requires that the optical axis of the spatial filter setup is also parallel to the ground.
2. Using a detector card, judge the approximate height of the center of the Gaussian beam and adjust the height (***Z***) of the collimating lens to match this.
3. Place the lens in the path of the Gaussian beam and the detector card in front of the lens to get an idea of the shape and size of the collimated spot size. Move the detector card to various distances from the lens and notice how, if at all the collimated spot changes in diameter.
4. Aim to adjust the collimating lens in the ***Y*** axis so that the collimated spot size remains constant at any distance from the lens, use the detector card as done in step 3, to monitor this.
5. Finally, the collimating lens should be adjusted in the ***X*** axis to align the center of the collimated beam with the center of the Gaussian beam. Efforts must be made to ensure that this results in a cylindrically symmetrical collimated beam. This may be checked using a detector/sensor attached to a power meter setup to take measurements at λ= 405 nm (PM100D, Thorlabs Inc.).

The result should be a circular finite width laser beam. Step 4 will need to be repeated to ensure a symmetrical intensity variation across the beam. Consider Figure 3-11 for example where bright and dark areas correspond to high and low intensities on the collimated spot. A radially symmetric intensity variation like the one in Figure 3-11 (a) is expected and crucial for repeatability, while an intensity variation similar to Figure 3-11 (b) is undesirable and will only act to ruin the interference pattern. The intensity and its variation across the collimated spot should be noted down to compute the exact dosage and keep it constant as the output power is likely to vary slightly each time the laser is turned on.

Figure 3-11 - Intensity profiles (a) Expected and (b) Undesired collimated spot

Prior to detailing the setup of the prism, the following sub-section considers the effect that the partial reflectivity inherent to a mirror in the Lloyd's mirror setup might have on the completed interference pattern.

3.5.4 Partial reflectivity of Lloyd's mirror

As SILMIL employs the use of an immersed Lloyd's mirror, it is the reflectivity of this mirror that dictates the intensity of the secondary interference beam. A large variation in the intensities of the two interfering beams will result in a background exposure to the image. Hence, the possibility of this happening with SILMIL was investigated.

At an image *NA* of 1.824, the subject of our case study, the reflectivity r (for TE light) at the interface of Yttrium Aluminum Garnet (YAG) and Aluminum (Al) is 0.9367. Finite Element Method (FEM) simulations were employed to simulate the effects of an imperfect reflectivity on the final image for a *NA* of 1.824. Figure 3-12 (a) illustrates a cross sectional profile at 10 nm depth into the resist where an image has been formed with both beams having equal intensity, the FEM simulated image is presented as an inset. Figure 3-12 (b) presents results for the scenario where one of the beams has relative amplitude of 0.9367 to simulate the partial (imperfect) reflectivity of the Al mirror.

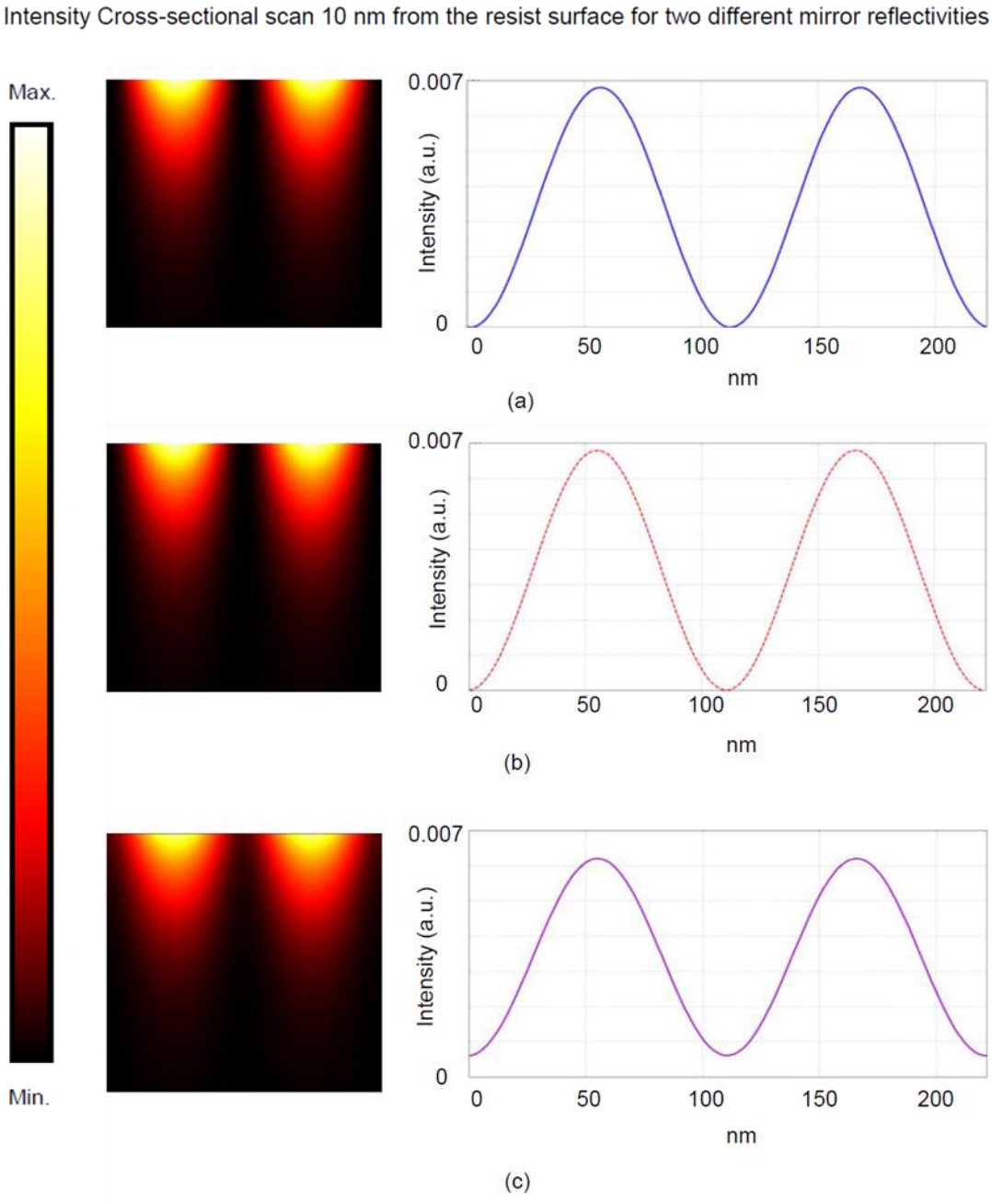

Figure 3-12 - Intensity Cross-sectional scan 10 nm from the resist surface for mirror reflectivity (a) *r* = 1, null = 0 and (b) *r* = 0.9367, null = 0 (c) Hypothetical case, *r* = 0.525, here nulls ~ 10% of peak amplitude.

Clearly, it is evident from the simulations in Figure 3-12 (b) that an imperfect reflectance of 0.9367 makes no visible contribution to the image (c.f. Figure 3-12 (a)) and hence should not result in any background exposure. In fact, further simulations (see Figure 3-12 (c)) also reveal that the reflectivity at the YAG-Al interface is required to be as low as 0.525 before the nulls of the interference pattern have an

amplitude as high as ~10% of the peaks of the interference pattern for imaging at the above *NA* of 1.824. The overview continues in the following sub-section with a description of the prism setup.

3.5.5 Prism plan & configuration

At λ = 405 nm, an undoped Yttrium Aluminum Garnet cube prism has a refractive index n = 1.857 [170] using the Sellmeier equation, where λ is in nm.

$$n^2 = 1 + \frac{2.2779\lambda^2}{\lambda^2 - 11420} \tag{3.2}$$

To make sure of this, the reflection of the direct 405 nm laser output from the surface of the prism at various angles was measured and overlaid on a plot containing the predicted Fresnel TE reflection at an Air-YAG interface using 1.857 as the prism refractive index calculated using (3.2). The two plots indicated reasonably good agreement with each other as is illustrated in Figure 3-13. It is believed that the visible discrepancy between the measured and modeled reflectance plots is because of a measurement error that has arisen due to the geometry of the prism and the contribution of the various adjacent faces to the measured reflectivity and that this error is higher for higher angles of incidence.

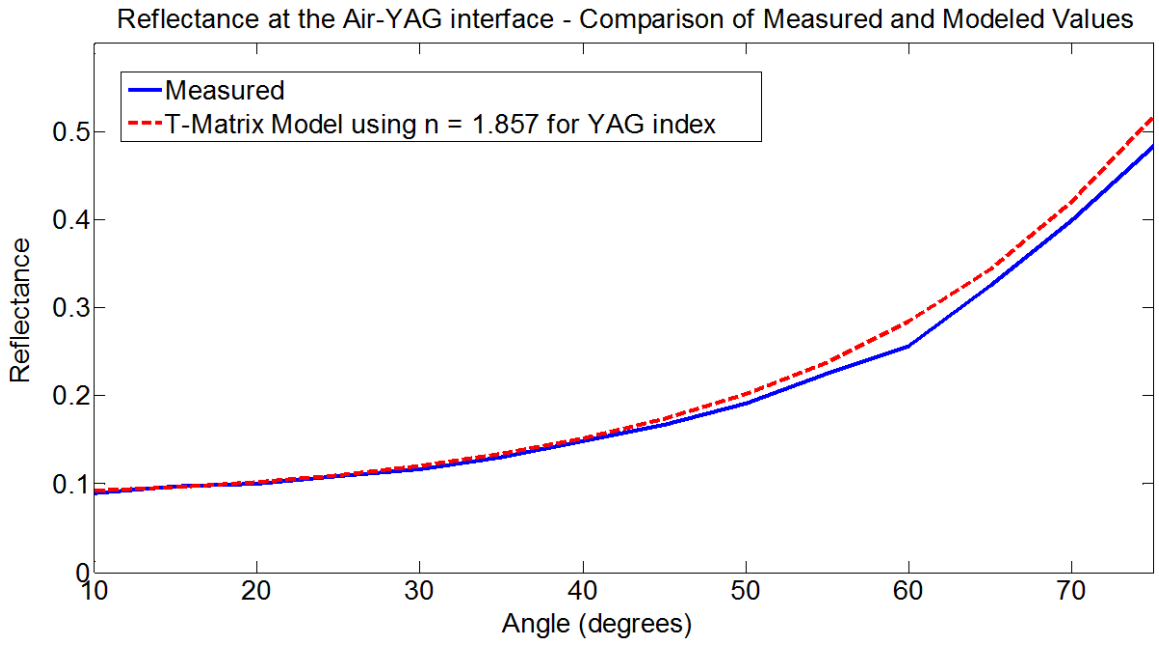

Figure 3-13 – Reflectance at the interface between air and YAG prism. Measured (solid line) and modeled using T-Matrix using n = 1.857 as the refractive index of the prism (dashed line).

The results of SILMIL to be presented in later sections and measurement of pattern pitch using a highly accurate interferometer in the scanning electron microscope further confirms that 1.857 is an acceptable

value to use for the refractive index of YAG. A schematic of the open plan view of the prism setup for SILMIL is given in Figure 3-14.

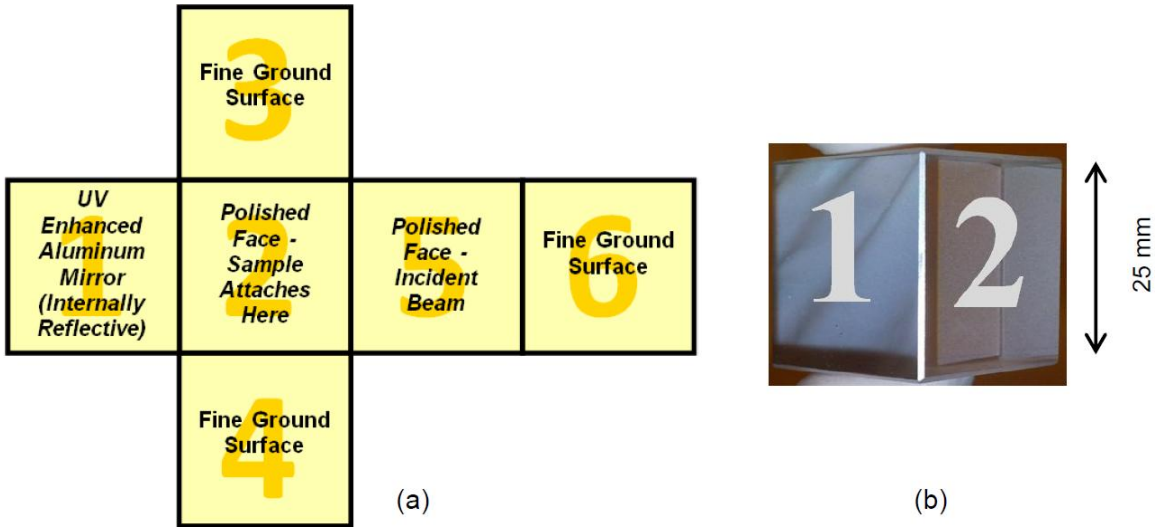

Figure 3-14 – (a) Open plan view of all the faces of the Prism used in SILMIL (b) Photograph of prism used for SILMIL

Figure 3-14 (b) shows a photograph of the prism with the configuration depicted in Figure 3-14 (a). The prism is held in a custom designed cage (see Figure 3-15) that fits on a rotational substrate (PR01, Thorlabs Inc.). The cage is constructed out of stainless steel to avoid conformation when pressure is applied to achieve intimate contact between the sample and prism face (face 2). Another important aspect of SILMIL is the backing plate, discussed in section 3.5.7. This needs to be designed carefully so that the sample experiences a uniform pressure over as large an area as possible.

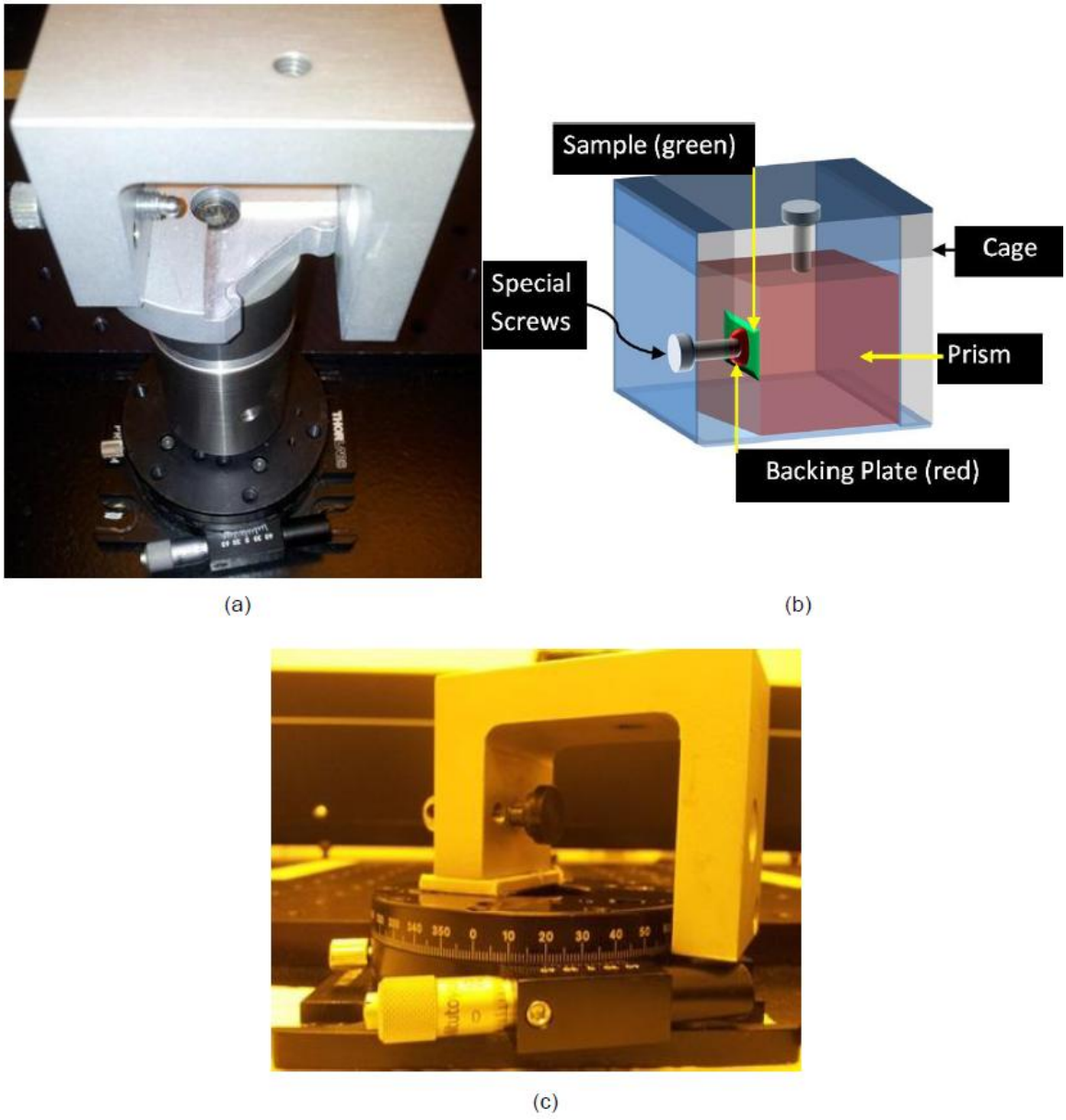

Figure 3-15 – (a) Photograph of the prism cage setup used for SILMIL (b) Annotated schematic of the setup with backing plate, thumb screws and sample for SILMIL (c) Photograph of the prism cage setup used for attenuated total reflectance (ATR) and prism index measurements

In Figure 3-15 (a) a photograph of the cage on a rotational substrate is presented as it was utilized for SILMIL, which is taken without the backing plate. Figure 3-15 (b) shows an annotated schematic. In Figure 3-15 (c), the cage is depicted at a lower height, as it is detached from the columnar structure, but still attached to the rotational substrate. This was required to carry out attenuated total reflectance (ATR) and prism index measurements as the height of the direct laser output is much lower than that of the collimated beam used for SILMIL. A procedure is now presented to allow for the alignment of the prism with the collimated beam from section 3.5.3.

3.5.6 Prism & Beam Alignment

With the high index of YAG at our disposal the prism and mount may be orientated along the rotational axis of the substrate to achieve the desired *NA*. Without loss of any generality, an angle of rotation of 20^o with respect to the incident beam was chosen for imaging, as depicted in Figure 3-16. At this angle, the interference pattern is expected to have at an ultra-high *NA* of 1.824 (λ/7.3 or 55.5 nm half-pitch), resulting in an exposure in the resist that is dominated by evanescent fields. This is a result of the geometry of the setup and also the refraction that an incident beam experiences; this is also illustrated in Figure 3-16. This *NA* will be used as the case study for the subsequent experiments in this chapter and also in Chapter 7.

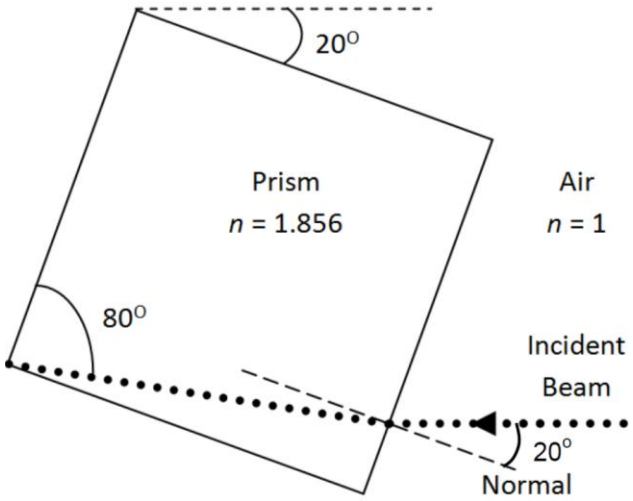

Figure 3-16 - Yttrium Aluminum Garnet prism rotation required for a *NA* = 1.824 at λ = 405 nm

In an earlier section, setup and alignment of the collimating lens with respect to the spatial filter was discussed. Equally important for the repeatability of SILMIL is the proper alignment of the prism with respect to the collimated beam. Consider Figure 3-17, a simplified setup consisting only of the prism and the collimating lens mount. The goal here is to make sure that the incident and internally reflected beams inside the prism that create the interference pattern are similar in intensity. A difference in intensity between the two beams can result in a background/DC component that acts to add a background exposure much like the TM polarized case discussed earlier in Chapter 2. To achieve the said alignment, the path and appearance of the collimated beam as it travels towards the prism is first monitored and then monitored again when it is back reflected from the inside of the prism as depicted in Figure 3-17.

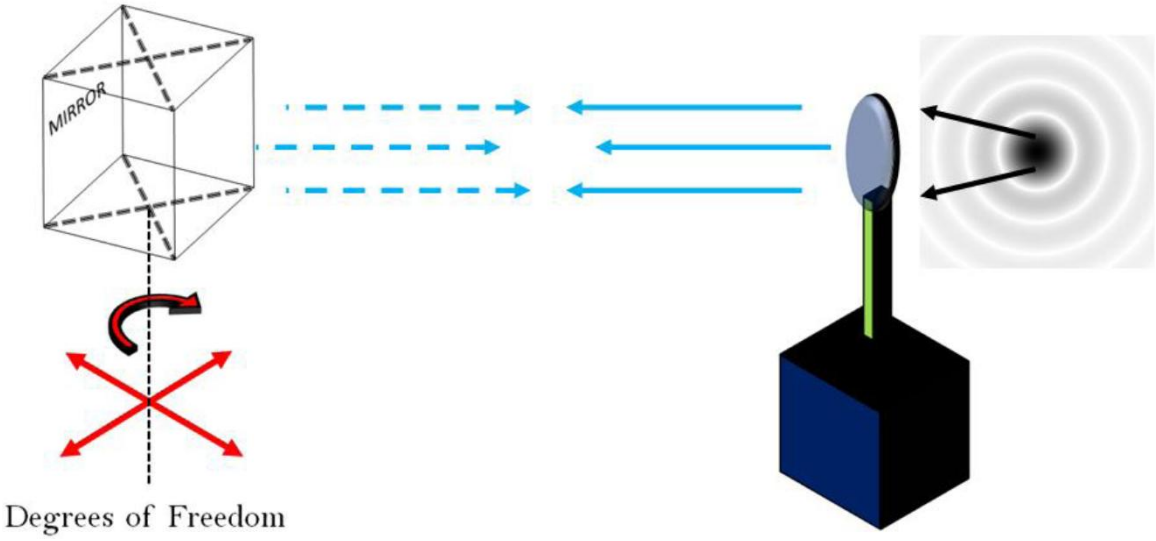

Figure 3-17 - Proper prism alignment with beam by observing the reflected beam

The prism needs to be adjusted in both the ***X*** and ***Y*** axis so that collimated spot is bisected by the interface between faces 1 and 2 (see Figure 3-18) inside of the prism. The easiest way to achieve this is to first deliberately shift the collimating lens a slight amount in the direction normal to the lens so that the spot size reduces in diameter with increasing distance from the lens. Next, the back reflection is monitored as the prism is adjusted in the ***X*** and ***Y*** axis. Upon correct adjustment, the back reflection (monitored with a detector card) should show two diverging semi-circular spots.

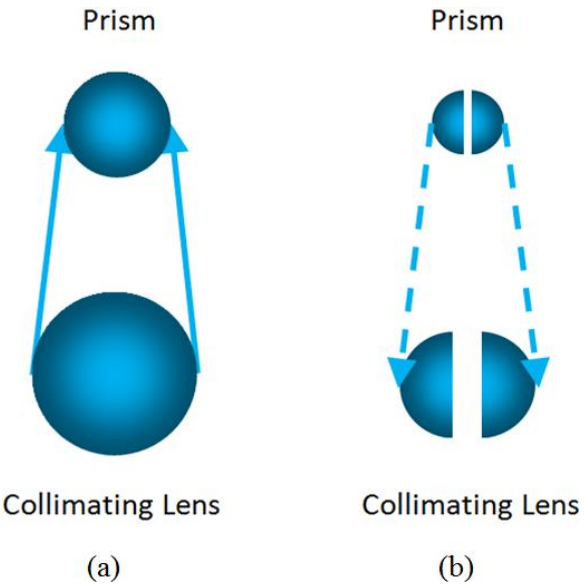

Figure 3-18 – Achieving proper prism alignment (refer to text) (a) the beam travels towards the prism, (b) aligning the prism such that the reflected spot is split in two equal parts.

Figure 3-18 (a) indicates the intentional misalignment of the lens to achieve a decreasing spot size. Figure 3-18 (b) illustrates the expected back reflection from the prism when prism alignment is complete. The collimating lens should be moved back to the correct position following the prism alignment. Figure 3-19 demonstrates the alignment process using a sequence of photographs and Figure 3-20 shows a photograph of the full setup and an overlay of shapes to illustrate the path of the laser beam.

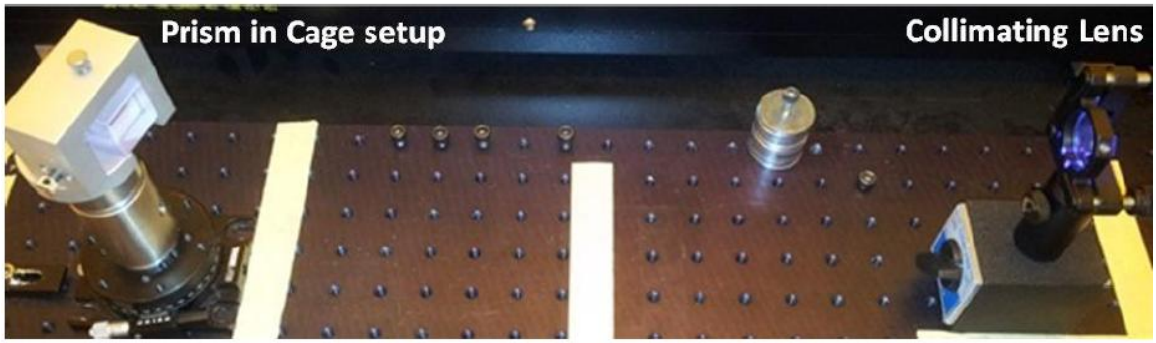

(a)

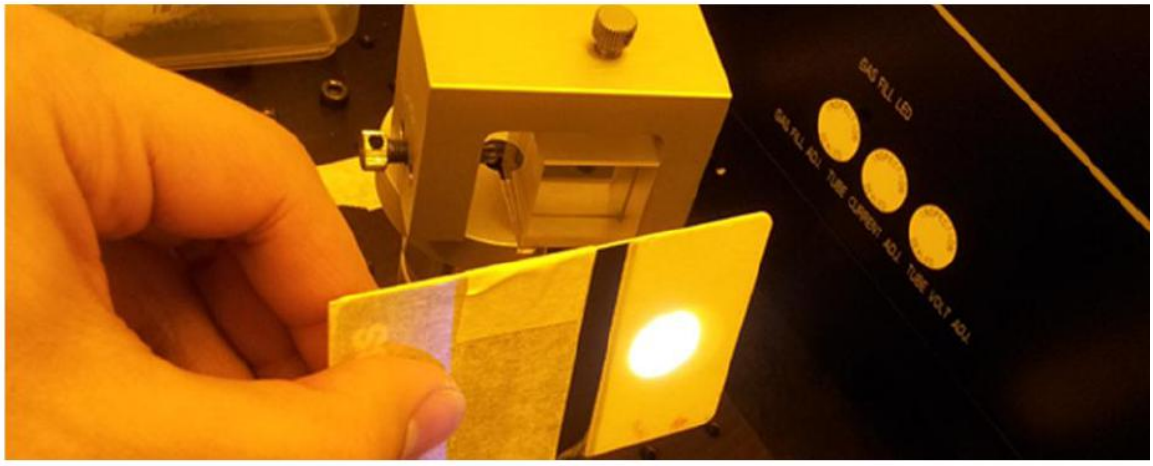

(b)

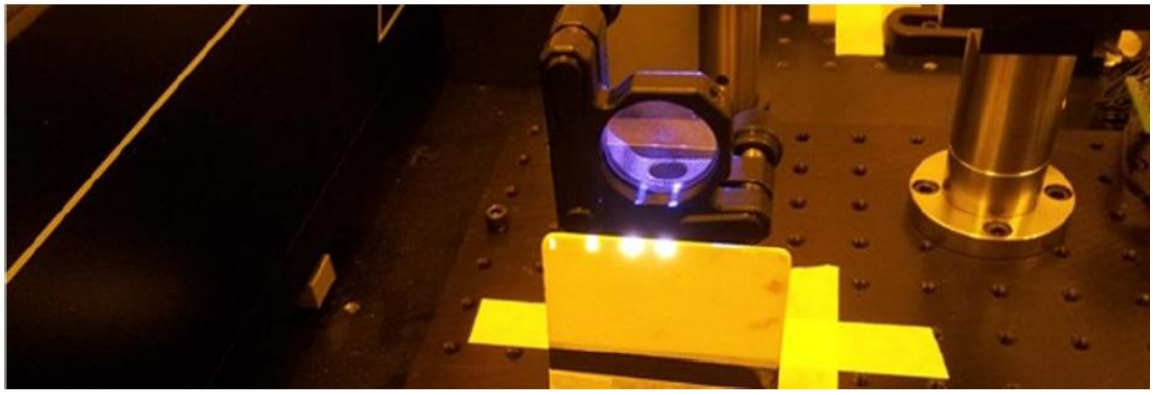

(c)

Figure 3-19 – Sequence of images demonstrating proper prism alignment prior to SILMIL exposure (a) Bird's eye view after collimated lens is adjusted to produce a symmetrical beam (b) Use of a detector card on the prism side to ensure beam is incident on prism face (c) Use of a detector card on the collimating lens side. Align the prism such that reflected light from inside the prism is split into two equal portions and is equidistant about the centre of the lens

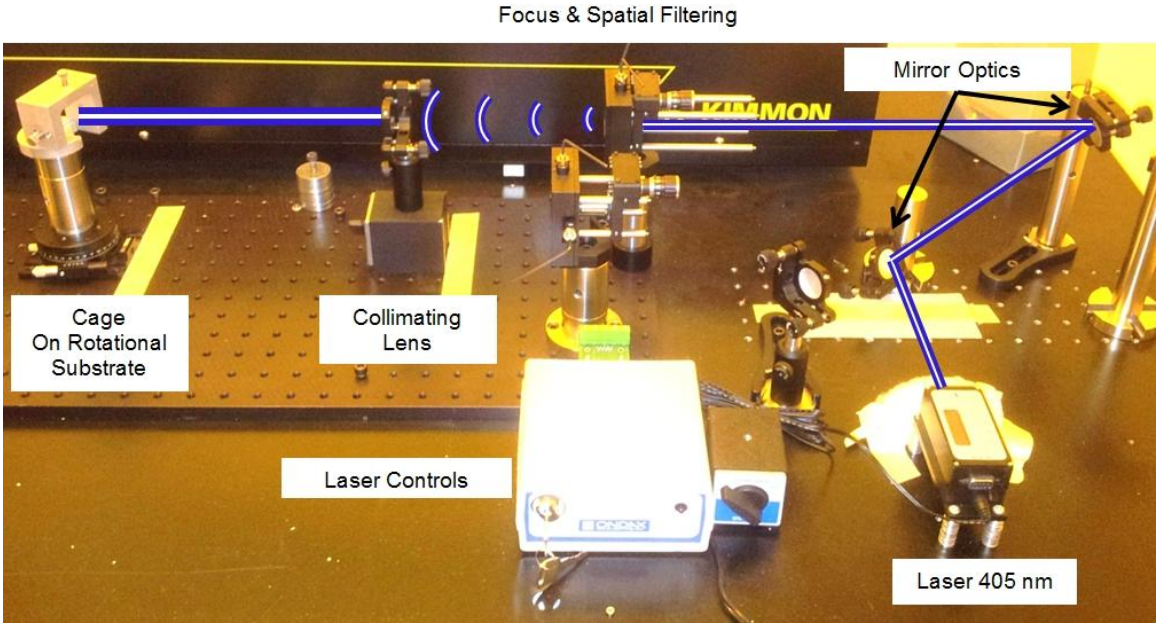

Figure 3-20 – Full setup photograph for SILMIL operation, the various elements are noted

Another aspect of SILMIL that deserves special attention is the need for intimate contact between the sample and prism face, which is to be achieved by utilizing the correct back plate. The following sub-section summarizes the results of this task.

3.5.7 Back plate - material & design

Initially aluminum backing plates with a machine worked flat surface finish were used to clamp the sample to the prism. Design modifications were made to the back end of the plate to determine the optimum shape that would allow the largest area of contact. Some of these designs are presented in Figure 3-21 (a) – (d). Figure 3-21 (a) depicts the flat finish of the aluminum backing screw. Figure 3-21 (b), (c) and (d) illustrate the conical, and non-conical back ends. The conical design Figure 3-21 (b) was ultimately found to allow the largest contact area.

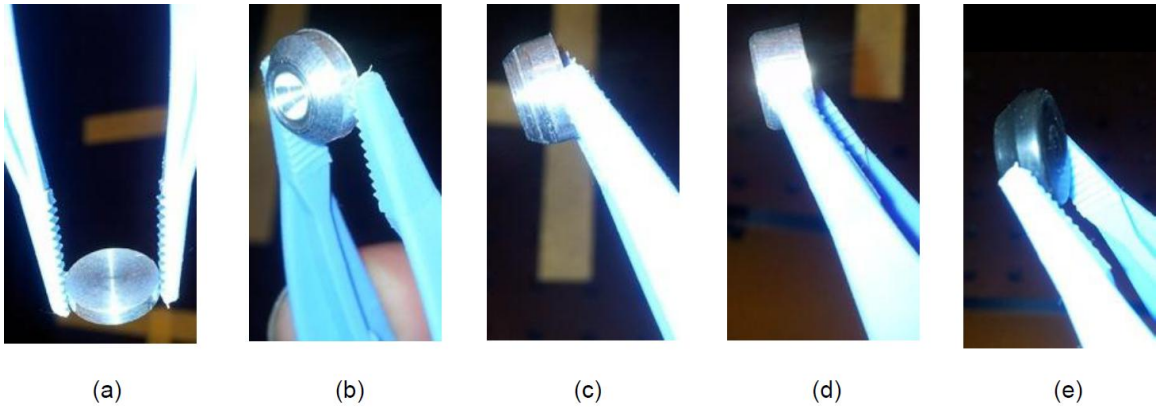

Figure 3-21 – Photographs of (a)-(d) various Aluminum backing plate designs (a) Flat finish of the surface (b) Conical back end (c) partially conical – partially cylindrical back end (d) cylindrical back end and (e) Teflon, a more flexible material used as a backing plate. The back end maintains a conical shape, however the surface is now made convex so that it protrudes outwards and deforms under pressure.

The area of contact reduced with continued usage of the aluminum back plate indicating deformation of the plate's surface due to pressure. In addition, the area of contact was never sufficiently large to start with, this is owing to the rigidity of the backing plate material *i.e.* aluminum which does not deform as much as is required under pressure. Hence, a more deformable material like Teflon was chosen, which resulted in reproducible exposures. However, a significant improvement in the contact area was seen when the surface of the Teflon back plate was made slightly convex, i.e. a protruding surface that is intended to deform upon contact. A photograph of the Teflon back plate is provided in Figure 3-21 (e), although the convex surface is difficult to see here. Note also that the reverse sides of all of the above back plates have a spherical groove so that pressure from the thumb screws is uniform over the area of the plate.

The thumb screws are therefore ball-ended and fit into the grooves. The preparation of the imaging stack and a procedure for proper sample installation is detailed in the following sub-section, after which the results of SILMIL are presented.

3.5.8 Imaging stack preparation & sample installation

The imaging stack consists of various layers of materials stacked together to transfer the evanescent interferometric field profile into the photoresist. The stack that is used in this chapter is made up of a 400 nm layer of photoresist spun on a silicon wafer with some ARC to encourage adhesion, with ~12nm of a sacrificial poly-vinyl alcohol (PVA) spun on the photoresist. Finally, the sample is blown dry with compressed nitrogen to remove dust before a few drops of index matching liquid (IML) are placed on the stack. The purpose of the PVA layer is to prevent the IML from attacking the photoresist.

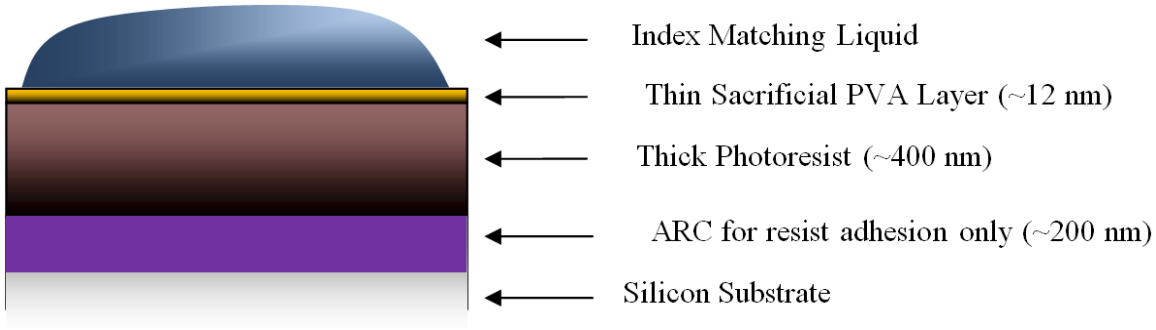

Figure 3-22 - Basic Imaging stack for SILMIL

For the stack of Figure 3-22, an 11.4 mg/ml solution of PVA solution was created and spun at 4000 rpm to achieve an average layer thickness of ~12 nm. Table 1 details the optical properties of various materials, and some of which are also used in the stack later. The IML is not a constant thickness thin film and while it is required to wet the surface of the three layer stack uniformly, effects such as difference in surface energies come into the picture.

Table 1. Optical properties of several materials discussed in the thesis

Optical properties of various media			
Material	**Refractive Index/Optical Property**	**Thickness**	**Reference**
Yttrium Aluminum Garnet prism	n = 1.856 @ λ = 405 nm	Not applicable	[170]
Index Matching Liquid (Cargille, Series B 17000)	n = 1.7714 @ λ = 404.7 nm	Few drops	[171]
Poly-vinyl Alcohol	n ~1.5 @ λ = 405 nm	12 nm with Silicon substrate. 24 nm with Quartz substrate	[172]
Photoresist	*AZ HiR 1075 –* n = 1.682+0.031i @ λ = 405 nm *Industry standard -* n = 1.7 + 0.02i @ λ = 193 nm	Controlled & Varies with experiment	[173]
SiO_2/Quartz	n = 1.47 @ λ = 405 nm		[174]
Hafnium Oxide (HfO) (RF target)	n ~2 *(varies)* @ λ = 405 nm		Measured with ATR
Aluminum Oxide	n ~2.08 (film), n ~1.92 (prism) @ λ = 193 nm		[139, 175]
Poly (methyl methacrylate) PMMA	n = 1.517 + 0.0005*1i @ λ = 405 nm		[176]
Silicon	n = 5.42 + 0.329i @ λ = 405 nm	Semi-infinite	[174]

The sample installation step needs to be carried out meticulously to minimize possible aberrations to the prism's surface. The locked prism along with the cage setup is oriented such that the sample face (face 2, see Figure 3-14) of the prism is parallel to and facing the floor. The sample, held with tweezers is then

brought up into contact with this face. The presence of the IML allows the sample to glide freely. This orientation is better illustrated by the photograph in Figure 3-23.

The setup is then reoriented via a flip vertically so that the sample face of the prism is parallel to and faces the ceiling. The backing plate is then placed on the back of the sample that rests on the prism surface. The sample and backing plate are then translated along the prism surface and lined up with the ball appendage of the backing thumb screw. While turning the thumb screw, care is taken to ensure that its ball appendage fits in to the socket of the backing plate. The refractive index of the IML (n = 1.77) is lower than the *NA* that is being imaged and this implies a decay for the evanescent image in the IML layer. A higher refractive index liquid was also considered, but this also had a higher extinction coefficient at λ = 405 nm and so resulted in rapid image decay. For this reason, a thin IML layer is necessary and it is essential that the thumb screw is sufficiently tightened so that excess IML has been drained out. In addition to this, a few exposures might be necessary to determine whether the pressure applied has been sufficient or not. An easy way to monitor the pressure is by marking the back of the thumb screw and recording the number of turns or angle that it has been rotated. This number varies, since different materials conform by different amounts under the same pressure.

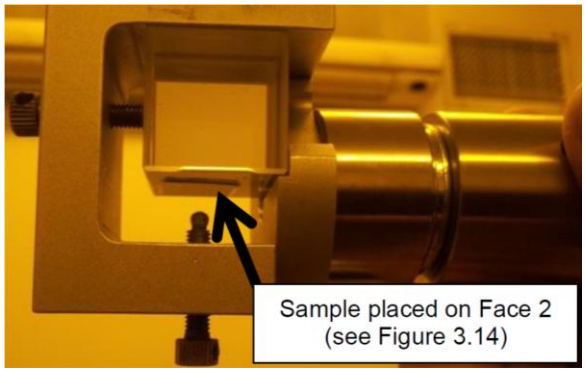

Figure 3-23 – Sample installation. Sample glides due to the presence of the IML. The back plate is not present in this photograph

This concludes the setup of SILMIL and the following section presents details on the mechanism of and what is required for proper repeatable exposures. A metric is introduced to measure the dosage and allow a simple comparison between different exposures. Various exposures are carried out and the results presented as AFM scans, these are analyzed in detail shortly after.

3.6 Exposure & Post-processing

If the actual power dissipation were to be computed in the photoresist during a certain exposure using SILMIL, a few issues arising due to the geometry of the setup would first need to be taken into

consideration. A method is suggested here on how one may go about doing this. Firstly, the changes experienced by the beam's cross section as depicted by double sided red arrows in the schematic in Figure 3-24 would need to be understood.

The goal is to compute the power density of the beam that is incident upon the sample. This requires computing the transmittance of the beam into the prism at the particular angle of incidence. Following this, a new transmitted power density would need to be computed using the new cross sectional area of the beam that results due to refraction. The beam undergoes a change in cross-sectional area once again as it travels to the sample face ***DE***. Here, half of the beam is partially reflected by the mirror face and interferes with the other half that travels directly to the sample. It is well known that a partial reflectivity may act to add a background component to the interference pattern. All of this may be represented as an equation. Finally, also recall that a collimated beam ideally has a Gaussian intensity distribution. This would need to be taken into account by multiplying the equation for the interference pattern by the Gaussian intensity distribution; allowing the computation of the dosage variation across ***DE***. Hence, depending upon where on ***DE***, the sample is placed, an equation for the intensity of the resulting interference pattern may be computed in terms of the beam's incident power density using all of the above details.

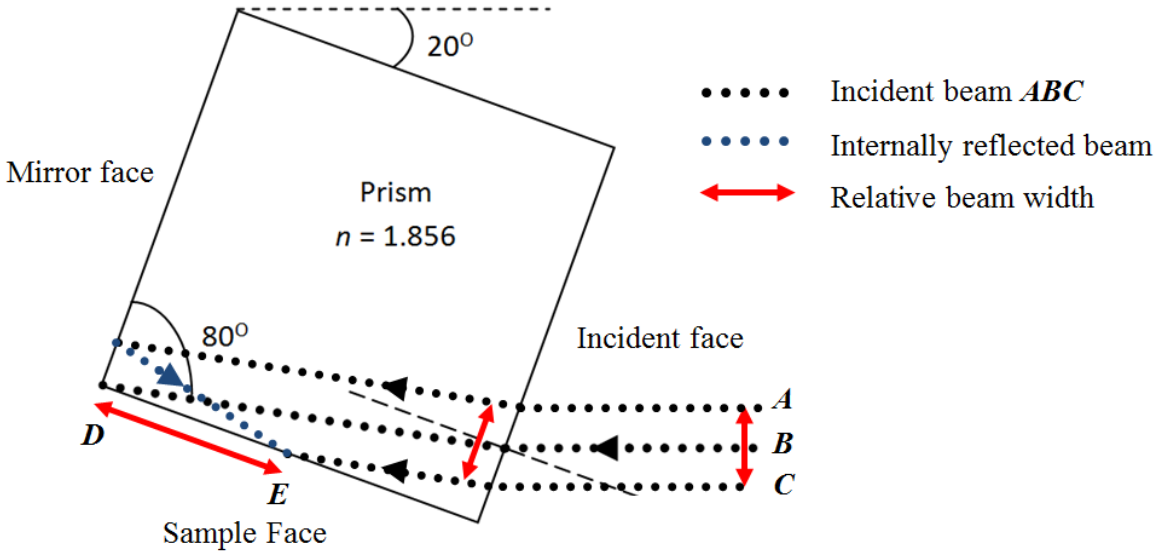

Figure 3-24 - Illustrated beam path

In practice however, one may choose to ignore the contribution from the partial reflectivity of the mirror owing to the result of FEM simulations in section 3.5.4 which suggest that the magnitude of the partial reflectance is sufficiently high such that it plays a negligible/immeasurable role in contrast reduction. If consistent measurements were taken at the same location on the sample face, then for a particular *NA*, the

computed equation would simplify to a constant. This implies that for a particular *NA*, all of the experiments may be compared with each other using a pseudo dosage term as opposed to the actual dosage and hence the need to compute the said equation is avoided. In this thesis, a pseudo dosage term is used and computed as the product of the exposure time with the intensity at the center of the incident beam.

$$PD = I_{collimated\ spot}(mW) * t(minutes) \tag{3.3}$$

After the laser is first turned on, it takes a few minutes before the intensity of the beam has stabilized (due to heating up of the optics in the path). For this reason, the laser output is simply blocked either with a shutter or a beam blocker as opposed to turned off after an exposure. This allows a constant operating power and hence avoids the need for a waiting time between successive exposures. It is recommended that the laser output be covered rather than turned off at intervals between exposures as every reboot also results in a slightly different spatial profile, which will mitigate the need for repeated re-alignments.

The power intensity is measured by always placing the detector in front of the prism in cage setup; the detector is of course moved away during an exposure. A stop watch is used to time the exposure. The sample is removed from the cage by unscrewing the backing plates and care is taken to support the now unlocked prism. Latex hand gloves and a face mask are used to prevent contamination of sample and prism faces and also to avoid exposure to the IML.

The first step in sample post processing involves removing away the IML layer. This is done by agitating the sample in a beaker of toluene, for ~10-15 seconds. The remaining toluene on the sample is blown away using a compressed nitrogen gun. It is recommended that these steps be performed in a fume cupboard due to the harmful effects of toluene to the human body. The sample is then rinsed in DI water for 20 seconds to dissolve the water soluble PVA layer. Following this the sample is developed for 1 minute in 1.59% solution of tetra-methyl ammonium hydroxide (AZ326 MIF developer diluted 2:1 with deionized water, AZ Electronic Materials). Finally the sample is washed once again in DI water and dried with compressed nitrogen. Atomic Force Microscope (AFM) scans of the sample reveal regular line and space patterns. Some details regarding the careful use of an AFM are presented in the next section. Results of experiments regarding the dosage variation are now presented, along with a discussion of the results.

3.6.1 Dosage variation

Here, the effects of dosage variation are explored and the capability of SILMIL is demonstrated at various pseudo-dosages (PDs) at a *NA* of 1.824 using λ = 405 nm. Figure 3-25 shows a photograph of the various

samples. The contact area is increasingly visible at higher dosages because of the increase in the amount of resist that is removed. This will be further evident from the plot in Figure 3-28 later.

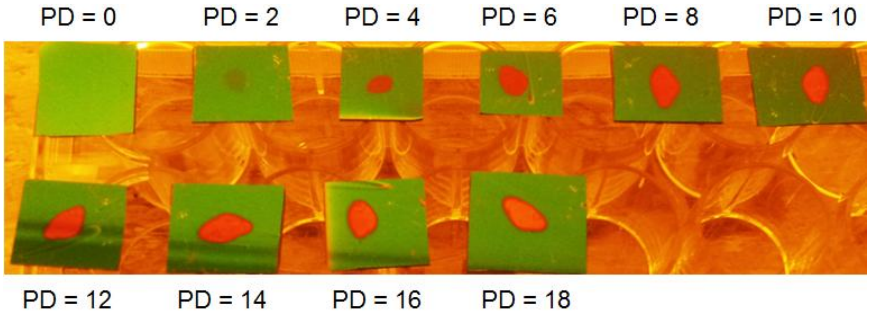

Figure 3-25 – Photograph of the samples with Pseudo-Dosages (PDs) ranging from 0 to 18 mW-min

A Digital Instruments atomic force microscope was used to scan the recorded interference patterns. A Tap300Al-G tip (BudgetSensors, Innovative Solutions Bulgaria Ltd.) was used for the measurements; this has a tip radius of less than 10 nm, and sloping angles of 20^{o}-25^{o} and 25^{o}-30^{o} along the cantilever axis and the side respectively. The maximal height, slope angle and minimum radius of a tip all play an important role in affecting the accuracy of a scan. For instance, a tall tip with a small radius and narrow slope angle has the capability to image finer resolution, deeper structures. However, such a tip is generally more expensive per unit, reasonably fragile and hence not very cost effective. In addition, such AFM tips are still inferior in their capability to image high resolution structures when compared to other measurement techniques such as scanning electron microscopy (SEM) or transmission electron microscopy (TEM), however these techniques do require a greater sample preparation and loading time.

For comparable AFM scans, several parameters need to be kept constant between scans, for e.g. the tip type and quality, scan size, scan rate, scan angle, grating angle and the adjustment of feedback controls, etc. Since the tip is asymmetric, i.e. narrower in one axis than it is in the other, it is essential that the scans are always carried out in the direction of the narrow axis and the gratings are always placed such that the tip is able to image into the structure. A series of AFM scanned images and cross-sectional scope plots are presented in Figure 3-26 and Figure 3-27 to demonstrate the quality and pattern depth of the images at various PDs. A discussion of these results is presented in the sub-section that follows.

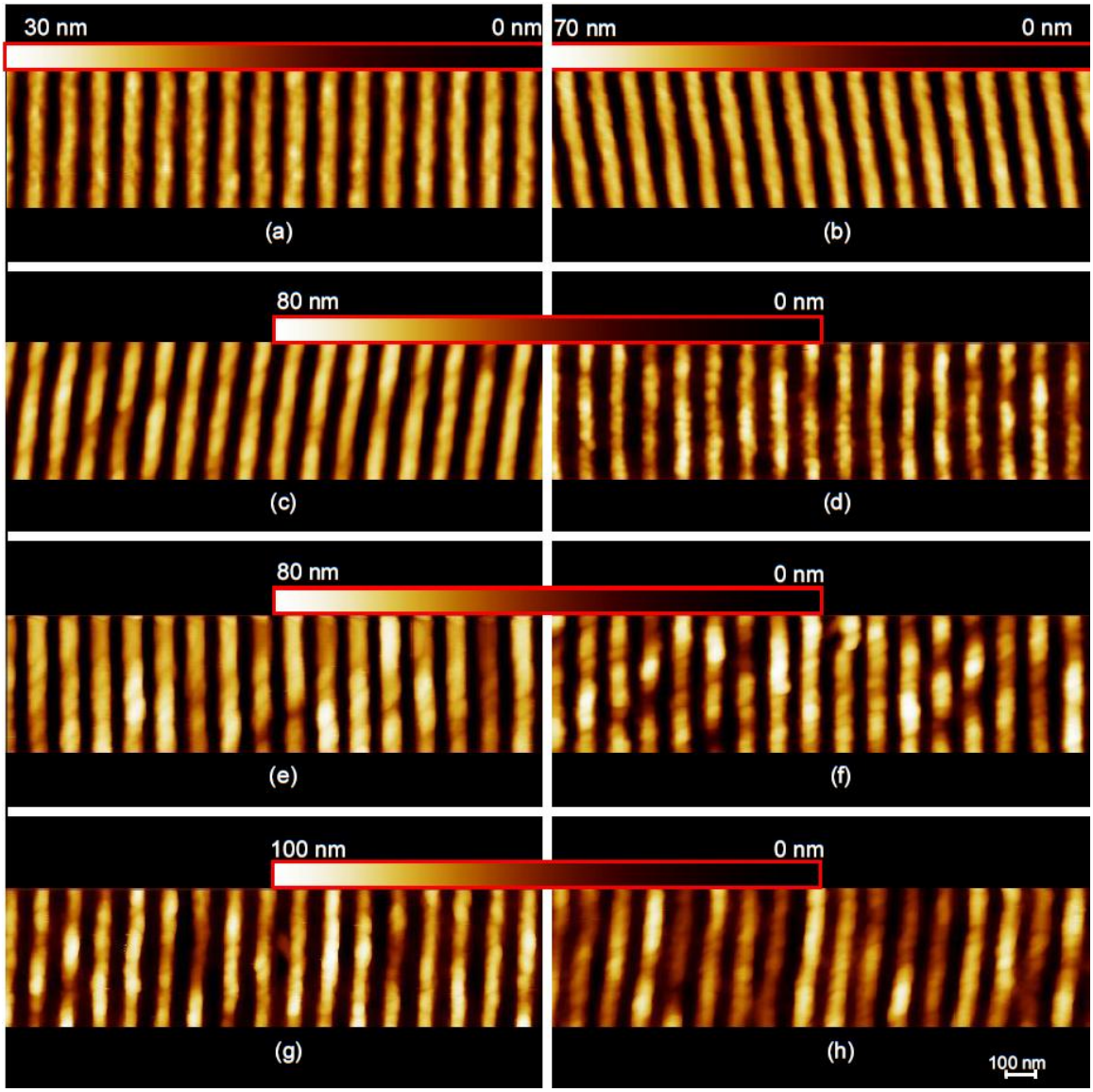

Figure 3-26 – Evanescent Interference Lithography using SILMIL for *NA* = 1.824 at λ = 405 nm resulting in 111 nm pitch. Pattern quality demonstration using 2µm by 0.5µm AFM scans for Pseudo-dosages (PDs) of (a) 2 (b) 4 (c) 6 (d) 8 (e) 10 (f) 12 (g) 14 (h) 16 mW-min

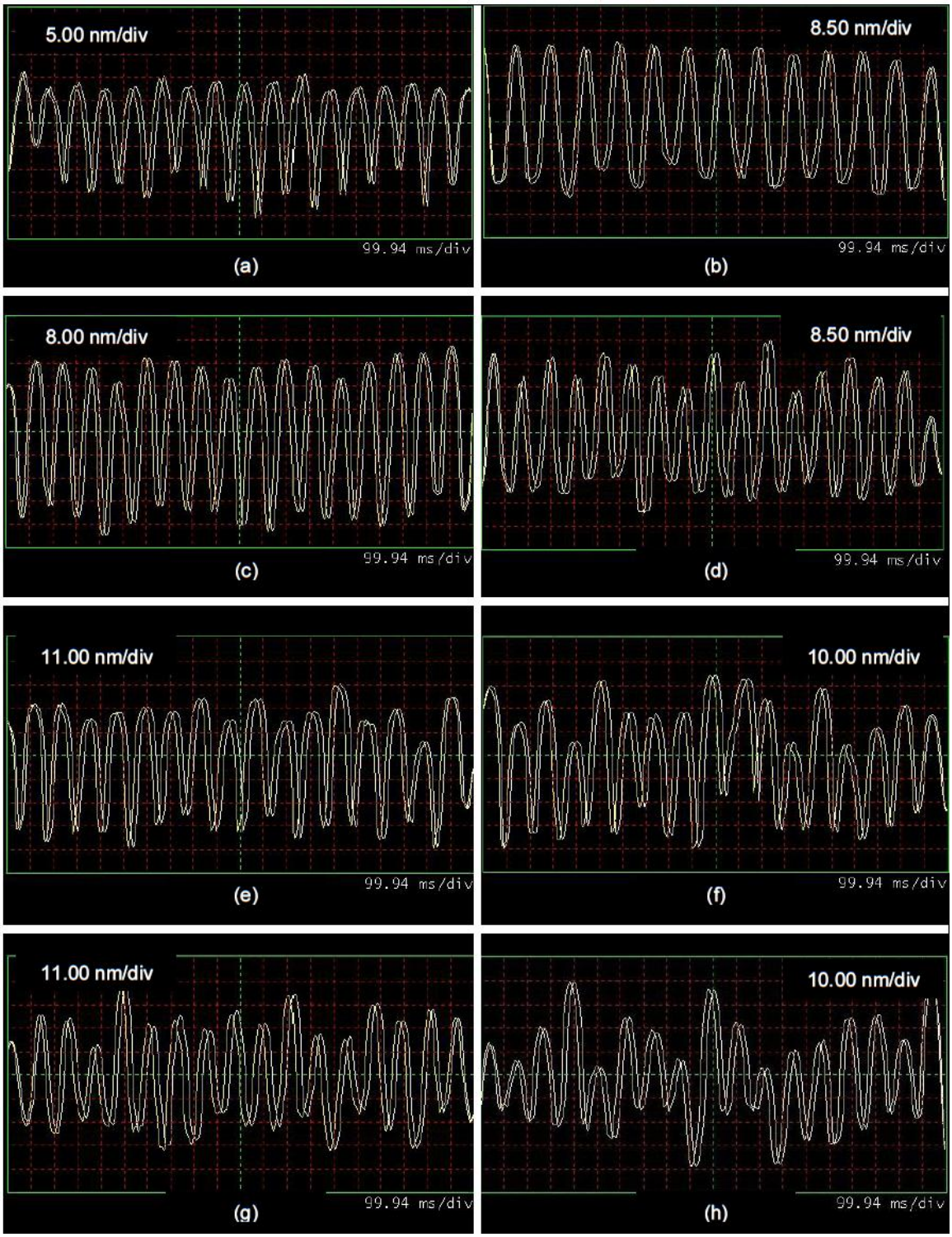

Figure 3-27 - Evanescent Interference Lithography using SILMIL for *NA* = 1.824 at λ = 405 nm resulting in 111 nm pitch. Pattern depth demonstration using 2µm by 0.5µm AFM scope plots for Pseudo-dosages (PDs) of (a) 2 (b) 4 (c) 6 (d) 8 (e) 10 (f) 12 (g) 14 (h) 16 mW-min corresponding to the AFM scans in Figure 3-26

3.6.2 Discussion

It is evident that EIL using SILMIL offers better image quality at lower PDs in terms of the clarity of the peak and null visibility and uniformity of the pattern in general. Figure 3-26 and Figure 3-27 (a) to (c) corresponding to PDs of 2, 4 and 6 mW-min demonstrate better EIL than do those depicted by Figure 3-26 and Figure 3-27 (f), (g) and (h) (PDs of 12, 14 and 16 mW-min respectively). It is believed that Figure 3-26 and Figure 3-27 (d) are anamolies as (e) clearly demonstrates better image quality even at a higher PD. The maximal pattern depth that is achievable with high figure quality is ~50 nm, however this is at the cost of considerable background development (background exposure, explained below) as is illustrated by the plot of the amount of resist removed in Figure 3-28.

Initially, it was believed that the reason for better EIL at a lower PD was that a lower PD implied a lower exposure time and for this reason any noise in the system (defined as anything that acts to degrade the intended signal) was being non-linearly processed. As a result the noise was making a negligible contribution when the exposure times were smaller. One of the obvious sources of noise in SILMIL is the IML layer. The IML layer is not a finite thickness thin film, hence, the interference pattern is experiences a spatial variation in pattern intensity that is incident upon the photoresist, acting as additive noise to the primary signal.

To test out whether our theory regarding the non-linear scaling of system noise with respect to time was true, EIL was carried out for three different exposure times, however the PD was kept constant at 6 mW-min. This was done by attenuating the laser beam output by 3dB, 6dB and 9dB, by making use of neutral density filters (NDUV03B, NDUV06B, Thorlabs Inc.). However, all of these exposures resulted in AFM scans (not shown here for brevity) that were very similar to those depicted in Figure 3-26 and Figure 3-27 (c) indicating that the results were directly dependent upon the dosage and not on the exposure time and that the speculated theory regarding non-linear noise scaling was incorrect.

It is now believed that, the IML does contribute noise to the final image, however, the reason that this noise is only being visible at higher doses is due to the increased sensitivity of the resist development rate at higher doses. Hence, it is likely that at a high dosage, the irregular pattern intensity that results from a non-constant IML layer instigates a higher development rate variation. This gets translated into an undesired variation in resist topography or as a ‘bumpy’ profile as is seen in the scans and scope plots of Figure 3-26 and Figure 3-27 for higher PDs. Figure 3-28 summarizes the results of Figure 3-26 and also includes the resist removed data, which was calculated using a profilometer to measure the depth of a resist trench created on the exposed sample with a scalpel. This measurement was subtracted from the

measured depth of a similar resist trench created on an unexposed sample to obtain the resist removed data.

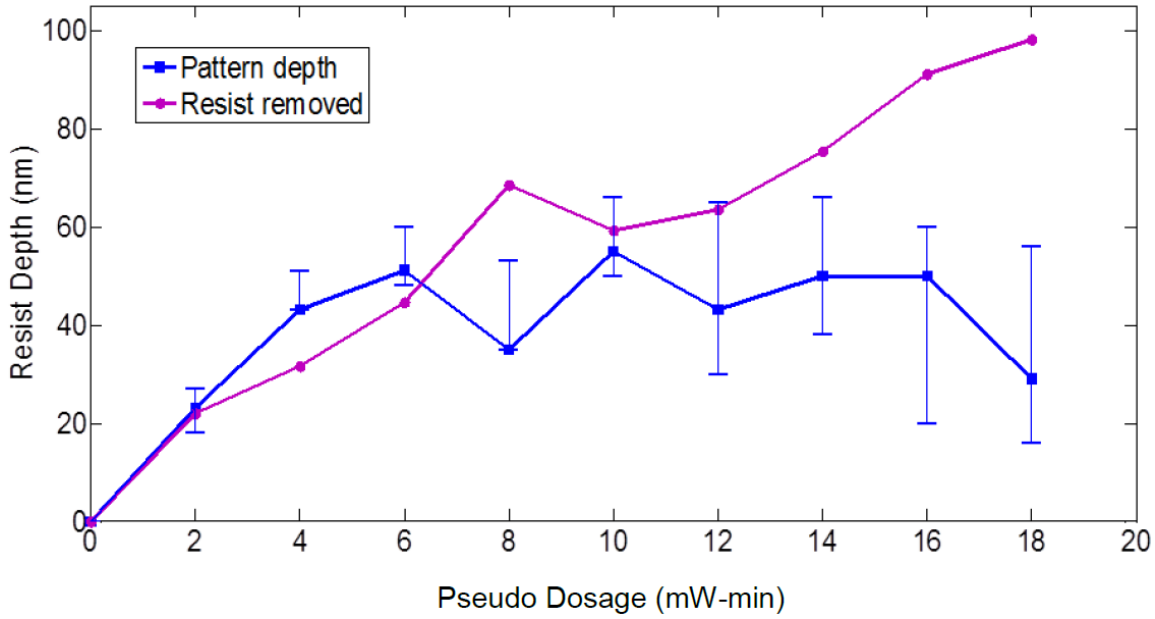

Figure 3-28 – Summary of Figure 3-26 and Figure 3-27 showing the depth of the grating patterned into the resist (square markers) with uncertainties as well as the depth of resist removed (circular markers).

As noted, the PD = 8 mW-min case, is most likely an anamoly as the resist removed and pattern depth markers corresponding to it are severely offset from the general trend. In general, the amount of resist removed appears to be a linear function of the dosage. The pattern depth seems to stabilize to ~50 nm after at a PD of 4 mW-min, even though one would expect this to get deeper with dosage. A likely reason for this is that the background exposure component catches up with the pattern (modulation) component and develops away a thin layer of resist, resulting in a maximal 50 nm depth regardless of increased dosage. It is also noted that the uncertainty presented for the grating depth in Figure 3-28 is much higher for higher doses. Once again, this is evident upon visual inspection of the AFM scans in Figure 3-26, where the imaged patterns seem to lose their regularity at higher doses and exhibit a larger depth variation. This is what was referred to as the noise in the image and the reason for this was presented in the previous paragraph.

Critique 1

The scope plot in Figure 3-27 (a) does not clearly depict the pattern trench, it is essential that this point is not ignored. This was despite careful efforts that involved adjusting the imaging control parameters on the AFM software. In all other cases Figure 3-27 (b)-(h), the tip has been able to make contact with the pattern trench. A likely cause for this is that the duty cycle of the pattern in Figure 3-27 (a) is such that the

AFM tip is unable to make contact with the null. Hence, then it is also true that the scan of Figure 3-27 (a) does not give us the correct pattern depth. By making use of SEM scans at a comparable dosage, as shown in the next section, it is confirmed that in fact the patterns achieve a depth of ~32-40 nm.

Critique 2

Finally, there is a need to address another issue. All of the above now begs the question, why is there a background exposure (or DC component) in the interference of two TE waves in the results above, when it is clearly known that such is the case only with the TM polarization of light (see Chapter 2). An attempt to explain this is phenomenon is given below.

The background exposure acts to reduce image contrast, this is despite the fact that the TE polarization of light was utilized. Through FEM simulations it was also confirmed that the partial reflectivity of the Aluminum mirror internal to the prism plays a negligible (or invisible) role in reducing the image contrast. After much thought, it is now believed that a highly likely cause for this was an essential change that had to be made to the experiments. While the use of a collimated beam has been strictly enforced, the lens type that was used actually resulted in a beam diameter size that was not sufficiently small at the particular *NA* (1.824) that is required to be imaged. A larger beam diameter (than the prism face) increases the possibility of edge diffraction effects and hence, additive noise. For this reason, an imperfectly collimated beam was used, in that it created a reducing spot size much like the one used for the prism alignment in Figure 3-18. This ensured that the spot size was sufficiently small when incident upon the prism face to allow for solid-immersion IL. While this caused an immeasurable change to the *NA*, it did result in a slight focusing effect as one might expect from an imperfectly collimated beam. It is believed that this unintentional focusing has resulted in difference between the two beam intensities that create the interference pattern and hence a resultant background exposure component. Let us briefly explain why this is so. Again, consider Figure 3-24, the location of the backing plate (not shown), is in fact closer to point ***E*** than it is to point ***D***. Hence, the top half of the beam, ***AB*** traverses a slightly larger path in getting to point ***E*** than does the bottom half of the beam, ***BC***. This implies that ***AB*** in fact undergoes more of the focusing and is hence more intense than ***BC***, resulting directly in the aforementioned difference in intensities and thereby causing a background exposure.

This section concludes with some large area AFM scans to demonstrate the imaging capability of SILMIL.

3.6.3 Large area AFM scans

Two large area AFM scans are presented here for two different doses to demonstrate that large area exposures were carried out just as easily SILMIL. Figure 3-29 illustrates a 5 µm by 5 µm *NA* = 1.824 image using λ = 405 nm TE light imaged at a PD of 2 mW-min, part (b) illustrates the same scan in an expanded perspective view.

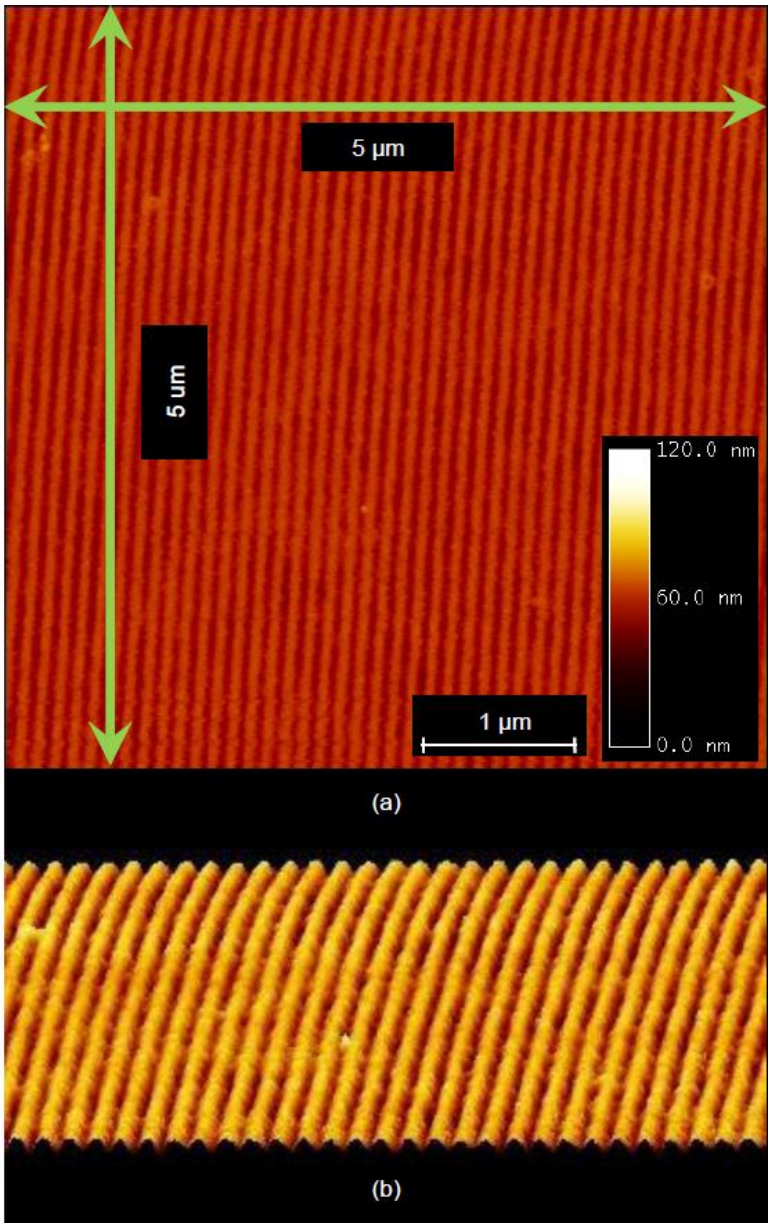

Figure 3-29 - Pseudo-Dosage = 2 mW-min, λ = 405 nm, *NA* = 1.824, conventional EIL using SILMIL, 12-15 nm deep weak modulation with 0 nm background development (a) 5 µm X 5 µm scan (b) expanded perspective view of scan in part (a)

Figure 3-30 (a) and (b) illustrates exposures at a PD of 6 mW-min, demonstrating as expected a higher pattern depth at the cost of a fixed background development. The depths mentioned in the caption are those which were seen in the AFM scope plots.

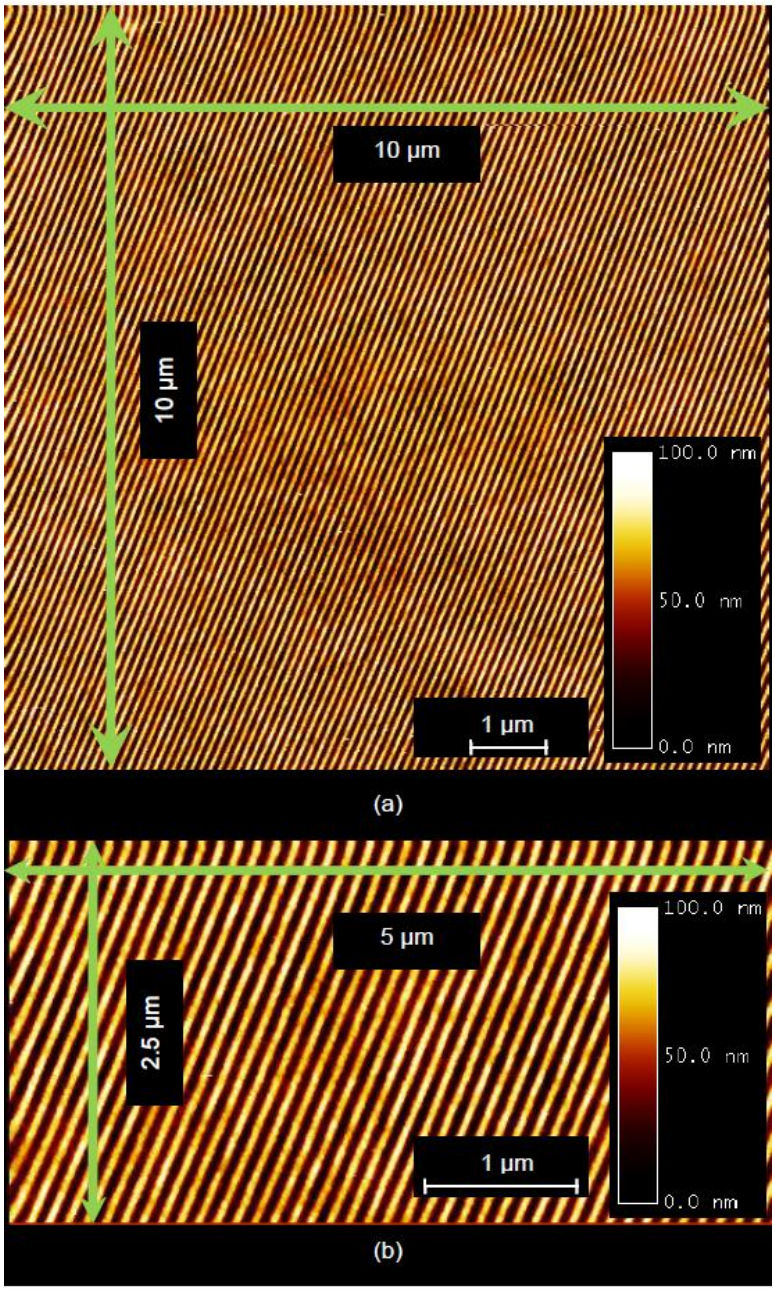

Figure 3-30 - Pseudo-Dosage = 6 mW-min, λ = 405 nm, *NA* = 1.824, conventional EIL using SILMIL, 55 nm deep structures with 27 nm background development (a) 10 µm X 10 µm scan (b) 2.5 µm X 5 µm scan

This next section introduces scanning electron microscopy (SEM) as another powerful measurement tool. The sample preparation required to use the scanning electron microscope is detailed and various scans are

presented for the lower PDs using an optical stack with a quartz substrate to facilitate a fair comparison with the optical stack that is to be utilized in Chapter 7. Following this, the chapter concludes with a short summary of SILMIL and the key ideas and results that have been presented in this chapter.

3.7 Scanning Electron Microscopy (SEM) & Optical Stack to Allow Comparison with Enhancement in Chapter 7

This section demonstrate an alternative means (to AFM) to measure some of the patterns that have been imaged using SILMIL. This is particularly essential for example for the scan of Figure 3-26 (a), where the image depth was not clearly known due to limitation of the AFM tip.

A Raith EBL 150 tool, modified to also work as a scanning electron microscope (see Figure 3-31 for photograph), was used to carry out scanning electron microscopy (SEM) on the samples. The use of an interferometer and a high accuracy stage movement in the scanning electron microscope (SEM) also helped to confirm the exact pitch of the pattern. The numerical aperture and the YAG prism index were then computed through simple back calculation. The prism index value found here was well in accordance with that deduced by direct laser reflection measurements and the Sellmeier equation.

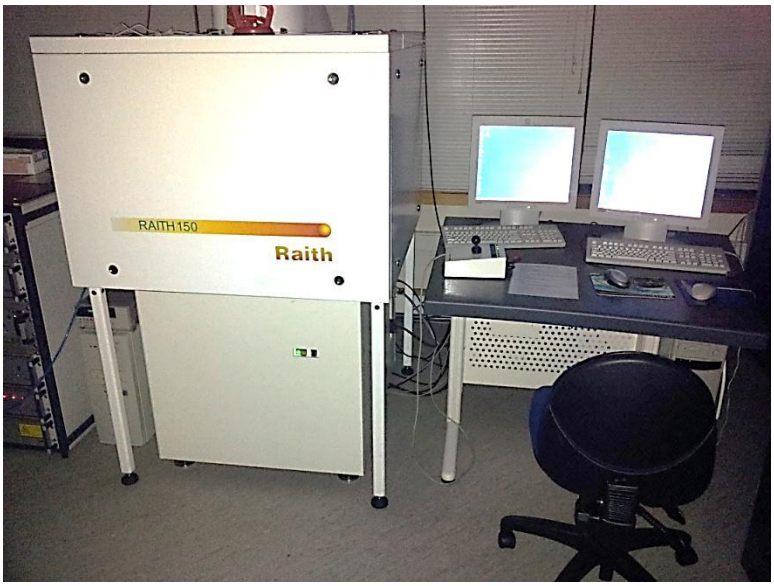

Figure 3-31 – Photograph of the Raith 150 EBL system that doubles as a Scanning Electron Microscope

This chapter is concluded with some SEM scans of low dosage EIL using SILMIL, as these will be used as a basis of comparison in Chapter 7. A slight change is made to the stack here. A 25 mm by 25 mm quartz coverslip is now utilized as the bottom substrate, upon which spin thick resist is spun, followed by PVA. A uniform thickness PVA layer as low as 12 nm was unachievable on a substrate of this size

despite further dilution. Another PVA solution of 8.55 mg/ml was created and spun at 7000 rpm with a 500 rpm/s acceleration to achieve a thickness of ~24 nm.

EIL using SILMIL was carried out using this stack (see photograph in Figure 3-32). The change is made to allow a direct and fair comparison with the stack of Chapter 7 which also utilizes a quartz coverslip as a bottom substrate as a necessary component of the optical stack. The difference that such a substrate makes for SILMIL in this chapter is the increased amount of charging when it is viewed under an SEM and so certain procedures are to be followed to minimize this charging, these are also briefly outlined here.

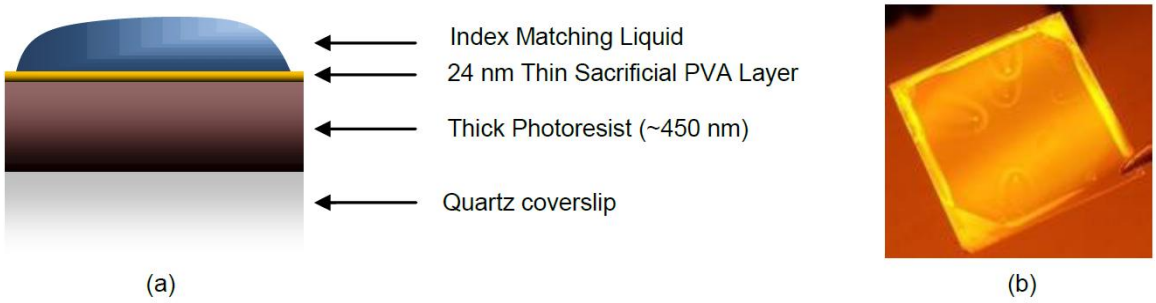

Figure 3-32 – Quartz substrate with thick resist (a) Schematic (b) Photograph

It is recommended that the sample be sputtered with gold to allow conduction of targeted electrons within the SEM. The sample side (top side) should be sputtered with ~50 nm of gold, and the bottom side of the quartz should be sputtered with several 100 nm of gold to allow a conductive back plane. Following this, it must be ensured that the electrons are conducted away to ground as opposed to charging any insulating layers in the stack (such as quartz in this case). Here the use conductive tape to first form a pathway between the top and bottom sides of the sample, followed by a connection to the metallic sample holder should suffice. The use of sufficient conductive tape ensures a low resistance path way for the targeted electrons.

Cross-sectional viewing requires special sample preparation as cleaving a quartz coverslip might prove to be quite difficult. In such a case, a dicer or a saw must be used to first make a reasonably deep (~0.5µm) scratch on the bottom side of the sample, while ensuring that the top side of the sample is free from environmental contamination or damage. This may be done by placing the sample face down on a silicon wafer and taping the sample's edges down while the saw blade makes the required scratch. Once this scratch is made and is sufficiently deep, sample cleaving is much easier. The cleaved side should be coated with ~20 nm of gold in addition to the making the other preparations for SEMing as mentioned above to obtain SEM images that are free from charging effects.

SEM scans are presented here with detail within some of the figure captions. A 10kV beam and a 30 mm aperture were used to produce the following images. The results show instances of where a pseudo-dosage of 2.5 mW-min has resulted in image depths of ~32 to 40 nm, i.e. a maximum aspect ratio (height to width ratio) of 0.72. This is a particularly important piece of measurement if the end goal as it is here, is to demonstrate an image depth comparison. The reader would find it helpful to refer to these results again in Chapter 7.

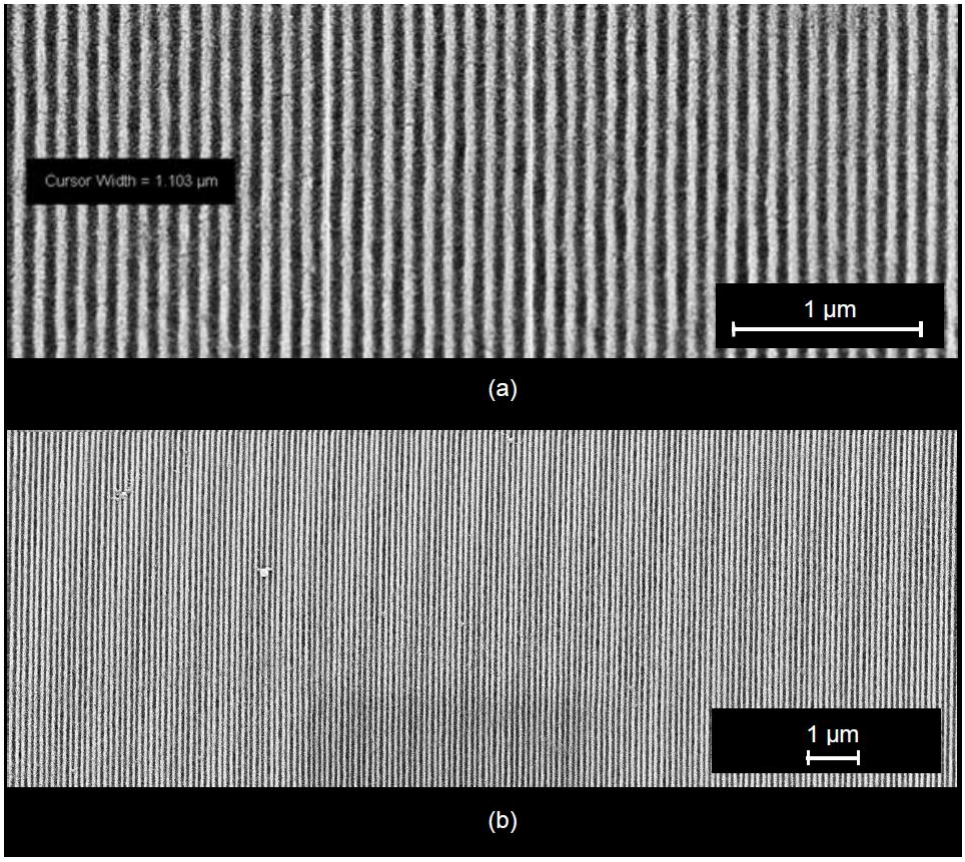

Figure 3-33 – SEM plan views, at pseudo-dosage of 3 mW-min, *NA* = 1.824, λ = 405 nm, conventional EIL using SILMIL, Resulting pitch ~111 nm (55.5 nm half-pitch) (a) small area and (b) large area scan

In Figure 3-34, SEM cross-sectional views at a PD of 3 mW-min with *NA* = 1.824, λ = 405 nm are shown. These demonstrate pattern depths of ~32 - 40 nm. The effects of charging in several instances can make this difficult to see and so annotations have been provided to guide the reader. This is supported by the AFM scans in Figure 3-34 (c) which clearly indicates the AFM tip has been unable to properly image structures that are any deeper than ~35 nm. Finally, some slant views of such a pattern at a PD of 2.5 mW-min are also presented (Figure 3-35) to demonstrate pattern quality.

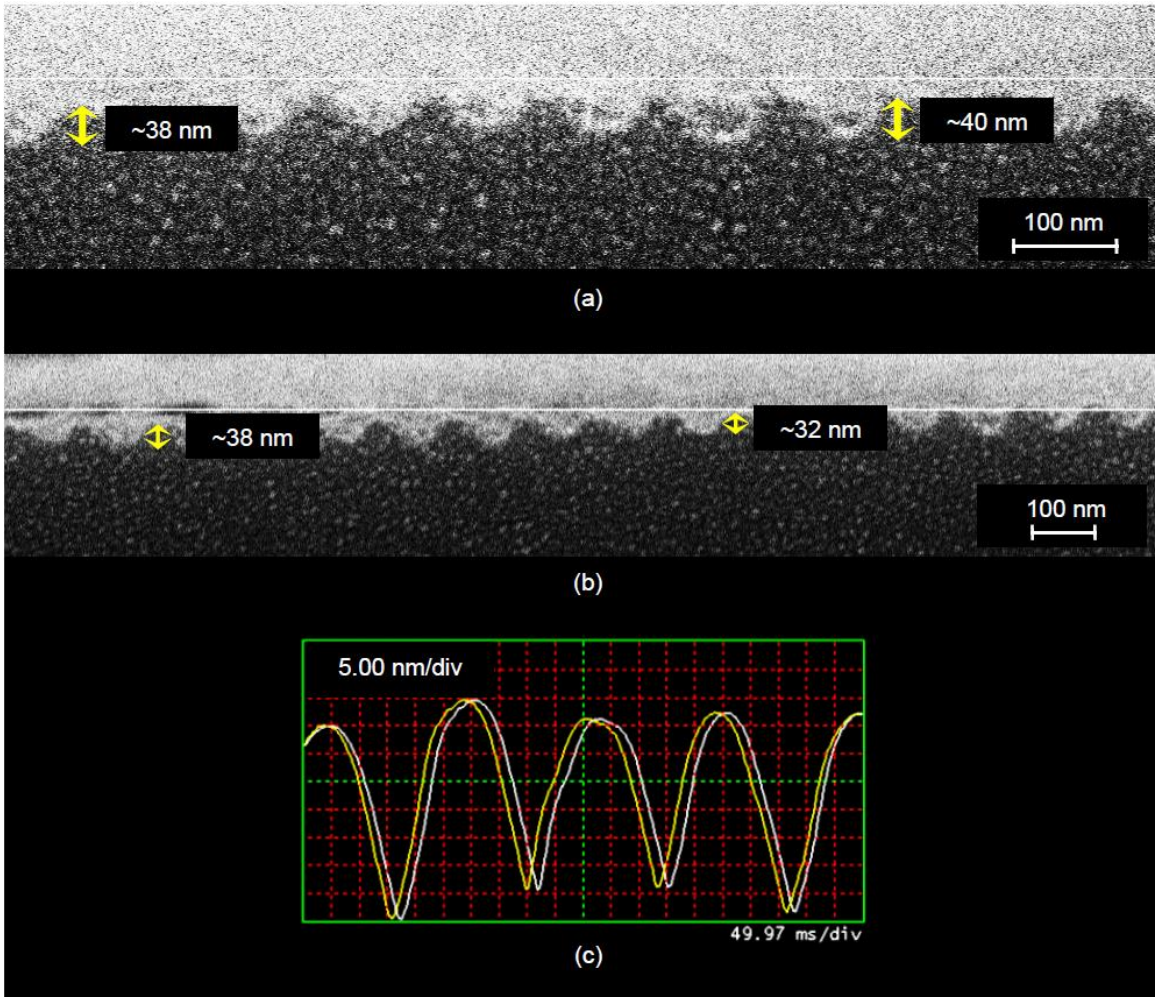

Figure 3-34 - Cross-sectional views/plots, at *NA* = 1.824, λ = 405 nm, conventional EIL using SILMIL, Resulting pitch ~111 nm (55.5 nm half-pitch) (a) and (b) SEM scans at pseudo-dosage (PD) of 3 mW-min, giving 30 – 40 nm image depths (a maximum aspect ratio of 0.72) (c) AFM scope plot at a PD of 2.5 mW-min indicating that the image may be deeper than that which the tip is successfully able to image. This is in accordance with what is discovered in parts (a) and (b)

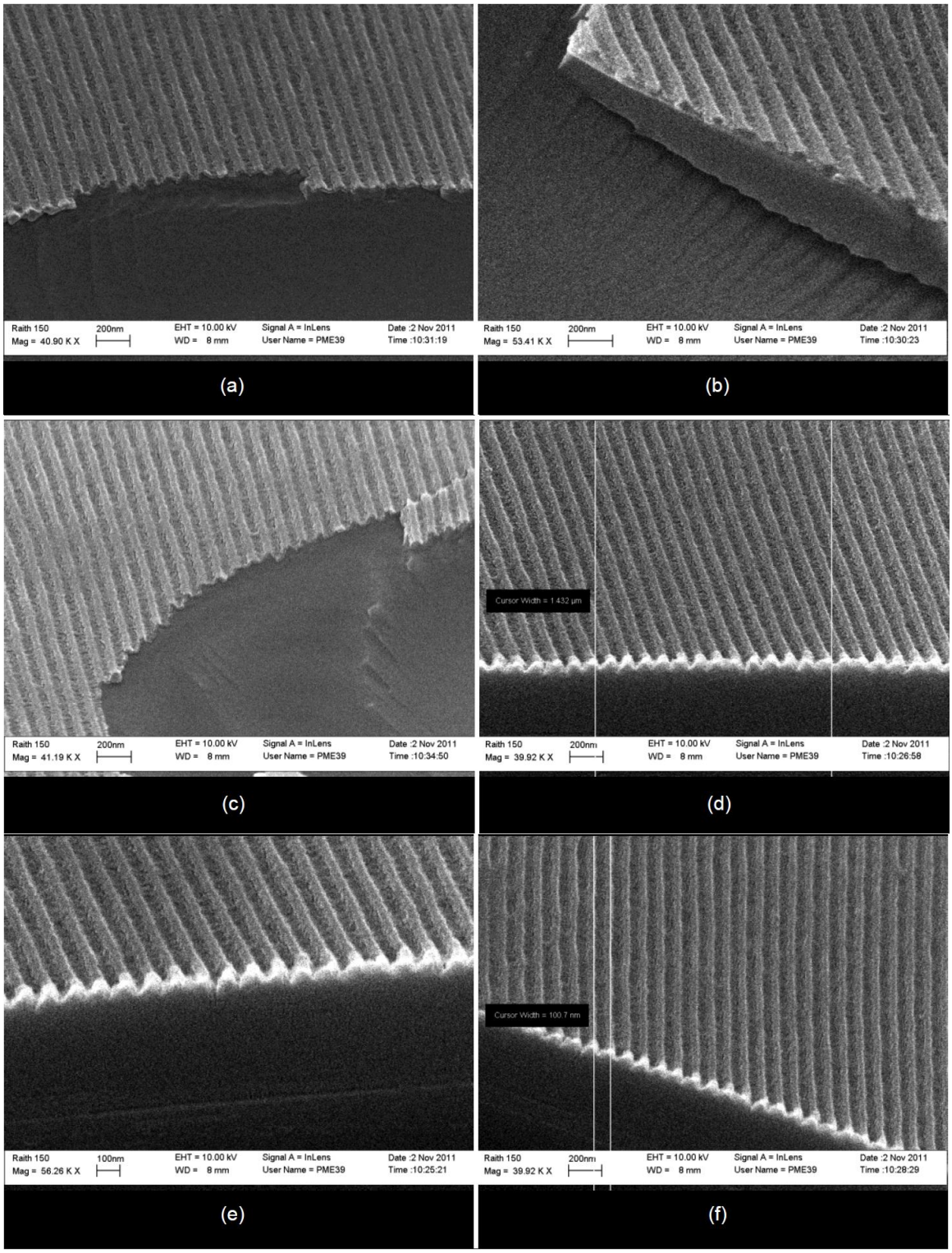

Figure 3-35 - SEM slant views, at pseudo-dosage (PD) of 2.5 mW-min, *NA* = 1.824, λ = 405 nm, conventional EIL using SILMIL, Resulting pitch ~111 nm (a) to (f)

3.8 Summary

A successful demonstration of the design and operation of the SILMIL system was presented for λ = 405 nm. SILMIL is a low cost solid-immersion interference lithography tool created using off-the-shelf equipment that is readily available to researchers. A *NA* of 1.824 was used as a case study that resulted in a 111 nm pitch (or 55.5 nm half-pitch) and a pattern depth of up to 40 nm or ~λ/10 for low doses and up to ~50 nm for higher doses. At low doses, this is a maximum aspect ratio of 0.72. This value is small as one would expect from EIL.

The primary goal of the system has been successfully achieved. Some limitations of the system have been pointed out. One of these is the introduction of background exposure. It was discussed that this is potentially a result of beam focusing that acts to create a variation in the intensity of the two waves that generate the interference pattern. This results in imperfect or non-zero nulls and therefore a background exposure. At lower doses however, the background exposure component may be avoided owing to the development threshold of the photoresist.

It was also noted that at higher doses, the pattern experienced significant degradation and appeared to be 'noisy'. After much trial and error it is believed that the cause of this noise is in fact the non-uniform thickness of the index matching liquid (IML) layer that results in a spatial variation of the intensity pattern and hence a dosage variation over the sample face. The reason this effect becomes significant at higher doses is due to the increased sensitivity of conventional photoresists at higher doses (or operating point on a contrast curve).

The SILMIL technique is utilized again later in Chapter 7 to demonstrate image depth enhancement after considerable theory related to this is developed in Chapters 5 and 6.

Chapter 4. T-Matrix Modeling

The previous chapter detailed the setup and performance of a simple solid immersion interference lithography system and an optical imaging stack was utilized. The knowledge of the behavior of the electric fields within such an imaging stack is essential if one wishes to understand the imaging process or predict or improve it. This chapter details the development and implementation of a transmission matrix method that was used to observe image evolution within the imaging stack and later improve it. Such a model also allows prediction of the imaging behavior as several parameters such as the numerical aperture (*NA*), wavelength, electrical permittivity and thickness of media; numbers of layers of media, etc. are varied.

The first section presents a derivation of the T-Matrix method. This is followed by an added implementation that allows visualization of field evolution in the 2-D plane for interference lithography for both the TM and TE polarizations. Finally, validations are presented with other research employing the basic T-Matrix method and with a commercially available finite element method tool, known as COMSOL Multiphysics [177]. Several examples are presented in the subsequent chapters to illustrate 2-D field evolution and many variable parametric searches that have been performed using our modified method.

4.1 T-Matrix Derivation

The analytical transfer matrix (T-Matrix) method was used to model the behavior of optical stacks of non-magnetic media. The method involves establishing Maxwell's relations at the interface of two homogenous media that constitute the optical stack. Using this, a relationship is established between the fields on opposite sides of the interface and stored in a matrix. By making use of phase shifting, the relationships are then transferred from one interface to the next. This transfer of the relationship matrix gives the method its name.

The T-Matrix technique has been extensively utilized [82, 178] for several years due to its ease of use and the simplicity with which it may be programmed in a matrix solver package. MATLAB [179] was used as the matrix solver package to implement all aspects of the T-Matrix that are presented in this chapter. The

resulting code was then used as an interference lithography simulator and has been heavily utilized in the remainder of this thesis.

A derivation of the T-Matrix technique is provided for the TM polarization of light for an optical stack such as the one depicted in Figure 4-1. In addition, the modifications made to observe the field intensity evolution within a particular layer are also detailed. This is useful for instance when one wishes to understand the image formation inside a photoresist cavity.

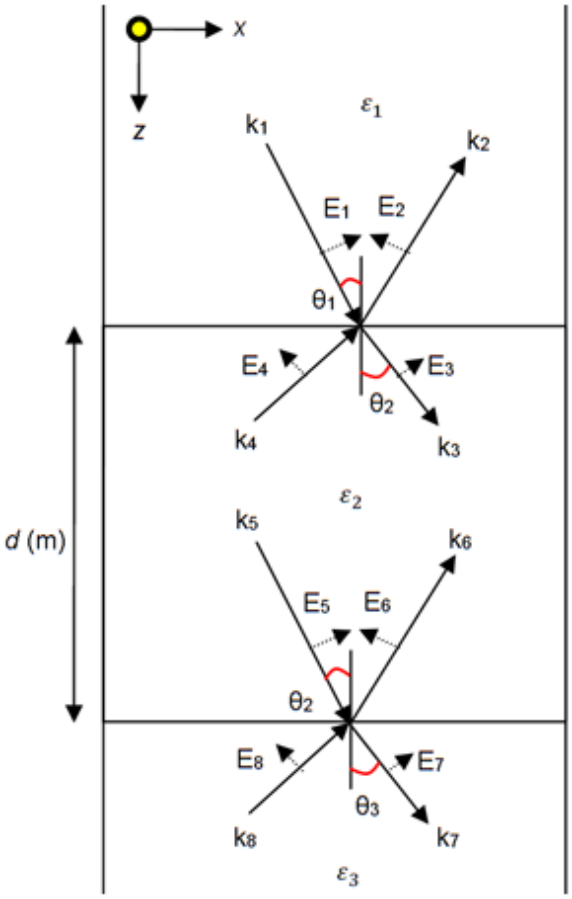

Figure 4-1 – A three layer (ε_1-ε_2-ε_3) homogenous optical stack excited by a transverse magnetic (TM) polarized wave k_1

Figure 4-1 depicts a stack consisting of 3 distinct media, namely ε_1 , ε_2 and ε_3. Here, individual waves are identified by their wave vectors. The wave vector for a layer l is itself defined as,

$$k_l = \frac{2\pi}{\lambda} n_l = \frac{2\pi}{\lambda}\sqrt{\varepsilon_l} \quad \text{with,} \quad k_{l,x} = k_l \sin(\theta_l),\ k_{l,z} = k_l \cos(\theta_l) \tag{4.1}$$

For example, in Figure 4-1 k_1, k_3 and k_7 are the forward and k_2, k_4 and k_8 are the backward propagating waves in media ε_1 , ε_2 and ε_3 respectively. The wave k_1 is incident upon the stack with electric field amplitude E_1 and k_2 is a wave reflected from the stack with electric field amplitude E_2. The respective amplitudes of the electric-fields of waves k_1 to k_7 are simply E_1 to E_7. All media are considered to be infinite in spatial extent i.e. they exist from $x = -\infty$ to $x = +\infty$.

The thickness, measured in the z direction of media ε_2 is d. The directions of the E-fields depicted in Figure 4-1 are in accordance with the right-hand rule that states that the cross product vector $E \times H$ must point in the direction of the wave propagation.

The derivation begins by applying Maxwell's equations at the boundary of media ε_1 and ε_2 in Figure 4-1. Firstly the sum total of the tangential electric fields must be the same on both sides of the boundary resulting in (4.2).

$$\begin{gathered} E_{x,1} - E_{x,2} = E_{x,3} - E_{x,4} \text{ or,} \\ E_1\cos(\theta_1) - E_2\cos(\theta_1) = E_3\cos(\theta_2) - E_4\cos(\theta_2) \end{gathered} \tag{4.2}$$

Secondly, the total electric flux at the surface must be zero in the absence of any free surface charge, i.e. flux in must equal flux out.

$$\begin{gathered} -\varepsilon_1 E_{z,1} - \varepsilon_1 E_{z,2} = -\varepsilon_2 E_{z,3} - \varepsilon_2 E_{z,4} \text{ or,} \\ -\varepsilon_1 E_1\sin(\theta_1) - \varepsilon_1 E_2\sin(\theta_1) = -\varepsilon_2 E_3\sin(\theta_2) - \varepsilon_2 E_4\sin(\theta_2) \end{gathered} \tag{4.3}$$

However, Snell's law implies the following relationship which states that the in plane momentum must be conserved or that the numerical aperture (*NA*) of the system must be the same in each media.

$$\begin{gathered} NA = n_1\sin(\theta_1) = n_2\sin(\theta_2) \\ \text{or as,} \\ \sqrt{\varepsilon_1}\sin(\theta_1) = \sqrt{\varepsilon_2}\sin(\theta_2) \end{gathered} \tag{4.4}$$

Using (4.4) with (4.3), gives,

$$\sqrt{\varepsilon_1}E_1 + \sqrt{\varepsilon_1}E_2 = \sqrt{\varepsilon_2}E_3 + \sqrt{\varepsilon_2}E_4 \tag{4.5}$$

Now two simultaneous equations (4.2) and (4.5) need to be solved to give a matrix relationship between the fields on both sides of the interface. Carrying out $\frac{\cos(\theta_2)}{\sqrt{\varepsilon_2}} \times$ (4.5) + (4.2), results in,

$$E_3 = \frac{1}{2}\left[E_1\left(\frac{\sqrt{\varepsilon_1}}{\sqrt{\varepsilon_2}} + \frac{\cos(\theta_1)}{\cos(\theta_2)}\right) + E_2\left(\frac{\sqrt{\varepsilon_1}}{\sqrt{\varepsilon_2}} - \frac{\cos(\theta_1)}{\cos(\theta_2)}\right)\right] \tag{4.6}$$

Similarly, carrying out $\frac{\cos(\theta_2)}{\sqrt{\varepsilon_2}} \times$ (4.5) - (4.2) results in,

$$E_4 = \frac{1}{2}\left[E_1\left(\frac{\sqrt{\varepsilon_1}}{\sqrt{\varepsilon_2}} - \frac{\cos(\theta_1)}{\cos(\theta_2)}\right) + E_2\left(\frac{\sqrt{\varepsilon_1}}{\sqrt{\varepsilon_2}} + \frac{\cos(\theta_1)}{\cos(\theta_2)}\right)\right] \tag{4.7}$$

Now the fields E_3, E_4 have been successfully related to E_1, E_2. This results in the following matrix relationship,

$$\begin{bmatrix}E_3\\E_4\end{bmatrix} = \frac{1}{2}\begin{bmatrix}\left(\frac{\sqrt{\varepsilon_1}}{\sqrt{\varepsilon_2}} + \frac{\cos(\theta_1)}{\cos(\theta_2)}\right) & \left(\frac{\sqrt{\varepsilon_1}}{\sqrt{\varepsilon_2}} - \frac{\cos(\theta_1)}{\cos(\theta_2)}\right)\\ \left(\frac{\sqrt{\varepsilon_1}}{\sqrt{\varepsilon_2}} - \frac{\cos(\theta_1)}{\cos(\theta_2)}\right) & \left(\frac{\sqrt{\varepsilon_1}}{\sqrt{\varepsilon_2}} + \frac{\cos(\theta_1)}{\cos(\theta_2)}\right)\end{bmatrix}\begin{bmatrix}E_1\\E_2\end{bmatrix} \tag{4.8}$$

or as,

$$\begin{bmatrix}E_3\\E_4\end{bmatrix} = S_1\begin{bmatrix}E_1\\E_2\end{bmatrix} \tag{4.9}$$

where,

$$S_1 = \frac{1}{2}\begin{bmatrix}\left(\frac{\sqrt{\varepsilon_1}}{\sqrt{\varepsilon_2}} + \frac{\cos(\theta_1)}{\cos(\theta_2)}\right) & \left(\frac{\sqrt{\varepsilon_1}}{\sqrt{\varepsilon_2}} - \frac{\cos(\theta_1)}{\cos(\theta_2)}\right)\\ \left(\frac{\sqrt{\varepsilon_1}}{\sqrt{\varepsilon_2}} - \frac{\cos(\theta_1)}{\cos(\theta_2)}\right) & \left(\frac{\sqrt{\varepsilon_1}}{\sqrt{\varepsilon_2}} + \frac{\cos(\theta_1)}{\cos(\theta_2)}\right)\end{bmatrix} = \begin{bmatrix}S_{1_{11}} & S_{1_{12}}\\ S_{1_{21}} & S_{1_{22}}\end{bmatrix} \tag{4.10}$$

The wave k_1 is the incident wave and its amplitude may be set to 1 without loss of generality. Then, one is left with the task of deducing the amplitude of the reflected wave k_2, which is known as the reflection coefficient r from the optical stack. If the stack has only one interface such that media 2 is semi-infinite in extent in the positive z direction, then E_4 will be zero and E_3 becomes the transmission coefficient. This gives,

$$\begin{bmatrix} t \\ 0 \end{bmatrix} = S_1 \begin{bmatrix} 1 \\ r \end{bmatrix} \tag{4.11}$$

The reflection is simply computed as,

$$r = -\frac{S_{1_{21}}}{S_{1_{22}}} \tag{4.12}$$

And the transmission coefficient as,

$$t = S_{1_{11}} - \frac{S_{1_{21}}}{S_{1_{22}}} S_{1_{12}} \tag{4.13}$$

Note these are the full E-field reflection and transmission coefficients for the TM polarized light. They are also known as the Fresnel's TM reflection and transmission coefficients.

As an interesting aside that will be referred to in a later chapter, consider only a two media interface. The reflection coefficient is the same for both the *x* and *z* components of the electric field, however their signs are reversed. This is better illustrated by Figure 4-2. A negative reflection is defined as one which inverts the direction of the magnetic field, this is marked by a dot or a cross indicating that the magnetic field is either emerging outwards from or inwards to the paper in accordance with the right-hand rule.

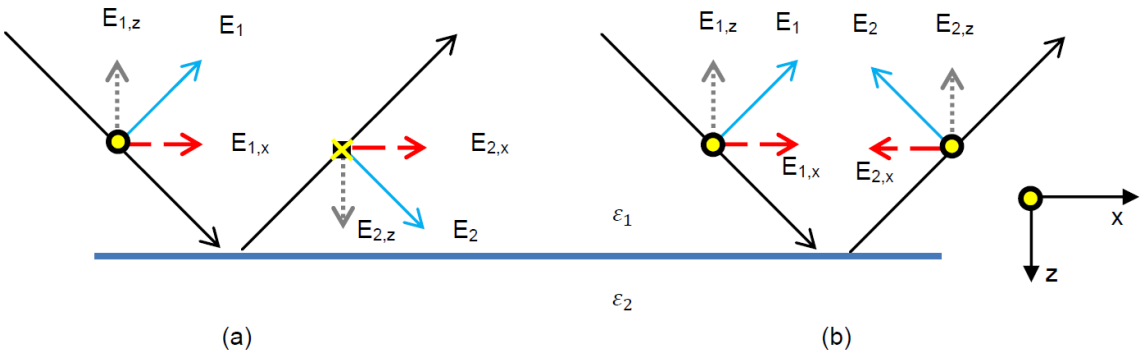

Figure 4-2 – Reflection of the wave for two different reflection values illustrates that the signs of the E_x and E_z fields are opposites of each other (a) Negative reflection (b) Positive reflection

In contrast, the transmission coefficients of the *x* and *z* electric field components always have the same sign but differ in their amplitudes. This is illustrated in Figure 4-3.

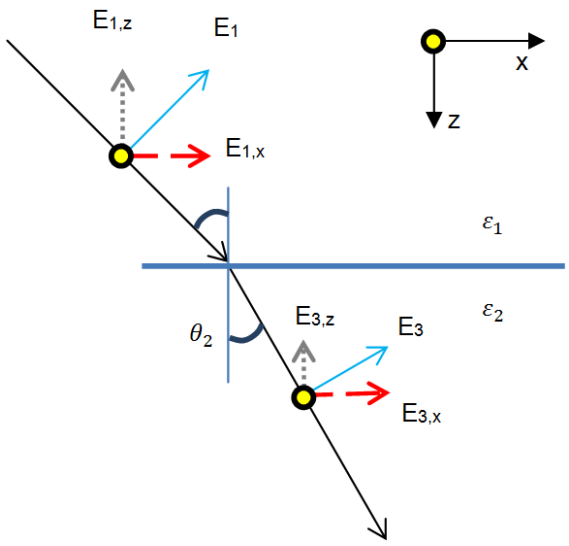

Figure 4-3 – Transmission of a wave from media $\boldsymbol{\varepsilon_1}$ to $\boldsymbol{\varepsilon_2}$

Figure 4-3 again depicts a two media interface. If the amplitude E_1 is 1 again, then $E_3 = t$. Using simple trigonometry and (4.4), the transmission of the x and z components may be computed individually and their ratio is given as,

$$t_z = t * \sin(\theta_2) = t * \frac{NA}{\sqrt{\varepsilon_2}}$$

and so,

$$\frac{t_z}{t_x} = \frac{NA}{\sqrt{\varepsilon_2 - NA^2}} \tag{4.14}$$

When the NA of the system is higher than the refractive index of any media in the multilayer stack, then there is a complex angle in that media. This can be messy to deal with and so to avoid mention of complex angle, the following substitution is made in the S matrices,

$$\frac{\cos(\theta_l)}{\cos(\theta_{l+1})} = \frac{k_{z,l}\sqrt{\varepsilon_{l+1}}}{k_{z,l+1}\sqrt{\varepsilon_l}} \tag{4.15}$$

which may be derived easily by combining equations (4.1) and (4.4). This gives,

$$S_l = \frac{1}{2}\begin{bmatrix} \left(\frac{\sqrt{\varepsilon_l}}{\sqrt{\varepsilon_{l+1}}} + \frac{k_{z,l}\sqrt{\varepsilon_{l+1}}}{k_{z,l+1}\sqrt{\varepsilon_l}}\right) & \left(\frac{\sqrt{\varepsilon_l}}{\sqrt{\varepsilon_{l+1}}} - \frac{k_{z,l}\sqrt{\varepsilon_{l+1}}}{k_{z,l+1}\sqrt{\varepsilon_l}}\right) \\ \left(\frac{\sqrt{\varepsilon_l}}{\sqrt{\varepsilon_{l+1}}} - \frac{k_{z,l}\sqrt{\varepsilon_{l+1}}}{k_{z,l+1}\sqrt{\varepsilon_l}}\right) & \left(\frac{\sqrt{\varepsilon_l}}{\sqrt{\varepsilon_{l+1}}} + \frac{k_{z,l}\sqrt{\varepsilon_{l+1}}}{k_{z,l+1}\sqrt{\varepsilon_l}}\right) \end{bmatrix} \tag{4.16}$$

For a multilayer stack however, the goal is to obtain the relationship between fields E_1, E_2 in media 1 and the fields in the end media. For this E_3, E_4 must be related to E_5, E_6. This may be achieved by simply propagating the field E_3 forward and the field E_4 backward in the cavity of media 2 that is d metres thick resulting in,

$$\begin{aligned} E_5 &= e^{ik_{z,2}d} * E_3 \\ E_6 &= e^{-ik_{z,2}d} * E_4 \end{aligned} \tag{4.17}$$

Here, $k_{z,2}$ is the z-component of the wave vector in media 2 and is expressed in (4.1). In matrix form a post multiplier matrix is used and the relationship implied by (4.17) is then simply,

$$\begin{bmatrix} E_5 \\ E_6 \end{bmatrix} = \begin{bmatrix} e^{ik_{z,2}d} & 0 \\ 0 & e^{-ik_{z,2}d} \end{bmatrix} \begin{bmatrix} E_3 \\ E_4 \end{bmatrix} = P_2 \begin{bmatrix} E_3 \\ E_4 \end{bmatrix} \tag{4.18}$$

Hence, a P matrix is defined, that evolves the fields through the thickness of a media. Now one is in a position to represent fields E_1, E_2 in terms of E_5, E_6. Using (4.10), (4.9) and (4.18),

$$\begin{bmatrix} E_5 \\ E_6 \end{bmatrix} = P_2 * S_1 * P_1 \begin{bmatrix} E_1 \\ E_2 \end{bmatrix} \tag{4.19}$$

Where P_1 is defined as a 2 by 2 identity matrix,

$$P_1 = \begin{bmatrix} 1 & 0 \\ 0 & 1 \end{bmatrix} \tag{4.20}$$

Then, using the previous approach (such as equation (4.9)), one knows that fields E_7, E_8 may be related to E_5, E_6 as such,

$$\begin{bmatrix} E_7 \\ E_8 \end{bmatrix} = \frac{1}{2} \begin{bmatrix} \left(\frac{\sqrt{\varepsilon_2}}{\sqrt{\varepsilon_3}} + \frac{k_{z,2}\sqrt{\varepsilon_3}}{k_{z,3}\sqrt{\varepsilon_2}}\right) & \left(\frac{\sqrt{\varepsilon_2}}{\sqrt{\varepsilon_3}} - \frac{k_{z,2}\sqrt{\varepsilon_3}}{k_{z,3}\sqrt{\varepsilon_2}}\right) \\ \left(\frac{\sqrt{\varepsilon_2}}{\sqrt{\varepsilon_3}} - \frac{k_{z,2}\sqrt{\varepsilon_3}}{k_{z,3}\sqrt{\varepsilon_2}}\right) & \left(\frac{\sqrt{\varepsilon_2}}{\sqrt{\varepsilon_3}} + \frac{k_{z,2}\sqrt{\varepsilon_3}}{k_{z,3}\sqrt{\varepsilon_2}}\right) \end{bmatrix} \begin{bmatrix} E_5 \\ E_6 \end{bmatrix} = S_2 \begin{bmatrix} E_5 \\ E_6 \end{bmatrix} \tag{4.21}$$

This is known as the T-Matrix approach and the intermediate transfer matrix that relates the fields from one interface to the other through boundary condition matching and evolution is simply,

$$T_l = S_l * P_l \tag{4.22}$$

The multiplication of all of the intermediate transfer matrices results in a total transfer matrix. An

approach such as the one given by equations (4.11)-(4.13) may then be used to compute the reflection from and transmission through the stack using the total transfer matrix.

Finally,

$$\begin{bmatrix} E_7 \\ E_8 \end{bmatrix} = T_2 * T_1 * \begin{bmatrix} E_1 \\ E_2 \end{bmatrix} \tag{4.23}$$

One can see how, such a relationship may be easily programmed in a matrix solver package for several layers. The derivation for the TE case is trivial and is hence omitted. The *P* matrix for the TE case is the same, while the *S* matrix is now given as,

$$S_l = \frac{1}{2} * \begin{bmatrix} 1 + \frac{k_{z,l}}{k_{z,l+1}} & 1 - \frac{k_{z,l}}{k_{z,l+1}} \\ 1 - \frac{k_{z,l}}{k_{z,l+1}} & 1 + \frac{k_{z,l}}{k_{z,l+1}} \end{bmatrix} \tag{4.24}$$

4.2 Field Evolution with T-Matrix

In (4.18), the *P* matrix was introduced and it was noted that it is responsible for the field evolution within media. If a slight modification is made to this matrix, one can in fact compute the fields at any point inside the medium and not just at the interfaces. This makes the T-Matrix method considerably more useful as it allows visualization of the field evolution and effects such as the creation of surface states at the interface of two media. The method requires first following all of the procedures in the previous section to establish the T-Matrix such that the amplitudes of fields at all interfaces are known. This is followed by setup of a routine that then replaces the *P* matrix with the following,

$$P_{l,new}(u) = \begin{bmatrix} e^{ik_{z,l}u} & 0 \\ 0 & e^{-ik_{z,l}u} \end{bmatrix} \tag{4.25}$$

Here u is a variable that begins at 0 and terminates at the thickness of the particular layer. For example, to compute the fields setup within media 2, it is required to compute (4.26) for every progression of the variable u as it varies from $u = 0$ to $u = d$, resulting in the knowledge of the individual forward and backward propagating fields within media 2,

$$\begin{bmatrix} E_{forward,media2} \\ E_{backward,media2} \end{bmatrix} = \begin{bmatrix} e^{ik_{z,2}u} & 0 \\ 0 & e^{-ik_{z,2}u} \end{bmatrix} \begin{bmatrix} E_3 \\ E_4 \end{bmatrix} \tag{4.26}$$

The *x* and *z* components of the fields at any point in media 2 may then be obtained simply by computing (4.27) at every progression of u.

$$E_{x,media2} = E_{forward,media2} * \cos(\theta_2) - E_{backward,media2} * \cos(\theta_2)$$
$$E_{z,media2} = -E_{forward,media2} * \sin(\theta_2) - E_{backward,media2} * \sin(\theta_2) \quad (4.27)$$

The total field intensity is the sum of the modulus of the *x* and *z* components as always. A further extension then also allows visualization of the field profile in the *x* direction as well and hence a complete picture of the field intensities. This is essential for instance if one needs to model the intensity profile that results from the interference of two counter propagating wave forms.

A TM interference pattern is made up of the sum of the two separate interference patterns created by the E_x and E_z components. It is important to then note that the peaks of the E_z components are spatially out of phase with those of the E_x component as is better depicted below in Figure 4-4.

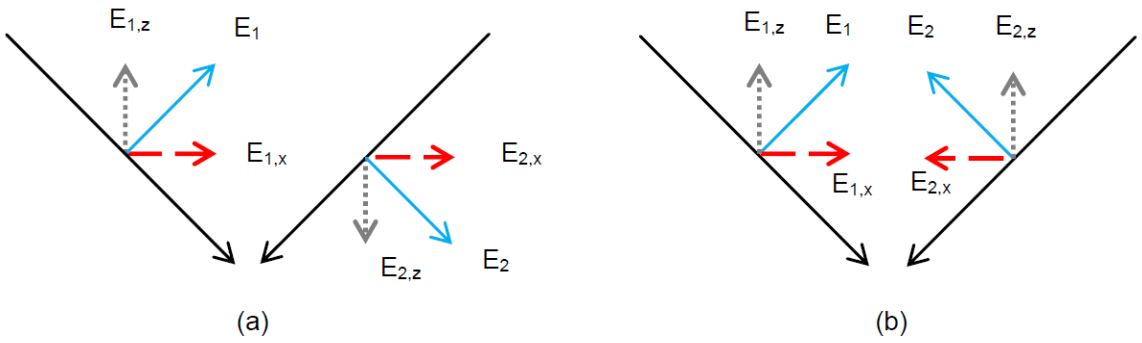

Figure 4-4 - Interference of two waves with E-field amplitudes E_1 and E_2 (a) X and Z components constructively and destructively interfere respectively (b) vice-versa of scenario in part (a)

Let us finish the investigation of the fields within media 2 by incorporating this necessary sign change. The respective intensities of E_x and E_z everywhere in media 2 are simply given as,

$$I_{x,media2,Interference} = \left|E_{x,media2}\left(e^{ik_{x,2}x} - e^{-ik_{x,2}x}\right)\right|^2 = 4\left|E_{x,media2}\right|^2\left(\sin\left(k_{x,2}x\right)\right)^2$$
$$I_{z,media2,Interference} = \left|E_{z,media2}\left(e^{ik_{x,2}x} + e^{-ik_{x,2}x}\right)\right|^2 = 4\left|E_{z,media2}\right|^2\left(\cos\left(k_{x,2}x\right)\right)^2 \quad (4.28)$$

Several examples depicting field evolution using both the T-Matrix method and the FEM setup as briefly described in the following section are presented in the chapters that follow.

Here, a demonstration is shown of the successful validation of the performance of our routine with those by other researchers [66, 82, 180-181] to test the spatial transfer function of a superlens as an example.

The setup is simply an Ag slab of thickness 36.5 nm that is suspended in a vacuum. The setup is excited at a distance of 18.25 nm from the surface of the slab and the measurement is also taken at the same distance on the opposite side of the slab as described in [82]. The resulting transmittance is plotted in Figure 4-5 (a) and compared with the results of other researchers in Figure 4-5 (b). The final results proposed in Chapter 6 have also been successfully validated using PROLITH, an industry standard lithography simulation tool.

The reader shall note that in the figures that follow in this chapter, there are transmission ratios many times larger than unity. This is normal and physically possible in the evanescent regime. The reasoning behind this is detailed in Chapter 5, however for now it should suffice to note that such a scenario does not violate the conservation of energy.

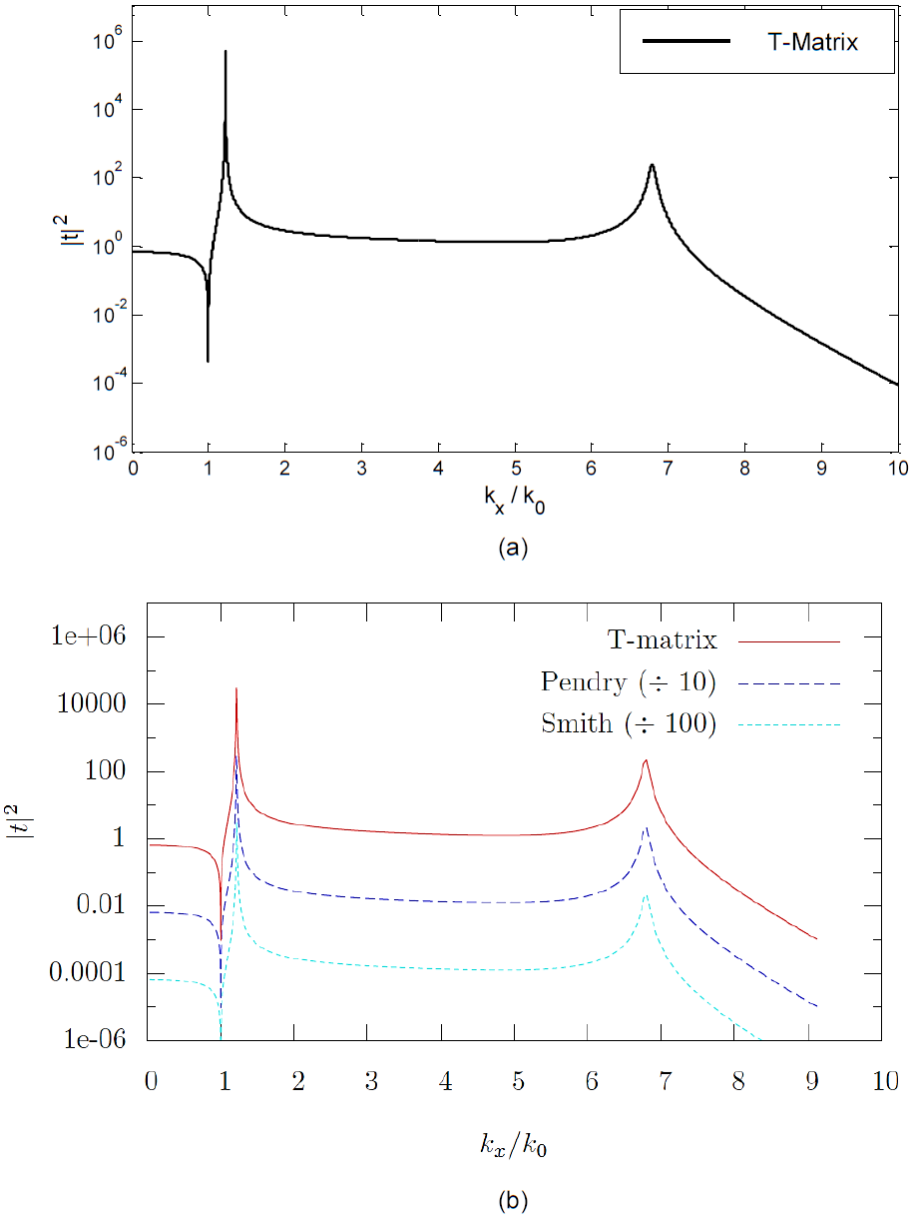

Figure 4-5 - Validation of the T-Matrix method – Transmission vs. spatial frequency. Note that the transmission $|t|^2$ can be greater than 1 when $k_x > k_0$, which represents enhancement in the evanescent regime. (a) A 36.5 nm-thick Ag slab suspended in vacuum, as described in [82]. (b) Identical results obtained by other researchers, reprinted from [82].

4.3 Validation using the Finite Element Method with COMSOL Multiphysics

While the T-Matrix method was primarily relied upon and heavily utilized, a finite element method (FEM) setup has also been used using COMSOL Multiphysics [177], a simulation tool, to achieve higher quality images and also to demonstrate that the same solution may be achieved by making use of an

industry standard computational electromagnetics tool. The FEM simulations have dealt primarily with evanescent phenomena which forms a core component of this thesis.

The results were successfully validated with the T-Matrix approach presented in the previous sections. The setup was used to successfully simulate the interference of two counter propagating wave vectors of either TM or TE polarized light and to observe image formation within the photoresist layer.

Material constants were supplied and a global expression was used to define the equation of two counter propagating waves. The source port was setup with special identity boundary pair criteria to allow it to create the specific wave vector required. The mode type could be setup as either TE or TM for the respective polarization. All internal boundaries were setup as continuity boundary conditions, whereas the port, top and bottom boundaries were setup to be perfect magnetic conductors for the TM case and perfect electric conductors for the TE case. The side walls which are required to be of infinite spatial extent were setup as Floquet periodic boundaries. The actual width of this spatial extent is setup to be equal to an integer multiple of $\lambda/(4*NA)$, so that the periodicity of the model is realized in COMSOL. Figure 4-6 depicts this setup for a simple two beam evanescent interference lithography setup that consists of a source which is realized using an identity boundary pair embedded within a high index prism. A resist stack is then adjacent to this design using a continuity boundary condition. The mesh contains solely triangular elements and as the mesh statistics vary with the particular design in use, it is the minimum element quality and the element area ratio criteria that are of significance here. For the design in Figure 4-6, these values are 0.7521 and 0.2633 respectively.

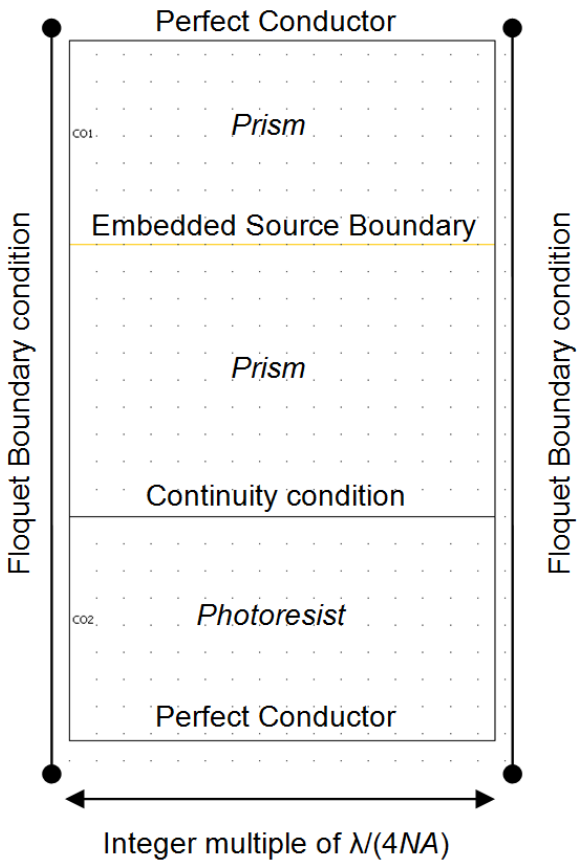

Figure 4-6 – Simple two beam evanescent interference lithography setup in COMSOL using a prism and a resist stack. The source is realized using an identity boundary pair embedded within the prism material.

The chapter concludes with a demonstration of the transmittance of the silver superlens validated with a FEM setup. The resulting transmittance for various handpicked spatial frequencies is depicted in Figure 4-7 (blue) and this is overlaid upon the results of the T-Matrix approach (red) and indicates a successful match.

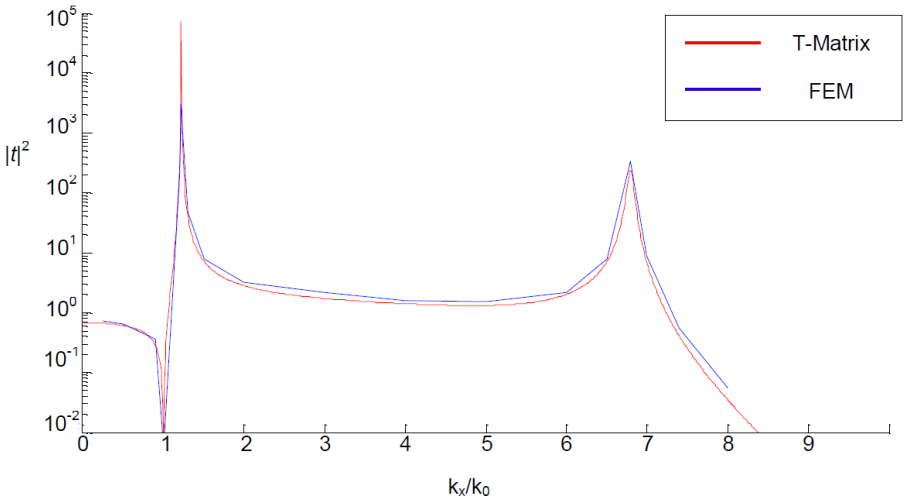

Figure 4-7 – Validation of the FEM setup in COMSOL with the T-Matrix approach – Transmission vs. spatial frequency. Note that the transmission $|t|^2$ can be greater than 1 when $k_x > k_0$, which represents enhancement in the evanescent regime.

4.4 Summary

The T-Matrix method was described in this chapter; including modifications that we have made to it allow visualization of the full electric field intensity profile in the *x*-*z* plane. Such an implementation lends itself nicely to the study of interference lithography and studying the behavior at the interface of two media. The technique was implemented in MATLAB and has been successfully validated with implementations by other researchers and also with the use of a commercially available FEM program known as COMSOL Multiphysics. The T-Matrix implementation presented in this chapter is extensively utilized in the chapters that follow to understand field intensity evolution for the design of optical stacks to couple onto evanescent images. The implementation has also been used to run multi-variable parametric searches to optimize the result of image qualifying metrics and model the behavior of optical stacks comprising of real media and also of optical stacks consisting of artificial media.

The next chapter discusses the need for evanescent wave coupling in evanescent interference lithography and presents some methods to considerably enhance the depth of images produced using evanescent interferometric lithography, such as those created using SILMIL in the previous chapter.

Chapter 5. Surface-state Enhancements for EIL

In the last chapter the T-Matrix technique was discussed to model the behavior of an optical stack when it is excited with a particular wave vector. The focus of this chapter is analytical, beginning by providing a motivation to find means to enhance evanescent waves. The conditions required for the enhancement of evanescent wave vectors through reflections is discussed. In doing so, a detailed analysis of the Fresnel reflection equations for both TM and TE polarizations is carried out so that material requirements may be derived to achieve reflections greater than unity. The conditions needed to create an infinite reflector have also been investigated and are presented in the appendix of this thesis. Following this, ideas and simulations are presented to show the potential of evanescent wave enhanced imaging with EIL. The physical reasoning behind the enhancement phenomena is also detailed.

5.1 System Overview

Consider Figure 5-1 that depicts a schematic of a solid-immersion interference lithography system constituted of three separate materials. The performance of the SILMIL system has already been demonstrated in Chapter 3, and an expected result from this was the reduced image depth in the photoresist due to evanescence phenomena. A key goal of this chapter is to understand the behavior of an evanescent field at the interface of photoresist (ε_2) and another underlying substrate (with permittivityε_3) and to determine the properties of the substrate that will allow us to control the enhancement of the evanescent field within the resist to produce images with greater depths of field and/or higher contrast.

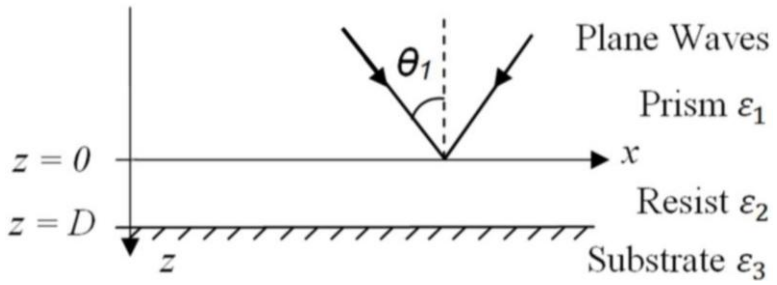

Figure 5-1 – Schematic of solid immersion two beam interference lithography

The interaction of an evanescent wave vector at an interface such as the resist-substrate may be measured using two quantities, namely the reflectivity and the transmissivity. Of interest is the evanescent field

inside the resist and so the following analysis will be concerned with only the reflectivity as it is the reflected field that contributes to the image within the resist. For this reason, the following section deals with the Fresnel reflection equations. Conventional lithography has aimed to minimize the effects of this reflectance to avoid the creation of standing waves within the photoresist. However, conventional lithography does not deal with evanescent waves and hence, the proposal here is that a properly tuned reflected field may be advantageous. Figure 5-2 succinctly describes that the purpose of understanding this interaction is to allow the use of evanescent interference lithography to form an image in thick photoresist by summing the original exponentially decaying image with a reflected version of itself using an underlying substrate. This will allow a non-decaying intensity profile into the depth of the photoresist and hence result in a depth of field enhancement.

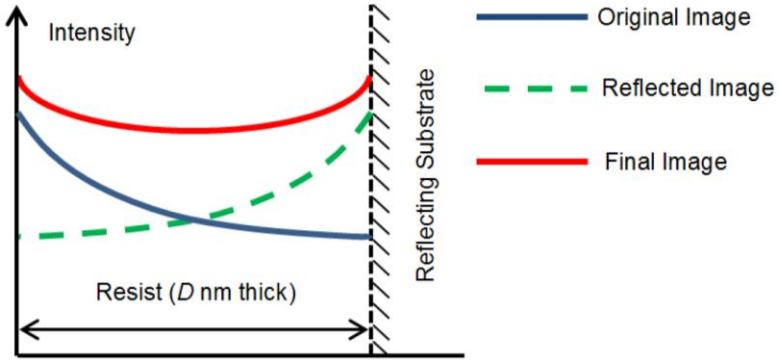

Figure 5-2 – Motivation to consider evanescent field interaction with an underlying substrate

5.2 Fresnel Equations

Figure 5-2 suggests that such an enhancement will require a reflectivity that is much greater than unity in order to compensate the evanescent decay of the original image. To understand how this counter-intuitive condition may be achieved, the Fresnel equations are analyzed. These may be obtained by solving Maxwell's equations at the boundary of two media. The Fresnel reflection equations [28] for the Transverse Magnetic (TM) and the Transverse Electric (TE) polarizations of light will be considered. The effect that these polarizations have on EIL was discussed in detail in Chapter 2. All mathematical quantities should be assumed complex with the exception of those describing distances, and the numerical aperture (*NA*) and unless denoted with a prime or double prime, in which case they are the real and imaginary components respectively.

The various terms and relationships between the optical properties in a medium used or mentioned in this chapter are listed in Table 5.1, where l is used to refer to a particular layer. Frequent references will be

made to distinct columns of Table 5.1 to make the subject matter more comprehendible. The analysis is limited to non-magnetic media due to the lack of availability of magnetic materials at optical frequencies.

Table 5.1 – Definitions and identities used in this chapter

Wavelength	Wave number	Refractive Index	Electrical permittivity	Numerical Aperture	X & Z Wave numbers (k_x & k_z)	
λ	$k_0 = \frac{2\pi}{\lambda}$	$n_l = n_l' + in_l''$	$\varepsilon_l = \varepsilon_l' + i\varepsilon_l''$ $= (n_l' + in_l'')^2$	$NA > n_2'$	$k_x = NA * k_0$	$k_{z,l} = k_{z,l}' + ik_{z,l}''$ $= k_0\sqrt{\varepsilon_l' + i\varepsilon_l'' - NA^2}$

Firstly, the Fresnel reflection equations are solved for conditions where a reflectivity greater than unity can be achieved in the evanescent regime (aka. an evanescent wave enhancement); the results are then used to determine the substrate properties that will allow this. The analysis is limited for now to only the magnitude of this reflection, and not its phase. Media 1, 2 and 3 are indicated in Figure 5-1 and these will also be referred to in the text. The equations relating the transmission and reflection coefficients of the x, y and z components of the E-field for the TM and TE polarizations at the interface between two media ε_a and ε_b are tabulated in Table 5.2 and Table 5.3, see Chapter 4 and [28]. Here, the term transmission denotes the transmitted amplitude into medium *b* from medium *a* and reflection denotes the reflected amplitude back into medium *a* from medium *b*.

Table 5.2 - E-field Fresnel Transmission and Reflection coefficients at an interface between medium *a* and *b* for the TM polarization of light

TM Polarized case – Fresnel Transmission & Reflection coefficients			
	E_{Total}	E_X	E_Z
Transmission	$\frac{E_t}{E_i} = t_{ab,TM}$ $= \frac{2k_{z_a}\sqrt{\varepsilon_a\varepsilon_b}}{\varepsilon_a k_{z_b} + \varepsilon_b k_{z_a}}$	$\frac{E_{t,x}}{E_{i,x}} = t_{ab,TM_x}$ $= \sqrt{t_{ab,TM}{}^2 - t_{ab,TM_z}{}^2}$ $= t_{ab,TM}\sqrt{1 - \frac{NA^2}{\varepsilon_b}}$	$\frac{E_{t,z}}{E_{i,z}} = t_{ab,TM_z}$ $= t_{ab,TM}\frac{NA}{\sqrt{\varepsilon_b}}$
Reflection	$\frac{E_r}{E_i} = r_{ab,TM}$ $= \frac{\varepsilon_b k_{z_a} - \varepsilon_a k_{z_b}}{\varepsilon_b k_{z_a} + \varepsilon_a k_{z_b}}$	$\frac{E_{r,x}}{E_{i,x}} = -r_{ab,TM}$	$\frac{E_{r,x}}{E_{i,x}} = r_{ab,TM}$

Table 5.3 - E-field Fresnel Transmission and Reflection coefficients at an interface between medium *a* and *b* for the TE polarization of light

TE Polarized case – Fresnel Transmission & Reflection coefficients	
	$\mathbf{E_{Total} = E_Y}$
Transmission	$\frac{E_t}{E_i} = \frac{E_{t,y}}{E_{i,y}} = t_{ab,TE} = \frac{2k_{z_a}}{k_{z_a} + k_{z_b}}$
Reflection	$\frac{E_r}{E_i} = \frac{E_{r,y}}{E_{i,y}} = r_{ab,TE} = \frac{k_{z_a} - k_{z_b}}{k_{z_a} + k_{z_b}}$

5.2.1 The TM Fresnel Reflection

The TM Fresnel equation can be derived as (see [28])

$$r_{23,TM} = \frac{\varepsilon_3 k_{z,2} - \varepsilon_2 k_{z,3}}{\varepsilon_3 k_{z,2} + \varepsilon_2 k_{z,3}} \tag{5.1}$$

For a reflection larger than unity, $|r_{TM}| > 1$,

$$|r_{23,TM}| = \frac{|\varepsilon_3 k_{z,2} - \varepsilon_2 k_{z,3}|}{|\varepsilon_3 k_{z,2} + \varepsilon_2 k_{z,3}|} > 1 \tag{5.2}$$

Let us first assume a finite loss in the photoresist such that ε_2 has both non-zero real & imaginary components. Expanding (5.2) in its complex form,

$$|r_{23,TM}| = \frac{|(\varepsilon_3' + i\varepsilon_3'')(k_{z,2}' + ik_{z,2}'') - (\varepsilon_2' + i\varepsilon_2'')(k_{z,3}' + ik_{z,3}'')|}{|(\varepsilon_3' + i\varepsilon_3'')(k_{z,2}' + ik_{z,2}'') + (\varepsilon_2' + i\varepsilon_2'')(k_{z,3}' + ik_{z,3}'')|} > 1 \tag{5.3}$$

This gives,

$$\begin{aligned} &\left|(\varepsilon_3' + i\varepsilon_3'')(k_{z,2}' + ik_{z,2}'') - (\varepsilon_2' + i\varepsilon_2'')(k_{z,3}' + ik_{z,3}'')\right| \\ &> |(\varepsilon_3' + i\varepsilon_3'')(k_{z,2}' + ik_{z,2}'') + (\varepsilon_2' + i\varepsilon_2'')(k_{z,3}' + ik_{z,3}'')| \end{aligned} \tag{5.4}$$

Upon rearranging and gathering like terms,

$$\begin{aligned} &\left|(\varepsilon_3' k_{z,2}' - \varepsilon_3'' k_{z,2}'' - \varepsilon_2' k_{z,3}' + \varepsilon_2'' k_{z,3}'') + i(\varepsilon_3'' k_{z,2}' + \varepsilon_3' k_{z,2}'' - \varepsilon_2' k_{z,3}'' - \varepsilon_2'' k_{z,3}')\right| \\ &\quad > |(\varepsilon_3' k_{z,2}' - \varepsilon_3'' k_{z,2}'' + \varepsilon_2' k_{z,3}' - \varepsilon_2'' k_{z,3}'') \\ &\quad + i\left(\varepsilon_3'' k_{z,2}' + \varepsilon_3' k_{z,2}'' + \varepsilon_2'' k_{z,3}' + \varepsilon_2' k_{z,3}''\right)| \end{aligned} \tag{5.5}$$

Equation (5.5) may be greatly simplified by taking the modulus of each side using the well-known identity $|x + iy| = \sqrt{x^2 + y^2}$. This, followed by a process of gathering and rearranging again is tedious and time consuming so the end result of this exercise is provided as,

$$\begin{aligned} & k'_{z,3}\left(\varepsilon''_3 k''_{z,2}\varepsilon'_2 - \varepsilon'_3 k'_{z,2}\varepsilon'_2 - \varepsilon''_3 k'_{z,2}\varepsilon''_2 - \varepsilon'_3 k''_{z,2}\varepsilon''_2\right) \\ & > k''_{z,3}(\varepsilon'_3 k''_{z,2}\varepsilon'_2 + \varepsilon''_3 k'_{z,2}\varepsilon'_2 + \varepsilon''_3 k''_{z,2}\varepsilon''_2 - \varepsilon'_3 k'_{z,2}\varepsilon''_2) \end{aligned} \tag{5.6}$$

Obviously, (5.6) seems overly complicated to allow us to get any idea of the material properties required of substrate 3, which is the primary goal of this exercise. However, note that the loss or extinction coefficient in conventionally used photoresists is more than 10 times smaller than its refractive index, and as will be seen later in Table 5.5, the extinction coefficient is close to a 100 times smaller than the resist index. This allows us to make a valid engineering approximation that the photoresist has negligible loss, $\varepsilon''_2 \ll \varepsilon'_2$.

In fact, this assumption greatly simplifies the analysis by allowing setting of $\varepsilon''_2 = 0$ and also $k'_{z,2} = 0$, since operation is in the evanescent regime of the photoresist (refer to columns 4, 5 and 7 of Table 5.1). Equation (5.6) then simplifies to,

$$\varepsilon''_3 k'_{z,3} > \varepsilon'_3 k''_{z,3} \tag{5.7}$$

Interestingly, it seems that (5.7) is now independent of the optical properties of the photoresist. However, this is so only if it is a lossless photoresist operating in the evanescent regime (so that $n_2 < NA$). If the conditions in the following paragraph are satisfied, then a method to achieve a reflection greater than unity in the evanescent regime will be found.

If $\varepsilon'_3 < 0$ and $\varepsilon''_3 \geq 0$, then the right hand side of (5.7) is always negative and its left hand side is always positive, therefore satisfying it. If $\varepsilon'_3 \geq 0$ and $\varepsilon''_3 > 0$, then (5.7) may still be satisfied under certain circumstances. In summary, this indicates that the underlying enhancer could either be a negative electrical permittivity material (i.e. a metal, with $\varepsilon'_3 < 0$) with or without loss, or a positive dielectric with significant loss. Hence, a lossless dielectric is not a valid solution.

The interface between a lossless dielectric (e.g. weakly absorbing photoresist) and a metal or high-loss dielectric is known to support surface states such as the surface plasmon polariton (SPP) or the surface exciton polaritons (SEP) respectively [111, 113-118]. Surface states have the property of coupling onto evanescent modes and causing E-field confinement and enhancement through resonant interaction [111].

In addition, both metals and lossy dielectrics cause a wave to decay in their bulk and hence are not capable of transferring energy through their bulk.

However, one may go beyond the well-known SPP & SEP solutions and a closer look reveals that (5.7) is also satisfied by a material with $\varepsilon_3' > 0$ and $\varepsilon_3'' < 0$ provided $k_{z,3}' > 0$ and $k_{z,3}'' < 0$. This requires a material with a negative loss (i.e. a gain medium requirement). The use of a complex plane and plot with relevant quantities illustrates this particular scenario, while also making use of column 7 of Table 5.1. The relevant quantities are labeled and depiction of the figure is explained as necessary in the caption of Figure 5-3, for e.g. ε_3 is labeled as Vector *C* and denoted by a dotted arrow.

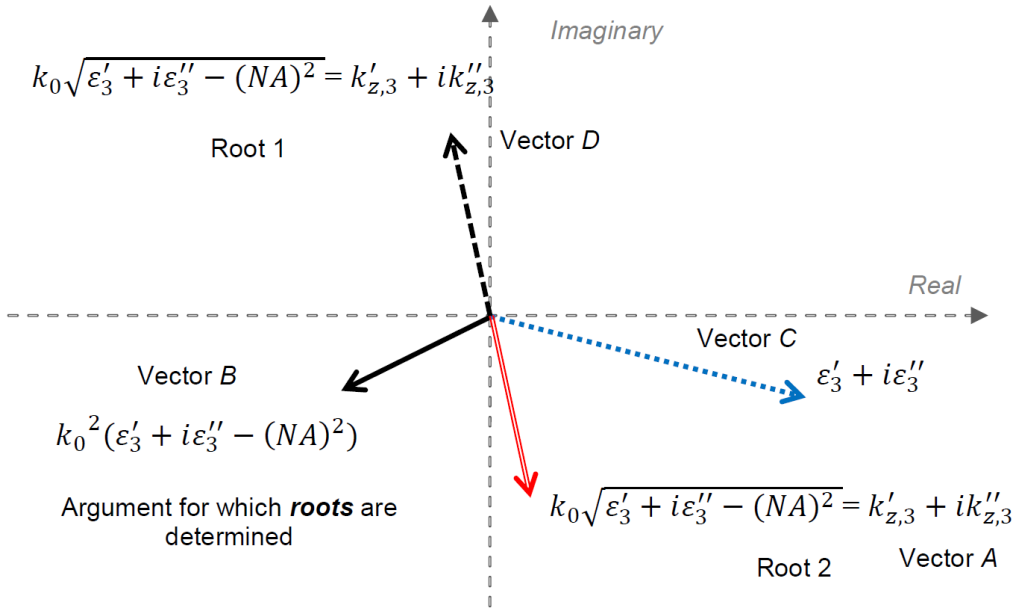

Figure 5-3 – Equation (5.7) is also satisfied if the substrate $\boldsymbol{\varepsilon_3}$ has a positive real part ε_3' and a negative imaginary part ε_3'', this is depicted by **Vector *C***. Although, this results in an argument (**Vector *B***) that has two possible *Roots* (to compute the z-wave number $\boldsymbol{k_z}$), namely *Root 1* (**Vector *D***) and *Root 2* (**Vector *A***); the correct solution is in fact *Root 2* (**Vector *A***) as this allows $k_{z,3}$ to have a positive real part $k_{z,3}'$ and a negative imaginary part $k_{z,3}''$ (substitute such a solution in (5.7) to see how this works). This figure indicates the relative positions of the vectors required to achieve the desired solution.

The quantity $k_0{}^2(\varepsilon_3' + i\varepsilon_3'' - (NA)^2)$ (Vector *B*) is the argument for which the roots are to be determined to compute $k_{z,3}$ so that the gain medium requirement may be satisfied; this argument is denoted as a solid arrow. Like any complex number, this quantity also has two possible roots (Vector *A* and Vector *D*), one of which satisfies the gain medium requirements and one which does not. The desired root is *Root 2* as labeled in Figure 5-3 as it is the only correct solution of the two possible roots (*Root 1* and *Root 2*) allows (5.7) and the above mentioned gain medium requirements to all be satisfied.

A similar analysis is carried out for the TE Fresnel reflection equation, as below.

5.2.2 The TE Fresnel Reflection

Next, the TE Fresnel reflection equations (see [28]) are analyzed as TE is the preferred polarization for interference lithography (see Chapter 2 for reasons). It is well known that metals and lossy dielectrics are not a possible solution to support TE surface waves for evanescent field enhancement, which this analysis confirms but we also seek new gain-like solutions. The TE reflection coefficient at the $\varepsilon_2 - \varepsilon_3$ boundary is,

$$|r_{23,TE}| = \left|\frac{k_{z,2} - k_{z,3}}{k_{z,2} + k_{z,3}}\right| > 1 \; or \; |r_{23,TE}| = \left|\frac{\left(k'_{z,2} + ik''_{z,2}\right) - \left(k'_{z,3} + ik''_{z,3}\right)}{\left(k'_{z,2} + ik''_{z,2}\right) + \left(k'_{z,3} + ik''_{z,3}\right)}\right| > 1 \tag{5.8}$$

Rearranging yields,

$$\left|\left(k'_{z,2} + ik''_{z,2}\right) - \left(k'_{z,3} + ik''_{z,3}\right)\right| > \left|\left(k'_{z,2} + ik''_{z,2}\right) + \left(k'_{z,3} + ik''_{z,3}\right)\right| \tag{5.9}$$

Gathering the real and imaginary terms separately, taking the modulus and squaring gives,

$$(k'_{z,2} - k'_{z,3})^2 + (k''_{z,2} - k''_{z,3})^2 > (k'_{z,2} + k'_{z,3})^2 + (k''_{z,2} + k''_{z,3})^2 \tag{5.10}$$

Further simplification results in,

$$k'_{z,2}k'_{z,3} + k''_{z,2}k''_{z,3} < 0 \tag{5.11}$$

Upon invoking the low loss resist assumption, this gives,

$$k''_{z,2}k''_{z,3} < 0 \tag{5.12}$$

Of course it is known that $k''_{z,2}$, the decay in the photoresist must be positive owing to the fact that the photoresist is a real medium operating in the evanescent regime. This directly implies that for (5.12) to be satisfied, $k''_{z,3}$, the decay in the substrate must be negative, i.e. a growing evanescent wave! Once again, this is only true if the substrate is a gain medium.

As a quick summary of the previous two sub-sections, metals, lossy dielectrics and hypothetical gain media were all found to be support reflections greater than unity (an enhancement) within a low loss dielectric (such as photoresist) operating in the evanescent regime when using the TM polarization of light. Such an enhancement may only be achieved with hypothetical gain media however when using the TE polarization of light. It is also known that both metals and lossy dielectrics are in fact capable of confining and enhancing an E-field at their interfaces by making use of SPP and SEP resonance.

A reflection larger than unity is an enhancement and E-field localization and enhancement is characteristic of a surface state [111]. This logic suggests that a hypothetical gain medium may also potentially be capable of hosting a surface resonance. We do not believe such a finding has been previously reported in literature; this is not surprising as it is not yet possible to create an active artificial medium, which supplies energy to a dying wave to make it grow.

However we took it upon ourselves to investigate this matter in further detail in the following chapter where we introduce the equivalent reflectance approach (ERA). Using this theory, we present methods to replicate the desired aspect, i.e. reflectance and develop the idea of the effective gain medium.

The results of the preceding two sub-sections are summarized in Table 5.4.

Table 5.4 – Substrate properties required for a reflection > 1, for TM and TE polarized light

Materials that allow a reflection greater than unity within a lossless dielectric (e.g. low loss resist)			
For TM polarized light	Lossy metals, Lossless metals	Lossy dielectrics	Gain medium
For TE polarized light	Gain medium		

While Fresnel reflection equations have been analyzed to show that certain scenarios may indeed allow reflections larger than unity and even infinity (see Appendix), it is still unclear how this happens, and whether energy conservation is violated or not. The following section sheds light on these questions and details the physical mechanism behind such enhancements. The reasoning is supported by provision of examples constructed using the T-Matrix modeling technique and FEM simulations. Fictitious and real world examples are presented to test the enhancements.

5.3 Plasmonic Enhancements & the Physical Mechanism

In an earlier chapter detail was given on the design and use of the SILMIL test-bed operating at *NA*s much higher than the refractive index of the photoresist. The obvious problem with an evanescent image is its decay into the photoresist that prevents proper pattern transfer rendering the solid-immersion lithography setup of little commercial use at such high-*NA*s.

With this in mind, Blaikie *et al*. [97] first suggested the use of metal underlays beneath the photoresist for evanescent wave enhancement to counter image decay. This was also the subject of a paper by Arnold *et al*. [98] discussing, among other aspects, the image contrast calculations. Mehrotra *et al*. [35] continued this work and presented the working principle behind the enhancement with a numerical example

involving a fictitious metal. That example is presented here and the principle is explained to bring the reader into the subject matter of this section.

When dealing with the transverse magnetic (TM) polarization of light, the component of the E-field normal to the substrate takes part in a field enhancement when the wave vector and materials are suitably chosen. At the interface of a dielectric such as photoresist and a metal, it is possible to initiate such a field enhancement using the surface plasmon polariton (SPP). A brief introduction on the plasmonics applicable to the subject matter was provided in Chapter 2. The SPP is a surface state that carries energy away from the incident beam when the energy and momentum of the beam is matched with that of the plasmons. Plasmons are a collective excitation of the free electron gas that make up a metal and are hence involved in this field redistribution.

Interestingly, however, energy is only carried away if it can be delivered elsewhere. This is the basis of operation behind several devices like SPP sensors where the energy is dissipated in the lossy portion of the dielectric, metal and the material that is being sensed. If the material is not present, no change in energy is detected. This is crucial to the understanding of evanescent wave enhancement phenomena. The phenomenon is observed simply by plotting the Fresnel reflection coefficients that have so far only been considered analytically in this chapter.

Equation (5.13) gives a well-known formula that gives the spatial frequency (or *x*-wave number) for an SPP state to exist at the interface of a dielectric and a metal [96] . The equation is easily derived by solving Maxwell's equations at the interface of two arbitrary unknown media where a field exists and enforcing the decay of fields into both media. The resulting equations indicate the presence of a surface state. Here, the dielectric is media 2 (photoresist) and the metal is media 3 respectively from Figure 5-1.

$$k_x = k_0 \sqrt{\frac{\varepsilon_2 \varepsilon_3}{\varepsilon_2 + \varepsilon_3}} \tag{5.13}$$

The examples that follow make use of several real and fictitious materials to discuss the use of surface states in evanescent wave coupling. For this reason, the optical properties for these materials at the necessary wavelengths are tabulated in Table 5.5 below to support the discussion and ease the readability. As done previously, the subscript on the electrical permittivity determines the position of the material in the stack.

Table 5.5 – Material optical properties used in the examples that follow

Optical properties of materials used in the examples that follow		
Material	**Electrical permittivity (ε)**	**Source**
Fictitious lossless metal at λ = 193 nm	$\varepsilon_3 = -29.8$	Defined
Lossless photoresist at λ = 193 nm	$\varepsilon_2 = 2.89$ or $n_2 = 1.7$	(C.A. Mack, *pers. comm.*)
Lossy photoresist at λ = 193 nm	$\varepsilon_2 = 2.89 + i0.068$ ($n_2 = 1.7 + i0.02$)	(C.A. Mack, *pers. comm.*)
Silver at λ = 405 nm	$\varepsilon_3 = -3.7726 + i0.6747$	[174]
Molybdenum at λ = 405 nm	$\varepsilon_3 = -1.1875 + i19.5132$	[174]
AZ HiR 1075 (with loss) at λ = 405 nm	$\varepsilon_2 = 2.8214 + 0.1042i$ or ($n_2 = 1.68 + i0.031$)	[173]

5.3.1 Attenuated Total Reflectance (ATR)

Consider the interface of a dielectric, the lossless photoresist ε_2 = 2.89 or n_2 = 1.7 and a fictitious metal ε_3 = -29.8 at λ = 193 nm, the industry standard wavelength for optical lithography. Such an interface as is shown in the inset of Figure 5-4, exhibits reflections much larger than unity at high-*NA*s (the non-propagating or evanescent regime) when excited with an evanescent field using a prism as the coupling mechanism. A hypothetical prism (ε = 9) is chosen without any loss of generality as all that is required of the prism is a refractive index higher than the particular *NA* that is being dealt with. Figure 5-4 plots the reflections at the prism-stack interface and also at the dielectric-metal interface, the dielectric is considered to be lossless. It is shown that reflections greater than unity are possible for all numerical apertures greater than 1.7 (i.e. the index of the lossless resist used here), with E-field enhancements many orders of magnitude higher than unity and even peaking to infinity. Note of course that this case utilizes a lossless resist and a fictitious lossless metal. The physical mechanism behind this is now explained and a demonstration of how one can take advantage of this property in evanescent interference lithography for practical imaging is also given.

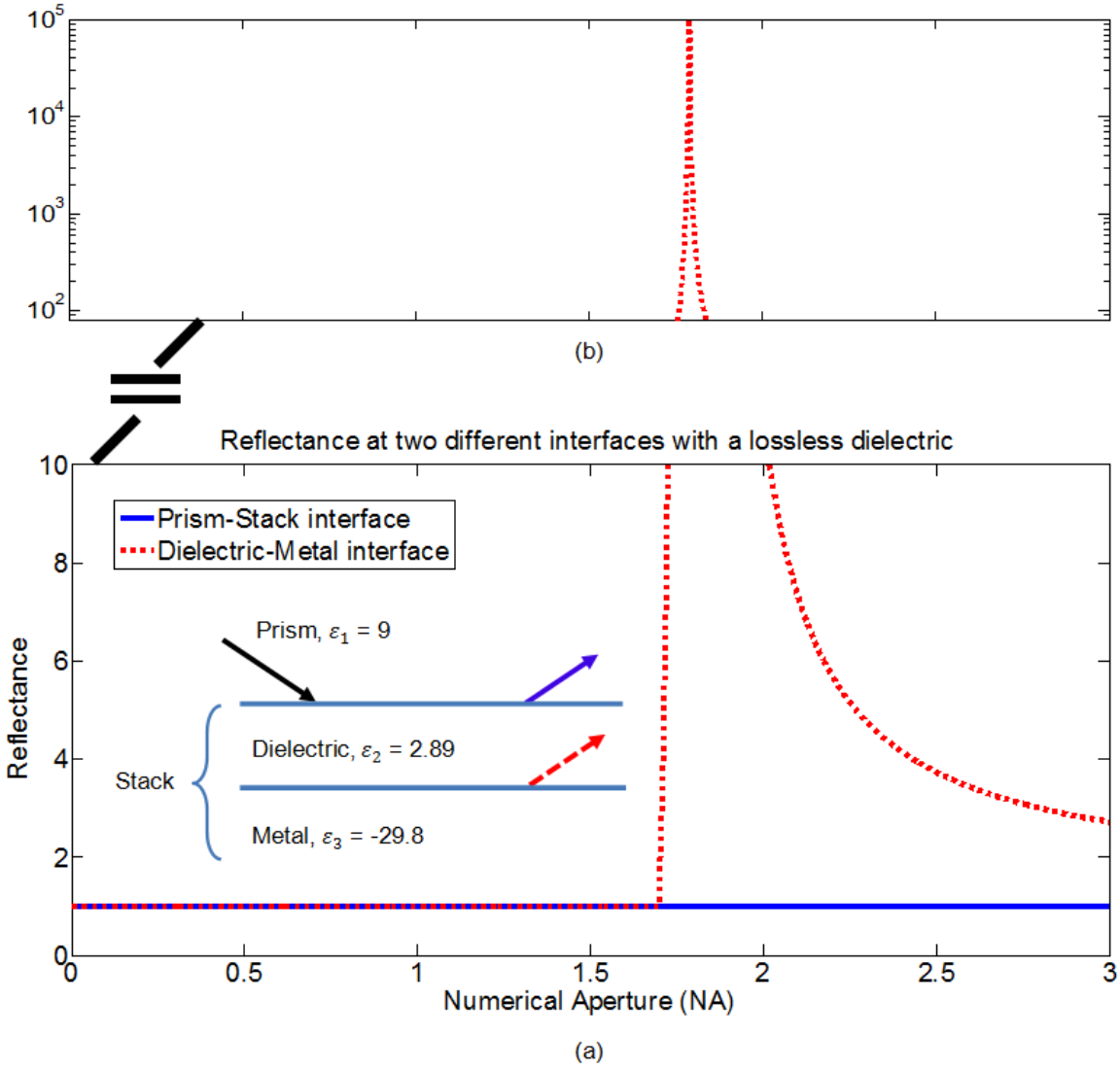

Figure 5-4 - Reflectance vs. *NA* for two interfaces with a Lossless dielectric (lossless photoresist) at λ = 193 nm (a) Linear-scale plot with setup shown as inset (b) Log-scale plot – an extension to part (a)

It is important to get used to the fact that the Fresnel equations merely inform us about the fields that form at an interface given an incident field. The fields on any one side of the interface are then some combination of the incident (driving) and the resulting field. The resulting field is not reflected away in the evanescent regime, but merely decays away from the interface. So it is said that in the evanescent regime, the fields are non-propagating and the electrical and magnetic components are no longer in time phase with each another. This results in a purely evanescent field carrying no energy and hence the real component of its Poynting vector is zero. Hence, as long as the conservation of energy is not violated, the reflection may take any value. Thus, a reflection greater than unity is not unphysical at the dielectric-metal interface (dashed curve in Figure 5-4); the reflection at the prism-stack interface however (solid curve in Figure 5-4) is never larger than unity as this reflection is in the propagating regime.

The analogy of a voltage spike across an inductor when it experiences a large change in current over a short period of time partially lends itself to the case that is being considered. Note that, the potential difference (in volts) across the terminals of the inductor is in fact a derivative of the function of the current flowing through it. This means that there is a phase difference present between the voltage and current waveforms. The average power dissipated is computed as the integral of the voltage and the current multiplied with each other. For a lossless inductor, this is zero.

In a similar manner, only the E-field is of concern here. The behavior of the H-field is of little interest to us as makes no contribution to the image within the photoresist. However, for the purpose of understanding this phenomenon and to indeed prove that energy is being conserved, the power dissipation may be computed as the negative divergence of the time averaged Poynting vector. As shown in section 2.7.3, this is,

$$Re\{-\nabla.\vec{S}\} = Re\{-\nabla.(\vec{E}\times\vec{H})\} = \omega\varepsilon_l^{"}I = 0 \text{ for } \varepsilon_l^{"} = 0 \tag{5.14}$$

Not surprisingly, the lack of any lossy medium results in this value to be zero as well. In Figure 5-4, the reflection at the prism-stack interface is unity for all *NA*s, this is because the wave does not propagate into the metal and is all reflected back with no loss of amplitude. The reflection at the dielectric-metal interface however peaks and is equal to infinity at the resonant wave vector given by (5.13) which corresponds to a *NA* of 1.789. Hence, an infinite reflector, discussed in the appendix is then simply a setup such as the one above operating at resonance. This can be verified by simply substituting k_{z2} and k_{z3} for $\sqrt{\varepsilon_2 k_0^2 - k_x^2}$ and $\sqrt{\varepsilon_3 k_0^2 - k_x^2}$ in equation (5.1), where the required value for k_x is given by (5.13). The resulting denominator of (5.1) then becomes zero, resulting in an infinite reflection.

Consider Figure 5-5, which is like Figure 5-4 except in this instance the photoresist contains a slight loss, just as one would expect in a real photoresist (its index is now $n_2 = 1.7 + 0.02i$). Now both curves have changed. The dashed (red) curve no longer peaks at infinity and the solid (blue) curve exhibits a strong dip at approximately the resonant wave vector. Effects such as the presence of the prism and finite loss in the dielectric prevent the dip from occurring exactly at the spatial frequency corresponding to the resonant wave vector (given by (5.13) and calculated for a lossless dielectric).

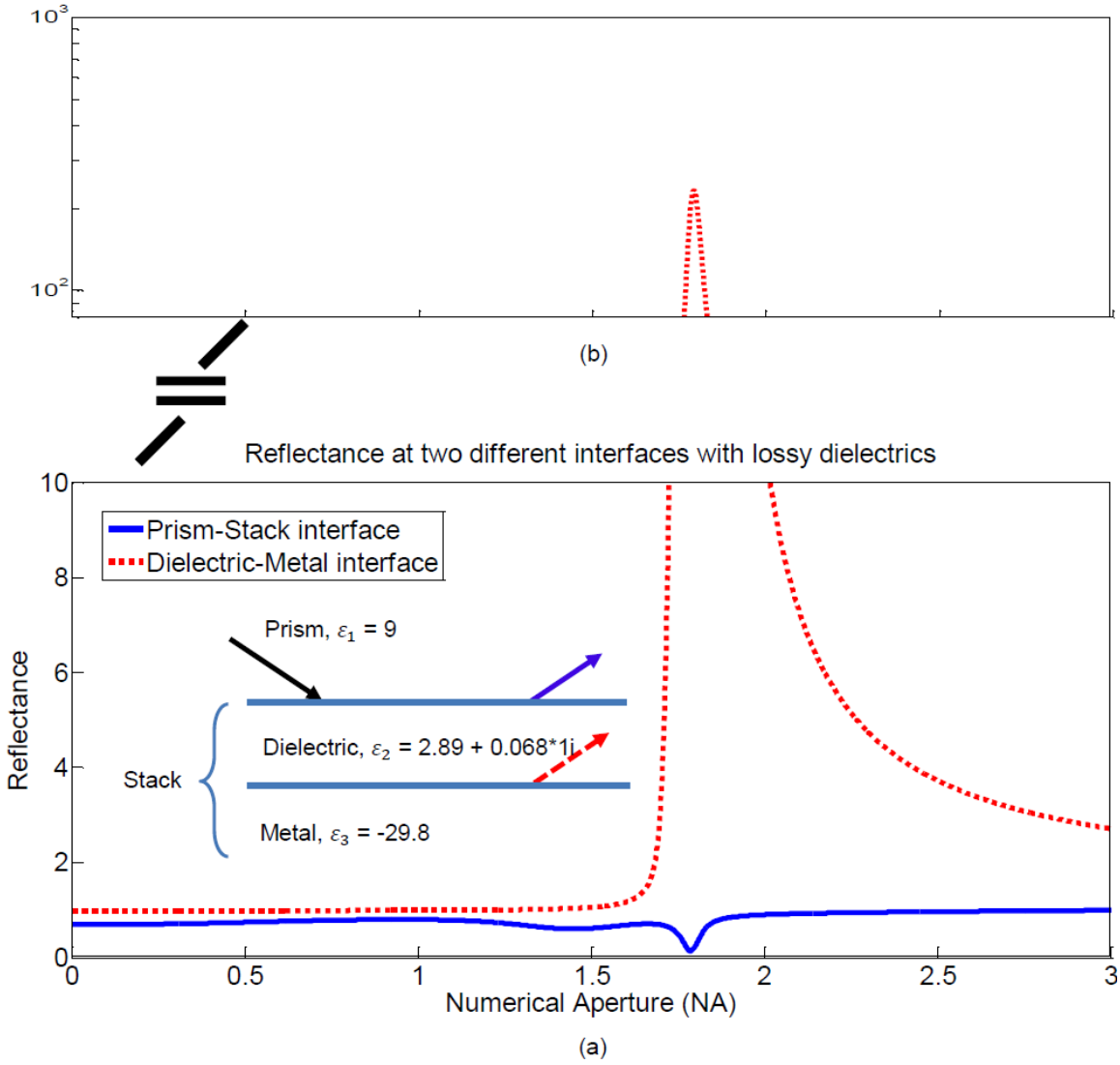

Figure 5-5 - Reflectance vs. *NA* for two interfaces with a Lossy photoresist at λ = 193 nm, (a) Linear-scale plot with setup shown as inset (b) Log-scale plot – an extension to part (a)

Figure 5-6 presents a more detailed plot of the Prism-stack reflectance from Figure 5-5. This plot is also known as the attenuated total reflectance (ATR) plot and is crucial to the characterization of our optical stacks as will be shown experimentally in Chapter 7.

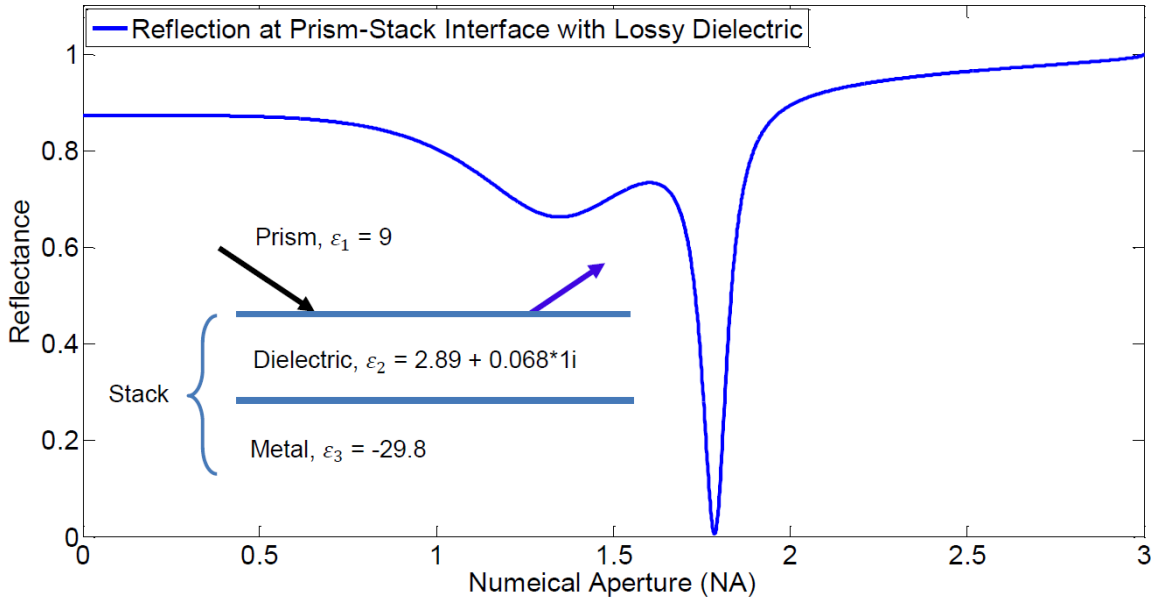

Figure 5-6 - Attenuated Total Reflectance plot

A key result that Figure 5-5 and Figure 5-6 show us is that surface states like the SPP have the potential to extract energy away from the incident beam but this potential is only realized if there is a way to dissipate the energy. Such dissipation takes place when absorption (loss) is added to the media for e.g. a real photoresist. However, another extremely useful quality of the surface state is its ability to redistribute the E-fields within the photoresist cavity. Note that for the surface state to exist, the E-fields must now be concentrated at the resist-metal interface as opposed to conventional EIL, where only the surface of the photoresist is exposed.

5.3.2 Simulated EIL Using Surface-States

It has already been mentioned earlier in this chapter that such phenomenon is advantageous in EIL. One of the goals is to counter the decay of evanescent fields by placing the said metal underlay beneath the photoresist, but it is also of interest to the lithographer to minimize the intensity variation into the depth of the photoresist so that a high aspect ratio structure may be patterned.

Figure 5-7 illustrates three scenarios; part (a) shows EIL without a metal underlay into thick resist, part (b) and (c) illustrate evanescent field coupling to the SPP momentum. Figure 5-7 (c) illustrates the system operation at the resonant wave vector given by (5.13) as,

$$\left[\frac{k_x}{k_0}\right]_{Photoresist-Fictitious\ Metal,SPP} = \sqrt{\frac{(2.89 + i0.068\,)(-29.8)}{(2.89 + i0.068\,) + (-29.8)}} \tag{5.15}$$

$$= 1.79 + i0.02 \sim 1.79$$

This causes E-field localization at the resist-metal interface at a *NA* = 1.79, which results in the greatest enhancement but an undesirable E-field distribution in the resist cavity. The ideal operating point is in fact illustrated by Figure 5-7 (b), this is off-resonance where not all of the energy is extracted from the incident beam and the momentum of the photons is mismatched to that of the SPP, but the E-field distribution is fairly uniform into the depth of the resist. Under these circumstances, the system operates at a spatial frequency that corresponds to a *NA* of 1.85. Clearly, the use of a fictitious metal has enabled an image depth of ~83 nm (see Figure 5-7 (b)) compared with only ~20 nm show in Figure 5-7 (a).

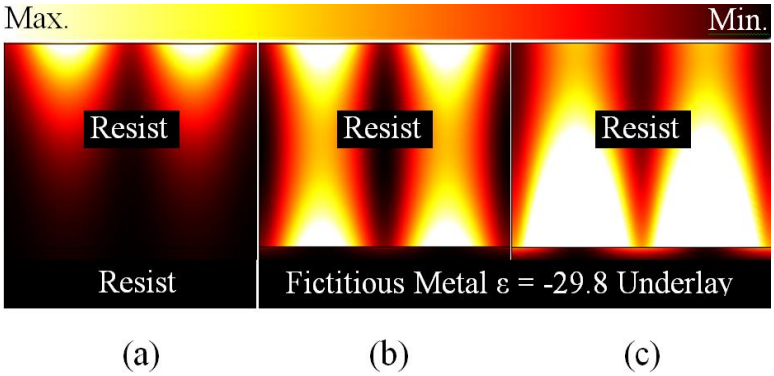

Figure 5-7 - Evanescent IL with transverse magnetic (TM) polarized light in 82.5-nm thick resist ($\varepsilon_2 = 2.89 + i0.068$), λ = 193 nm with (a) thick resist underlay, (b) metal ($\varepsilon_3 = -29.8$) underlay, optimal off-resonant enhancement (*NA* = 1.85), and (c) metal ($\varepsilon_3 = -29.8$) underlay, non-optimal resonant enhancement (*NA* = 1.79).

Figure 5-8 depicts the image evolution as cross-sectional scans for the cases in Figure 5-7 (a) and (b). The scans are provided specifically at distances of 0, 20, 40 and 82.5 nm from the resist surface as solid, dashed, dotted and dashed-dotted lines of blue, red, black and pink colors respectively.

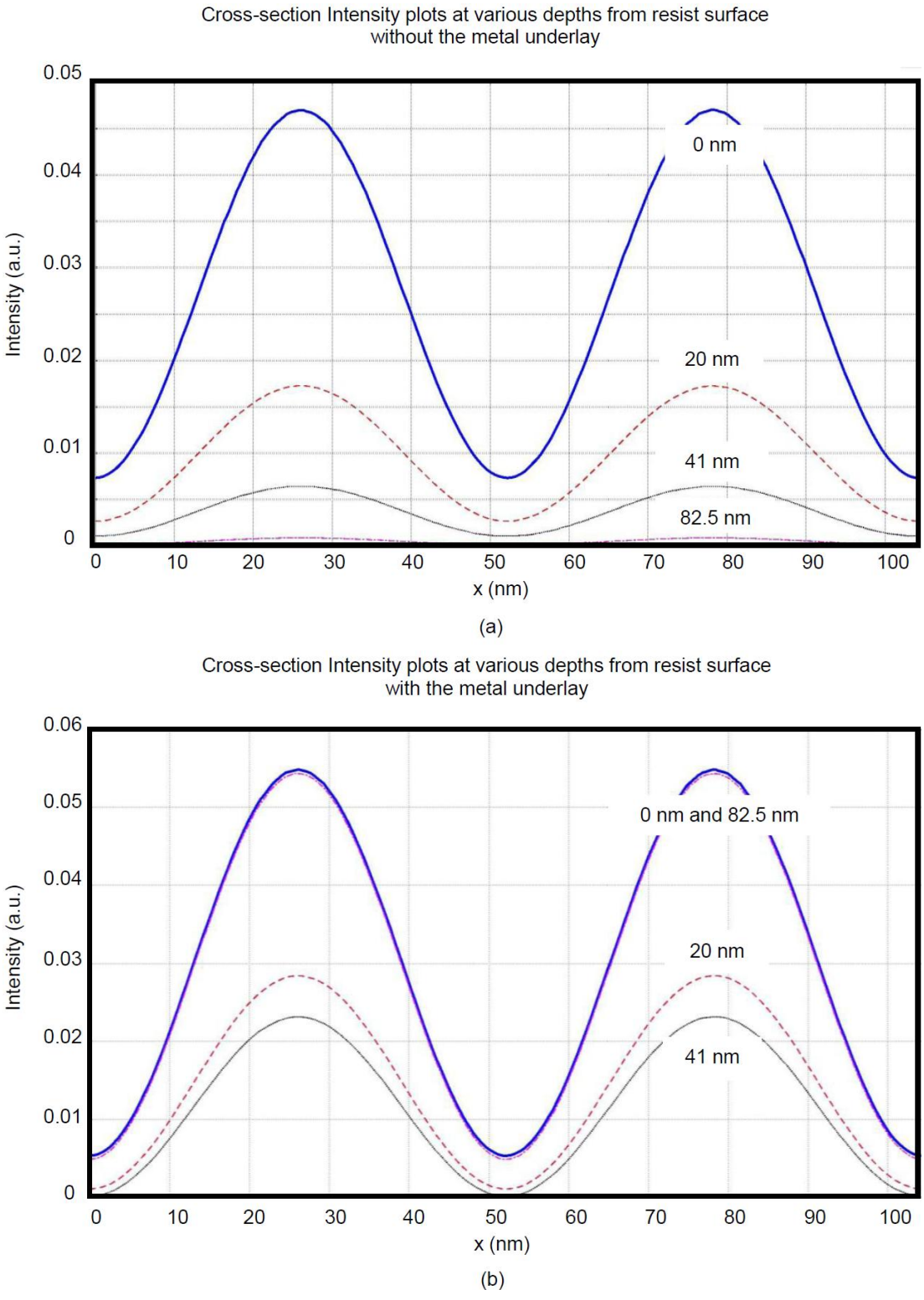

Figure 5-8 - Cross-section Intensity plots at various depths from resist surface for Figure 5-7 (a) and (b) (a) Without the presence of a metal underlay and (b) With the presence of a metal underlay

There are a few aspects that need to be noted here. Firstly for Figure 5-8 (a), neither of the interference minima are zero (*i.e.* they are imperfect nulls). This is owing to the use of the TM polarization of light, where the E_x field makes a contribution to the nulls. As expected for an evanescent field, In Figure 5-8 (a), the intensity maxima falls to 40% of its maximum at a depth of 20 nm and decays further into the depth of the resist and the maxima to minima ratio falls even further.

In the case of Figure 5-8 (b) firstly note that the maxima to minima ratio is higher for every cross-section compared to its counterparts in Figure 5-8 (a). This seems strange at first, however one reason for this is because the field that contributes to the nulls, in fact experiences a different (negative) reflection to the field that contributes to the peaks of the interference pattern. The reasons for this are briefly mentioned in Chapter 4 and also the next chapter that deals with image formation within the resist. In fact, this has allowed the null to touch zero in one of the cross-sections in Figure 5-8 (b) (see cross-section intensity scan at 41 nm). With the placement of a carefully tuned metal underlay, it can be ensured that the maxima of the interference pattern only falls to 40% of its maximum value at a depth of 41 nm (instead of 20 nm), however as the field rises again at the bottom of the photoresist, this allows a four-fold increase in image depth to ~82.5 nm.

In the next chapter, practical imaging limits are derived for both the TM and TE polarizations of light. Some real world materials are now used in simulations to get the feel for the type of enhancement that maybe expected.

5.4 EIL Feasibility at λ = 405 nm

While the simulation in Figure 5-7 (b) appears extremely attractive, the example utilizes a fictitious metal, which is an obvious hindrance for feasibility. Here, the use of two available metals are considered to use at λ = 405 nm as they exhibit high reflectivities at this wavelength. Silver (Ag) has been chosen specifically due to its low loss properties and the popularity that it has gained after successful demonstrations of the silver plasmonic superlens by two independent groups [76] and [67]. Molybdenum, a material that is not known for its plasmonic properties has also been chosen, and in contrast to Silver, has an extremely high loss at λ = 405 nm. However, it is also capable of significant enhancements through other interesting means as is soon discussed and illustrated. At λ = 405 nm, the optical properties of AZ HiR 1075 photoresist are used in the following FEM simulations.

Figure 5-9 shows a plot of the reflectance at the interface between photoresist and silver (solid line), molybdenum (dashed line). The photoresist-molybdenum reflectance curve peaks to certain value at a

particular *NA* and hence seems to have more in common with the dielectric-metal reflectance plot of Figure 5-5. The photoresist-silver reflectance curve however does not have a point at which it peaks.

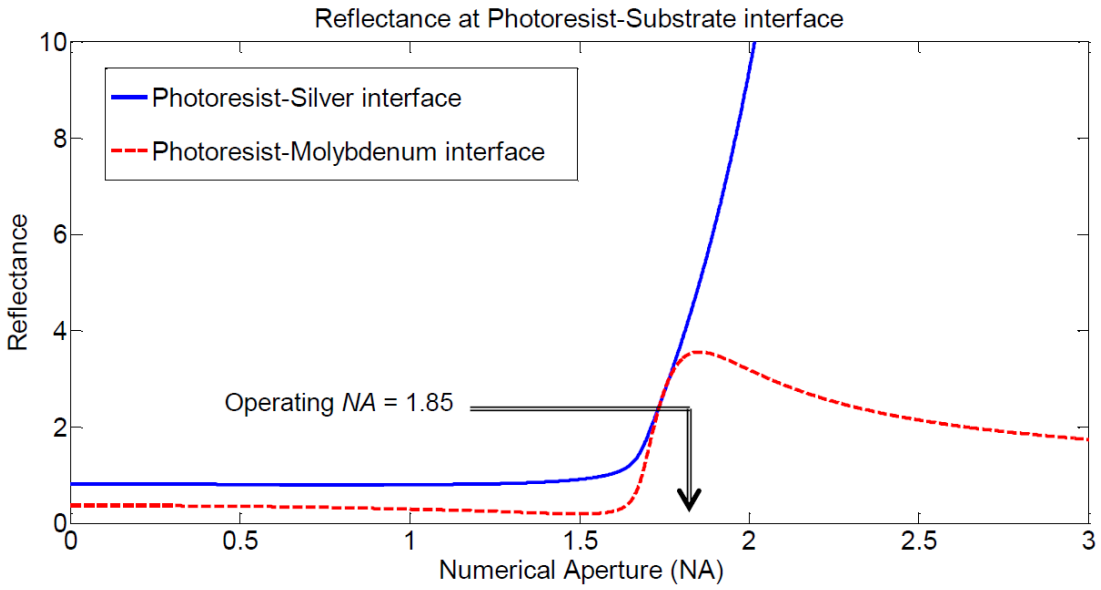

Figure 5-9 – Reflectance plots (using T-Matrix modeling) at the interfaces photoresist-silver (solid blue) and photoresist-molybdenum (dashed red) at λ = 405 nm

5.4.1 Silver

The nature of the peak as briefly mentioned in the previous sub-section is an indication of the momentum matching between the photons and the surface states (if one exists). If the optical properties of photoresist and silver are used in (5.13), then the *NA* at which a SPP will exist is computed to be,

$$\left[\frac{k_x}{k_0}\right]_{Photoresist-Silver,SPP} = \sqrt{\frac{(2.8214 + 0.1042i)(-3.7726 + i0.6747)}{(2.8214 + 0.1042i) + (-3.7726 + i0.6747)}} = 2.86 + i0.8 \quad (5.16)$$

As (5.16) suggests, this value has a high imaginary component. It would require exciting the interface with a complex *NA* that has a real component 2.86 and an imaginary component 0.8. Such a solution is of course of little use to us. This results in a momentum mismatch between the photons and the SPP. Ideally, one would like this wave vector to have a minimal imaginary component owing to the loss in the photoresist and a real component that is well within the proximity of the spatial frequency corresponding to the operating *NA* as is the case with the simulated example in Figure 5-7. As a comparison, the SPP in Figure 5-7 takes place at a *NA* of 1.79.

Nevertheless, simulations were undertakes to investigate the performance for such a scenario and attempt to image into 59 nm of resist at a *NA* of 1.85. This particular depth has been chosen to show comparison with the Molybdenum simulations that follows afterwards.

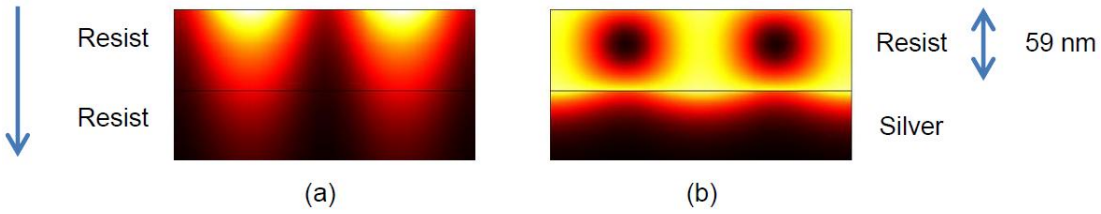

Figure 5-10 – Imaging at λ = 405 nm, *NA* = 1.85 (a) into semi-infinite photoresist (intensity range 0 to 0.02) (b) using silver as an underlay (see Table 5.5 for optical properties) and imaging into 59 nm photoresist (intensity range 0 to 0.006)

Figure 5-10 (b) shows that the SPP generated on the resist-silver interface is effective at making the intensity profile more uniform with depth through the resist layer, but the location of the peaks and nulls have been interchanged when compared with the plot in Figure 5-10 (a). This is due to the phase of the reflection (180^{o}) that acts to attenuate the peaks but enhance the nulls (the peaks and nulls experience reflections that are opposite in sign, this will be described in the next chapter). While there appears to be an improvement in the depth of field, it seems like a complete resist lift-off might take place when a sample with the intensity profile of Figure 5-10 (b) is developed, as the distinction between nulls and peaks almost disappears at a depth of 59 nm (bottom of the resist). This is perhaps better illustrated by cross-sectional intensity plots, see Figure 5-11.

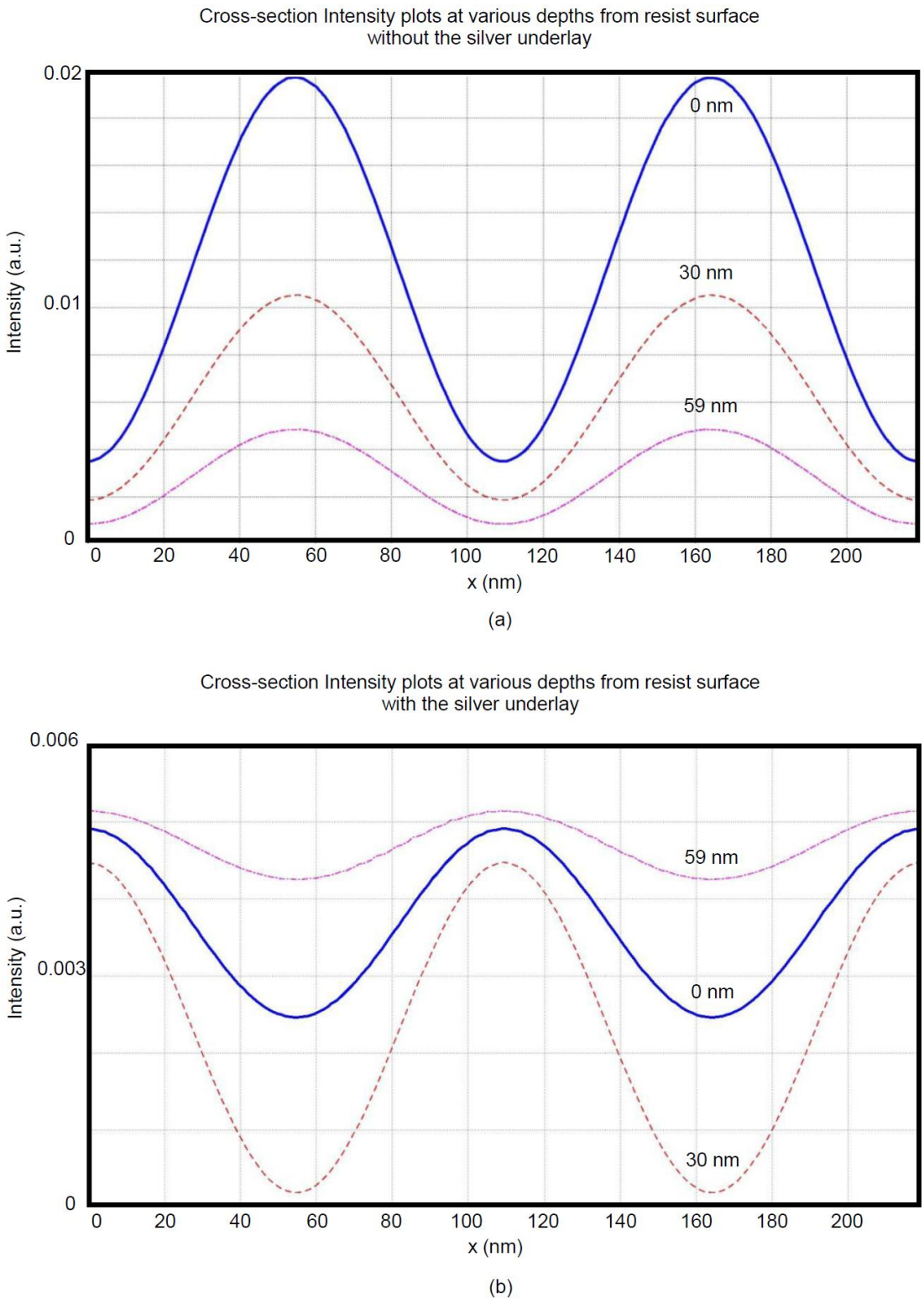

Figure 5-11 - Cross-section Intensity plots at various depths from resist surface for Figure 5-10 (a) and (b). (a) Without the presence of a silver underlay and (b) With the presence of a silver underlay

Also, keep in mind the vastly different intensity ranges for both Figure 5-10 (a) and (b). The intensity range of Figure 5-10 (b) is considerably lower than that of Figure 5-10 (a), indicating that such as setup is doing an extremely bad job of extracting energy from the incident beam; in fact it is actually causing the stack to lose energy to the external system.

Figure 5-11 (b) suggests that there is only a central region where the maxima to minima ratio is high. At a depth of 59 nm, this ratio falls considerably and hence may result in complete resist lift-off. Let us now consider how well molybdenum performs under a similar arrangement.

5.4.2 Molybdenum

The evanescent wave enhancement that takes place at the interface of a low loss dielectric and metal due to the presence of the SPP surface state has now been described. A similar, although not quite the same scenario also occurs at the interface of a low loss dielectric and a lossy dielectric as was suggested by the result of analysis carried out in section 5.2.1. Such an enhancement is in fact known as a Surface Exciton Polariton (SEP) and although not quite as popular as well known, it bears some similarities with the SPP.

While the SPP is created as a result of the free electron oscillation at a dielectric-metal boundary, the naturally occurring SEP is the result of bound electron vibrations. However, the optical response of any material varies with the driving frequency. Hence, a material that acts like a low loss metal at one frequency may in fact behave like a lossy dielectric at another frequency. For this reason, the SEP like response may even be achieved with a material that is made up of a free electron gas. In regards to its optical behavior, the material made up of the free electron gas might be indistinguishable from a lossy dielectric due to the inability of the electrons to respond sufficiently fast to an incident oscillating electric field.

There has been considerably little literature on the use of SEPs, and this was pointed out in the early 1990's by Professor Fuzi Yang, University of Exeter, UK who has several publications on the subject including a classical paper demonstrating such a SEP state at an air-vanadium interface. In [111], it is mentioned that for all metals the electrical permittivity is a complicated function of the frequency and almost all metals have a characteristic frequency at which the real part of the permittivity crosses through zero. Hence, near this frequency, one finds a small real permittivity and a large imaginary permittivity and the metal behaves like an exciton active medium. In Figure 5-12, a plot of the dielectric response of vanadium near an excitonic resonance is presented, that was originally published in [111] and is reprinted here with permission from Professor Yang.

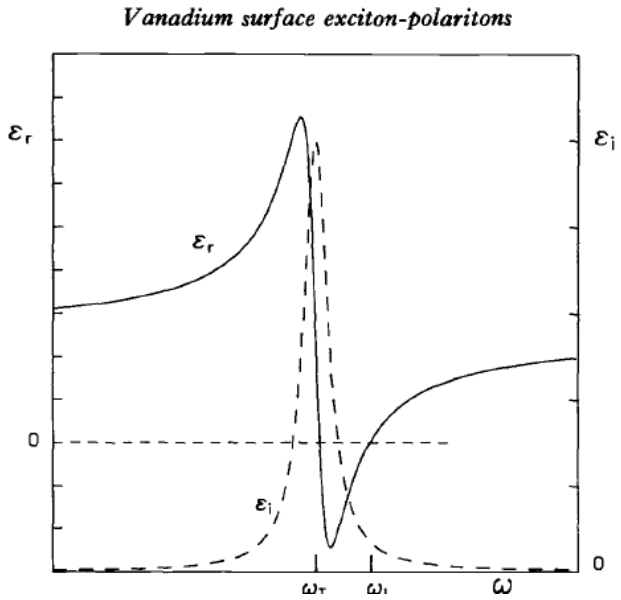

Figure 5-12 - Vanadium – Typical dielectric response near an excitonic resonance ([111])

Yang et. al. used this to experimentally show that vanadium also behaves like an excitonic dielectric at λ = 3391 nm (infrared) using a prism coupled setup similar to the one considered in this chapter.

In fact, the use of molybdenum at λ = 405 nm creates a similar scenario. At this wavelength, molybdenum has an electrical permittivity $\varepsilon_3 = -1.19 + 19.51\text{i}$, i.e. a small real component and a large imaginary component as the real part approaches zero. Note that, while the real component of the electrical permittivity is still negative owing to the free electron response, the imaginary component is more than 10 times larger in magnitude. The SEP resonance spatial frequency is also in fact given by (5.13) as,

$$\left[\frac{k_x}{k_0}\right]_{Photoresist-Silver,SPP} = \sqrt{\frac{(2.8214 + 0.1042i)(-1.1875 + i19.5132)}{(2.8214 + 0.1042i) + (-1.1875 + i19.5132)}} = 1.67 + i0.15 \quad (5.17)$$

This has a small imaginary component and hence there is only a slight mismatch between the photon and SEP momentum and hence, a photoresist-molybdenum interface may be excited at a *NA* of 1.67. Note that a *NA* of 1.67 is in fact in the limiting propagating regime of the photoresist ($n_2 = 1.68 + i0.031$) and so it may in fact be excited without the use of a prism coupling mechanism. This is another aspect that differentiates an SEP from an SPP. Of course, the use of a prism coupling mechanism makes it much easier as otherwise a near-grazing incidence is required. For this reason, if thick photoresist were to be used, then the appearance of dips will be seen even when TE polarized light is used. This is due to the emergence of waveguide modes in the photoresist cavity because operation is in the propagating region, rather than the appearance of the SEP. This is mentioned here so that a researcher new to the field of

evanescent waves is not confused when a dip is seen while using a TE polarization setup. Of course, our aim is to operate in a slightly off-resonant region to better distribute the E-field within the photoresist. As before, a molybdenum underlay beneath the photoresist is used to facilitate interaction with an evanescently decaying field at a *NA* of 1.85. FEM simulations and cross-sections scans are provided, this is followed by analysis. The reader is once again referred to the tabulated optical parameters in Table 5.5.

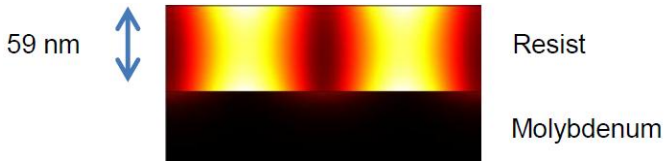

Figure 5-13 – Imaging at λ = 405 nm into 59 nm of photoresist at *NA* = 1.85 with a Molybdenum underlay

Figure 5-13 illustrates the creation of a symmetrical image into 59 nm of photoresist when Molybdenum is utilized as an underlay at a *NA* of 1.85. The peaks and nulls have not been transposed and as the cross-section intensity scans of Figure 5-14 illustrate, the intensity ranges are comparable to the non-underlay case in Figure 5-11 (a).

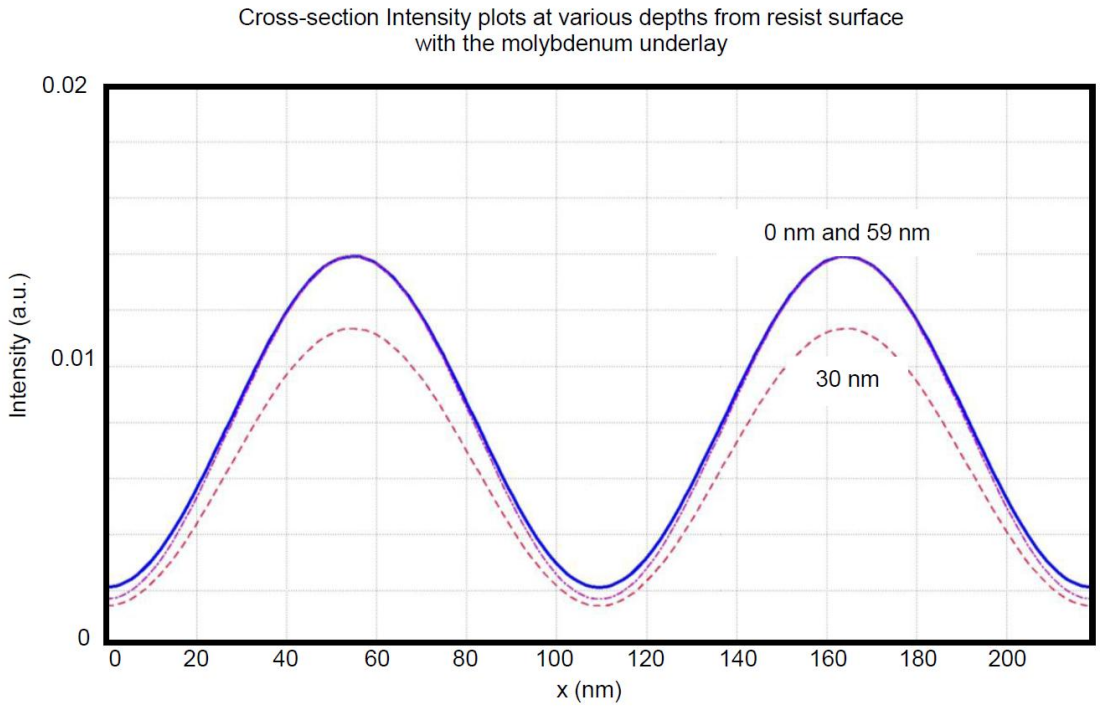

Figure 5-14 - Cross-section Intensity plots at various depths from resist surface for Figure 5-13 where a molybdenum underlay has been utilized.

Moreover, Figure 5-14 shows that a reasonably high and uniform maxima to minima ratio is maintained throughout the depth of the image. All of these points make molybdenum a good contender over the no underlay case and even over the use of silver as an underlay as illustrated by Figure 5-10. The high-loss in media such as molybdenum and silicon means that they are impenetrable to the E-fields [111]. These fields are thus evanescent from and confined and enhanced at the surface. The photosensitive imaging medium (resist) benefits from this phenomenon.

5.5 Summary

The aim of this chapter was to introduce the mathematical and physical basis for evanescent wave enhancements via the use of the Fresnel reflection equations and various surface states on fictitious and naturally occurring metals and lossy dielectrics for evanescent interference lithography. Through a mathematical analysis, it was confirmed that while the TM polarized evanescent waves may be enhanced via the use of such surface states, there exist no natural surfaces states to enhance TE polarized evanescent waves. However, it was discovered that this may in fact be possible if a hypothetical medium that exhibits a negative loss, i.e. a gain medium were to be used as an underlay. It is then such a hypothetical gain medium that we have used to bring to attention the presence of a new type of surface resonance, the gain medium surface state, to allow evanescent wave enhancement. The physical phenomenon responsible for the enhancement may be simply described as the extraction of the energy which is otherwise reflected away into free space and redistribution of this energy in the photoresist cavity. Of course, such extraction only takes place when the underlay is carefully chosen or designed to have an operating point near the surface state resonance and when there is a slight loss in the photoresist.

As an interesting finding to end with, and a lead on to some of the material presented in the following chapter, it was found that the use of stack consisting of ~9 nm of molybdenum deposited on silicon allows a mild but noticeable improvement over a semi-infinite molybdenum underlay with the TM polarized evanescent wave. More interestingly though, the reflectance achieved from this stack may also be obtained with a hypothetical material, $\varepsilon_3 = 3.3 - 0.4427i$, i.e. a gain medium underlay.

In the next chapter, practical imaging limits for both TM and TE polarizations of light are derived. The behavior of multilayered stacks is analyzed in detail using the equivalent reflectance approach (ERA) and feasible methods are proposed to create the hypothetical gain medium and allow the desired enhancement using the TE polarization of light. One such design proposed is at the use industry standard λ = 193 nm wavelength and should allow imaging and patterning of structures at high aspect ratios at an ultra-high *NA* of 1.85.

Chapter 6. Imaging Limits, Equivalent Reflectance Analysis and use of Effective Gain Media in EIL

This chapter explores the evolution of an evanescent image in the presence of a substrate layer. The practical limits of EIL imaging with evanescent-wave enhancements are derived based upon certain imposed requirements for image quality (related to lithography). T-Matrix field plots are shown for both the TE and TM cases for imaging at a hypothetical ultra-high *NA* of 3. Next the Equivalent Reflectance Approach (ERA) is developed, the results of the previous chapter are utilized and the effective gain medium stack is introduced that allows the discussed enhancements to be realized. A feasible design solution is then proposed using the industry standard λ = 193 nm TE polarized light to image high aspect ratio structures at *NA*s of 1.85.

6.1 Evanescent Interferometric Lithography

In the last chapter, evanescent wave coupling to various material substrates was discussed. This showed how large enhancements may be achieved and how these enhancements may be utilized in an off-resonant scenario to achieve a more uniform image distribution within a photoresist cavity, thereby allow imaging into thick photoresist, which is essential for pattern transfer in lithographic processing. The subject of this section is to derive limits for the maximum image depth that may be possible with practical photoresists, based upon certain criteria that are imposed to ensure a high quality image.

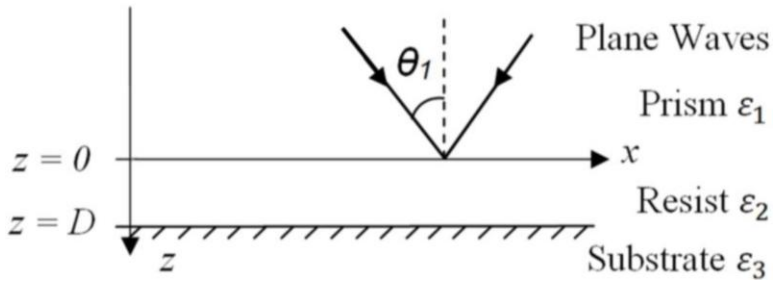

Figure 6-1 - Schematic of solid immersion two beam interference lithography

Firstly, it is required to determine the field profile within the resist cavity in the presence of a reflecting substrate. Figure 6-1 reprints the setup from the previous chapter to ease the readability of the analysis that follows. The analysis is begin by realizing that the image formed within the resist cavity is in fact periodic in the *x*-direction with period λ/2*NA*, resulting from the interference of two counter propagating waves at a *NA* of $n_1 \sin(\theta) = \sqrt{\varepsilon_1}\sin(\theta)$ where θ is a real angle. The evolution of the image into the depth of the resist (*z*-direction) may be computed either using the T-Matrix method described in Chapter 4 or by analytically summing the contributions of the multiple reflections that the wave undergoes. Both of these methods are described in detail in [178]. Although both methods yield the same results, the second method is used here as this allows representation of the image in terms of equations as opposed to matrices and vectors. The Fresnel transmission and reflection coefficients are once again used heavily in this chapter and the reader may refer to their tabulated forms in the previous chapter. To avoid confusion, ρ and τ have been used to denote the reflection and transmission for the TE case and r and t for the TM case.

6.2 Limits of EIL imaging with TE Polarized light

Let us begin with the TE polarized case and compare three regimes of reflection, namely $\rho < 1$, $\rho = 1$, and $\rho > 1$. Once this has been shown, for the TE case, it will be clear that $\rho > 1$ is the most advantageous scenario.

For TE polarization, the two-beam interference image in the resist has only a *y*-component to the electric field. For simplicity, assume that each interfering beam has electric field amplitude of 1.

$$E_y(x,z) = 2a_{1r}\cos(2\pi x/p)E_{sw}(\theta,z) \tag{6.1}$$

where

$$a_{1r} = \frac{\tau_{12}(\theta)}{1+\rho_{12}(\theta)\rho_{23}(\theta)\tau_D^2(\theta)} \tag{6.2}$$

the *p* is the pitch of the resulting electric field image given as,

$$p = \lambda/NA \text{ where } NA = n_1\sin\theta_1 = \sqrt{\varepsilon_1}\sin\theta_1 \tag{6.3}$$

the τ_D is the internal transmittance of the photoresist film of thickness *D* given as,

$$\tau_D = e^{ik_2 D\cos\theta_2} = e^{ik_{z,2}D} \tag{6.4}$$

and the standing wave *z*-dependence is (see [6])

$$E_{sw}(\theta,z)=e^{ik_2z\cos\theta_2}+\rho_{23}(\theta)\tau_D^2(\theta)e^{-ik_2z\cos\theta_2} \tag{6.5}$$

Where $k_{z,2}=k'_{z,2}+ik''_{z,2}=k_2\cos(\theta_2)$ is the complex z-wave number in media 2, i.e. the photoresist. The intensity of the image in resist becomes

$$I(x,z)=\frac{n_2}{n_1}\left|E_y(x,z)\right|^2=4\frac{n_2}{n_1}\left|a_{1r}\right|^2\cos^2(2\pi x/p)I_{sw}(\theta,z) \tag{6.6}$$

where

$$I_{sw}(\theta,z)=E_{sw}E_{sw}^* \tag{6.7}$$

Let us begin using the following notation to denote the scaled real and imaginary components of the *z*-directional wave vector as this will be referred to extensively in the analysis that follows,

$$\eta_{2R}=\frac{k'_{z,2}}{k_0},\eta_{2I}=\frac{k''_{z,2}}{k_0} \tag{6.8}$$

The analysis is continued by making the substitution, $e^{i\mathbf{k}_2z\cos\theta_2}=e^{-k''_{z,2}z}e^{ik'_{z,2}z}$ in (6.5). Thus, in the evanescent regime, the resist has an effective absorption coefficient given by

$$\alpha_e=2k''_{z,2}\text{ Or equivalently as }\alpha_e=\frac{4\pi}{\lambda}\left(\frac{k''_{z,2}}{k_0}\right)=\frac{4\pi\eta_{2I}}{\lambda} \tag{6.9}$$

Further, the propagation in the z-direction is governed by a propagation coefficient that is determined by the loss in the photoresist (i.e. the loss in the photoresist acts to produce a propagating component in the otherwise pure evanescent decay of the field in the *z* direction, however the total field will always be dominated by the exponential decay term).

The resulting standing wave intensity now becomes

$$I_{sw}(z)=e^{-\alpha_e z}+\left|\rho_{23}\right|^2e^{-\alpha_e(2D-z)}+2\left|\rho_{23}\right|e^{-\alpha_e D}\cos(4\pi\eta_{2R}(D-z)/\lambda+\phi_{23}) \tag{6.10}$$

where D is the resist thickness and ϕ_{23} is the phase angle of the substrate reflectivity, given by

$$\rho_{23} = |\rho_{23}| e^{i\phi_{23}} \tag{6.11}$$

6.2.1 Case I: Nonreflecting Substrate (|ρ| = 0)

If the substrate below the resist is perfectly non-reflecting, the standing wave intensity is just

$$I_{sw}(z) = e^{-\alpha_e z} \tag{6.12}$$

A constraint on how low the intensity can be at the bottom of the resist places a constraint on how thick the resist layer can be. The ratio of intensity at the top of the resist to that at the bottom is

$$RIR = \frac{I_{sw}(z=0)}{I_{sw}(z=D)} = e^{\alpha_e D} \tag{6.13}$$

Here, the term resist intensity ratio (*RIR*) is used to denote the ratio of the maximum and minimum intensity in a resist layer of thickness D. A typical maximum ratio of top to bottom intensity will be in the range of 2 to 2.5. Using the upper end of this range, *RIR* = 2.5, allows $(\alpha_e D)_{\max}$ = 0.92. For an evanescent interferometric imaging case where λ = 193 nm, *NA* = 1.85, and $\boldsymbol{n_2}$ = 1.7 + *i*0.02, this leads to a maximum resist thickness of 19 nm for a pattern with half-pitch line and space dimension of $\lambda/4NA$ ~ 26 nm. This result illustrates the general case that evanescent-wave imaging with a non-reflective substrate will result in image depths less than the feature size, making the formation of high aspect ratio resist structures difficult to achieve.

6.2.2 Case II: Ideal Conventional Mirror (|ρ| = 1)

As the above case illustrates, a big problem with evanescent imaging is the high effective absorbance of the resist. Thus, it is desirable to use the reflected waves in the resist to try to counteract the steep fall-off in intensity with depth into the resist. The difference between the intensity at the top and the bottom of the resist can be seen from

$$I_{sw}(z=0) = 1 + |\rho_{23}|^2 e^{-\alpha_e 2D} + 2|\rho_{23}| e^{-\alpha_e D} \cos(4\pi\eta_{2R} D/\lambda + \phi_{23}) \tag{6.14}$$

$$I_{sw}(z=D) = e^{-\alpha_e D}\left(1 + |\rho_{23}|^2 + 2|\rho_{23}|\cos(\phi_{23})\right) \tag{6.15}$$

Consider the case of a small η_{2R}, so that $\eta_{2R}D << \lambda$. For this case, the optimum ratio of standing wave intensities occurs when $|\rho_{23}| = 1$ and $\phi_{23} = 0$ (achieved by setting $n_3 = n_3' = NA$), becoming

$$RIR = \frac{I_{sw}(z=0)}{I_{sw}(z=D)} \approx \frac{e^{\alpha_e D} + e^{-\alpha_e D} + 2}{4} \tag{6.16}$$

Using a maximum ratio of intensities of *RIR* = 2.5, now allows $(\alpha_e D)_{\max}$ = 2.08. For the weakly absorbing resist case and using (6.9) this leads to

$$D \le \frac{\lambda(\alpha_e D)_{\max}}{4\pi\eta_{2I}} \approx \frac{\lambda(\alpha_e D)_{\max}}{4\pi\sqrt{NA^2 - n_2'^2}} \tag{6.17}$$

But the thickness of the resist is also constrained by etch resistance considerations. In manufacturing, the minimum allowed resist thickness usually scales with the minimum feature size (*CD*), so that the aspect ratio is kept fixed at $AR_{\min}$ (typically about 2). Applying this constraint,

$$\frac{D}{CD} = AR_{\min} = \frac{\frac{\lambda(\alpha_e D)_{\max}}{4\pi\eta_{2I}}}{\frac{\lambda}{4NA}} = \frac{NA(\alpha_e D)_{\max}}{\pi\eta_{2I}} = \frac{NA(\alpha_e D)_{\max}}{\pi\sqrt{NA^2 - n_2'^2}} \tag{6.18}$$

or

$$\frac{NA}{\sqrt{NA^2 - n_2'^2}} = \pi\frac{AR_{\min}}{(\alpha_e D)_{\max}} \tag{6.19}$$

or

$$NA_{\max} = \frac{n_2}{\sqrt{1 - \left(\frac{(\alpha_e D)_{\max}}{\pi AR_{\min}}\right)^2}} \tag{6.20}$$

If $(\alpha_e D)_{\max}$ = 2.08 and $AR_{\min}$ = 2, (6.20) gives $NA_{\max} = 1.06n_2$. For a typical photoresist (n_2' = 1.7), this leads to a maximum numerical aperture of ~1.8. Relaxing the minimum aspect ratio to 1, the *NA* can be made as high as 2.27. In looking at the denominator in (6.20), any *NA* can be achieved if the constraints can be relaxed so that

$$\frac{(\alpha_e D)_{\max}}{AR_{\min}} \le \pi \tag{6.21}$$

To illustrate the above case, let NA = 1.85 and n_2 = 1.7 + i0.02, producing 26.1 nm lines and spaces (p = 52.2 nm). Allowing D = 43.7 nm (so that $\alpha_e D$ = 2.08), giving a best-case intensity at the bottom of the resist that is about 2.5 times smaller than at the top.

6.2.3 Case III: Evanescent Mirror (|ρ| > 1)

If one could increase the substrate reflectivity to larger values, one could increase the light intensity at the bottom of the resist. For the typical case of small η_{2R},

$$I_{sw}(z=0) = 1 + |\rho_{23}|^2 e^{-\alpha_e 2D} + 2|\rho_{23}| e^{-\alpha_e D} \cos(\phi_{23}) \tag{6.22}$$

$$I_{sw}(z=D) = e^{-\alpha_e D}\left(1 + |\rho_{23}|^2 + 2|\rho_{23}| \cos(\phi_{23})\right) \tag{6.23}$$

The desired case is when the intensity at the bottom of the resist equals the intensity at the top. The value of the substrate reflectivity that provides this solution is

$$|\rho_{23}|^2 = \frac{e^{\alpha_e D} - 1}{1 - e^{-\alpha_e D}} \approx e^{\alpha_e D} \tag{6.24}$$

For this condition, the absorbance limitation will be determined by the intensity of light at the middle of the resist.

$$RIR = \frac{I_{sw}(z=0) = I_{sw}(z=D)}{I_{sw}(z=D/2)} = \frac{1 + |\rho_{23}|^2 + 2|\rho_{23}| \cos(\phi_{23})}{e^{\alpha_e D/2} + |\rho_{23}|^2 e^{-\alpha_e D/2} + 2|\rho_{23}| \cos(\phi_{23})} \tag{6.25}$$

At the optimum substrate reflectivity,

$$RIR = \frac{\frac{1}{2}\left(e^{-\alpha_e D/2} + e^{\alpha_e D/2}\right) + \cos(\phi_{23})}{1 + \cos(\phi_{23})} \tag{6.26}$$

If this ratio of intensities is allowed to reach RIR = 2.5, then this allows $(\alpha_e D)_{\max}$ = 4.1, using the best case ϕ_{23} = 0. This allows the resist thickness to be twice as great as could be achieved with an ideal

conventional mirror ($|\rho_{23}|=1$). To achieve any possible NA, the constraint on the minimum aspect ratio becomes

$$AR_{\min} \le \frac{(\alpha_e D)_{\max}}{\pi} = 1.3 \tag{6.27}$$

While not as high as desired, an aspect ratio of 1.3 is reasonable. If the minimum aspect ratio is set to 2.0, then the highest NA achievable is $1.32n_2$, or about 2.24 for a typical photoresist using equation (6.20).

The key result from the above analysis is that for a *RIR* of 2.5, it is only a substrate reflectivity greater than unity $|\rho_{23}| > 1$ that allows the largest imaging depth in resist, when compared with scenarios and $|\rho_{23}| < 1$ and $|\rho_{23}| = 1$.

This section is concluded with a field plot of the TE polarization scenario demonstrating EIL with and without enhancement at λ = 193 nm at a *NA* of 3, corresponding to a 16 nm half-pitch pattern, this is of course a hypothetical example for prism-coupled EIL (unless ultra-high index materials were developed), but may be possible using gratings to couple into the appropriate evanescent orders to give an effective *NA* as high as this. Figure 6-2 illustrates the view without the enhancement, the image is shallow ~5.6 nm depth but being TE polarized exhibits perfect nulls.

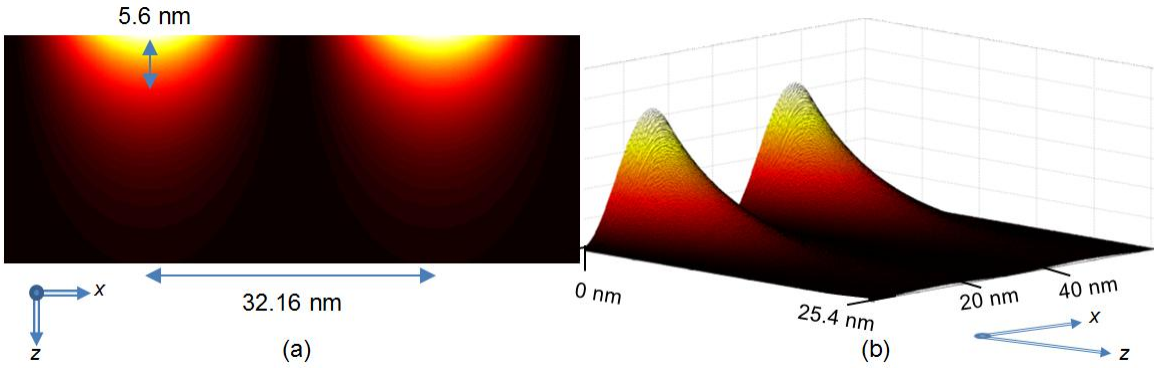

Figure 6-2 - EIL in photoresist at λ = 193 nm, *NA* = 3 with TE polarized light (a) Plan view (b) 3D perspective view. Image half-pitch – 16.08 nm, image depth – 5.6 nm

The evanescent enhanced EIL case utilizing a reflective gain medium ($\varepsilon_3 = 5.38 - \delta i$, where δ tends to 0) underlay is illustrated in Figure 6-3. The refractive index of the imaging media (resist) is set to $n_2 = 1.7$. The 2-3 interface in Figure 6-3 under these conditions exhibits a reflectivity of 7.69 and an image depth of 25.4 nm is achieved with a *RIR* of 2.47. The enhanced image also exhibits perfect nulls. The modeling is carried out using the T-Matrix model presented in Chapter 4.

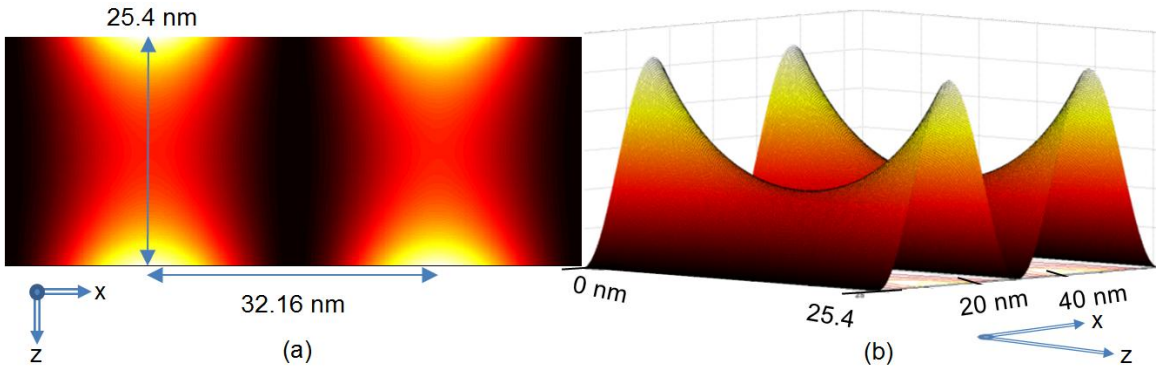

Figure 6-3 – EIL in photoresist at λ = 193 nm, *NA* = 3 with TE polarized light using a reflective gain medium underlay. Image half-pitch – 16.08 nm and depth of 25.4 nm giving an aspect ratio of 1.58 (a) Plan view (b) 3D perspective view

A similar analysis for the limits of imaging with the TM polarization is now presented in the following section. This analysis is more involved as the effects of the background exposure also need to be accounted for.

6.3 Limits of EIL imaging with TM polarized light

In the previous sub-section the limits of imaging using TE polarized light were derived and three different regimes of reflections were explored. Here the focus is on deriving imaging limits for the TM polarized case for which a reflection greater than unity is possible using SPP or SEP type surface states. The analysis is limited to the case where the reflection is greater than unity as this was shown to be the most desirable scenario in the previous sub-section in that it allowed the use of relatively thick resist to allow high aspect ratio imaging and hence meet the etch necessary resistance requirements. For the TE case, two constraints were placed to ensure image fidelity. One of these was the requirement of a symmetrical image; the second was a maximum tolerable intensity ratio of 2.5. The challenge here is somewhat different, it is to achieve a fine balance between the two components of the E-field that make up the image. An imbalance will act to severely reduce the image fidelity. While it would be desirable to carry out the analysis by imposing similar constraints for the TM polarized case, additional conditions are required in order to exercise control of the intensity of the resulting imperfect nulls in the interference pattern.

As the image formation using a standing wave image profile has already been discussed in the TE scenario, it will not be discussed here again. Instead the formula for the image intensity for the TM case is directly presented. At any point within the resist, the intensity is the sum the intensities of the *x* and *z* components of E-field.

$$I(x,z) = |E_x|^2 + |E_z|^2 \tag{6.28}$$

Hence, image formation using the E_x and E_z components may be computed independently as,

$$E_x(x,z) = 2\sin(k_x x)\, a_x(e^{i*k_{z_2}*z} - r_{23} * e^{2i*k_{z_2}*D} * e^{-i*k_{z_2}*z}) \tag{6.29}$$

$$E_z(x,z) = 2\cos(k_x x)\, a_z(e^{i*k_{z_2}*z} + r_{23} * e^{2i*k_{z_2}*D} * e^{-i*k_{z_2}*z}) \tag{6.30}$$

$$a_x = \frac{t_{12_x}}{1 + r_{12}r_{23} * e^{2i*k_{z_2}*D}} \tag{6.31}$$

$$a_z = \frac{t_{12_z}}{1 + r_{12}r_{23} * e^{2i*k_{z_2}*D}} \tag{6.32}$$

Note that, while the format of the above equations is similar to (6.1), the *x* and *z* field profiles have three important differences. Firstly, the scaling factors a_x and a_z indicate a difference in the amplitude of each E-field component.

Secondly, the respective interference patterns of the E_x and E_z fields are spatially out of phase with respect to each other. This arises due to the difference in the physical location where the *x* and *z* components each form the peak and null of the interference pattern. This is better illustrated by Figure 6-4, where two waves with E-field amplitudes E_1 and E_2 are interfered with each other and the constructive and destructive interference of each of the *x* and *z* components is noted. Referring to equations (6.29) and (6.30), It is clear that at an arbitrary point $x = 0$, it is only the E_z component that contributes to the image formation. Similarly, at $x = \pi/2k_x$, it is only the E_x component that contributes to image formation. Hence, the spatial displacement is of $\lambda/4NA$ and corresponds to the half-pitch of the pattern that is being imaged.

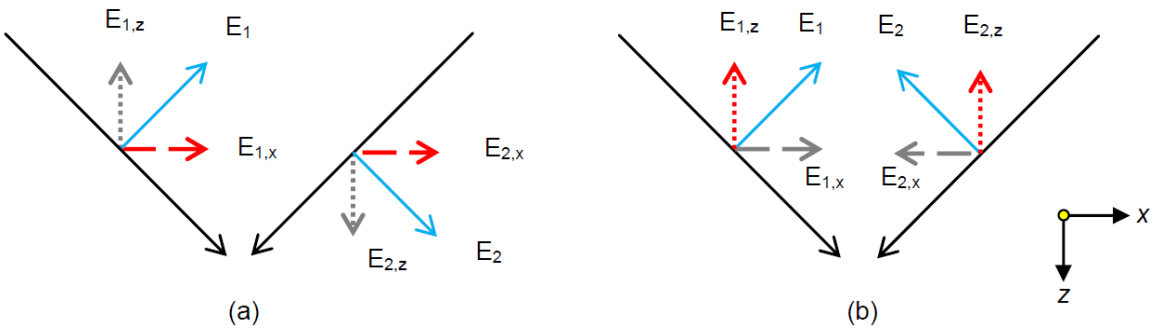

Figure 6-4 – Interference of two waves with E-field amplitudes E_1 and E_2 (a) X and Z components constructively and destructively interfere respectively (b) vice-versa of scenario in part (a)

Finally, also note that the E_x field in fact faces a reflection from the substrate that is the negative of the E_z field, this was illustrated in Chapter 4. This acts to our advantage as it allows null minimization when the substrate has a positive reflection and hence contributes to improving the maxima to minima ratio of the interference pattern when a carefully designed/chosen reflecting underlay is put in place.

Let us assume for an instant that imaging is being carried out into semi-infinite resist without a reflecting substrate, *i.e.* if $r_{23} = 0$ (the effect of the reflector is included again after this brief analysis), and compare the relative peak intensities of the E_z and E_x components for the weakly absorbing resist case,

$$\left|\frac{E_z(0,0)}{E_x(\pi/2k_x,0)}\right|^2\Bigg|_{r_{23}=0} = \left|\frac{a_z}{a_x}\right|^2 = \left|\frac{t_{12_z}}{t_{12_x}}\right|^2 = \left|\frac{t_{12}\,NA/\sqrt{\varepsilon_2}}{t_{12}\sqrt{1-(NA/\sqrt{\varepsilon_2})^2}}\right|^2$$
$$= \frac{NA^2}{NA^2 - n_2'^2} \; or \; \frac{NA^2}{NA^2 - \varepsilon_2'} \qquad (6.33)$$

Equation (6.33) informs us that the contribution of the E_z component to imaging is greater than the E_x component because $NA^2 > NA^2 - \varepsilon_2'$. In fact note that, as *NA* increases, (6.33) tends to one, which is a manifestation of the increasing amount of background exposure in the image.

Why is this important for us to know? It is because, knowing this fact allows us to designate the maxima and minima of the interference pattern. The peaks of the E_z field may be labeled as the maxima of the interference pattern and the peaks of the E_x fields as the minima of the interference pattern. In addition to this, the image formation may also be analyzed separately for both fields.

Let us once again consider the inclusion of a reflecting substrate and limit the analysis to the weakly absorbing resist case. The analysis is split into two parts and the relevant requirements are developed for each of the two fields.

The desired case as before is when the intensity at the bottom of the resist equals the intensity at the top. Let us consider the maxima first,

$$I(0,z) = |E_z(0,z)|^2 \tag{6.34}$$

The requirement for a symmetrical image is,

$$\begin{gathered} I(x=0,z=0) = I(x=0,z=D) \\ |E_z(0,0)|^2 = |E_z(0,D)|^2 \\ |1 + r_{23} * e^{2i*k_{z_2}*D}|^2 = |e^{i*k_{z_2}*D} + r_{23} * e^{i*k_{z_2}*D}|^2 \end{gathered} \tag{6.35}$$

As before, the best case reflection is when r_{23} is real and has a zero phase. Also for the weakly absorbing resist case, the equations become real and so $k_{z_2} = ik_{z_2}{}''$.

$$1 + 2r_{23}e^{-2k_{z_2}{}''D} + r_{23}{}^2e^{-4k_{z_2}{}''D} = e^{-2k_{z_2}{}''D} + 2r_{23}e^{-2k_{z_2}{}''D} + r_{23}{}^2e^{-2k_{z_2}{}''D} \tag{6.36}$$

Once again let us denote the effective absorbance in the photoresist using (6.9). The value of r_{23} that satisfies (6.35),

$$r_{23} = e^{\alpha_e D/2} \tag{6.37}$$

Secondly, the *RIR*, that is the ratio between the maximum and minimum intensities along the interference maxima needs to be no more than 2.5,

$$RIR = 2.5 \geq \frac{I(x=0,z=0)}{I(x=0,z=D/2)} \tag{6.38}$$

Recall that we have already carried out a very similar derivation in section 6.2.3, however some part of this is repeated here to set the scene for the analysis that follows.

$$|E_z(0,0)|^2 \leq 2.5 * |E_z(0,D/2)|^2 \tag{6.39}$$

Using $r_{23} = e^{\alpha_e D/2}$ as the optimum substrate reflectivity,

$$1 + 2e^{-\alpha_e D/2} + e^{-\alpha_e D} \leq 10e^{-\alpha_e D/2} \tag{6.40}$$

results in a quadratic in $e^{-\alpha_e D/2}$,

$$e^{-\alpha_e D/2} \geq \frac{8 \pm \sqrt{64-4}}{2} = 0.127 \; or \; 7.873 \tag{6.41}$$

The correct solution is of course 0.127, resulting in the constraint given by (6.42) (as was also found in section 6.2.3). Let us name this *constraint 1* and define it as,

$$\alpha_e D \leq -2\ln(0.127) = 4.1 \tag{6.42}$$

If the only field of concern was the E_z field, then the required reflection would simply be $r_{23} = e^{\alpha_e D/2} = 7.87$, the maximum allowable depth for the image would be $4.1/\alpha_e$ or ~86 nm for photoresist with $n_2 = 1.7$, *NA* = 1.85 and λ = 193 nm and such a reflection may be attained using a hypothetical metal with $\varepsilon_3 \sim -29.8$. A similar example was demonstrated with lossy resist in Chapter 5. However, there is another limiting constraint in some cases for the maximum allowable image depth. This is defined by the intensity of the E_x field which forms the imperfect null of the TM image. A condition needs to be enforced such that the maximum intensity of the E_x field is limited to below the minimum intensity of the E_z field. Let us use (6.43) for this and name it *constraint 2*,

$$I(x = 0, z = D/2) \geq f * I(x = \pi/2k_x, z = 0) \tag{6.43}$$

In (6.43), the factor f controls the ratio between minimum E_z field intensity and the maximum E_x field intensity. At this stage, we must point out to the reader that the ability to do so is a privilege resulting from the presence of a reflecting substrate. This is well demonstrated by the examples that are to follow in Figure 6-5 to Figure 6-7.

$$\begin{aligned} |a_z|^2 * 4e^{-\alpha_e D/2} &\geq |a_x|^2 f(1 - 2e^{-\alpha_e D/2} + e^{-\alpha_e D}) \\ 4e^{-\alpha_e D/2} &\geq \frac{|a_x|^2}{|a_z|^2} f(1 - 2e^{-\alpha_e D/2} + e^{-\alpha_e D}) \\ 4e^{-\alpha_e D/2} &\geq \left|\frac{\varepsilon_2' - NA^2}{NA^2}\right| f(1 - 2e^{-\alpha_e D/2} + e^{-\alpha_e D}) \end{aligned} \tag{6.44}$$

Let,

$$c = \left|\frac{\varepsilon_2' - NA^2}{NA^2}\right| f \tag{6.45}$$

Then a quadratic results,

$$ce^{-\alpha_e D} - (2c + 4)e^{-\alpha_e D/2} + c \leq 0 \tag{6.46}$$

If $f = 2$, to ensure that the maximum intensity of the E_x field is less than half the minimum intensity of

the E_z field, then for a photoresist with index 1.7, and an operating *NA* of 1.85 this results in the following constraint,

$$e^{-\alpha_e D/2} \geq 0.0676, \alpha_e D \leq 5.4 \tag{6.47}$$

Clearly, (6.42) is still the determining constraint of the two equations ((6.42) and (6.47)) and so the imperfect nulls satisfy our requirements in this particular case.

Let us now briefly discuss the scenarios under which the intensity of the E_x field may act as the determining constraint to limit the depth of imaging. For the above case, this will occur if $f \geq \sim 4.25$.

However, if the lithographer is able to tolerate $f = 2$ as sufficient condition, then in such a case, it is the *NA* that controls the dominance of the two constraints. Through a numerical simulation it was determined that at a *NA* beyond 2.081, it is the intensity of the E_x field that acts to limit the image depth.

Finally, let us also determine the ultimate imaging limit as the *NA* tends to extremely high values. Under such a scenario, using (6.45)

$$\begin{aligned} c &\rightarrow f \text{ as} \\ NA &\rightarrow \infty \end{aligned} \tag{6.48}$$

and for $f = 2$, (6.46) simplifies to

$$e^{-\alpha_e D} - 4e^{-\alpha_e D/2} + 1 \leq 0 \tag{6.49}$$

resulting in the following constraint,

$$\begin{aligned} e^{-\alpha_e D/2} &\geq 0.268 \\ (\alpha_e D) &\leq 2.634 \end{aligned} \tag{6.50}$$

Note that (6.50) is now much more limiting than either of the constraints in equations (6.42) and (6.47). This clearly indicates the dominance of the E_x field at higher *NA*s. Now let,

$$g = 2.634 \geq (\alpha_e D) \tag{6.51}$$

The aspect ratio of a feature (assuming half-pitch) is given as

$$\begin{aligned} AR &= \frac{D}{\lambda/4NA} \\ D \leq \frac{g}{\alpha_e} &= \frac{g}{2k_0\sqrt{NA^2 - \varepsilon_2}} \end{aligned} \tag{6.52}$$

or

$$\frac{\lambda}{4NA}AR \leq \frac{g}{2k_0\sqrt{NA^2-\varepsilon_2}}$$
$$AR \leq \frac{\lambda * g}{4\pi\sqrt{NA^2-\varepsilon_2}}\frac{4NA}{\lambda} \quad (6.53)$$
$$AR \leq \frac{gNA}{\pi\sqrt{NA^2-\varepsilon_2}}$$

and finally as,

$$NA \rightarrow \infty,$$
$$AR \leq \frac{g}{\pi} = 0.838 \quad (6.54)$$

Note, how this ultimate minimal theoretical *AR* limit is much lower than that derived for the TE case in equation (6.27). Relaxing the requirements on f allows us to increase this limit, however with f already equal to 2, lowering its value any further will strongly attenuate and worsen the contrast of the resulting interference pattern.

To provide an example, consider imaging at a *NA* of 3 at λ = 193 nm for two different values of f. Figure 6-5 depicts the intensity profile without the presence of an underlying enhancer. The half-pitch at this *NA* is 16.08 nm and the image depth is only ~5.6 nm, however being TM polarized, the nulls are extremely imperfect and hence the pattern-able depth is expected to be significantly lower than 5 nm.

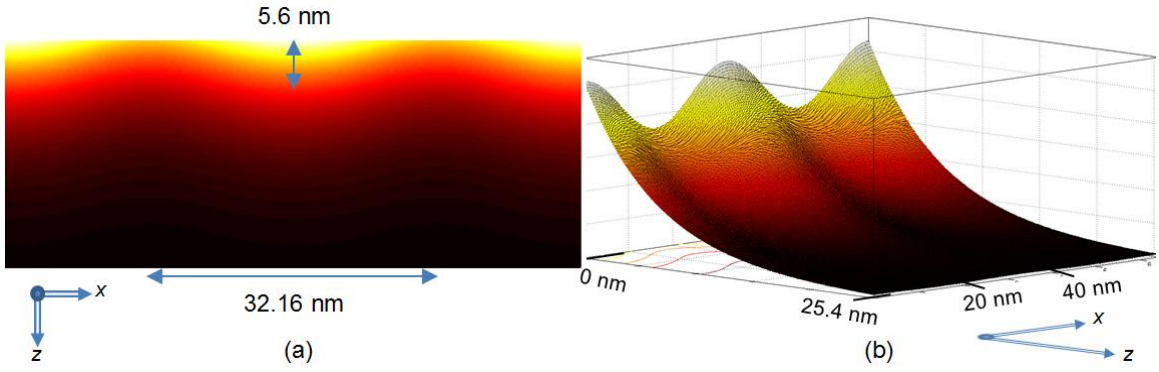

Figure 6-5 – EIL at *NA* = 3 with TM polarized light at λ= 193 nm without any reflective underlay

Next, the effect of changing f is investigated. Figure 6-6 depicts the intensity profile for the $f = 1$ case, where constraint 1 is still the dominant one of the two constraints. The image depth is 25.4 nm (a 5 fold increase over the case depicted in Figure 6-5), however Figure 6-6 suffers from relatively shallow minima

as is expected for $f = 1$. A reflection r_{23} of 7.72 is needed and a metal $\varepsilon_3 = -5.85$ is required to achieve this. This results in an aspect ratio of 1.58.

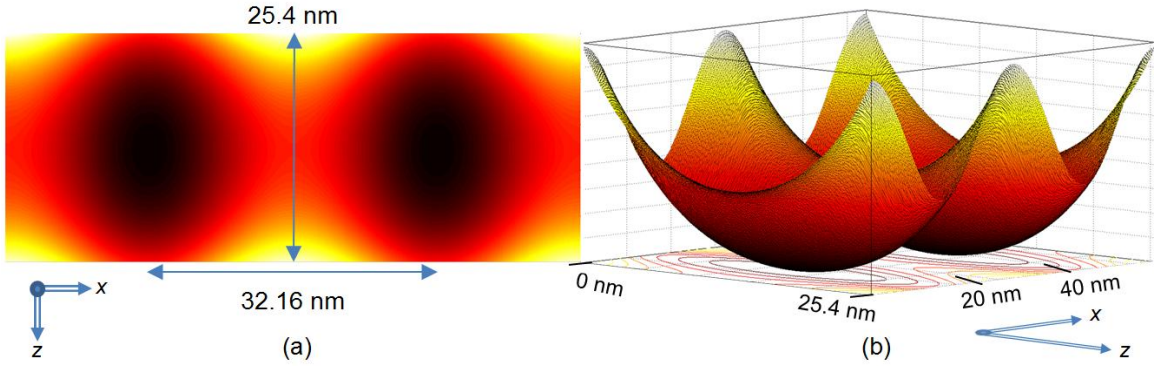

Figure 6-6 - EIL in photoresist at λ= 193 nm, *NA* = 3 with TM polarized light with a reflective metal underlay and using $\boldsymbol{f}$ = 1 so that the maximum point along the null is at least as low as the minimum point along the peak. Image half-pitch – 16.08 nm and depth of 25.4 nm giving an aspect ratio of 1.58

Finally, for the $f = 2$ case, constraint 2 becomes the dominant one. Figure 6-7 illustrates that the minima of the interference pattern are now deeper, but this is at the expense of a lower image depth (19.3 nm) than that in Figure 6-6. A reflection r_{23} of 4.73 is needed and a metal $\varepsilon_3 = -7.22$ is required to achieve this. The aspect ratio for this case also lowers to ~ 1.2.

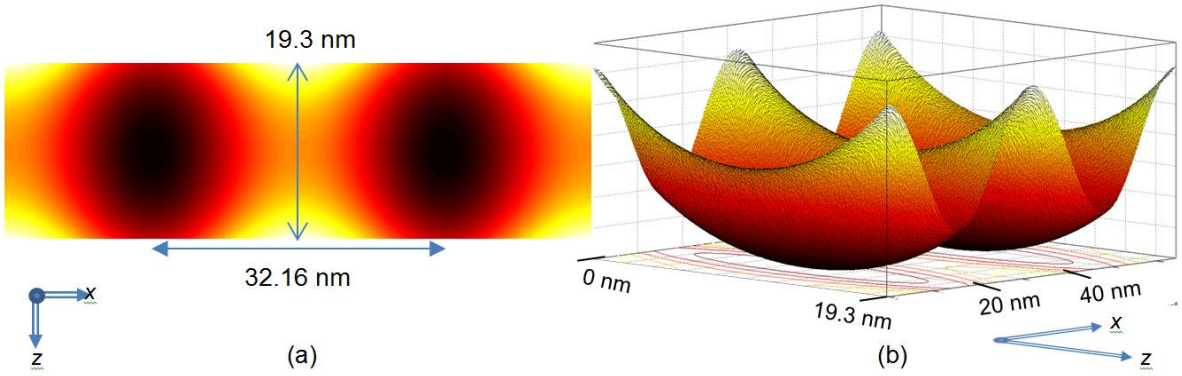

Figure 6-7 - EIL in photoresist at λ= 193 nm, *NA* = 3 with TM polarized light with a reflective metal underlay and using $\boldsymbol{f}$ = 2 so that the maximum point along the null is at least twice as low as the minimum point along the peak. Image half-pitch – 16.08 nm and depth of 19.3 nm giving an aspect ratio of 1.2

This process may be continued further by increasing f. This will allow an even higher contrast but at the expense of a lower image aspect ratio. The key result from this section is that it proves that EIL imaging may be carried out with TM polarized light when a carefully chosen reflective substrate is employed as this helps in considerably boosting the maxima to minima ratio. At very high *NA*s however, the aspect ratio may need to be traded off in order to improve the quality of the interference minima (nulls). This

trade-off may then defeat the purpose of enhanced EIL imaging. This problem is local to the TM polarization of light and does not have to be dealt with the TE polarization of light. Without the use of a carefully chosen/designed underlay, the TM evanescent wave shows little promise in EIL imaging as is evident when Figure 6-2 and Figure 6-5 are compared with each other.

A mathematical tool is introduced at this stage to deal with the problem of evanescent wave enhancements that may be possible if the underlay was to be composed of an arbitrary multi-layered stack as opposed to the single semi-infinite media stack that have been thus far discussed. The tool also allows the effective realization of non-naturally occurring materials, such as the gain material that has been introduced in Chapter 5 and shown to enhance the performance of evanescent interference imaging in section 6.2.3.

6.4 ERA - Equivalent Reflectance Approach

The above discussion has yet been limited to semi-infinite homogenous slabs of materials. However it does beg the question whether there are possible multilayer scenarios which may allow for further enhancements. To answer these questions and shed light on the unconventional results (regarding gain media), a tool that we call ERA is introduced here, it is a variant of effective medium theory for thin film multilayers (see [182]). The end result will be to aim for a solution that allows the reflectivity to be larger than one. Of particular interest is the TE polarized solution as this allows perfect nulls and thereby higher aspect ratios when enhanced EIL is carried out. However, the ERA is not limited to only TE solutions and applies just as well to the TM case.

ERA states that any stack of underlying one-dimensional (1-D) materials that have a positive or zero absorbance (i.e. non-gain materials) except for the bottom most semi-infinite material in the stack that may have a negative absorbance (i.e. gain), may all be replaced with a single semi-infinite slab of homogenous material for a specific NA at a specific wavelength that will provide the same reflectance as the original stack. The equivalent reflection homogenous material may even have a negative absorbance (i.e. gain). ERA is derived only for non-magnetic materials. The stack is also assumed to be infinite in spatial extent.

Firstly let us review what it is that needs to be proven. Consider the stack in Figure 6-8(a), the aim is to find the material ε_r that gives an equivalent reflection at the particular *NA* and wavelength Figure 6-8(b). The first proof requires showing that for a fixed numerical aperture at a certain wavelength, this is always possible.

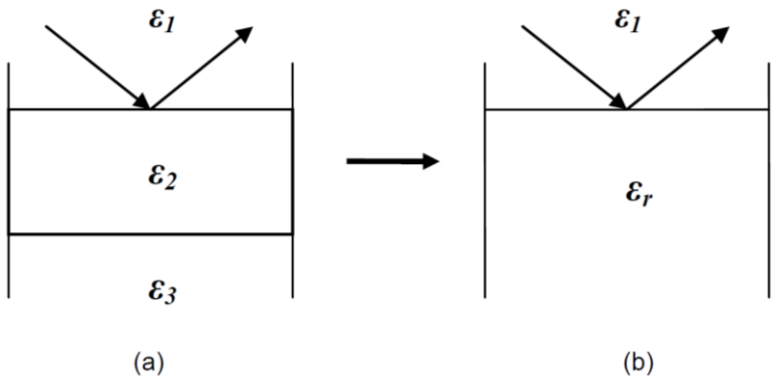

Figure 6-8 - Transformation of 1D stack to Equivalent reflectance material

The T-Matrix technique that is based on satisfying Maxwell's relations at material boundaries is described in Chapter 4 and has been heavily used in the analysis that follows. Some parts are re-iterated here to aid the analysis as this avoids back references to Chapter 4.

The E-fields at the interface between two materials as shown in Figure 6-9 for TM polarized light are then described by (6.55) - (6.57).

$$\begin{bmatrix} E_3 \\ E_4 \end{bmatrix} = \frac{1}{2} * \begin{bmatrix} \frac{\sqrt{\varepsilon_1}}{\sqrt{\varepsilon_2}} + \frac{k_{z,1}\sqrt{\varepsilon_2}}{k_{z,2}\sqrt{\varepsilon_1}} & \frac{\sqrt{\varepsilon_1}}{\sqrt{\varepsilon_2}} - \frac{k_{z,1}\sqrt{\varepsilon_2}}{k_{z,2}\sqrt{\varepsilon_1}} \\ \frac{\sqrt{\varepsilon_1}}{\sqrt{\varepsilon_2}} - \frac{k_{z,1}\sqrt{\varepsilon_2}}{k_{z,2}\sqrt{\varepsilon_1}} & \frac{\sqrt{\varepsilon_1}}{\sqrt{\varepsilon_2}} + \frac{k_{z,1}\sqrt{\varepsilon_2}}{k_{z,2}\sqrt{\varepsilon_1}} \end{bmatrix} \begin{bmatrix} E_1 \\ E_2 \end{bmatrix} \tag{6.55}$$

$$\begin{bmatrix} E_5 \\ E_6 \end{bmatrix} = \begin{bmatrix} e^{ik_{z,2}d} & 0 \\ 0 & e^{-ik_{z,2}d} \end{bmatrix} \begin{bmatrix} E_3 \\ E_4 \end{bmatrix} \tag{6.56}$$

$$\begin{bmatrix} E_7 \\ E_8 \end{bmatrix} = \frac{1}{2} * \begin{bmatrix} \frac{\sqrt{\varepsilon_2}}{\sqrt{\varepsilon_3}} + \frac{k_{z,2}\sqrt{\varepsilon_3}}{k_{z,3}\sqrt{\varepsilon_2}} & \frac{\sqrt{\varepsilon_2}}{\sqrt{\varepsilon_3}} - \frac{k_{z,2}\sqrt{\varepsilon_3}}{k_{z,3}\sqrt{\varepsilon_2}} \\ \frac{\sqrt{\varepsilon_2}}{\sqrt{\varepsilon_3}} - \frac{k_{z,2}\sqrt{\varepsilon_3}}{k_{z,3}\sqrt{\varepsilon_2}} & \frac{\sqrt{\varepsilon_2}}{\sqrt{\varepsilon_3}} + \frac{k_{z,2}\sqrt{\varepsilon_3}}{k_{z,3}\sqrt{\varepsilon_2}} \end{bmatrix} \begin{bmatrix} E_5 \\ E_6 \end{bmatrix} \tag{6.57}$$

Equation (6.56) takes into account the phase of fields as they evolve over distance.

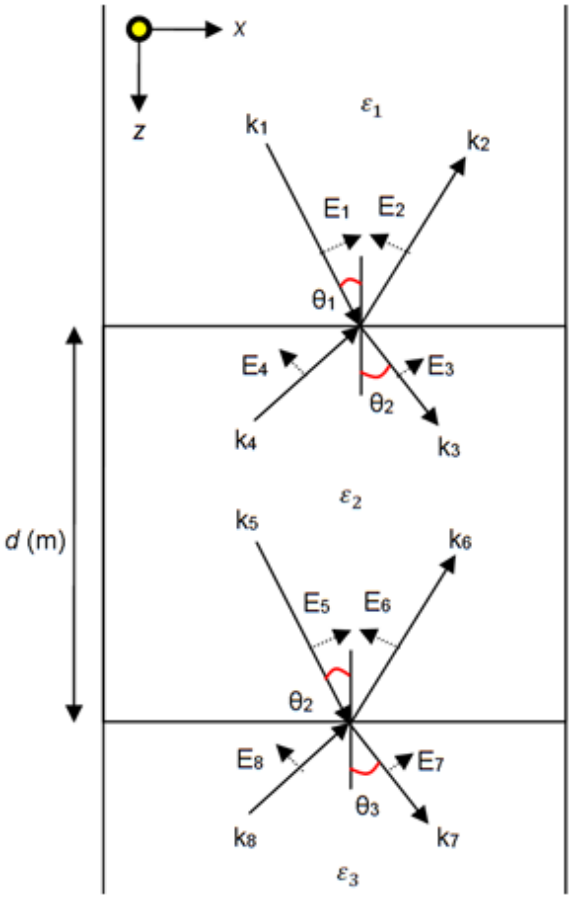

Figure 6-9 - T-Matrix technique fundamentals – Above is a three layer (ε_1-ε_2-ε_3) homogenous optical stack excited by a transverse magnetic (TM) polarized wave k_1

and so,

$$\begin{bmatrix} E_7 \\ E_8 \end{bmatrix} = [T] \begin{bmatrix} E_1 \\ E_2 \end{bmatrix} \tag{6.58}$$

where,

$$T = \begin{bmatrix} T_{11} & T_{12} \\ T_{21} & T_{22} \end{bmatrix} \tag{6.59}$$

The reflection coefficient for the *T* matrix technique is given as

$$r = \frac{E_2}{E_1} = -\frac{T_{21}}{T_{22}} \tag{6.60}$$

Combining (6.55)-(6.58), the values of T_{21} and T_{22} are obtained to be,

$$\mathrm{T}_{21} = \frac{1}{4}\left[e^{ik_{z,2}d}\left(\frac{\sqrt{\varepsilon_2}}{\sqrt{\varepsilon_3}} - \frac{k_{z,2}\sqrt{\varepsilon_3}}{k_{z,3}\sqrt{\varepsilon_2}}\right)\left(\frac{\sqrt{\varepsilon_1}}{\sqrt{\varepsilon_2}} + \frac{k_{z,1}\sqrt{\varepsilon_2}}{k_{z,2}\sqrt{\varepsilon_1}}\right)\right.$$
$$\left. + \; e^{-ik_{z,2}d}\left(\frac{\sqrt{\varepsilon_2}}{\sqrt{\varepsilon_3}} + \frac{k_{z,2}\sqrt{\varepsilon_3}}{k_{z,3}\sqrt{\varepsilon_2}}\right)\left(\frac{\sqrt{\varepsilon_1}}{\sqrt{\varepsilon_2}} - \frac{k_{z,1}\sqrt{\varepsilon_2}}{k_{z,2}\sqrt{\varepsilon_1}}\right)\right] \tag{6.61}$$

$$\mathrm{T}_{22} = \frac{1}{4}\left[e^{ik_{z,2}d}\left(\frac{\sqrt{\varepsilon_2}}{\sqrt{\varepsilon_3}} - \frac{k_{z,2}\sqrt{\varepsilon_3}}{k_{z,3}\sqrt{\varepsilon_2}}\right)\left(\frac{\sqrt{\varepsilon_1}}{\sqrt{\varepsilon_2}} - \frac{k_{z,1}\sqrt{\varepsilon_2}}{k_{z,2}\sqrt{\varepsilon_1}}\right)\right.$$
$$\left. + \; e^{-ik_{z,2}d}\left(\frac{\sqrt{\varepsilon_2}}{\sqrt{\varepsilon_3}} + \frac{k_{z,2}\sqrt{\varepsilon_3}}{k_{z,3}\sqrt{\varepsilon_2}}\right)\left(\frac{\sqrt{\varepsilon_1}}{\sqrt{\varepsilon_2}} + \frac{k_{z,1}\sqrt{\varepsilon_2}}{k_{z,2}\sqrt{\varepsilon_1}}\right)\right] \tag{6.62}$$

Let us define the terms that make up T_{21} and T_{22}, as *A*, *B*, *C*, *D*, *E*, *F* and *G* before beginning the proof,

$$A = \; e^{ik_{z,2}d}\frac{\sqrt{\varepsilon_1}}{\sqrt{\varepsilon_3}}$$
$$B = \; e^{ik_{z,2}d}\frac{k_{z,1}\varepsilon_2}{k_{z,2}\sqrt{\varepsilon_1\varepsilon_3}}$$
$$C = \; e^{ik_{z,2}d}\frac{k_{z,2}\sqrt{\varepsilon_1\varepsilon_3}}{k_{z,3}\varepsilon_2}$$
$$D = \; e^{ik_{z,2}d}\frac{k_{z,1}\sqrt{\varepsilon_3}}{k_{z,3}\sqrt{\varepsilon_1}}$$
$$E = \; e^{-ik_{z,2}d}\frac{\sqrt{\varepsilon_1}}{\sqrt{\varepsilon_3}} \tag{6.63}$$
$$F = \; e^{-ik_{z,2}d}\frac{k_{z,1}\varepsilon_2}{k_{z,2}\sqrt{\varepsilon_1\varepsilon_3}}$$
$$G = \; e^{-ik_{z,2}d}\frac{k_{z,2}\sqrt{\varepsilon_1\varepsilon_3}}{k_{z,3}\varepsilon_2}$$
$$H = \; e^{-ik_{z,2}d}\frac{k_{z,1}\sqrt{\varepsilon_3}}{k_{z,3}\sqrt{\varepsilon_1}}$$

6.4.1 Proof 1 – Replacing a multilayered stack with an equivalent reflectance medium

Now let us prove that the multilayered stack may indeed be replaced with a single semi-infinite medium that provides the same reflectance, under specific conditions. For this, T_{21}/T_{22} from (6.60) is written in the form of a difference of terms divided by a sum of terms,

$$\frac{T_{21}}{T_{22}} = \frac{(A+E+G-C) - (D+F+H-B)}{(A+E+G-C) + (D+F+H-B)} \tag{6.64}$$

Next, use (6.55), replace E_4 with 0 and instead of ε_2, use ε_r to denote the equivalent reflectance medium that needs to be found. Then the Fresnel reflection equation (see column 1 of Table 5.2, Chapter 5) between ε_1 and ε_r may be rearranged to result in an equation that mimics the arrangement of some equivalent unknown T parameters (6.65). Our goal is to then equate (6.64) and (6.65) and solve to obtain the value of ε_r.

$$\frac{T_{\text{Equivalent }21}}{T_{\text{Equivalent }22}} = \frac{\frac{\sqrt{\varepsilon_1}}{\sqrt{\varepsilon_r}} - \frac{k_{z,1}\sqrt{\varepsilon_r}}{k_{z,r}\sqrt{\varepsilon_1}}}{\frac{\sqrt{\varepsilon_1}}{\sqrt{\varepsilon_r}} + \frac{k_{z,1}\sqrt{\varepsilon_r}}{k_{z,r}\sqrt{\varepsilon_1}}} \tag{6.65}$$

The primary goal for this proof is to show that (6.64) = (6.65) or equivalently

$$-\frac{T_{21}}{T_{22}} = -\frac{T_{\text{Equivalent }21}}{T_{\text{Equivalent }22}} \tag{6.66}$$

so that the reflection from the stack of Figure 6-8 (a) equals the reflection from the stack of Figure 6-8 (b). For the proof to work the following relationships are needed,

$$\begin{aligned} (A+E+G-C) &= s * \frac{\sqrt{\varepsilon_1}}{\sqrt{\varepsilon_r}} \\ (D+F+H-B) &= s * \frac{k_{z,1}}{k_{z,r}}\frac{\sqrt{\varepsilon_r}}{\sqrt{\varepsilon_1}} \end{aligned} \tag{6.67}$$

where s is introduced as an arbitrary scaling factor. From equations (6.67) we can obtain,

$$\frac{(D+F+H-B)}{(A+E+G-C)}\frac{\varepsilon_1}{k_{z,1}} = \frac{\varepsilon_r}{k_{z,r}} \; or \; \frac{\varepsilon_r}{k_0\sqrt{\varepsilon_r - NA^2}} \tag{6.68}$$

Of course, the L.H.S of (6.68) may be equal to any value (any optical stack may be chosen), i.e. it may be

equal to any complex number. It then follows on that it needs to be proved that the R.H.S of (6.68) is also capable of such a feat by variation of ε_r. If this is possible then the desired proof has been reached. Let us do that now, by proving (6.69) i.e. that the R.H.S of (6.68) maybe written as a complex number p/q.

$$\frac{\varepsilon_r}{k_0\sqrt{\varepsilon_r - NA^2}} = \frac{p}{q} = \frac{s*p}{s*q} \tag{6.69}$$

where,

$$\begin{aligned} \varepsilon_r &= s*p \\ k_0\sqrt{\varepsilon_r - NA^2} &= s*q \end{aligned} \tag{6.70}$$

Equation (6.70) may then be used to create the quadratic

$$q^2s^2 - k_0^2ps + (k_0*NA)^2 = 0 \tag{6.71}$$

Since the scaling factor s may always be chosen to satisfy (6.71), the proof is complete and s is given as,

$$s = \frac{k_0^2p \pm \sqrt{(k_0^2p)^2 - 4q^2(k_0*NA)^2}}{2q^2} \tag{6.72}$$

Hence it can now be said that the reflectance of a two layer medium stack $(\varepsilon_2 - \varepsilon_3)$ such as the one depicted in Figure 6-8 (a) operating at a specific *NA* and wavelength may be replicated by an equivalent medium $\varepsilon_r = \varepsilon_r' + i\varepsilon_r''$. Using (6.64), it can be written that,

$$\frac{(D+F+H-B)}{(A+E+G-C)} = \frac{T_{22} - T_{21}}{T_{22} + T_{21}} \tag{6.73}$$

As a result (6.68) may be written as,

$$\frac{\varepsilon_r}{k_0\sqrt{\varepsilon_r - NA^2}} = \left(\frac{T_{22} - T_{21}}{T_{22} + T_{21}}\right)\frac{\varepsilon_1}{k_{z,1}} \tag{6.74}$$

The R.H.S of (6.74) is a known value and thus rearranging (6.74) gives a quadratic, which upon solving gives (6.75) where one or both roots may be correct.

$$\varepsilon_r = \frac{-b \pm \sqrt{b^2 + 4 * b * (NA)^2}}{2}$$

where,

$$b = -\left(k_0 \frac{\varepsilon_1}{k_{z,1}} \frac{\mathrm{T}_{22} - \mathrm{T}_{21}}{\mathrm{T}_{22} + \mathrm{T}_{21}}\right)^2 \tag{6.75}$$

Now, the proof extends itself easily to a multilayered setup by recursion. Consider an n-layered medium, the n^{th} layer of which is a semi-infinite slab. Then, both the n^{th} and $(n-1)^{th}$ layers may be replaced by a single semi-infinite medium using the method shown above. This process carried out a total of n-1 times leaves the T_{21} and T_{22} parameters of the system unchanged and thereby replaces the n-1 layers with a single semi-infinite layer that gives an equivalent reflectance. Hence, by determining the T matrix for a particular multilayered stack and using (6.75), the medium providing the equivalent reflectance may be easily found.

The proof for the TE is case follows the same process but is much simpler. Hence, only the result of this derivation is presented here,

$$\varepsilon_r(TE) = \left(\frac{1}{k_0} \frac{T_{21} + T_{22}}{T_{21} - T_{22}} k_{z,1}\right)^2 + NA^2 \tag{6.76}$$

The E-field at the interfaces for the TE case are related as

$$\begin{bmatrix} E_3 \\ E_4 \end{bmatrix} = \frac{1}{2} * \begin{bmatrix} 1 + \frac{k_{z,1}}{k_{z,2}} & 1 - \frac{k_{z,1}}{k_{z,2}} \\ 1 - \frac{k_{z,1}}{k_{z,2}} & 1 + \frac{k_{z,1}}{k_{z,2}} \end{bmatrix} \begin{bmatrix} E_1 \\ E_2 \end{bmatrix} \tag{6.77}$$

The phase evolution relationship is the same as that given by (6.56).

6.4.2 Proof 2 – Replacing a single semi-infinite medium with a multilayered medium – The converse proof

Next, the goal is to prove that the converse of the previous proof is also true, in that any semi-infinite complex medium ε_r may be replaced with a multilayered setup to provide the same reflectance at a specific *NA* and wavelength (refer to Figure 6-8). This proof is a little trickier than the previous one but imperative to ERA because it is this that will allows us to realize the effective reflectance property of a

hypothetical gain medium as is detailed in the next section. Once again the TE scenario follows the same methodology, but is much simpler to derive; hence its derivation is also omitted.

It needs to be shown that the R.H.S of (6.68) may always be transformed into the L.H.S of (6.68), for any value of ε_r, and since the R.H.S of (6.68) may be written as any complex number, it needs to be shown that the L.H.S of (6.68) is also capable of such a feat.

For this the L.H.S of (6.68) is first simplified (working omitted) for a two layer system (i.e. a system that has a total of two layers below the first layer such as in the stack depicted in Figure 6-8 (a)). Refer to (6.63) for the terms A to H. Equation (6.68) is then rewritten as

$$\frac{(D+F+H-B)}{(A+E+G-C)}\frac{\varepsilon_1}{k_{z,1}} = \frac{\frac{\varepsilon_3}{k_{z,3}} - i\frac{\varepsilon_2}{k_{z,2}}\tan(k_{z,2}d_2)}{1 - i\frac{\varepsilon_3}{k_{z,3}}\frac{k_{z,2}}{\varepsilon_2}\tan(k_{z,2}d_2)} = \frac{\varepsilon_r}{k_0\sqrt{\varepsilon_r - NA^2}} = \psi \tag{6.78}$$

The term d_2 corresponds to the thickness of medium ε_2. As mentioned previously, the R.H.S of (6.68) may now be any complex number. We use ψ to represent this complex number. Let us make the following assignments to further simplify (6.78).

$$\begin{aligned} v &= \frac{\varepsilon_3}{k_{z,3}} \\ w &= -i\frac{\varepsilon_2}{k_{z,2}}\tan(k_{z,2}d_2) \\ u &= -i\frac{k_{z,2}}{\varepsilon_2}\tan(k_{z,2}d_2) \end{aligned} \tag{6.79}$$

Now let us select ψ as $f * \frac{w}{u}$, (note this is not the same f that was used in deriving the EIL imaging limits for TM) where f is a chosen complex scaling factor that when multiplied by $\frac{w}{u}$, yields ψ, then (6.78) may be written as (6.80),

$$\frac{v+w}{1+vu} = \psi = f\frac{w}{u} \tag{6.80}$$

The assumption is that the values for w and u have already been chosen (i.e. ε_2 and d_2 have been selected) and the value of v will be varied as necessary by selecting the appropriate value for ε_3. Solving (6.80) for v then yields,

$$v = \frac{w(f-u)}{u(1-fw)} \tag{6.81}$$

The question is whether v can in fact be made to be equal to the R.H.S of (6.81)?

However, we know that it is possible to satisfy this demand from (6.81) because v (given in (6.79)) is in the same form as (6.69) and using equations (6.69) to (6.72) we earlier proved that an equation of the form of (6.69) maybe written as any complex number.

Then expanding (6.81) by substituting the values of u v and w, yields v in terms of the other known parameters,

$$v = \frac{\varepsilon_3}{k_{z,3}} = \frac{i\varepsilon_r \frac{k_{z,2}}{\varepsilon_2}\tan(k_{z,2}d_2) - k_{z,r}(\tan(k_{z,2}d_2))^2}{ik_{z,r}\frac{k_{z,2}}{\varepsilon_2}\tan(k_{z,2}d_2) - \varepsilon_r\left(\frac{k_{z,2}}{\varepsilon_2}\tan(k_{z,2}d_2)\right)^2} \tag{6.82}$$

Since the R.H.S of (6.82) is made up of known parameters, all that needs to be done is to expand the L.H.S of (6.82) by making use of the identity, $k_{z,3} = k_0\sqrt{\varepsilon_3 - NA^2}$ and as a result create and solve a quadratic in ε_3 to determine the value of ε_3.

Thus we have been able to prove that what was needed to be proven. Once again, the proof extends to the multilayer system by recursion and consecutive layers may need to be employed in order to equate the reflectance that is available from ε_r.

The above analysis has shown us that a non-naturally occurring optical property such as a reflection or transmission may be effectively obtained by making use of a carefully designed multilayer. This is somewhat similar to the concept of a metamaterial where the careful structuring of naturally occurring materials results in an optical behavior that is not observed in nature.

6.5 Effective Gain Medium (EGM) & TE polarized light

In the analysis at the beginning of this chapter dealing with imaging limits, the reflection > 1 scenario seemed to be the most favorable as it allowed the greatest image depth for a particular *RIR*. In the previous chapter however, the Fresnel reflection equations were analyzed for the TE polarization of light and it was found that to achieve a reflection > 1, a gain medium was required, *i.e.* a medium that would exhibit a negative loss.

While this seems like a hypothetical solution, it actually holds information regarding a multilayer setup, which this chapter is now well equipped to deal with as ERA has been introduced. One way to create an effective gain medium (EGM) is in fact simply by stacking a high index dielectric on a low index dielectric as depicted in Figure 6-10. The high index on low index medium stack is an EGM using effective medium theory or ERA when the analysis is only concerned with the reflection at a particular *NA*.

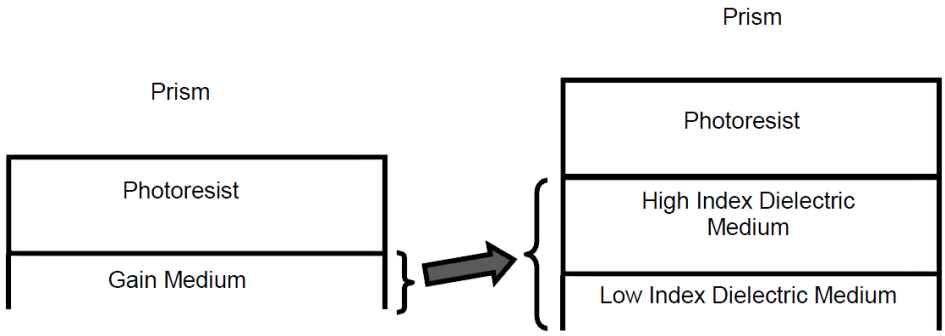

Figure 6-10 - Gain medium underlay required for evanescent wave enhancement with TE polarization

From an intuitive perspective this is not difficult to comprehend; the high index dielectric is capable of converting an evanescent wave to a propagating state. Moreover material choices and the thickness of the high index layer allow control over the particular wave vector that is resonated. Hence, the high index dielectric acts like a pseudo-interface to serve a similar purpose to the photoresist-metal interface considered earlier. The low-index dielectric cannot support a propagating mode of the wave causing it to be evanescent, thus serving a similar purpose to the bulk of the metal which also cannot allow a propagating wave to exist. Figure 6-11 illustrates and summarizes this paragraph.

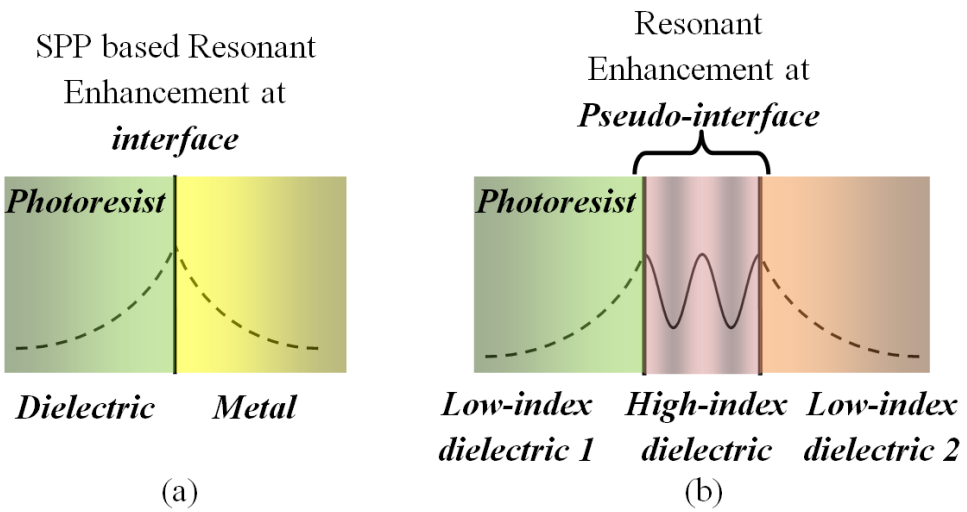

Figure 6-11 - Evanescent wave enhancement (a) at a metal-dielectric interface through SPP resonance, and (b) at a pseudo-interface formed by sandwiching a high index dielectric between two low-index dielectrics.

Naturally, it would be beneficial to take advantage of this phenomenon at the industry standard λ = 193 nm. Smith *et al*. [34, 139, 146-148, 150] have published several papers stating the use of their solid-immersion interference lithography system also known as the Amphibian to allow imaging at a *NA* as high as 1.85. They have used a sapphire prism with a refractive index of n = 1.92 and taken precautions to ensure any effects of birefringence were minimal. Now that the material properties required are understood, let us investigate how such a system may be built to be optimal and also allow practical evanescent wave enhancement via resonance for a *NA* of 1.85 at λ = 193 nm.

6.5.1 Feasible Design Proposal at λ = 193 nm

Consider a thin film (layer 3) placed between the resist and a semi-infinite substrate (layer 4). The reflectivity between the resist and the film stack, let us call this new reflectivity ρ_{234}, will be

$$\rho_{234} = \frac{\rho_{23} + \rho_{34}\tau_{D3}^2}{1 + \rho_{23}\rho_{34}\tau_{D3}^2} \tag{6.83}$$

An infinite reflectivity can be obtained if $\rho_{23}\rho_{34}\tau_{D3}^2 = -1$. This requires first that $\left|\tau_{D3}^2\right| = 1$, so that layer 3 must be non-absorbing and must be operating in a propagating (not evanescent) regime, *i.e.* $n_3 > NA$. Further, it is required that $\left|\rho_{23}\rho_{34}\right| = 1$. We have, $n_2 < NA$ as before and thus the resist is in the evanescent

regime, once again assuming weakly absorbing resist. If the substrate is also non-absorbing and in the evanescent regime, $n_4 < NA$, the resulting reflectivity product is

$$\rho_{23}\rho_{34} = \left(\frac{i\eta_{2I} - \eta_{3R}}{i\eta_{2I} + \eta_{3R}}\right)\left(\frac{\eta_{3R} - i\eta_{4I}}{\eta_{3R} + i\eta_{4I}}\right) = \frac{\left(\eta_{2I}\eta_{4I} - \eta_{3R}^2\right) + i\eta_{3R}\left(\eta_{2I} + \eta_{4I}\right)}{-\left(\eta_{2I}\eta_{4I} - \eta_{3R}^2\right) + i\eta_{3R}\left(\eta_{2I} + \eta_{4I}\right)} \tag{6.84}$$

One can see that this does indeed have a magnitude of 1. Since the phase of τ_{D3}^2 can be adjusted to any value by changing the thickness of layer 3, it is possible to make $\rho_{23}\rho_{34}\tau_{D3}^2 = -1$ and the overall reflectivity go to infinity.

As a special case, consider $\eta_{3R} = \sqrt{\eta_{2I}\eta_{4I}}$. Putting this value into equation (6.84) gives $\rho_{23}\rho_{34} = 1$. Infinite reflectivity is obtained when $\tau_{D3}^2 = -1$, or when $D_3 = \lambda / 4\eta_{3R}$. Interestingly, these equations are identical in form to the conditions required to make a perfectly transmitting antireflection coating in the propagating regime. In the evanescent regime, they produce an infinite reflector.

The goal is not to make an infinite reflector, but one with the optimum reflectance. As discussed in section 6.2, the reflectivity needs to be

$$\rho_{234} \approx e^{\alpha_e D/2} \tag{6.85}$$

This film stack reflectivity (ρ_{234}) will have zero phase when $\tau_{D3}^2 = -1$, giving

$$\rho_{234} = \frac{\eta_{2I}\eta_{4I} + \eta_{3R}^2}{\eta_{2I}\eta_{4I} - \eta_{3R}^2} \tag{6.86}$$

If η_{3R} were adjusted to give the optimum reflectivity, the result would be

$$\eta_{3R} = \sqrt{\eta_{2I}\eta_{4I}\left(\frac{\rho_{234} - 1}{\rho_{234} + 1}\right)} \tag{6.87}$$

For example, if one allowed $\alpha_e D$ = 4, the optimum reflectivity would be, from Eq. (17), $\rho_{234} \approx 7.39$. If NA = 1.85, n_2 = 1.7 and n_4 = 1.56 (e.g. SiO_2 at λ = 193 nm), the resulting η_{3R} for layer 3 would be 0.743, requiring an index of refraction of n_3 = 1.9938 and a thickness of 65 nm, while the resist thickness would be 82.5 nm. In reality, all materials with the required optical properties may not be available. Hence a real world design is presented here with some modifications. Figure 6-12 (a) illustrates imaging of 26-nm

features where the image depth is only 20 nm in an infinitely thick photoresist. Figure 6-12 (b) illustrates the significant enhancement when a tuned stack of 43 nm layer of Al_2O_3 (sapphire) with index n_3 = 2.08 [175] upon ~50nm SiO_2 with index n_4 = 1.56 is used. The resulting image is 82.5 nm deep. The photoresist loss is included in this design (so that n_2 = 1.7 + 0.02i) and the new reflection from the real world stack is $\sim 6.77\, e^{i0.212}$ instead of the optimum 7.39 however still allowing ultra-high *NA* patterning at an aspect ratio of ~3.2.

Note that there are three adjustable parameters in the evanescent mirror film stack: n_3, D_3, and n_4. To achieve the desired phase and magnitude of the reflectivity, only two adjustments are required. Thus, there will be a family of solutions, making practical implementation easier.

The use of this method of evanescent field enhancement together with the Amphibian imaging system should allow feasible patterning of 26 nm (half-pitch) features with aspect ratios as high as 3.2.

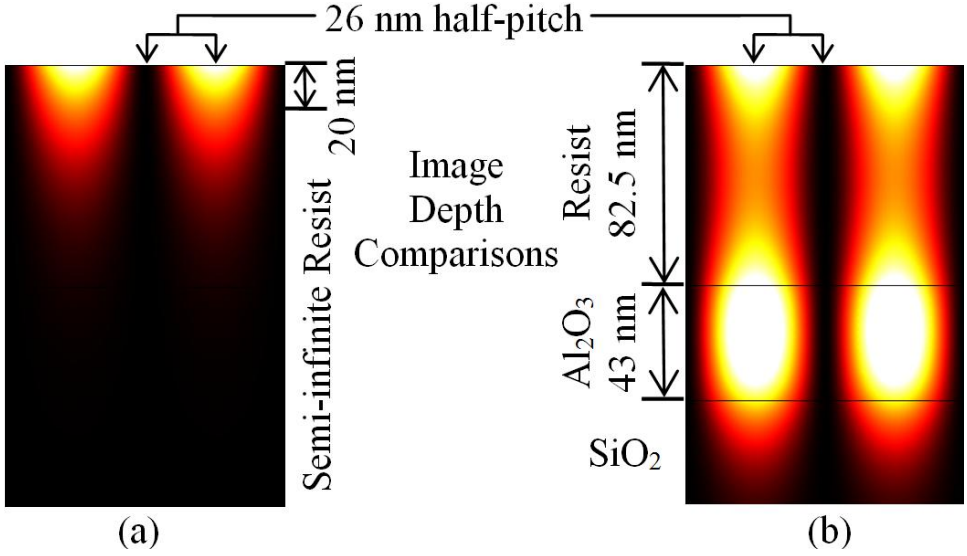

Figure 6-12 - Imaging of 26-nm (half-pitch) evanescent features into (a) semi-infinite lossy resist giving 20-nm image depth, and (b) 82.5 nm thick lossy resist on an effective gain medium made up of 43 nm of Al_2O_3 (Sapphire) on SiO_2, giving an image depth of 82.5 nm.

Clearly, the proposed design fairs well in comparison to the existing technique, a fourfold increase in the image depth is visible. Here the analysis has ensured that the image is symmetric and that the minimum intensity of the interference maxima is never below 40% of the peak intensity (i.e. *RIR* = 2.5), these requirements were laid down in section 6.2. SiO_2 in its fused silica form has a refractive index of ~1.56 [183]. Other values have also been reported. An alternative to SiO_2 is MgF_2 that has an index of 1.6. We believe that a 50 nm SiO_2 on any substrate to should be sufficiently thick. The refractive index of Al_2O_3 is ~2.08 as reported by [175], where electron beam evaporation was used for deposition on fused silica.

Other values have also been reported elsewhere, however these are all greater than the *NA* of 1.85 and so still allow resonant enhancement. It is important to note that an Al_2O_3 thin film is the only material that we know of with transparency and such a high refractive index available at $\lambda = 193$ nm. In its crystalline form, Al_2O_3 is more commonly known as Sapphire, the prism material used to generate the evanescent wave vector in the first place. This is interesting and suggests that given a high index prism material to excite a certain *NA*, the material itself may be deposited to bring the particular wave vector into resonance. Hence, the above technique may be utilized to image at any *NA* as was proven in section 6.2.3 provided the prism material is available.

6.6 Effective Gain Medium (EGM) with TM light – An Interesting Note

This chapter is concluded with an interesting note regarding possible methods to create an EGM when using the TM polarization of light. Although, the previous section suggested the use of a high index on low index dielectric stack to resonant evanescent images, an EGM may also in fact be created by stacking a variety of materials to tailor the required response. For example a layer of silver deposited upon hafnium oxide deposited upon molybdenum acts to provide an EGM response, even though the workings of the enhancement here is not limited to any one particular naturally occurring surface state but is an aggregate of several surface states. The use of a stack of several materials allows us to tune to a reflectance that cannot have been achieved with either material individually.

Of course, such a composite surface state is only useful for very high numerical apertures at which materials with a sufficiently high refractive index do not exist to resonate the wave vectors. However, this might be an interesting approach to image *NA*s as high as 3 if one discovers alternative methods to create such wave vectors, for example by coupling with a multilayered grating that achieves a high quality factor for the desired *NA*.

6.7 Summary

The limits of EIL imaging with TE and TM have been analyzed in detail and compared with one another. The analysis suggests that no limit exists for TE EIL, as long as a limiting aspect ratio of 1.3 is acceptable. For TM however, interference maxima to minima ratio of only 2, results in an aspect ratio limit of 0.838, which is considerably lower. A higher maxima to minima ratio would be desirable to further improve contrast, but this would only worsen the aspect ratio limit even further. An example is presented and modeling was carried out using the T-Matrix method to compare the performance of TE and TM at a *NA* of 3. It was found that while it may still be possible to make use of TM, the aspect ratio is

lower as one would expect. Once again an interference maxima to minima ratio of only 2 was used for the TM case, whereas the TE case exhibited perfect nulls (corresponding to a maxima to minima ratio of ∞).

It was noted that the greatest image depth is achievable when the reflection from an underlying substrate is tunable to a value larger than one. Not surprisingly, this was chosen as the case to proceed with. For the TE case however, a reflection greater than unity is only obtainable when the underlying substrate is a gain medium.

The equivalent reflectance approach (ERA) was then presented and an interesting result was that a multilayered setup may in fact act like a gain medium in that it may offer a reflectivity larger than unity. We term this an effective gain medium. A dielectric waveguide type multilayered stack was then presented which resonated the evanescent wave vector inside a high index dielectric sandwiched by low-index dielectrics. This sufficed as an effective gain medium as the underlay allowed the creation of a pseudo-interface at which evanescent enhancement took place. Further analysis was presented and used to determine optimal operating conditions and film thickness and indices requires for EIL at λ = 193 nm at a *NA* of 1.85 .Using this a design proposal was made for feasible EIL with TE light at λ = 193 nm at a *NA* of 1.85 by employing aluminum oxide as the high index dielectric on a thin film of silicon dioxide. In the next chapter experimental demonstration of an enhancement similar to the one above is presented, at a wavelength λ = 405 nm. In addition, a considerable amount of simulations are used to back the experimental results, these are also used to demonstrate a range of allowable real world solutions to obtain a high quality image using hafnium oxide as the high index dielectric and silicon dioxide as the low index dielectric to create the effective gain medium.

Chapter 7. High Aspect Ratio Patterning using Resonant Reflectors

In this chapter, the use of SILMIL is demonstrated (see Chapter 3) in conjunction with the theory developed in the preceding two chapters to experimentally demonstrate high aspect ratio evanescent interference lithography. While the analysis in the previous chapters suggested more than one way to store energy in a surface state via evanescent coupling and use this for evanescent interference lithography, in this chapter the focus is on the waveguide effective gain medium (EGM) approach which is the simplest and best option as it is perhaps the most applicable to industry and other researchers, it allows the use of existing TE systems and readily available materials to image very high aspect ratio structures at ultra-high-*NA*s. The contrast variation issue that one would face with the TM polarization of light is also avoided.

The waveguide EGM consists of a high index dielectric deposited upon a low index dielectric. When such an arrangement is placed under the photoresist, it couples to the evanescent image and while Maxwell's equations provide us with the necessary E-field profiles and intensities, it is not immediately obvious from them that it takes the stack a finite amount of time to establish fields and facilitate energy extraction from the incident beams, followed by the storage of this energy and its return into the photoresist.

The enhancements are presented using this approach and compared with solid immersion evanescent interference lithography as demonstrated in Chapter 3. To facilitate comparison and get the concept across in a clear manner, an extensive case study is carried out for a *NA* of 1.824 (as in Chapter 3). The chapter begins by describing the optical stack that has been used for experiments and simulations, as this is different from the optical stack used in Chapter 3. The relevant material properties and preparation steps are presented. This is followed by the description of the attenuated reflectance (ATR) method to characterize the optical property of a stack that is used later. A metric is defined for the qualification of an evanescent image.

A first example is then presented depicting the allowable operating region for a particular unintentionally ill-designed effective gain medium (EGM) underlay using the qualifying metric. A method is suggested and experimentally verified to resonance compensate for this ill-design and it is shown how such a

compensation helps to also considerably enhance the allowable operating region with respect to variation in the optical properties of media. The before and after allowable operating regions are computed using a multi-variable parametric search in the T-Matrix implementation (see Chapter 4) in MATLAB. A second example is then presented to demonstrate the imaging capability of a suitable EGM underlay. Modeling and simulations are carried out using the T-Matrix method and COMSOL. This is followed by presentation of experimental results that demonstrate EIL using SILMIL with the use of the suitably designed EGM underlays giving considerably enhanced image depths compared with those obtained in Chapter 3. A third case is then presented to illustrate how a stack that is not completely unsuitable, but results in reduced evanescent coupling, may be used with thinner resist to achieve a lower image depth.

Finally, effects of exposure dosage variation are carried out on another EGM as was done in Chapter 3 and the results are discussed. That chapter concludes with a summary highlighting the key results of simulations and experiments.

Details of the setup, experiments, system behavior and innovative work around are presented so that another researcher may replicate results and avoid common pitfalls.

7.1 Optical Stack

The constituents, preparation and characteristics of the optical stack are detailed here. The SILMIL stack was introduced in Chapter 3 and the top three layers of the stack consisting of IML, PVA and photoresist were also discussed. Here, the stack is modified by placing an EGM beneath a finite thickness photoresist layer as depicted in the schematic of Figure 7-1. The EGM consists of a thin film of hafnium oxide deposited upon a quartz substrate.

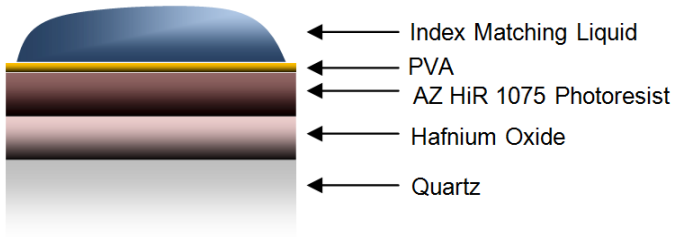

Figure 7-1 – Schematic of stack used for Experiments

Hafnium Oxide (HfO) is a homogenous high index thin film material that is transmissive at $\lambda = 405$ nm, the wavelength of interest. Silicon Dioxide (SiO_2), in comparison has a considerably lower refractive index at $\lambda = 405$ nm. The purpose of such a stack is to allow control of the enhancement of intensity of an evanescent wave vector. The details of such an enhancement have been discussed extensively in the

preceeding chapters. The optical properties of various materials, some of which are referred to in this chapter are presented in Table 1 in Chapter 3, and also reprinted here for ease of reading.

Table 7.1 - Optical properties of several materials discussed in the thesis (*Reprinted*)

Optical properties of various media			
Material	**Refractive Index/Optical Property**	**Thickness**	**Reference**
Yttrium Aluminum Garnet prism	n = 1.856 @ λ = 405 nm	Not applicable	[170]
Index Matching Liquid (Cargille, Series B 17000)	n = 1.7714 @ λ = 404.7 nm	Few drops	[171]
Poly-vinyl Alcohol	n ~1.5 @ λ = 405 nm	12 nm with Silicon substrate. 24 nm with Quartz substrate	[172]
Photoresist	*AZ HiR 1075* – n = 1.682+0.031i @ λ = 405 nm *Industry standard* - n = 1.7 + 0.02i @ λ = 193 nm	Controlled & Varies with experiment	[173]
SiO_2/Quartz	n = 1.47 @ λ = 405 nm		[174]
Hafnium Oxide (HfO) (RF target)	n ~2 *(varies)* @ λ = 405 nm		Measured with ATR
Aluminum Oxide	n ~2.08 (film), n ~1.92 (prism) @ λ = 193 nm		[139, 175]
Poly (methyl methacrylate) PMMA	n = 1.517 + 0.0005*1i @ λ = 405 nm		[176]
Silicon	n = 5.42 + 0.329i @ λ = 405 nm	Semi-infinite	[174]

7.2 Hafnium Oxide & Silicon Dioxide

There were two methods of HfO deposition available to us, namely radio frequency (RF) sputtering of a 3 inch solid target and electron beam deposition of HfO pellets. The RF sputtering method was chosen as it was found that this resulted in films with a generally higher refractive index than those deposited using electron beam deposition. As a quick comparison, RF sputtering generally tended to produce films with a refractive index of ~1.92 at λ = 632.8 nm, as measured using ellipsometry, while the electron beam method produced films with an index of ~1.88 and even as low as ~1.768. Figure 7-2 depicts the HeNe, λ = 632.8 nm ellipsometer that was used. A low index film requires a greater thickness, which in turn requires a larger deposition time. Colleagues have also suggested that thin films of most materials deposited using the electron beam method are generally found to be more porous and more easily scratch-able than RF sputtered films. This indicates adherence issues and possibly the presence of vacuum or air gaps between grains of the sputtered material, suggesting a possible explanation for a lower refractive index.

Figure 7-2 – HeNe (λ = 632.8 nm) Ellipsometer for thickness and index measurement

An Edwards sputtering system as pictured below in Figure 7-3 was used for RF sputtering. The Hafnium Oxide unbonded RF target was purchased from Kurt J. Lesker Ltd.

Figure 7-3 – Photograph of the Edwards system. The RF magnetron sputtering module was used to deposit thin films of HfO

The samples were cleaned with acetone and isopropanol (IPA) prior to deposition. As the color variation of the sample holder in Figure 7-4 suggests, there was a considerable difference in the sputtered beam distribution. For this reason, samples were placed at a precise location, a distance of 7.5 cm from the

centre of the sample holder for each deposition as depicted by Figure 7-4. Several films were deposited on silicon and quartz. Quartz served the purpose of an ideal semi-infinite silicon dioxide layer. The optical stack was characterized using the attenuated total reflectance method (ATR) as is discussed in a later section.

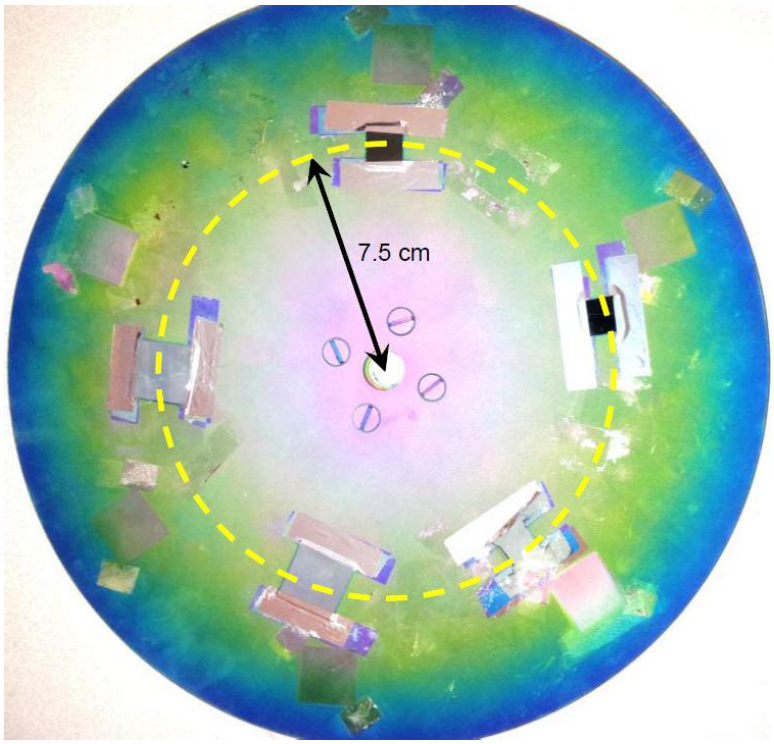

Figure 7-4 - Sample placement on the sputterer sample holder (7.5 cm from the centre)

The thickness and refractive index variation of the film as a function of distance from the center of the sample holder were measured for various deposition times to better understand the sputtered beam distribution. Measurements were made with a HeNe ellipsometer at $\lambda = 632.8$ nm (Figure 7-2). Not all of this data is provided here as a lot of it is immaterial to the focus of the subject matter that is to follow.

A constant vacuum pressure of 1.4×10^{-5} was achieved before the Argon plasma was initiated. An RF module was used to tune the desired recipe including power ramping from 0 Watts to 180 Watts in 30 minutes to prevent damage to the target. Sputtering was then carried out at 180 Watts for the desired amount of time and this was followed by a ramp down back to 0 Watts in 30 minutes. During deposition, the chamber pressure rose to 3.4×10^{-3} due to the presence of the Argon plasma.

It was later found that while an optical stack consisting of Quartz would allow proper evanescent interference lithography, it could cause charging drift when a cross-section of the sample is viewed under a scanning electron microscope (SEM). This effect can be considerably reduced if instead a thinner oxide

layer (~300 nm) was used as it would suffice to attenuate evanescent waves. Hence, a thermal oxide was grown on Si wafers. The plan was to utilize these SiO_2 on Si stacks as the substrates to grown HfO upon. However, during this period of time, there was significant equipment failure of the RF module in the sputterer; this resulted in non-uniform plasma during deposition time. This problem was worsened by the fact that the film thickness crystal monitor had also suffered significant failure and so depositions had to be carried out without any deposition rate feedback i.e. open loop. Attempts were made to make HfO thickness measurements as a function of deposition time under constant conditions. Not surprisingly, despite meticulous monitoring and adherence to all other constant deposition conditions, there was a large variation in the thicknesses and indices of HfO films that were deposited. The variation was significant enough to render several optical stacks useless. Unfortunately, the measurements suggested that in some cases, the average thickness achieved may deviate from the expected by as much as ~40 nm (or 30% for this instance). Figure 7-5 depicts several of our attempts to achieve a plot for the film thickness as a function of approximately 3 distinct deposition times 60, 70 and 80 minutes.

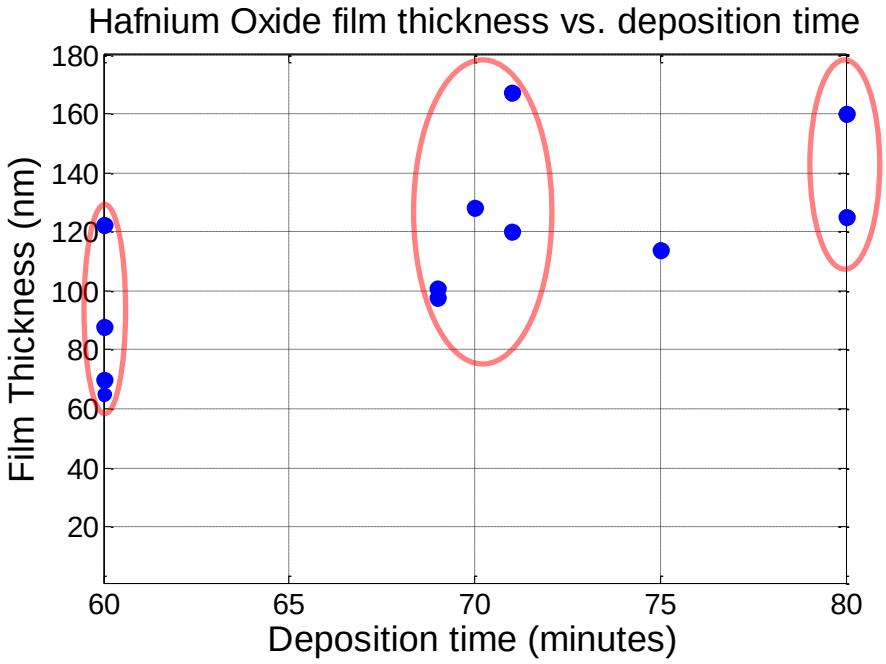

Figure 7-5 – Deposited HfO film thickness vs. time for approximately 3 distinct time depositions. The variation is too high to allow for the desired usage of the film in an imaging stack

Clearly, this indicates that such deposition cannot guarantee consistency, due to damaged equipment. The refractive indices at $\lambda = 405$ nm were measured using an attenuated total reflectance (ATR) method, which is described in the following section, this also resulted in a significant variation. As will be shown in a later section, the usability of a stack is dependent upon a figure of merit (FoM) (described in section

7.4). It is required to carefully tune the resonance in an optical stack so that it may provide the desired FoM. As the chapter proceeds several examples will be presented to demonstrate the effect of varying this FoM.

At this stage several optical stacks had been accumulated, through many months of depositions. These used quartz coverslips as the bottom substrate and very few films utilized a thermally grown oxide. The experimental results are presented through both atomic force microscope (AFM) scans first and then SEM scans as an end of life process for the sample. SEM can result in significant charging of oxides, however with careful sample preparation, such as that outlined in Chapter 3, the charging was greatly reduced or avoided altogether.

It is essential to determine the thickness variation that one may expect from sputtered deposition of thin films under the above described conditions. SEM was also used to carry this out and it was determined that the HfO film thickness has a variation of ±5 nm on both Si and SiO_2 substrates and was independent of any particular deposition run.

Now the ATR method is described, this is used to determine the refractive index of a particular HfO film at λ = 405 nm to determine whether a particular stack is suitable for imaging. The stack's suitability is qualified in section 7.4.

7.3 Attenuated Total Reflectance (ATR) method with Experimental demonstration

The extensive analysis of surface states in Chapter 5 showed that energy is extracted out of an incident beam and redistributed into the lossy photoresist as near-field coupling is facilitated with the presence of carefully chosen underlayers. While it is approximately known what the refractive index of Hafnium Oxide is at λ = 405 nm, it is also known that this varies with the deposition conditions. In fact, as will be seen in the following section, deviation from certain thickness and index criteria results in reduced or negligible evanescent coupling and thereby a drastically reduced image quality. For this reason, the optical performance of the stack is characterized by measuring the location of its attenuated total reflectance (ATR) resonant dip. Once the spatial frequency corresponding to the resonant dip is known, it is compared with a simulated ATR plot using the T-Matrix models.

Following this, the expected refractive index is adjusted in the T-Matrix models so that the simulated resonant dip occurs at the same spatial frequency as the one that was measured. This allows estimation of the refractive index of the HfO layer and while the ATR setup may itself be imperfect due to several real

world limitations, it still allows us to simulate the EIL imaging performance and to conclude whether the stack has the capability to image at a sufficiently high quality. This method is detailed below.

The ATR method requires measurement of the incident and reflected beam amplitudes at various angles as is illustrated by the schematic in Figure 7-6. It should be noted that point A as marked by a blue cross in Figure 7-6 is not fixed and moves across the incident face with varying angles of incidence. As a result point B (marked by a red cross) is also not fixed. Also note here that the prism depicted in Figure 7-6 is not mirror coated, as for the SILMIL exposures, but is the same in all other respects (and purchased as a pair with the SILMIL prism to ensure consistent material properties).

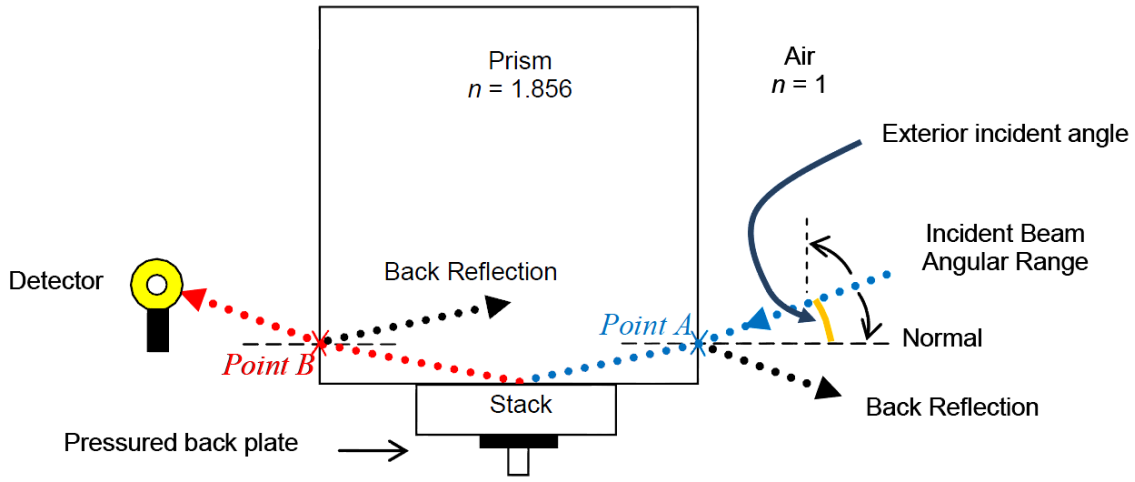

Figure 7-6 - Setup to characterize stack by means of Attenuated Total Reflection

Consider now that one needs to find the refractive index of a 90.3 nm thick HfO layer that was deposited by RF sputtering on a quartz coverslip. This particular example will also be used later to demonstrate high aspect ratio patterning at a *NA* of 1.824. The stack is first prepared as shown in Figure 7-7. In this experiment, a PVA layer is not used, which would otherwise have been a top coat over the photoresist if EIL was being carried out.

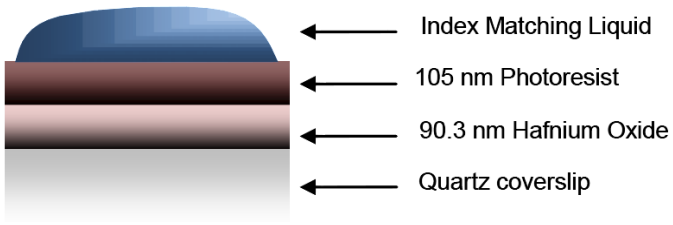

Figure 7-7 - Stack for Hafnium Oxide characterization by Attenuated Total Reflection

Figure 7-8 shows a photograph of the ATR setup that includes a rotational substrate to allow measurements to be taken at various angles (numerical apertures). As the setup is rotated about its axis, the location of point A is continually adjusted on the incident prism face so that the beam strikes the stack at the region of intimate contact. The small area of intimate contact is a limitation of SILMIL that was discussed in Chapter 3. Hence it is desirable for the spot size A to be small also so that more of beam takes part in ATR (and less of it gets totally internally reflected). This would also make the location of the resonant dip more prominent and accurate. This is achieved by using the direct laser output as opposed to a collimated one.

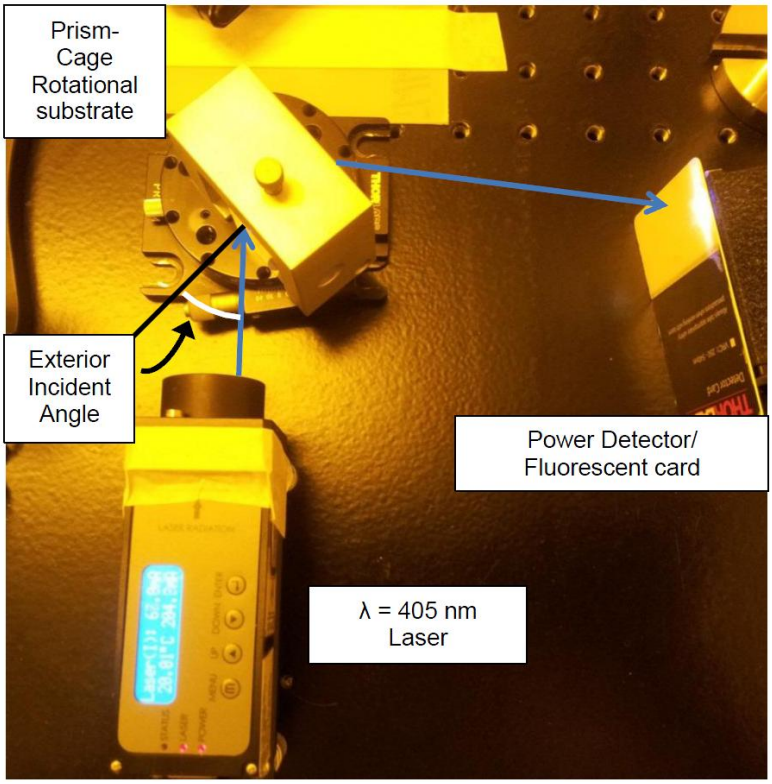

Figure 7-8 – Photograph of ATR setup

The direct laser output however in our case has an intensity of ~32 mW. This resulted in photo-aberration of the resist. For this reason, neutral density filters (NDUV03B, NDUV06B, Thorlabs Inc.) were installed in the path of the laser to attenuate the incident power by 9 dB to a value of ~5.8 mW, which was sufficient to prevent photo-aberration.

In the setup of Figure 7-6, the effects of back reflections from prism walls act to attenuate the data in such a manner, that the location of the resonant dip may appear to be at another spatial frequency. To remove these undesirable reflections measurements are first taken without the presence of a stack. Ideally, this

would result in total internal reflection. Due to back reflections however, the curve of Figure 7-9 (solid blue curve) was obtained.

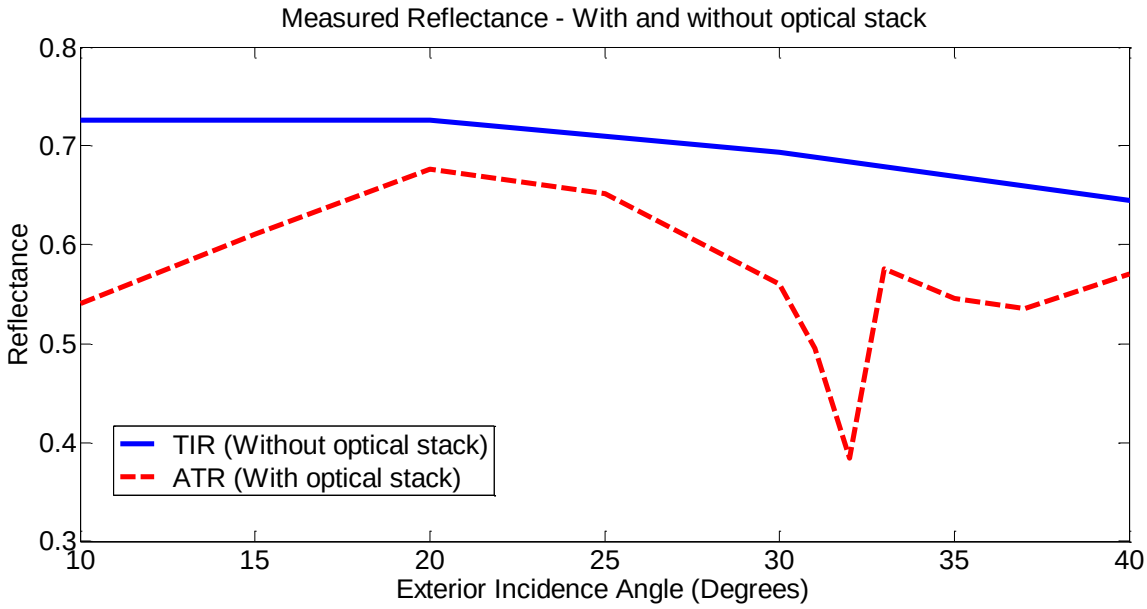

Figure 7-9 – Measured Reflectance using setup in Figure 7-8 with respect to exterior incident angle. Solid blue curve is without any stack and dashed red curve is with the underlying stack of Figure 7-7.

Following this, reflectance measurements are taken by now employing the stack in Figure 7-7, this data is plotted in Figure 7-9 (dashed red curve). Clearly, a resonant dip exists here near an external incident angle of ~32^{o}. The quality of the ATR curve is dependent upon the quality of the intimate contact that the stack has with the prism. In addition, the beam's cross-sectional area that interacts with the sample varies with the incident angle. Hence, one cannot expect the measured curve to have a resonance as deep as that predicted by the analytical T-Matrix formulation. For this reason, this approach was used only to locate the resonant dip and compute the index of the HfO layer using back calculation.

Note that measurements are taken at finer angular increments about the resonant dip so that its location may be more precisely found. A simple method to remove the inherent back reflection effects is by simply computing the ratio between the dashed and solid curves in Figure 7-9 (dashed red curve / solid blue curve). The new adjusted plot is shown in Figure 7-10 with the *x*-axis now modified to show the *NA*. The angle at which the resonant dip takes place corresponds to a *NA* of 1.779. The dip is indicative of the spatial frequency (or *NA*) at which the pseudo-surface state is excited.

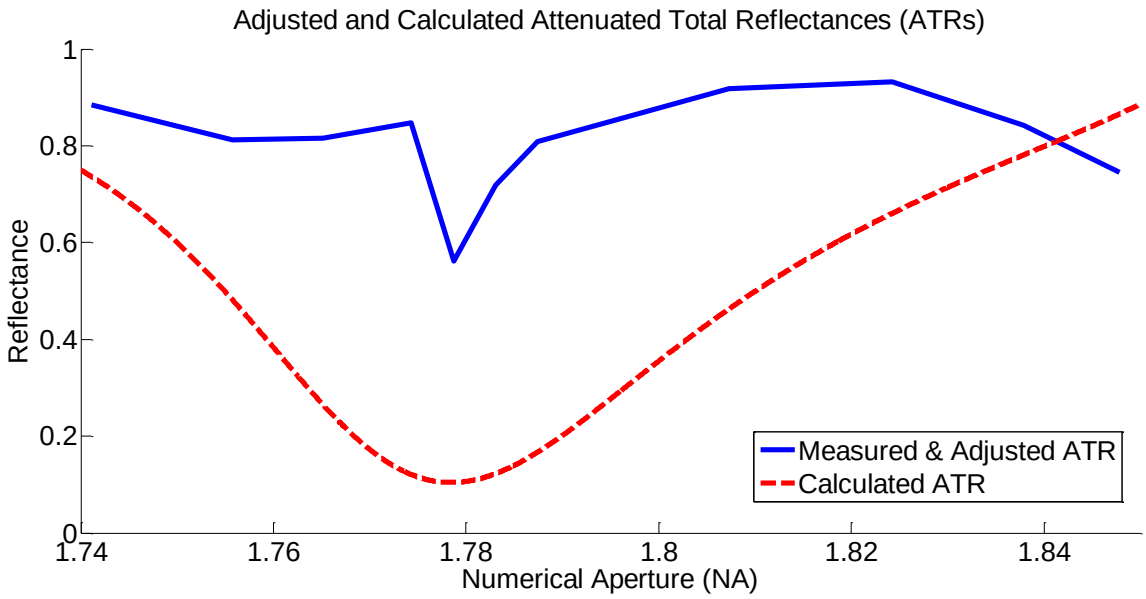

Figure 7-10 - Attenuated Total Reflectance vs. *NA* for the stack in Figure 7-7 (a) (solid blue) Calculated ATR = Measured ATR / Measured TIR and (b) (red dashed) Matlab ATR.

Figure 7-10 (b) is then created, it is a simulated ATR plot for when the stack of Figure 7-7 is modeled using the T-Matrix method. The refractive index of HfO is tweaked in the T-Matrix model so that the simulated resonant dip also lies at a *NA* of 1.779. This required the HfO index of this particular thin film to be ~2.008. This is well within the acceptable range of refractive indices for hafnium oxide at λ = 405 nm [184].

It is quite fascinating to note that the spatial frequency of the observed resonant dip is that at which maximal energy has been extracted away from the incident beam and redistributed at the bottom of the photoresist. In this case, it is a waveguide mode in the HfO layer, where the relevant boundary conditions are satisfied at a *NA* of 1.779. Interestingly, a bright glow was observed on the photoresist surface as seen through the prism face at and about the resonant *NA*. This phenomenon was noted for all ATR experiments that were carried out independent of HfO film thickness or refractive index. This was found to be quite fascinating and Figure 7-11 demonstrates our attempts to photograph this glow.

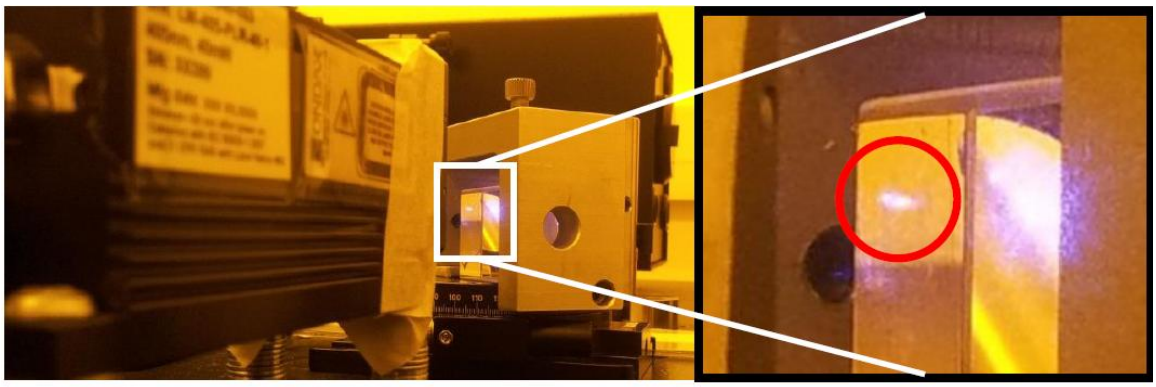

(a)

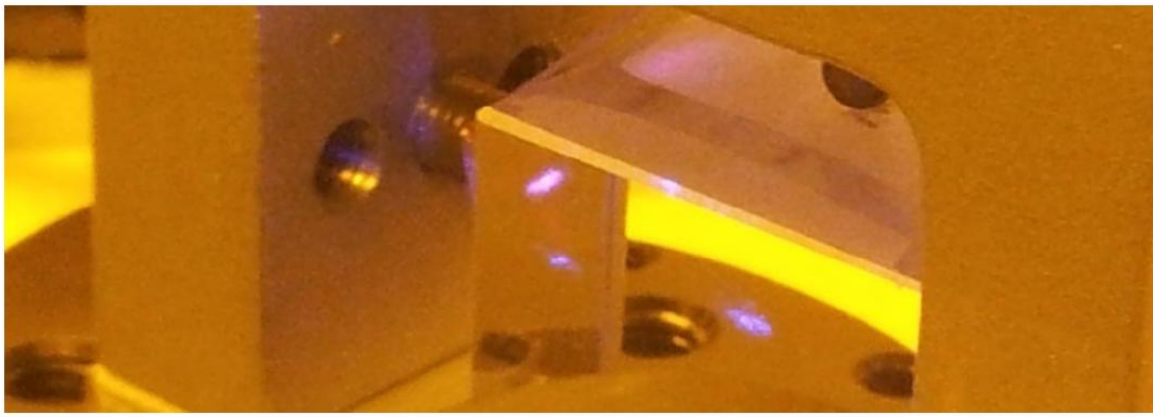

(b)

Figure 7-11 - Photograph of observed glow at the resonant *NA* (a) – (b)

The phenomenon demonstrates an increased scattering as increased evanescent coupling takes place. The following section explores the tolerances that a particular optical stack may have and still allow EIL imaging at a high quality.

7.4 Figure of Merit & Allowable Operating Region

The stack's suitability for imaging is qualified by simply enforcing that the minimum intensity along the maxima of the interference pattern be at least 40% of the peak intensity (as done previously in Chapter 6 for the TE polarized case). A stack operating at such a specification hence has a Figure of Merit (FoM) of 1. The FoM may be calculated using (7.1). The relevant quantities are illustrated in the mock-up interference intensity image of Figure 7-12 using a resist thickness of *D* nm and assuming that the image depth is required to be *D/2* nm.

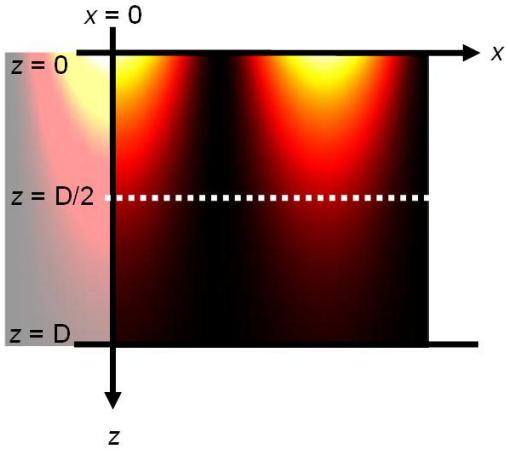

Figure 7-12 – Intensity of a mock-up interference image in *D* nm thick photoresist indicating the relevant quantities used in (7.1).

$$FoM = \frac{1}{RIR} * \frac{\max\left(I(x=0, z=0)\right)}{\min\left(I(x=0, z=D/2)\right)} \tag{7.1}$$

where, I is the intensity and RIR = 2.5. A high FoM is desirable, but a FoM of unity is absolutely the minimum we are prepared to accept based on the rules established in Chapter 6.

Several ATR experiments (such as those demonstrated in the previous sub-section) were carried out and, as mentioned earlier, a ±5 nm thickness variation on the sample was observed in the successful depositions. For this reason, it is was found to be necessary to be able to simulate the performance of an optical stack by taking into account all possible expected variations in the HfO film for a given photoresist thickness and for imaging at a fixed *NA*.

The task was set of imaging into a ~105 nm thick photoresist layer at a *NA* of 1.824, (c.f. only 30-40 nm maximum pattern depths in Chapter 3 for the same conditions) using the stack of Figure 7-13 (b).

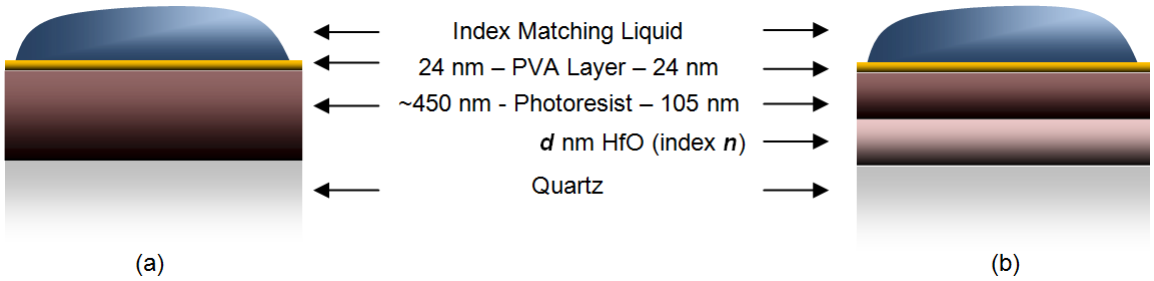

Figure 7-13 - Optical stacks for imaging at λ = 405 nm at *NA* = 1.824 (a) without an EGM underlay for conventional EIL (b) With an EGM underlay (characterized by ATR) for high aspect ratio imaging

Figure 7-15 presents the image quality as a surface plot of the FoM as described the previous section using (7.1) with a color map indicating the dynamic range of the FoM for the stack in Figure 7-13 (b) as the thickness and index of the HfO layer is varied. It depicts the operation of the stack under relatively large thickness and index variations of the HfO layer (60 nm to 120 nm and n = 1.9 to 2.2), allowing us to visualize the evolution of the FoM. Once again the criteria is enforced that a FoM of 1 is required and anything larger is ideal. In the previous section, a stack with a HfO layer thickness of d ~ 90.3 nm and index n ~ 2.008 was characterized, the FoM for this is ~1.36 for 105 nm thick resist and operation at NA = 1.824, λ = 405 nm (marked with a black cross in Figure 7-15). This is hence acceptable for imaging. This stack is shown in Figure 7-14 below and will be used to image high aspect ratio structures in a later section.

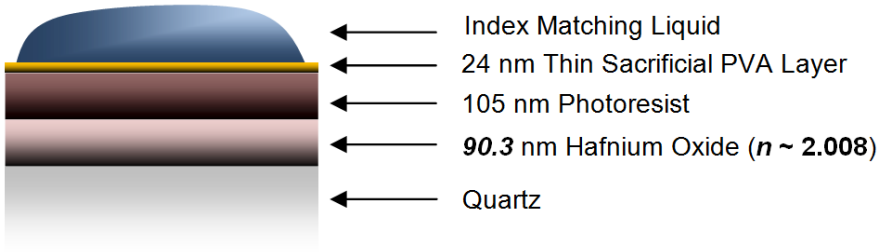

Figure 7-14 – The EGM underlay (HfO on Quartz) in this stack was characterized by ATR in the previous section

The allowable operating region is simply FoM >= 1, which is shown in Figure 7-16. In the following section, a method is proposed to widen the allowable operating region so that a higher variation in the HfO layer thickness and index may be tolerated. The new method was developed after significant equipment failure was faced and while simulations and even experimental evidence is proposed to support this method, we have not found the need to utilize it as the necessary optical stacks for suitable imaging became available shortly after.

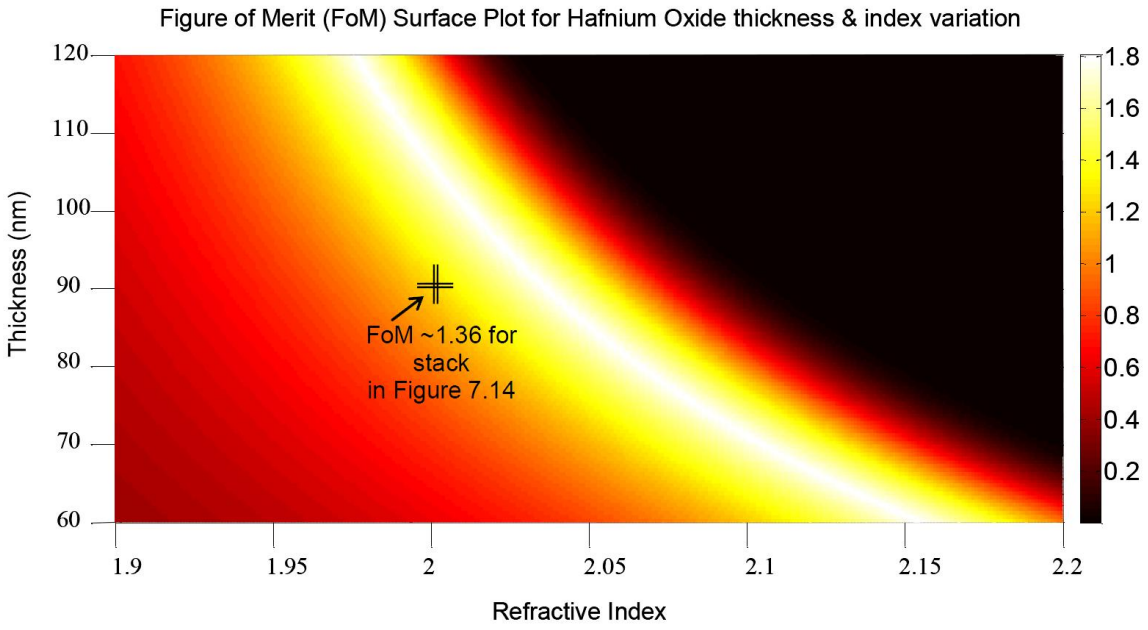

Figure 7-15 - Figure of Merit (FoM) Surface Plot for stack in Figure 7-13 (b) at *NA* = 1.824, λ = 405 nm for the given HfO thickness & index variation

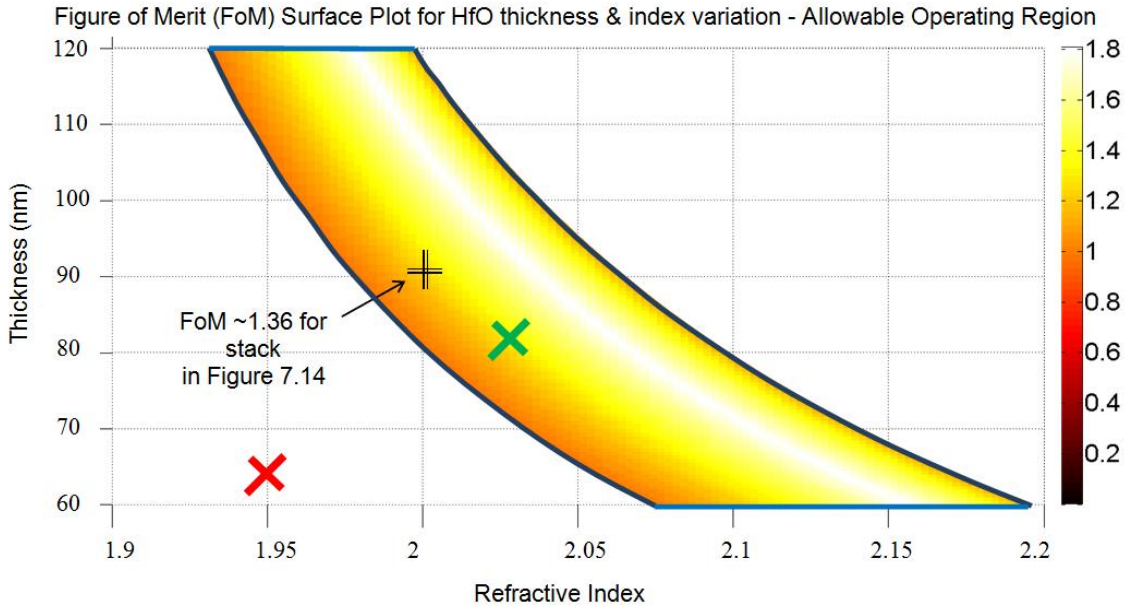

Figure 7-16 – Allowable operating region outlined in solid blue for Figure of Merit (FoM) for the stack in Figure 7-13 (b) at *NA* = 1.824 and λ = 405 nm for the given HfO thickness & index variation – The red & green crosses will be referred to later in Sections 7.6.2 & 7.6.3 respectively

Let us finally also note that there is a family of solutions available as briefly mentioned in the previous chapter on imaging. This is better illustrated using Figure 7-17 that depicts the FoM surface plot for greater thickness variation of the HfO film.

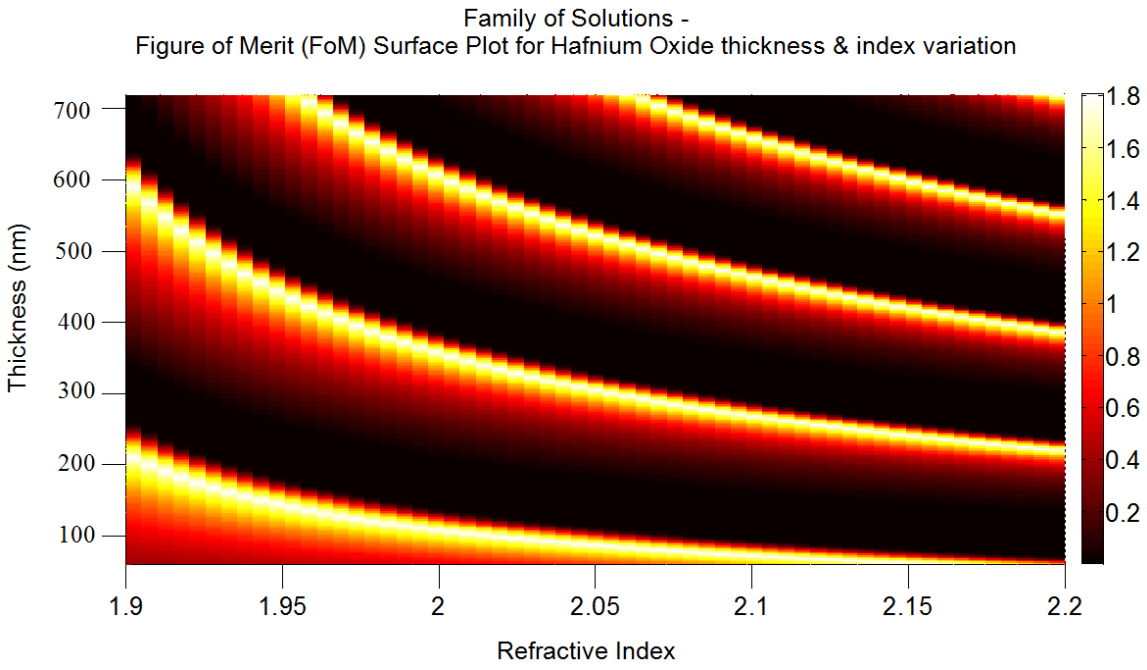

Figure 7-17 – Family of solutions available for a particular index or thickness of the HfO layer due to the family of wave-guide modes

7.5 Resonance Compensation & Experimental verification for Improved Fault Tolerance

As mentioned in a preceding section, there was little consistency in the HfO depositions due to equipment failure. As an interesting exercise, an innovative solution is proposed here to such a problem. It is demonstrated using simulations and experiments how such a solution could be of potential use to other researchers when facing similar issues regarding non-ideal properties of an optical stack.

We have a large number of HfO thin films deposited on quartz stacks at our disposal from several depositions; the downside is that all of these films have varying resonances due to undesired thickness and index variations. A few of these stacks will allow an image with a sufficiently high FoM, some are slightly imperfect, and will only allow imaging into much thinner resists than desired, while other stacks are completely non-ideal and their performance is comparable to or worse than the no-underlay stack of Figure 7-13 (a).

One possible method to achieve high FoM from any HfO deposition is to first sputter a relatively thick HfO film on Quartz and characterize its thickness and index. Following this, a wet etch of the film would be carried out using an ammonium hydroxide buffered HF acid solution to the point where the thickness of the HfO layer is such that the required resonance shift is achieved. Once this is done, the stack is

suitable for high FoM imaging. To find the required thickness for a particular index, one may simply look up the surface plot of Figure 7-17.

This method takes away the dependency on the consistency of HfO film depositions. It requires long deposition times, etch rate characterization and index and thickness characterization before and after the wet etch process. In addition, care would also need to be taken to ensure that the HfO film is uniformly etched and that the quartz etch rate is significantly lower, i.e. a high selectivity process would need to be created.

Another method, one a little less aggressive and one that adheres to the general effective gain medium theme of this thesis is to compensate the resonant dip using a further low index material layer. The proposition is to use Poly (methyl methacrylate) (PMMA) that is a low index spin on polymer which is insoluble in water. Under certain circumstances, such compensation is possible and would allow wider stack design tolerances than otherwise possible. This is a much simpler and more elegant solution than wet etching and is discussed here. Experimental evidence of its operation is also provided using the ATR characterization method that was introduced in a previous section.

Consider one of the optical stacks created in lab (Figure 7-18) that has a HfO film thickness, d = 110 nm and refractive index, $n = 2.04$ at $\lambda = 405$ nm.

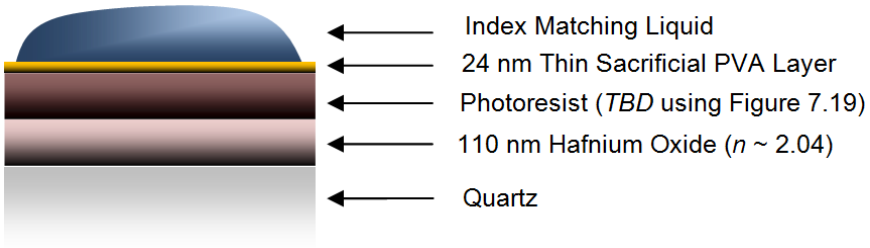

Figure 7-18 – Stack unsuitable for imaging, only allows ~37 nm image depth (see construction lines in Figure 7-19)

The FoM for this stack is ~0.1313 and so it is unsuitable for imaging. This may be looked up in Figure 7-16, the operating point lies outside the allowable region.

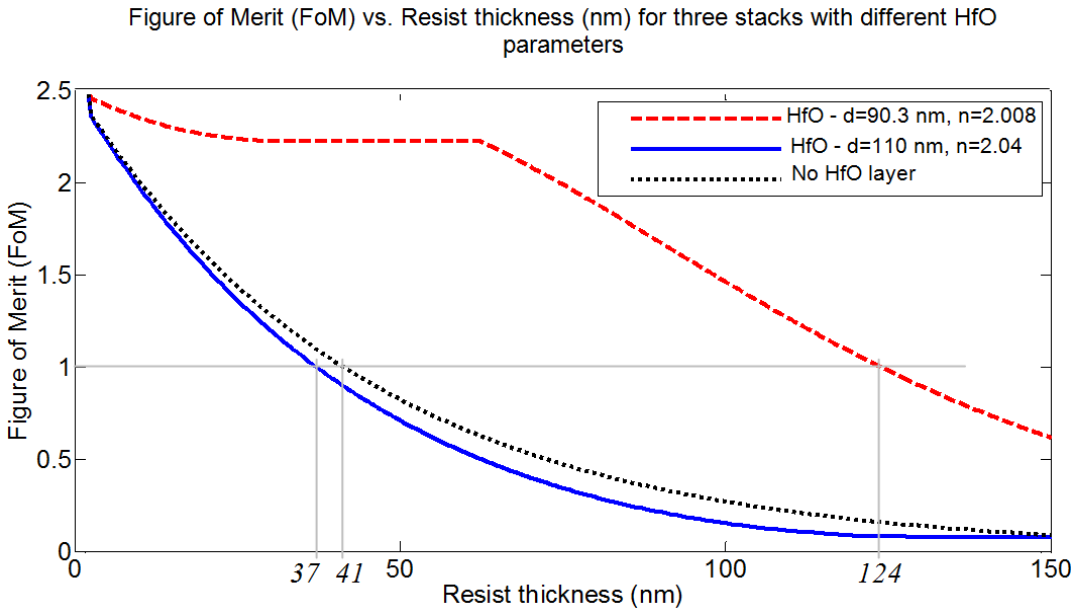

Figure 7-19 - Figure of Merit (FoM) vs. Resist thickness (nm) using T-Matrix models for three stacks with different HfO parameters (a) that from Figure 7-14 (red-dashed), (b) that from Figure 7-18 (solid-blue) and (c) that from Figure 7-13(a), the no-underlay case (black-dotted)

Figure 7-19 shows a plot of the FoM versus photoresist thickness for three different stacks. This was generated using (7.1) and two parameter run using the analytical T-Matrix models. This tells us that a resist thickness below 37 nm is needed to achieve a FoM of unity or higher for the stack of Figure 7-18.

This is a worse-off performance than the no-underlay case, Figure 7-19 (c) for the stack in Figure 7-13 (a), which is predicted to give ~ 41 nm image depth. In fact, this is almost exactly the image depth that was achieved in Chapter 3 for low pseudo-dosages of 2.5 – 3 mW-min. In strong distinction, Figure 7-19 (a) predicts that the stack of Figure 7-14 is capable of suitably imaging into 124 nm resist.

We propose that the use a 29 nm PMMA (n = 1.517 + i*0.00046) thin film spun on top of the HfO layer will adjust the resonance such that the stack of Figure 7-18 will be of considerably greater use for imaging at a *NA* of 1.824 at λ = 405 nm. The transformation is illustrated in Figure 7-20. The PMMA solution is a high molecular weight (HMW) 1.33% using Xylene as the solvent, spun at 4000 rpm for 1 minute and baked at 200^{o}C for 4 minutes on a hot plate.

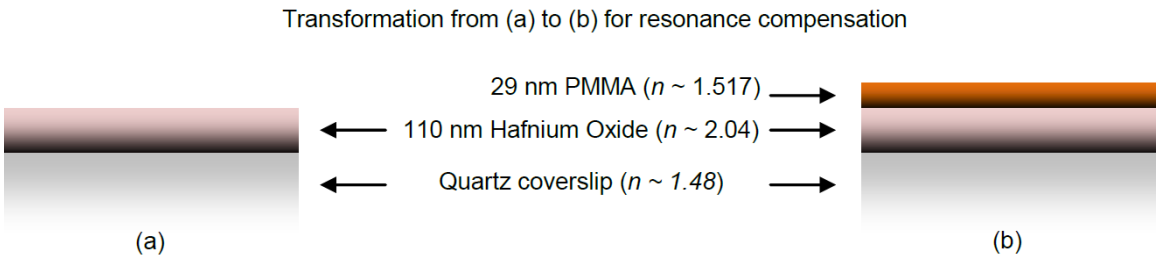

Figure 7-20 – Resist-underlay transformation from (a) Unsuitable for imaging to (b) Suitable for imaging by achieving resonance compensation using a thin film layer of PMMA

The effect of this transformation is observed using ATR plots. Figure 7-21 shows that the expected transformation of the resonance is from ~15° to 21° exterior incidence angle (the exterior incidence angle is depicted in both Figure 7-6 and Figure 7-8) using T-Matrix models. The expected FoM enhancement from this shift is illustrated in Figure 7-22, using the T-Matrix model.

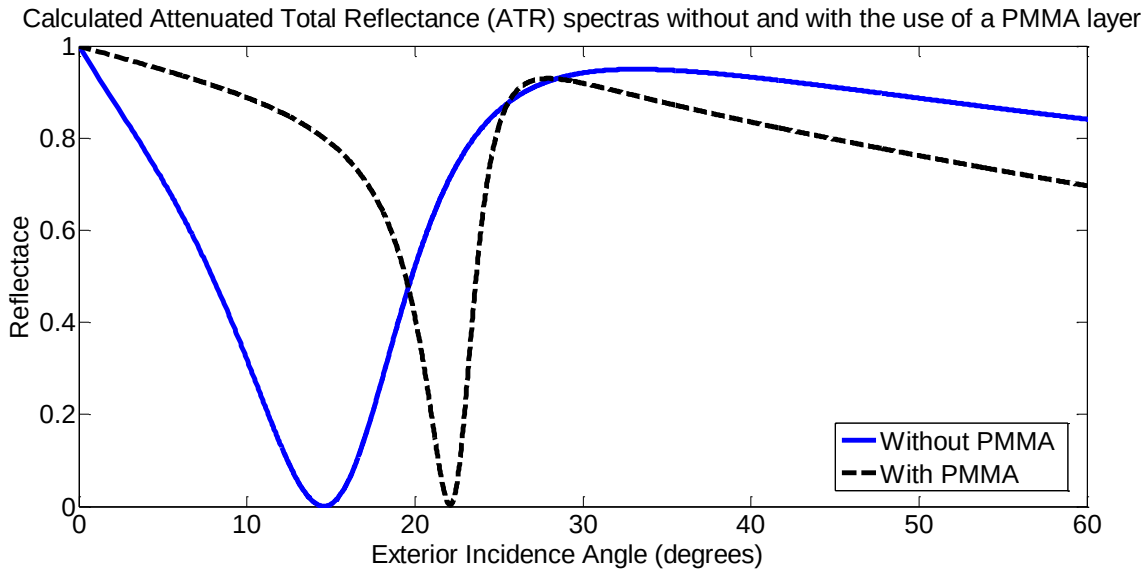

Figure 7-21 – Simulated Attenuated Total Reflectance (ATR) plots without and with the use of a PMMA layer as depicted in Figure 7-20

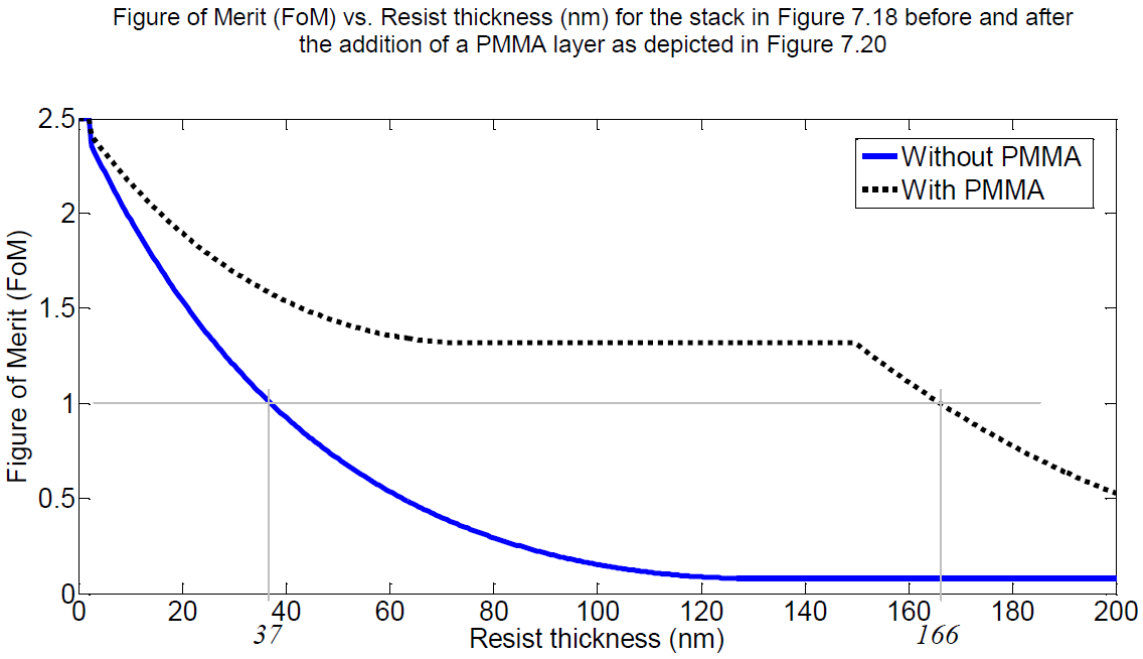

Figure 7-22 – Imaging in considerably increased resist depth by employing a resonance compensating PMMA layer, allowing imaging into 166 nm of resist (dotted black) (with PMMA on HfO Figure 7-20 (a)) as opposed to only 37 nm previously (solid blue) (without PMMA Figure 7-20 (b))

This was tested with ATR experiments to ensure that the concept was sound; the raw results are depicted in Figure 7-23 and demonstrate a resonant dip shift that bears a striking resemblance to that depicted in Figure 7-21. The resonance with the use of the PMMA layer is considerably narrower as predicted. Once again, the characteristic resonance glow that was described earlier (see Figure 7-11) was also observed for both plots.

It is essential to note that discrepancies in such experiments may be partly attributed to the fact that there is a ±5 nm thickness variation of the HfO thin film and little control over the IML layer thickness. In addition, the area and amount of intimate contact that was achieve with our setup is limited and at times dependent on the quality of the back plate and may also vary with consecutive measurements from changes in material properties due to pressure, incident laser energy and human error.

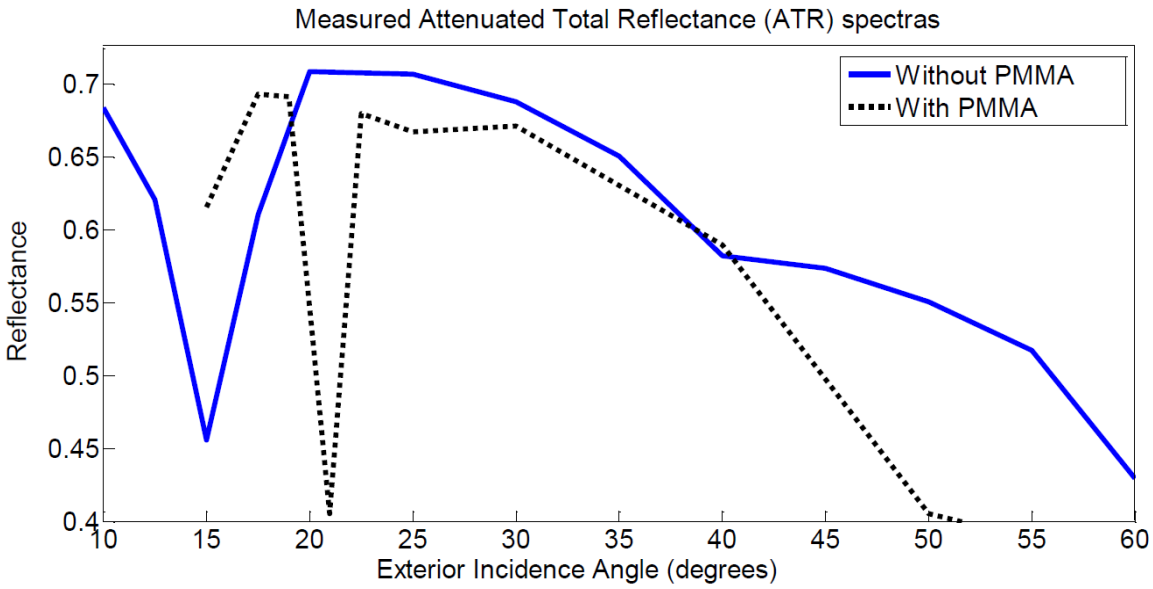

Figure 7-23 – Experimental demonstration of the resonance shift using a PMMA layer (c.f. Figure 7-21) (ATR raw data)

The FEM simulations for the image intensity profiles at the peaks of the interference before and after the addition of the PMMA layer are illustrated in Figure 7-24 and indicate that EIL may now be carried out in 166 nm thick resist as opposed to 37 nm which was previously the case. This is indeed a considerable improvement and one worth considering if a researcher faces non-ideal stack properties.

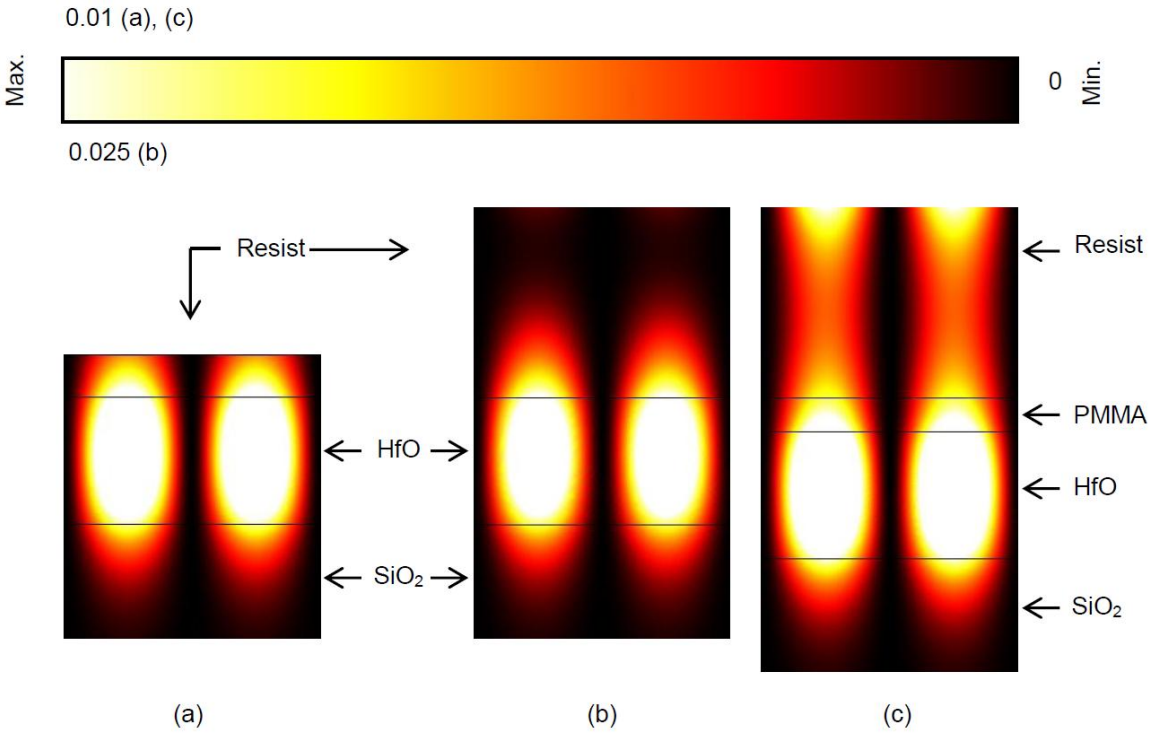

Figure 7-24 – FEM simulations with COMSOL demonstrating the image depth enhancement in photoresist after a non-ideal EGM is made ideal with resonance compensation using a layer of PMMA (see Figure 7-20 for details on HfO and PMMA index and thickness). EIL carried out at a *NA* = 1.824, λ = 405 nm, half-pitch = 55.5 nm (a) Image in 37 nm resist using the non-ideal EGM underlay (FoM = 1) (b) Image in 166 nm resist using the non-ideal EGM underlay (FoM = 0.081) (c) Image in 166 nm resist using the resonance compensated EGM underlay (FoM = 1) (best case)

7.5.1 Enhanced Allowable Operating Region

Let us use this method to show how the allowable operating region may be considerably enhanced. Assume that it is required once again to image into a 105 nm resist using the stack of Figure 7-13 (b). A three variable parametric simulation was run (using T-Matrix modeling) where the index and thickness of the HfO layer and the thickness of the PMMA layer were all varied simultaneously. The PMMA thickness layer that allows for the best FoM was chosen in each case. The results of this simulation, the new region for FoM >= 1 is illustrated (and outlined in solid blue) in Figure 7-25, and compared with the operating region without the presence of PMMA earlier (dashed blue). This approach not only maximizes the FoM wherever possible (limitations due to the index of the PMMA polymer) but, it also considerably widens the allowable operating region.

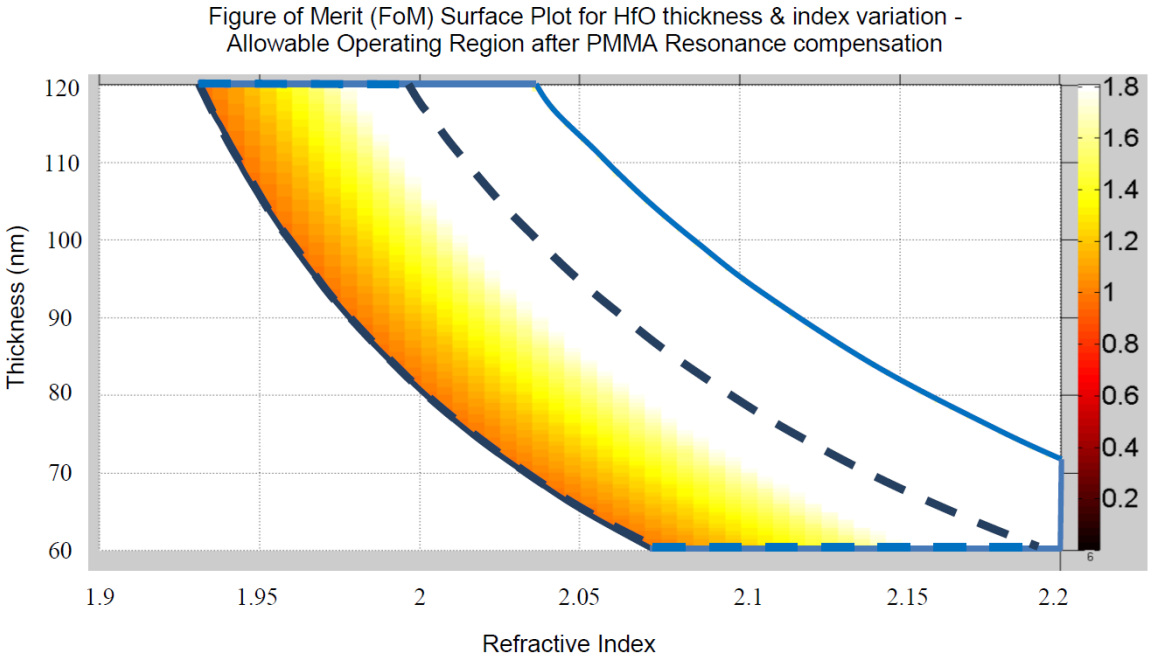

Figure 7-25 – Modeling of improved allowable operating region by using a resonance compensating PMMA overcoat upon the HfO layer. This was carried out for the stack in Figure 7-13 (b) to image into 105 nm thick resist at a *NA* of 1.824 at λ = 405 nm. The new allowable operating region is outlined with a solid border and the old allowable operating region is outlined in a dashed border.

The experimental demonstration of the use of an EGM to pattern high aspect ratio EIL structures is now described and the effects of parametric variations are also explored.

7.6 Experimental Results

The optical characterization of a particular optical stack has already been described in a previous section. Simulations that predict the performance of an optical stack have also been shown. In this section, the case study for EIL imaging at a *NA* of 1.824 is continued and focus is placed on the use of an EGM to significantly enhance the aspect ratio of structures as compared with those that were achieved using conventional EIL with SILMIL in Chapter 3.

The results of parametric variations are interpreted afterwards. An example is then also used to demonstrate reduced evanescent coupling produced with a non-ideal stack resulting in a low image FoM, however still providing a noticeable enhancement. Finally, the effects of dosage variation on pattern and resist depth are also analyzed and compare with those obtained in Chapter 3.

7.6.1 Imaging High Aspect Ratio Structures with a usable Effective Gain Medium underlay

The reader has now been introduced to the stack in Figure 7-26 (b). The ATR method was used to determine the index of the HfO layer using the stack in Figure 7-7. In this sub-section the stack of Figure 7-26 (b) is used to demonstrate high aspect ratio EIL at a *NA* of 1.824. Simulation results are provided, followed by several AFM and SEM scans.

The results are compared with a stack that does not have an EGM underlay (Figure 7-26 (a)). For a fair comparison, both stacks use a quartz substrate (of the same size 1 inch x 1 inch). This is essential for two reasons; firstly, the spun thickness of the PVA layer varies with the size of the substrate for the same spin recipe. Hence, keeping the size of the substrate constant ensures a constant thickness PVA layer. Secondly, this also ensures that the mechanical properties of both substrates are in fact the same so that, both stacks will conform almost equally under intimate contact.

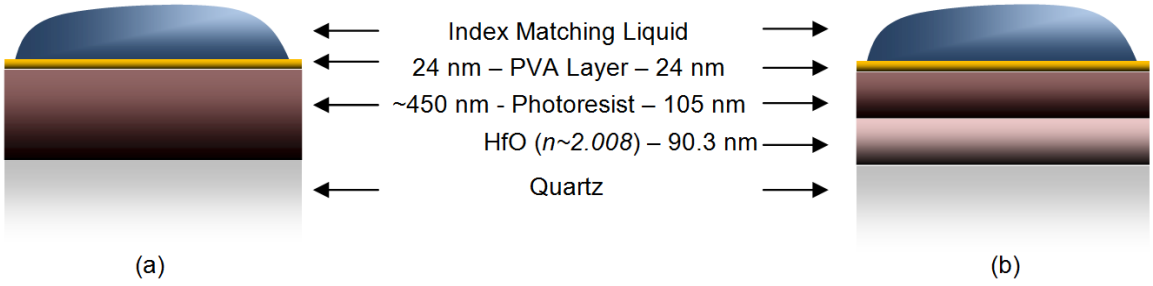

Figure 7-26 – Optical stacks for imaging at λ = 405 nm at *NA* = 1.824 (a) without an EGM underlay for conventional EIL (b) With an EGM underlay (characterized by ATR earlier) for high aspect ratio imaging

7.6.1.1 Modeling & Simulation

The T-Matrix model allows us to simply plot the intensity of the interference maxima as a function of depth into the resist. In Figure 7-27, this is plotted for both of the stacks from Figure 7-26. One can see that for the same dosage, the intensity of the interference maxima is higher for the EGM underlay case. The resulting FoM as we pointed out earlier is ~1.36.

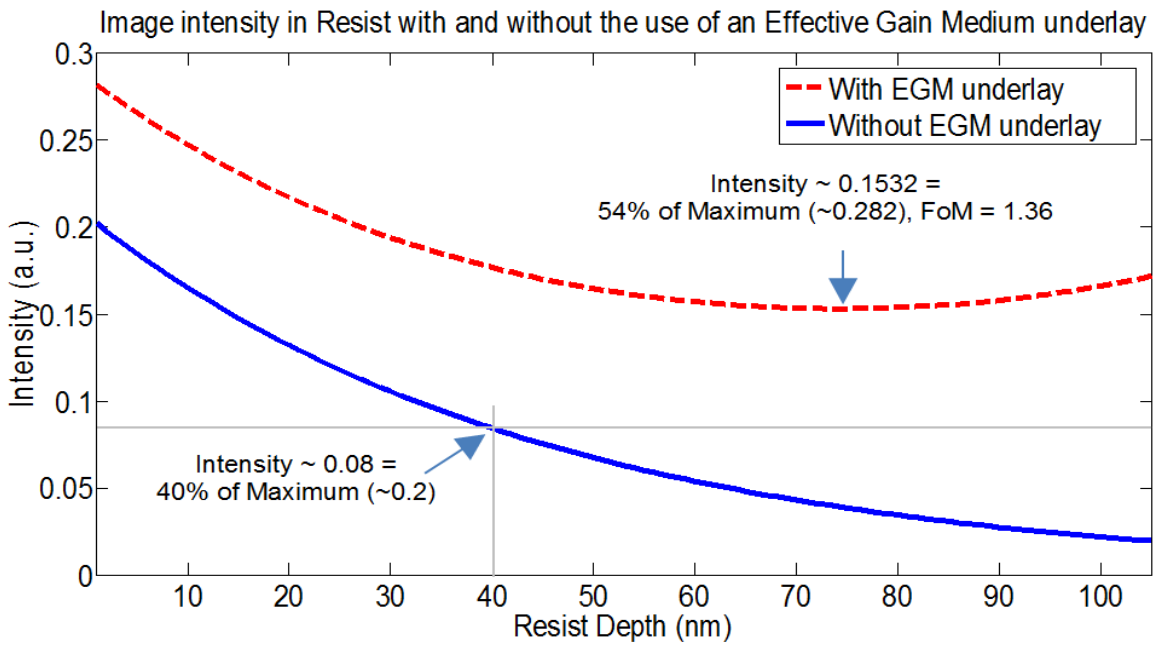

Figure 7-27 – Image intensity profile in resist with for the stacks in Figure 7-26 (a) – Solid blue and Figure 7-26 (b) – Red dashed

However this is not the complete story; the peak to null (or maxima to minima) ratio of the interference pattern is much higher for the EGM underlay case because the minima of a TE interference pattern are ideally zero. This performance improvement is better demonstrated via FEM simulations in Figure 7-28 and cross-section intensity profiles at various depths (Figure 7-29) to depict image evolution.

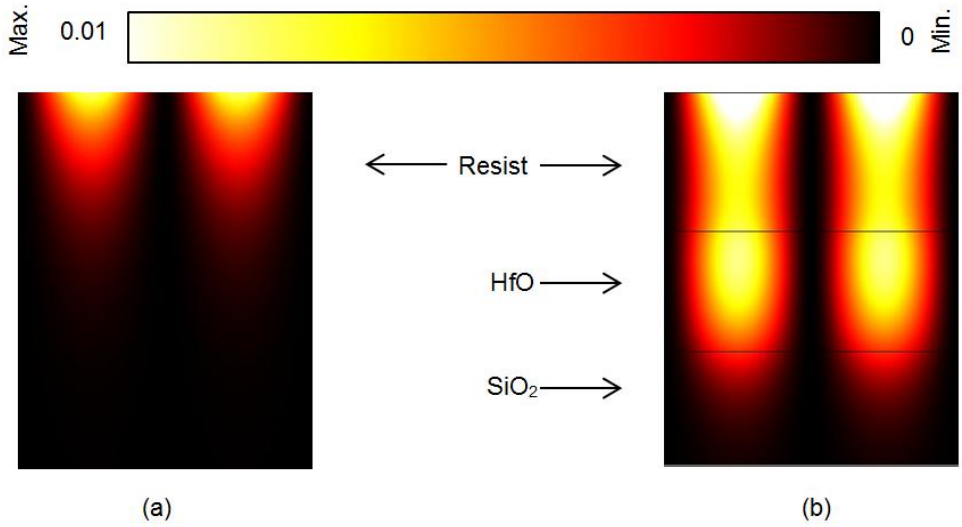

Figure 7-28 – FEM simulation for the imaging with the stacks in Figure 7-26 for *NA* = 1.824, λ = 405 nm, half-pitch = 55.5 nm into (a) Semi-infinite resist (b) 105 nm resist with an EGM underlay

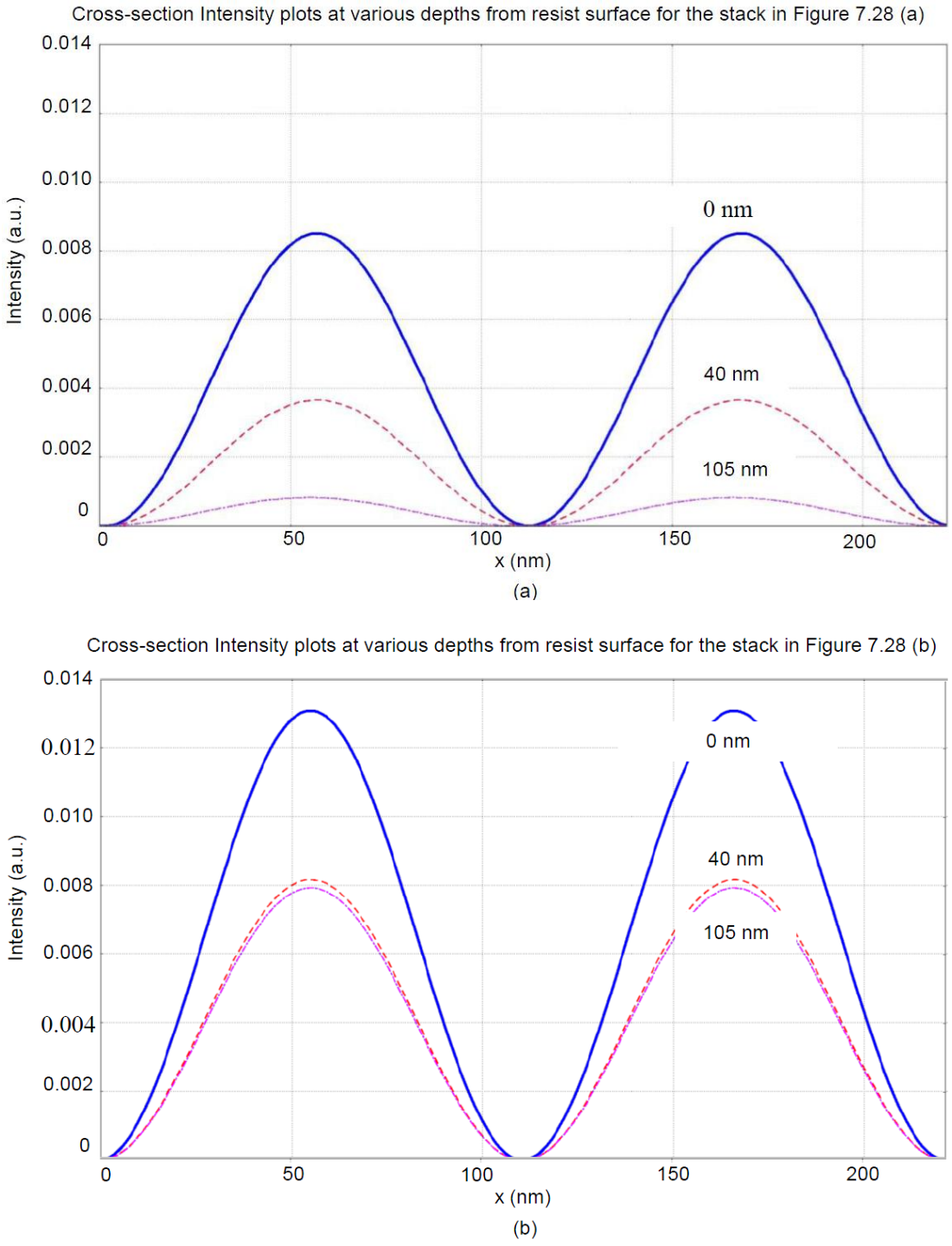

Figure 7-29 – Cross-section Intensity plots at various depths from resist surface for the simulations in (a) Figure 7-28 (a) and (b) Figure 7-28 (b)

7.6.1.2 Experimental Results

In Chapter 3, AFM and SEM scans were presented that demonstrated image depths of up to ~30-40 nm using conventional SILMIL at a pseudo-dosage of 2.5-3 mW-min. The stack in Figure 7-26 (a) was used to carry this out. By making use of the stack in Figure 7-26 (b), these image depths may be considerably enhanced. This is illustrated by our results in the AFM scans of Figure 7-30 and Figure 7-31 and the various AFM scope traces in Figure 7-32. A major difference between the scans presented here and those in Chapter 3 is the considerably large image depths of 90 - 105 nm for the same pseudo-dosage (PD) of ~2.5 mW-min. This enhancement is reported here for the first time. Figure 7-30 (b) depicts a side-view of these tall standing structures using the AFM software.

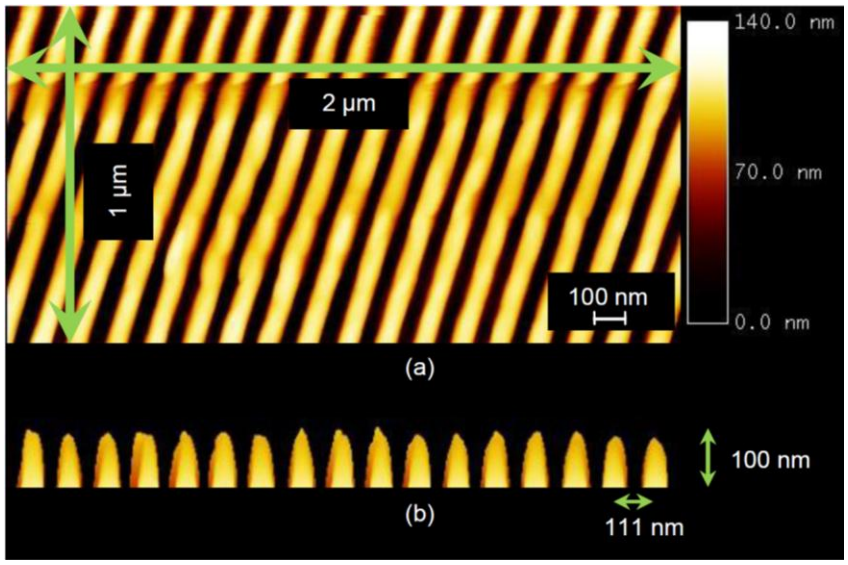

Figure 7-30 – AFM Scan demonstrating EIL using SILMIL using the imaging stack of Figure 7-26 (b), high aspect ratio (~1.8) structure imaged at a *NA* of 1.824 at λ = 405 nm with pattern half-pitch ~ 55.5 nm and average depth measured using AFM software to be 100 nm. (a) A 2 µm by 1 µm AFM scan (b) A corresponding 3D like perspective view to depict the tall standing structures

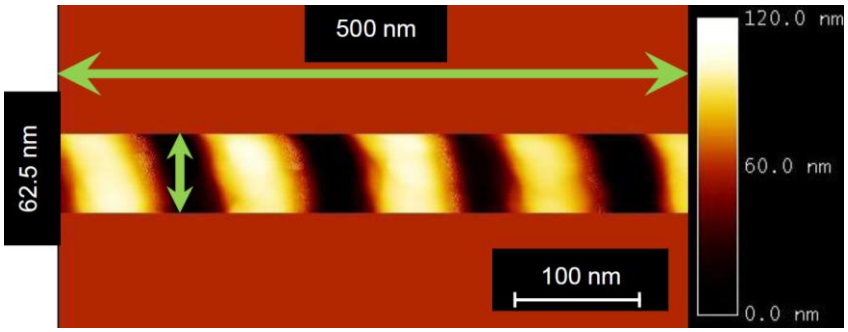

Figure 7-31 – Smaller area AFM Scan demonstrating high aspect ratio (~1.8) imaging, 100 nm pattern depth with EIL using SILMIL using the imaging stack of Figure 7-26 (b), at a *NA* of 1.824 at λ = 405 nm with pattern half-pitch ~ 55.5 nm. A 500 nm by 62.5 nm AFM scan is presented

It is essential to point out here that these samples employing the EGM were developed for 4 minutes instead of 1 minute to achieve such thicknesses. A development time of 1 minute resulted in ~55 nm depths. In fact, a development time of 4 minutes on the samples utilizing the stack of Figure 7-26 (a) resulted in extremely weak modulation of the resist.

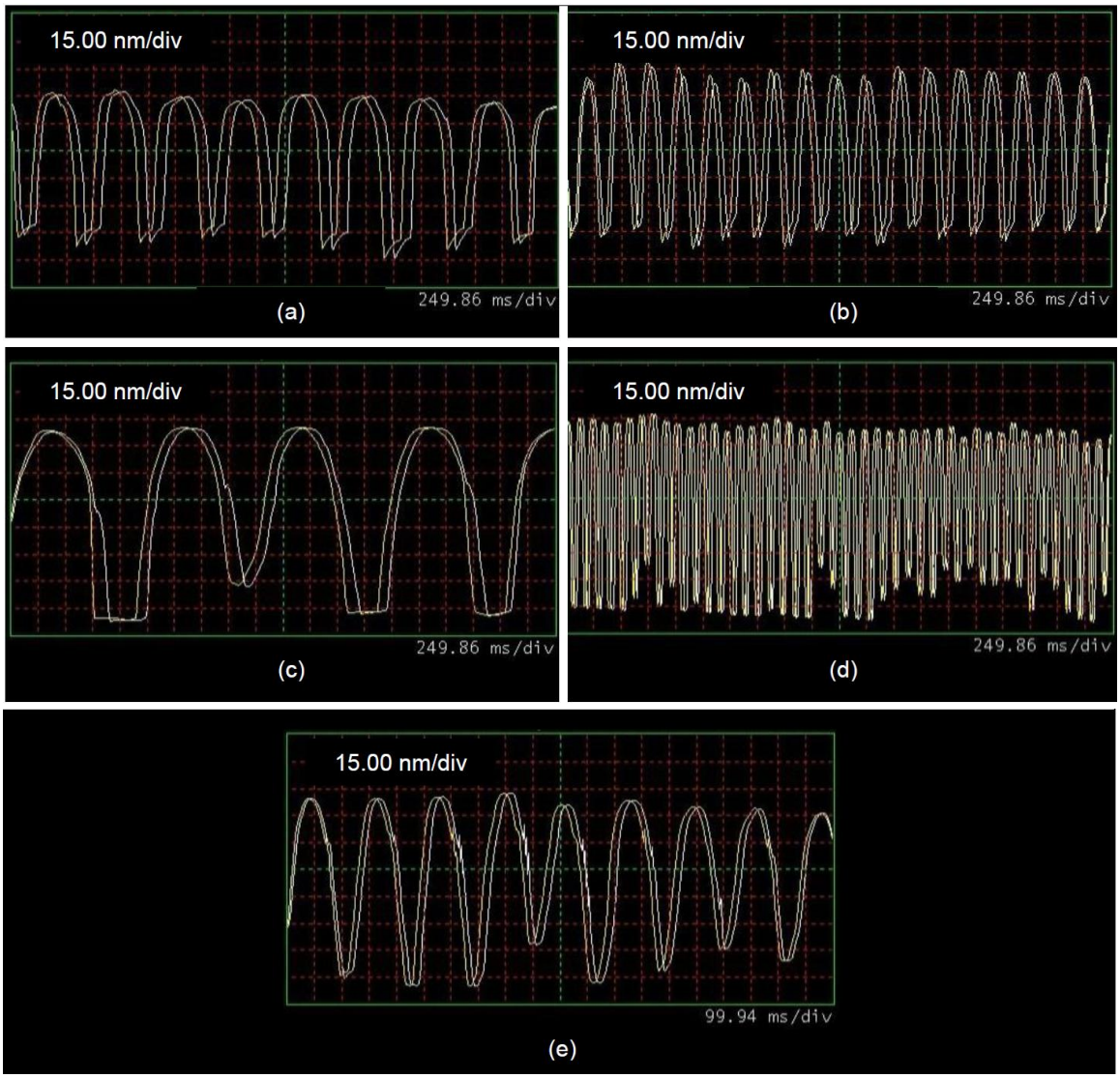

Figure 7-32 - Cross-sectional scope plots, at *NA* = 1.824, λ = 405 nm, EIL using SILMIL using the stack of Figure 7-26 (b), Resulting pitch ~111 nm at a PD of 2.5 mW-min. The scope plots (a) to (e) demonstrate enhanced image depths of 90 nm to 105 nm and allow the AFM tip to now image the trench of the pattern

Another major difference between the traces of Figure 7-32 and those in Chapter 3 is that the AFM tip is now able to image the bottom of the trench, indicating that the resist has been exposed and developed away over a wide area.

There is clear indication that the use of an EGM has made a significant difference. This is due to energy extraction and redistribution right down to the bottom of the resist which was facilitated through near-field interaction with the EGM *i.e.* evanescent coupling of the image with the EGM. A slightly larger area AFM scan is also presented below in Figure 7-33.

In Figure 7-33, there is also a clear indication of resist collapse. It was noted that this was a side-effect of over-exposure/development nevertheless very interesting, as resist collapse requires a very high aspect ratio and hence such collapse with EIL has never been thought possible earlier. It is necessary to also point out here that resist collapse is due to the amplification of the imperfect minima (nulls) in the interference pattern. Conventionally with interference lithography, imperfect nulls only contribute to the background exposure. However, as the effective reflection coefficient from the EGM amplifies/enhances all signals (even the imperfect minima of the interference pattern), and redistributes energy to the bottom of the resist, collapse takes places. The presence of imperfect minima was noted and discussed in Chapter 3. The AFM scans demonstrate aspect ratios as high as 1.8. Such results are the first of their kind to be reported here and we believe that with the use of a more robust solid immersion interference lithography system such as the Amphibian^{TM} [148] the results could also in fact be demonstrated at $\lambda = 193$ for a *NA* of 1.85.

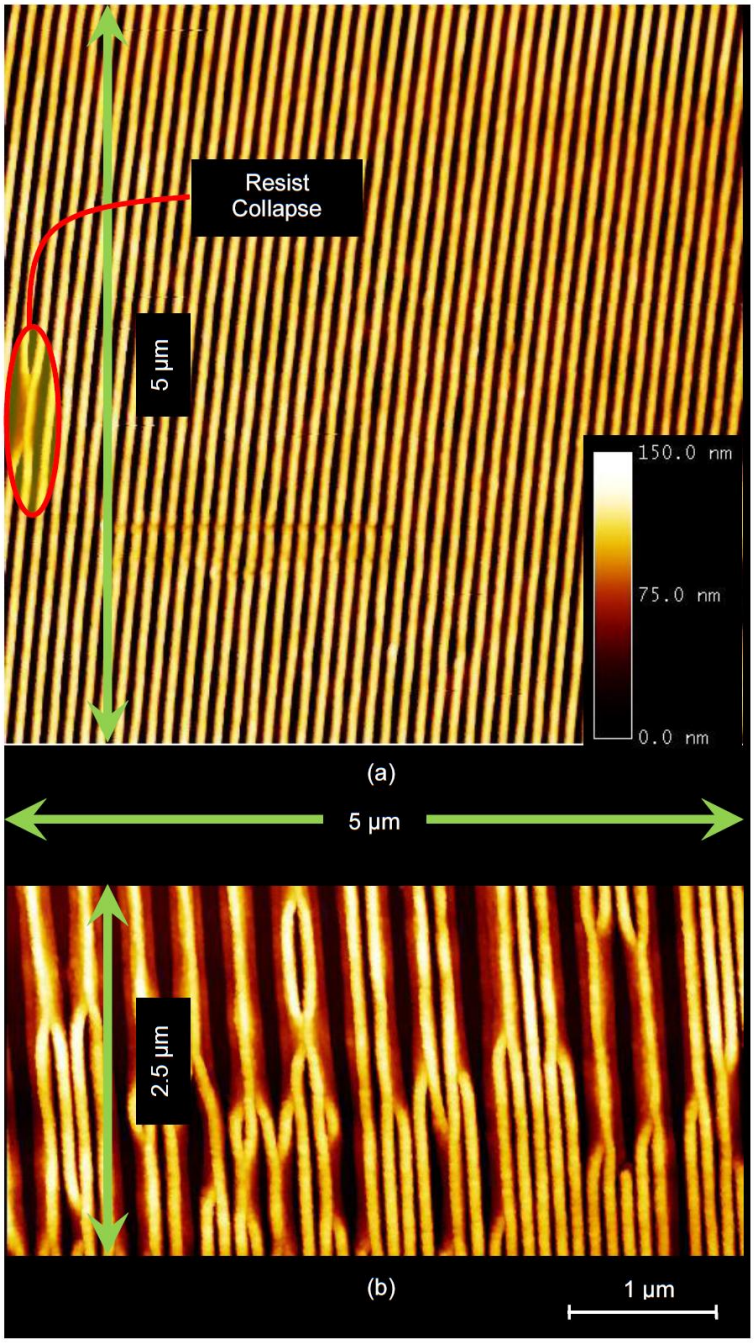

Figure 7-33 – Larger area AFM Scans demonstrating resist collapse with EIL using SILMIL using the imaging stack of Figure 7-26 (b), high aspect ratio structures imaged at a *NA* of 1.824 at λ = 405 nm with pattern half-pitch ~ 55.5 nm (a) A 5 µm by 5 µm AFM scan showing some resist collapse (b) A large area scan cropped to 5 µm by 2.5 µm demonstrating significant resist collapse, a result of over-dosage/exposure/development

This sub-section is summarized by presenting some SEM scans of the above samples. The SEM scans also demonstrate deeper features, however, cleaving the quartz (that has no regular cleave axis) substrate followed by gold deposition (to prevent charging due to oxide layers) on the cleaved edge, has in some cases reduced the visibility of such depths. The cleaving procedure was required to view cross-sectional profiles. The effects of charging needed to be reduced as otherwise they result in image drift, lack of resolution, inaccuracy in measurements and continuous aperture misalignment and stigmation. All of these act to degrade the final image that is recorded. A total of seven-hundred and eighty SEM scans were captured out in an attempt to measure the enhancement in image depths while a process was being developed to reduce the effects of charging when using a quartz substrate (described briefly in Chapter 3). Some of these which show promise are presented below. Firstly, the SEM plan views are presented in Figure 7-34. It is important to note that there are still issues with bridging faults and line-edge roughness that are evident from these images. Upon a closer inspection of Figure 7-34, the bridging fault lines appear to follow a periodic pattern superimposed over the main pattern at an angle of ~80 degrees. It is likely that such is the result of unwanted interfering beams in the SILMIL system (e.g. from prism-edge scattering) and hence could be engineered out with the design of a better solid-immersion experimental test-bed.

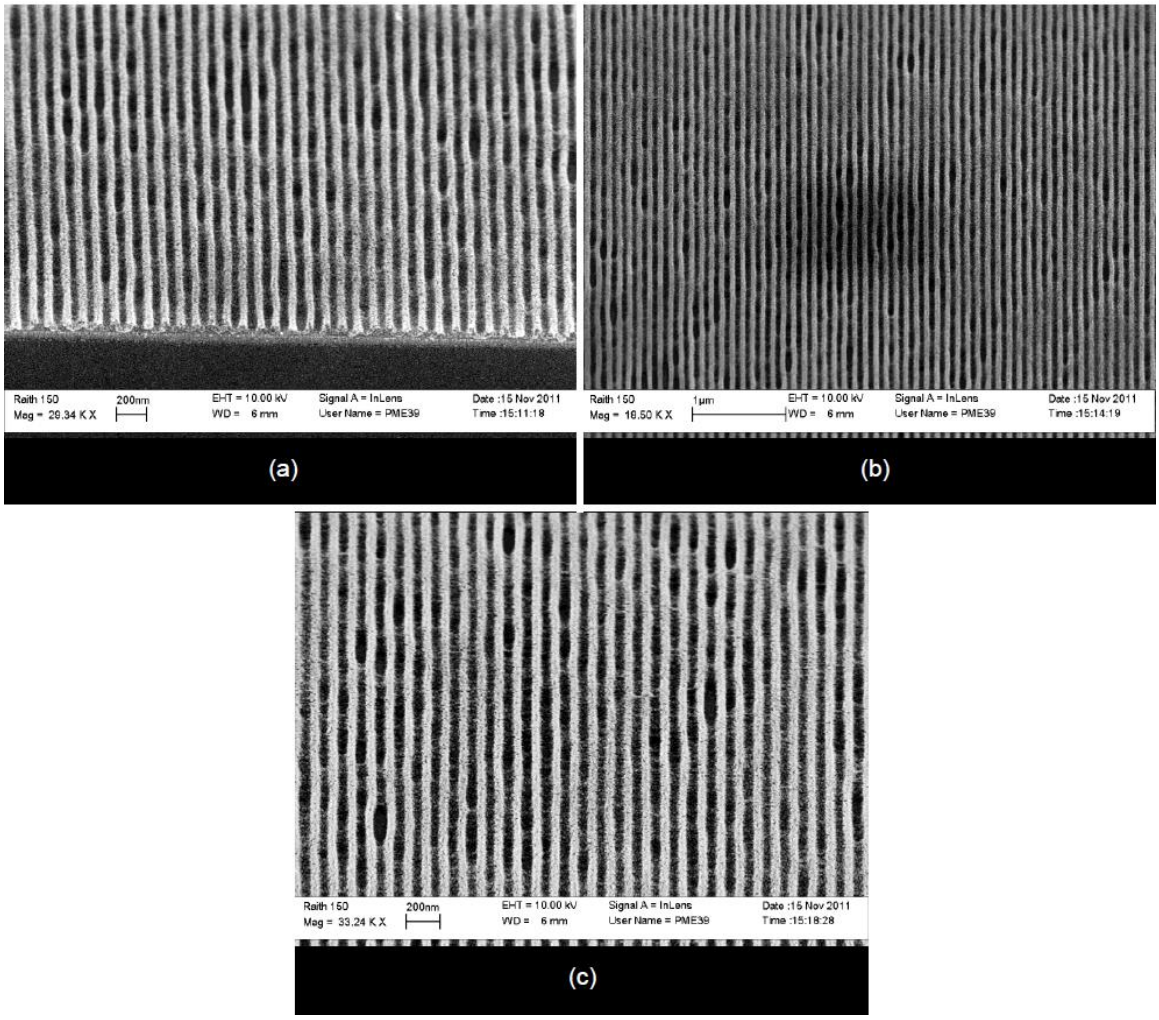

Figure 7-34 - SEM plan views, at PD of 2.5 mW-min, *NA* = 1.824, λ = 405 nm, EIL using SILMIL using the imaging stack of Figure 7-26 (b), Resulting half-pitch ~55.5 nm (a) – (c)

Figure 7-35 - Figure 7-37 show various cross-sectional SEM scans and demonstrate aspect ratio of high as 1.58, 1.72 and 1.84, in accordance with the results of the AFM scans. The following sub-section shows image formation when a non-ideal EGM (i.e. one that results in a low figure of merit (FoM) image) is used instead to demonstrate the effects of reduced evanescent coupling.

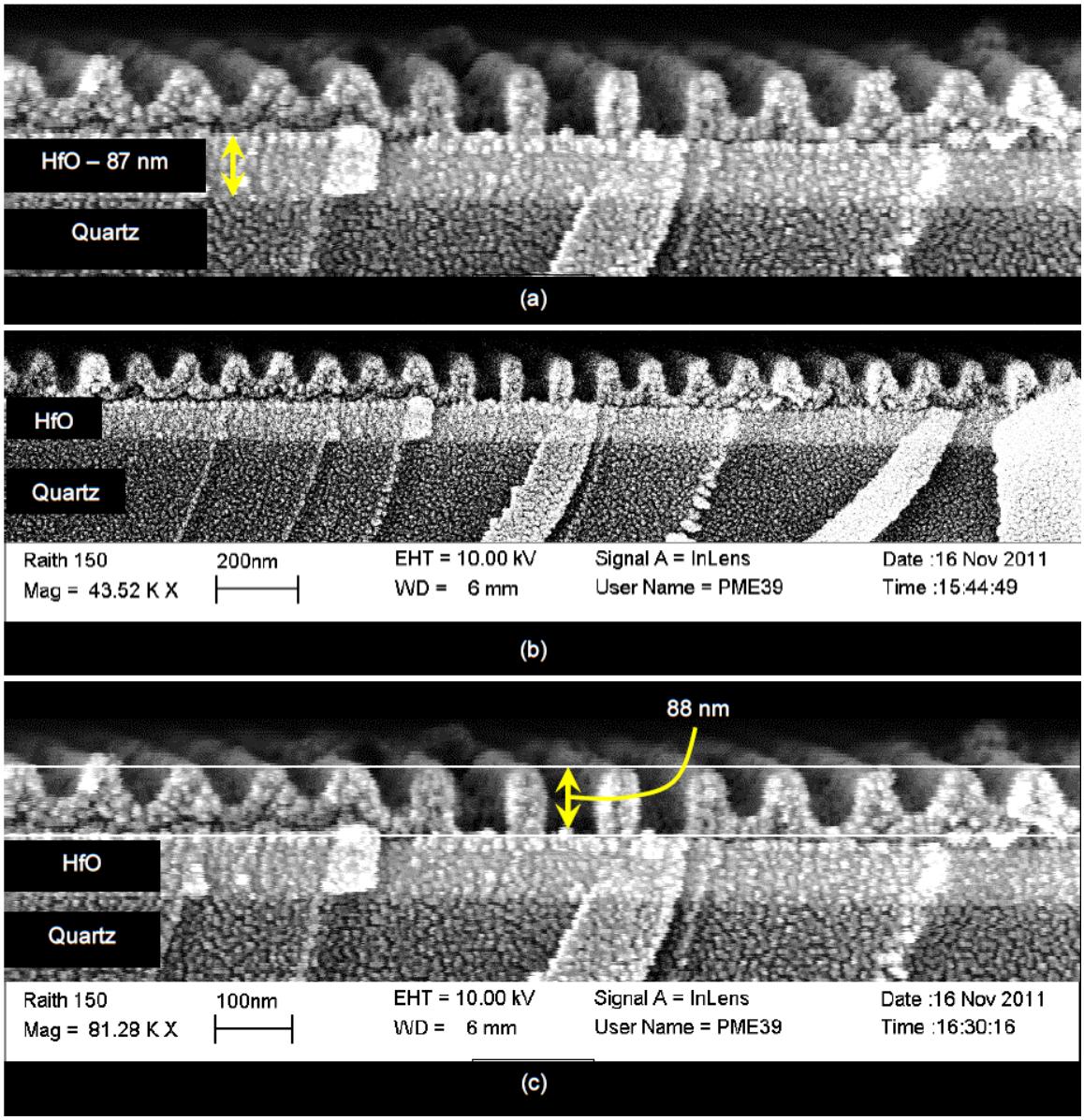

Figure 7-35 - SEM cross-sectional views showing tall standing structures, at PD of 2.5 mW-min, *NA* = 1.824, λ = 405 nm, EIL using SILMIL using the imaging stack of Figure 7-26 (b), Resulting half-pitch ~55.5 nm, with pattern depth ~88 nm (High Aspect Ratio of ~1.58). Note cleave marks on the Quartz substrate - (a) Scan depicting ~87 nm HfO layer thickness (expected 90.3 nm through ellipsometry, see Figure 7-26 (b)), (b) Scan with lower magnification and higher contrast (c) Annotated scan showing pattern depth

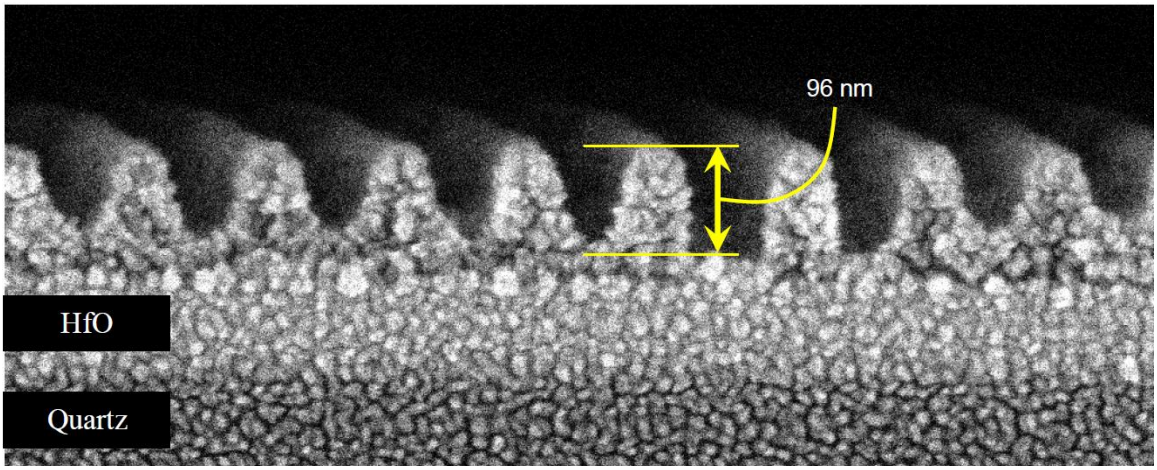

Figure 7-36 - SEM cross-sectional views showing tall standing structures, at PD of 2.5 mW-min, *NA* = 1.824, λ = 405 nm, EIL using SILMIL using the imaging stack of Figure 7-26 (b), Resulting half-pitch ~55.5 nm, with pattern depth ~96 nm (High Aspect Ratio of ~1.72).

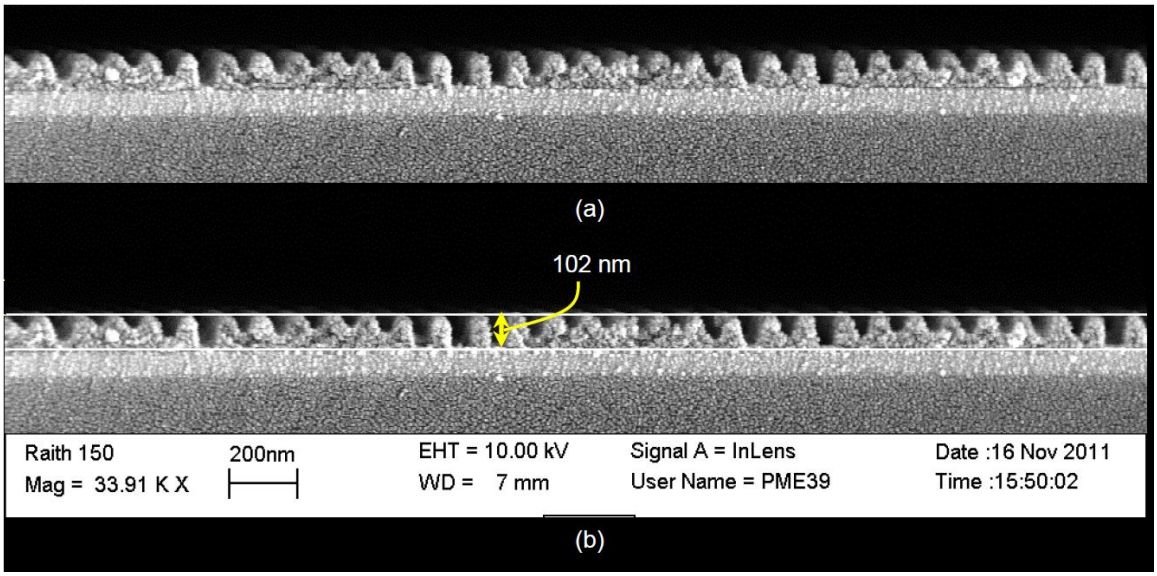

Figure 7-37 - SEM cross-sectional views showing tall standing structures, at PD of 2.5 mW-min, *NA* = 1.824, λ = 405 nm, EIL using SILMIL using the imaging stack of Figure 7-26 (b), Resulting half-pitch ~55.5 nm, with pattern depth ~102 nm (High Aspect Ratio of ~1.84). (a) Un-annotated scan (b) Annotated scan depicting ~102 nm pattern depth ~ initial resist depth

7.6.2 Reduced Evanescent Coupling from a non-ideal Effective Gain Medium (EGM) underlay

Here, the case of a non-ideal EGM is explored. We present the raw ATR plot that allowed us to deduce the refractive index of the HfO film, FEM simulations using COMSOL and finally experimental evidence. Using this model, in addition to information obtained from the SILMIL experiments, we predict an image depth that the non-ideal EGM is capable of providing and compare this with the image depth achieved using experiments. The stack consists of a 64 nm layer of HfO deposited on quartz. ATR experiments are carried out using the stack depicted in Figure 7-38.

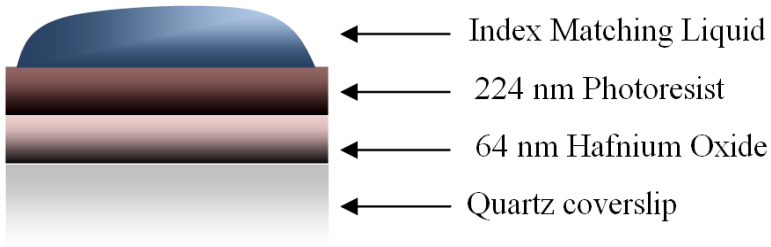

Figure 7-38 – Stack for ATR experiment to determine HfO layer refractive index. The EGM is a non-ideal one which will be used for EIL using SILMIL to demonstrate reduced evanescent coupling

The measured raw ATR data is presented below in Figure 7-39 and the resonant dip lies at a ~50^{o} exterior incidence angle, indicating that the HfO layer refractive index is ~1.95 upon comparison with the simulated ATR plot (not shown).

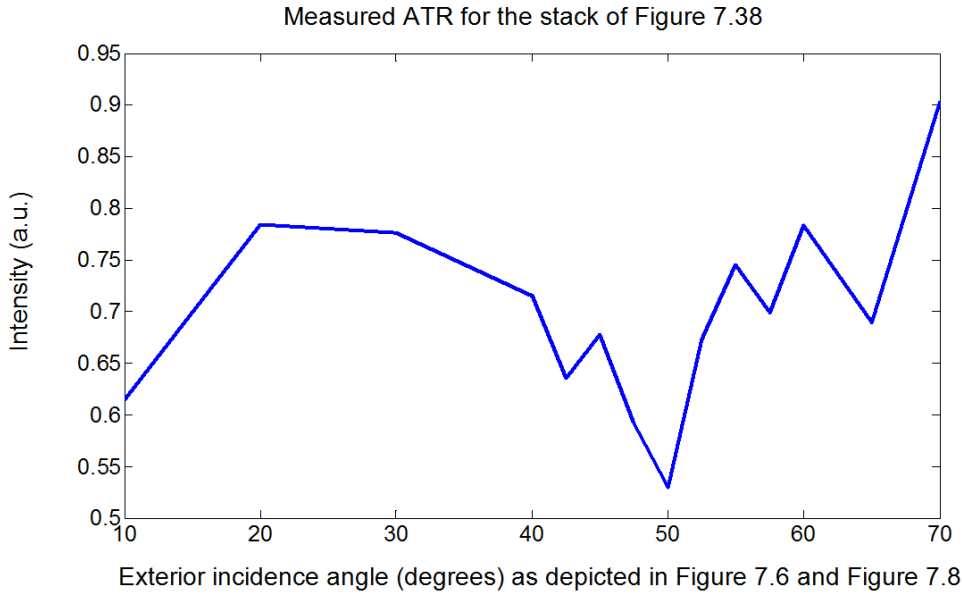

Figure 7-39 - Measured ATR for the stack of Figure 7-38 indicates a HfO layer refractive index of 1.95 upon comparison with a simulated ATR plot (not shown)

For imaging into ~105 nm of photoresist, the FoM for a stack with 64 nm of HfO (n = 1.95) is only 0.5154 and this point has been marked with a red cross on the surface plot of Figure 7-16. Clearly this will make for a non-suitable imaging stack, but this is exactly what is required to demonstrate reduced evanescent coupling! This is better achieved by making use of a thinner resist. Consider the proposed imaging stack in Figure 7-40 with a 69 nm thin layer of photoresist, this now has a FoM of ~1.024.

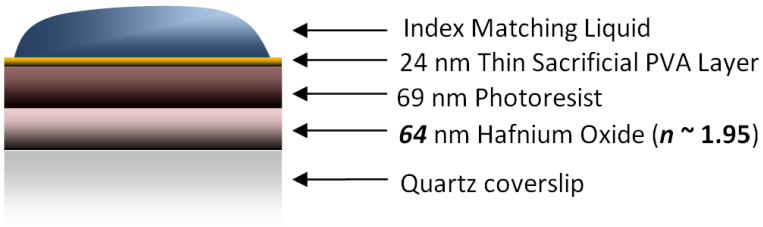

Figure 7-40 – Imaging stack to demonstrate reduced evanescent coupling

The FEM simulations using COMSOL for the image formation within the resist are shown in Figure 7-41 alongside a comparison with no EGM underlay (i.e. semi-infinite photoresist). The reduced evanescent coupling is visible here when compared with the simulations in Figure 7-28 (b). Note that the ratio between the maxima to minima (or peak to null ratio) is higher for case with an EGM underlay (compared to without the underlay) even though the expected image depth is not considerably large. The experiment involved exposing the imaging stack of Figure 7-40 at a PD of 2.5 mW-min with λ = 405 nm at a *NA* of 1.824.

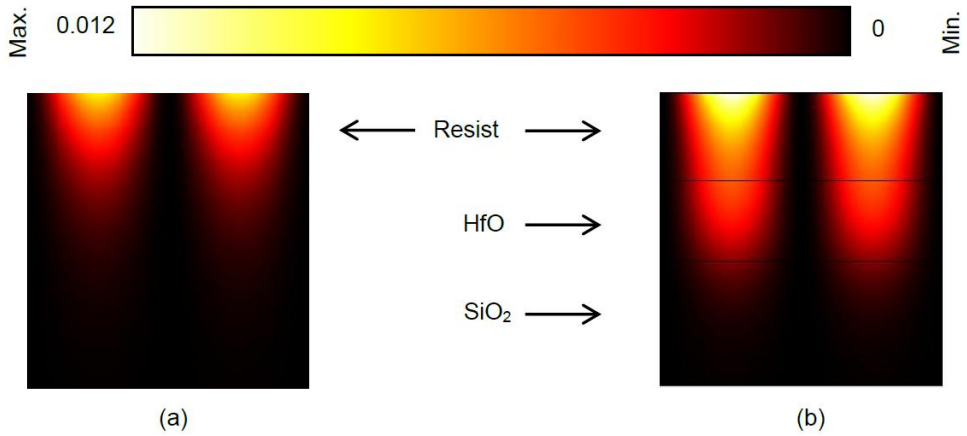

Figure 7-41 – FEM Simulations using COMSOL depicting the image formation into 69 nm of resist (a) without and (b) with the presence of a non-ideal EGM made up of 64 nm of HfO (n = 1.95) on a quartz substrate

AFM scans were carried out and these are illustrated in Figure 7-42. The reader may compare these scans with the scope plots presented in Figure 7-32 - Figure 7-31 and AFM scans presented in Chapter 3.

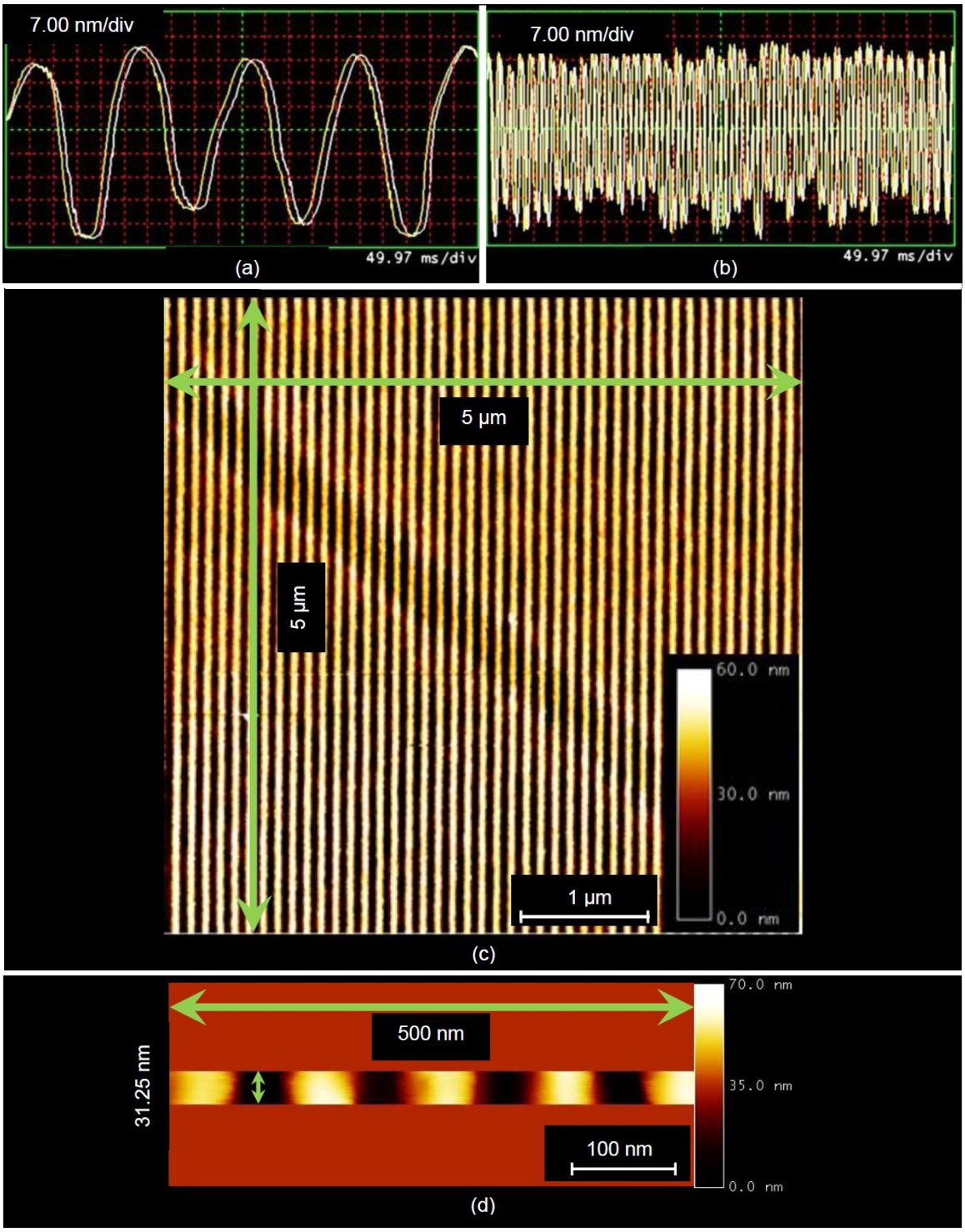

Figure 7-42 – AFM Scope plots & Scans demonstrating limited depth (~45-54 nm) when a non-ideal EGM is employed. As expected some enhancement is still clearly visible as a wider trench is now imaged but this is not as much as with a more ideal EGM (see Figure 7-32-Figure 7-37**)**. Parts (a) and (b) are AFM scope plots, part (c) A 5 µm by 5 µm AFM scan, while part (d) is a smaller area (500 nm by 31.25 nm) AFM scan

The scope plots and AFM scans reveal that the image has not been exposed all the way throughout the depth of the photoresist (as one would expect from a non-ideal EGM) and the pattern depth is only ~45 nm to 54 nm. However this is still an improvement over the 30-40 nm image depths that conventional EIL with SILMIL has offered (see Chapter 3). The AFM tip is now clearly able to image the trench of the pattern, this is a large improvement. It is due to the fact that there is a higher peak to null ratio that allows resist development over a wider area, while the dosage due to the null of the interference pattern stays below the development threshold.

7.6.3 Effects of Dosage variation & Analysis

The case study is summarized and this chapter concludes by experimentally demonstrating and exploring the effects of dosage variation on EIL imaging with an EGM underlay. The imaging stack depicted in Figure 7-43 was used for this. Once again, the ATR method was used to determine the index of the HfO layer, but the raw ATR measurements are not presented again. Referring back to Figure 7-16, one may see that a green cross marks the FoM for this particular stack, which is FoM = 1.394; this is clearly suitable for imaging. Figure 7-44 and Figure 7-45 present the AFM scans and corresponding scope plots for a dosage variation with PDs of 1, 2, 3, 4 and 6 mW-min. Higher PDs did not result in any new information, as the reader will be able to soon deduce and so are not presented here.

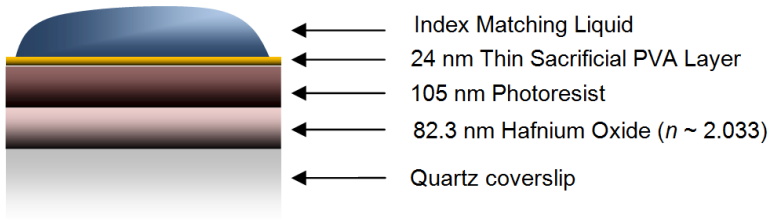

Figure 7-43 – Imaging stack used to carry out experiments with dosage variation

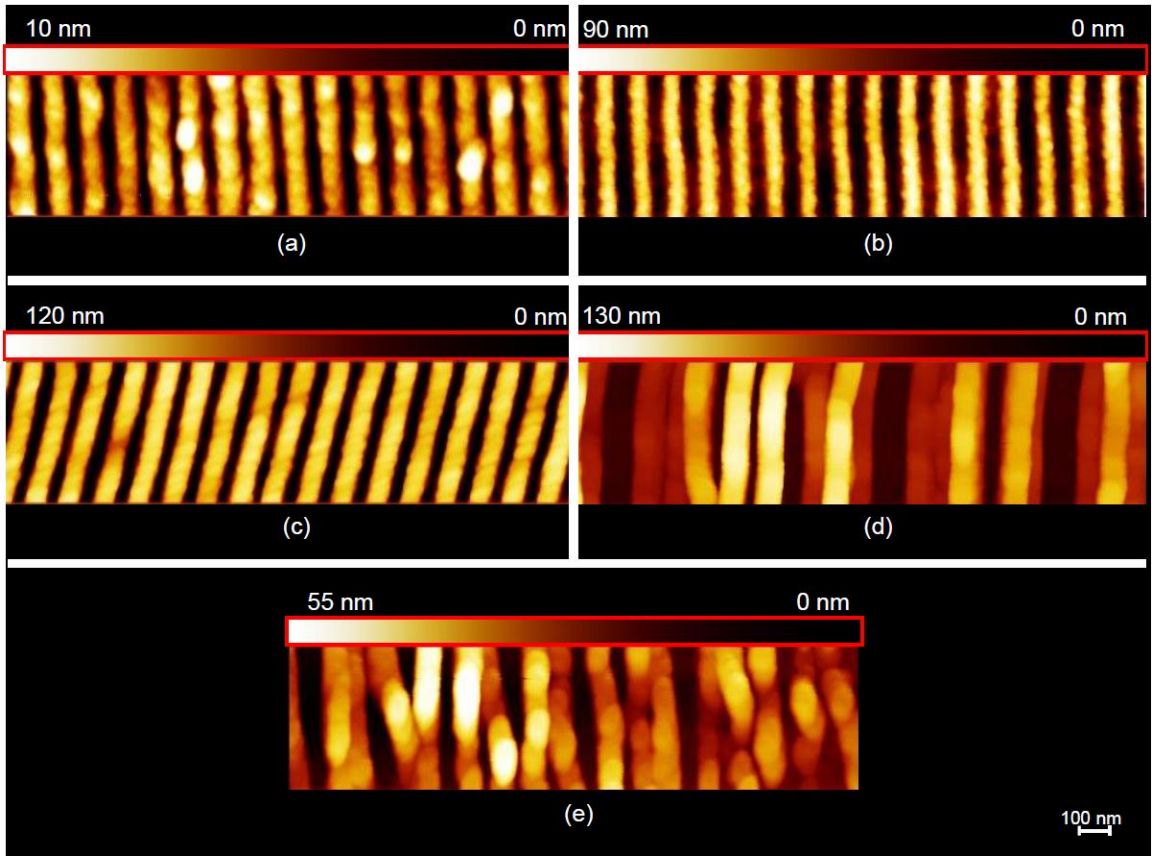

Figure 7-44 - EIL with SILMIL using the imaging stack of Figure 7-43. Pattern quality and depth demonstration via AFM scans (2µm by 0.5µm) at Pseudo-dosages (PDs) of (a) 1 (b) 2 (c) 3 (d) 4 (e) 6 mW-min. PDs larger than 3 mW-min show significantly more resist collapse and little or no pattern modulation

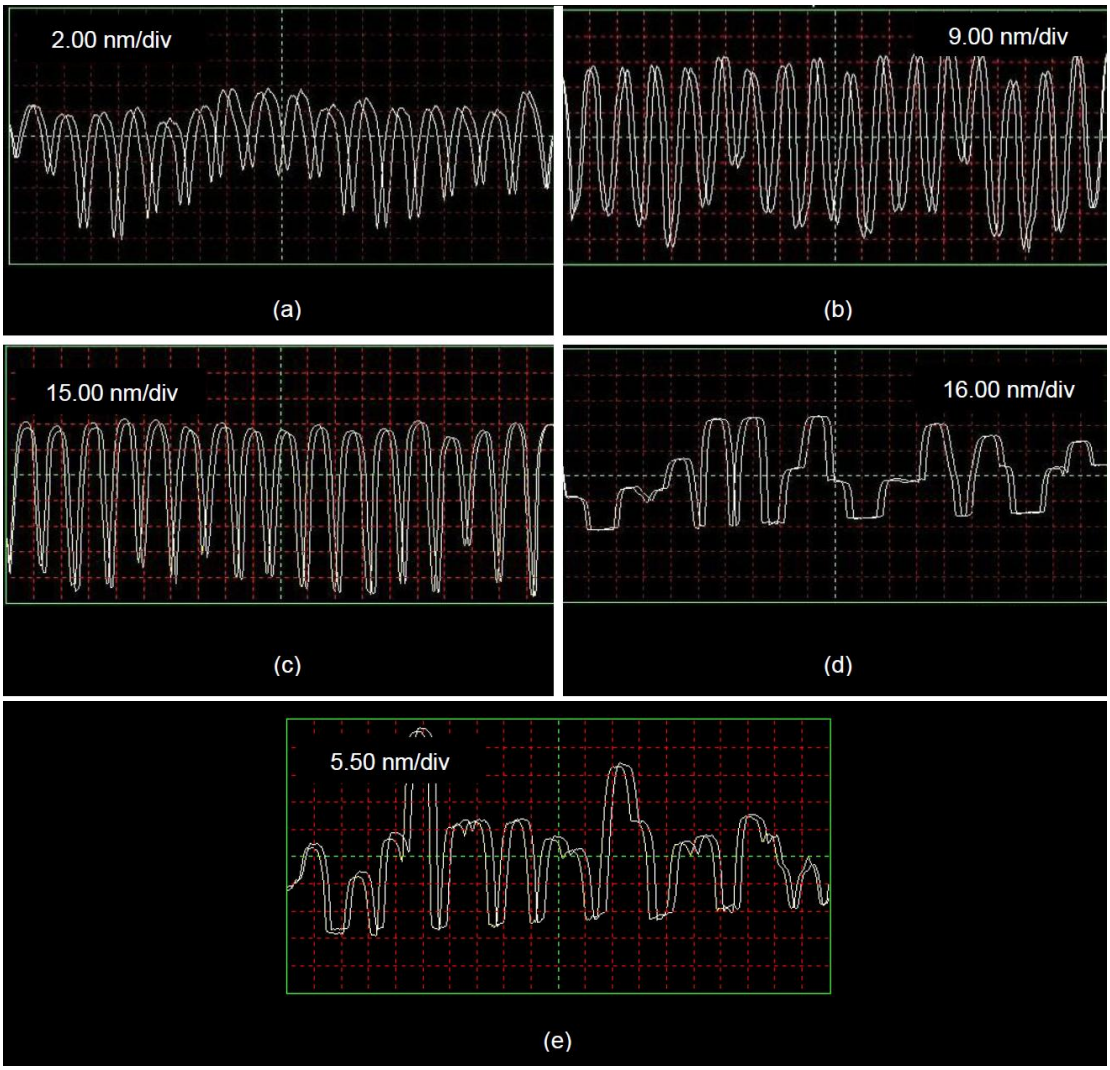

Figure 7-45 - EIL with SILMIL using the imaging stack of Figure 7-43. Pattern quality and depth demonstration via 2µm AFM cross section scope plots at Pseudo-dosages (PDs) of (a) 1 (b) 2 (c) 3 (d) 4 (e) 6 mW-min Once again, PDs larger than 3 mW-min show significantly more resist collapse and little or no pattern modulation

Figure 7-46 - Figure 7-48 depict further AFM plots and scans for PDs of 3,6 and 8 mW-min to highlight variations in the results or demonstrate better picture quality. From Figure 7-45 (a) and (b), it is noted that a PD of 1 or 2 mW-min is not sufficient to allow a full development through the 100 nm resist depth, whereas a PD of 3 mW-min (see Figure 7-45 (c) and Figure 7-46) shows a full development but in some cases also demonstrates resist collapse indicative of over dosage. This is in accordance with the results from section 7.6.1.2, which demonstrated that a PD of 2.5 mW-min was sufficient to allow a full development with minimal instances of resist collapse (of course this comparison is only permitted since the two imaging stacks, Figure 7-26(b) and Figure 7-43 have very similar FoMs of ~1.36 and ~1.39 respectively).

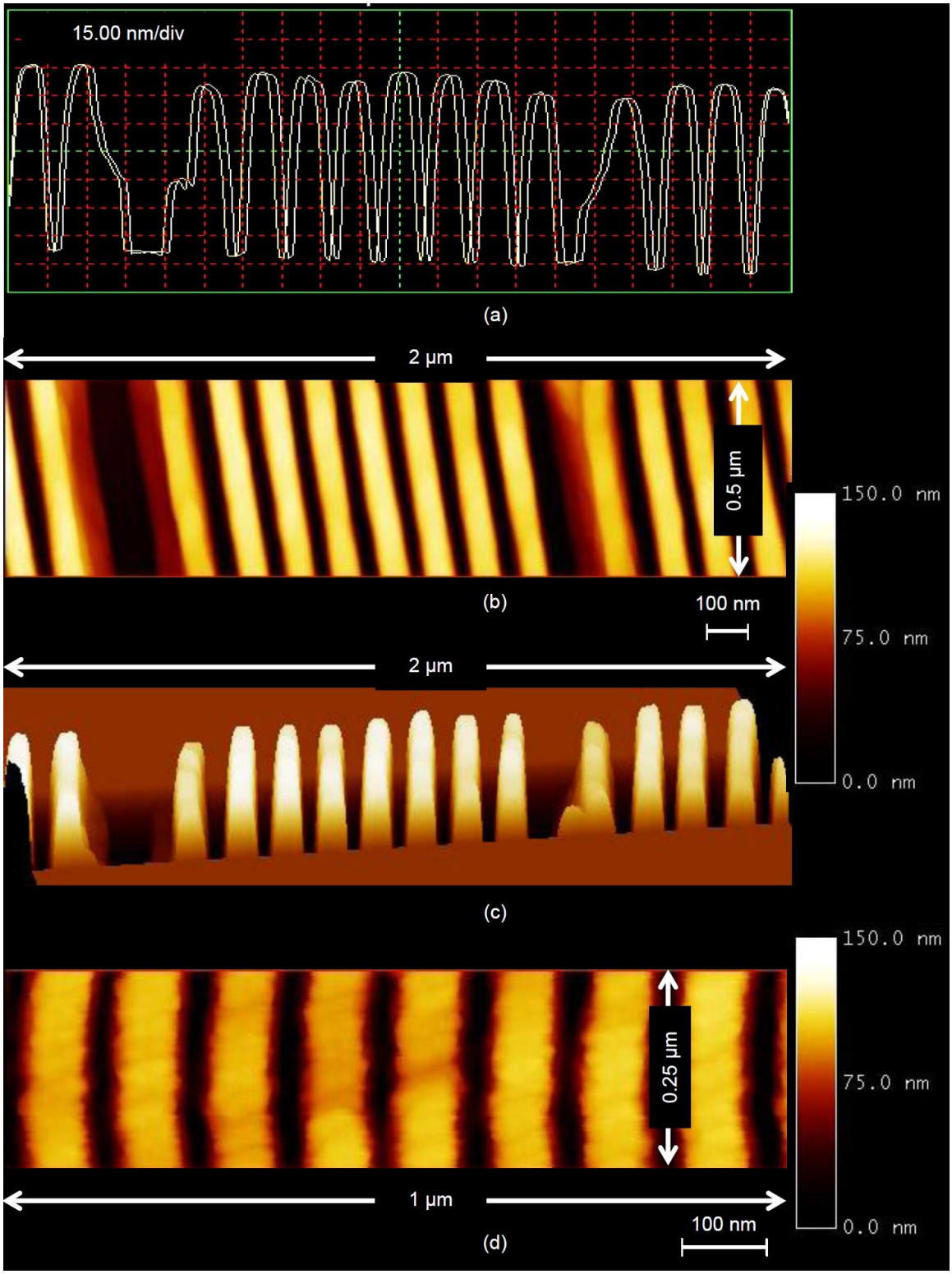

Figure 7-46 - EIL with SILMIL using the imaging stack of Figure 7-43. Pattern quality and depth demonstration for a PD of 3 mW-min only (a) 2 µm AFM scope plot showing some resist collapse (b) corresponding 2 µm by 0.5 µm AFM scan (c) corresponding perspective view for the scan in (b) and (d) separate smaller area 1 µm by 0.25 µm scan

At PDs > 3 mW-min, significant resist collapse is noted. This is seen in Figure 7-44 and Figure 7-45 parts (d) and (e) and from the scope plots in Figure 7-48 (c) and (d). Several scans also show a show a complete lack of modulation, one such example is depicted in Figure 7-47. In fact, the rubble left behind from resist collapse largely contributes to the topography measured by the scope plots in parts Figure 7-45 (d), (e) and Figure 7-48 (c), (d).

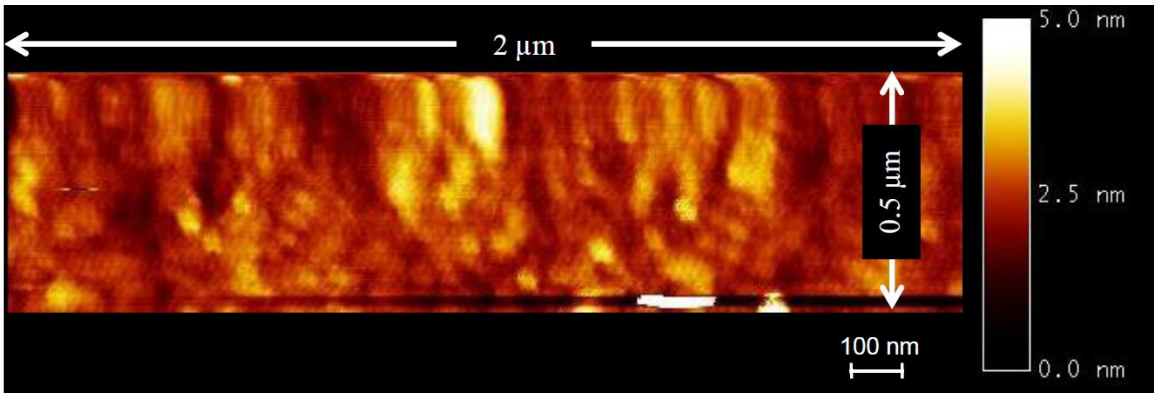

Figure 7-47 – EIL with SILMIL using the imaging stack of Figure 7-43. Alternative AFM scan for a PD of 6 mW-min showing no pattern

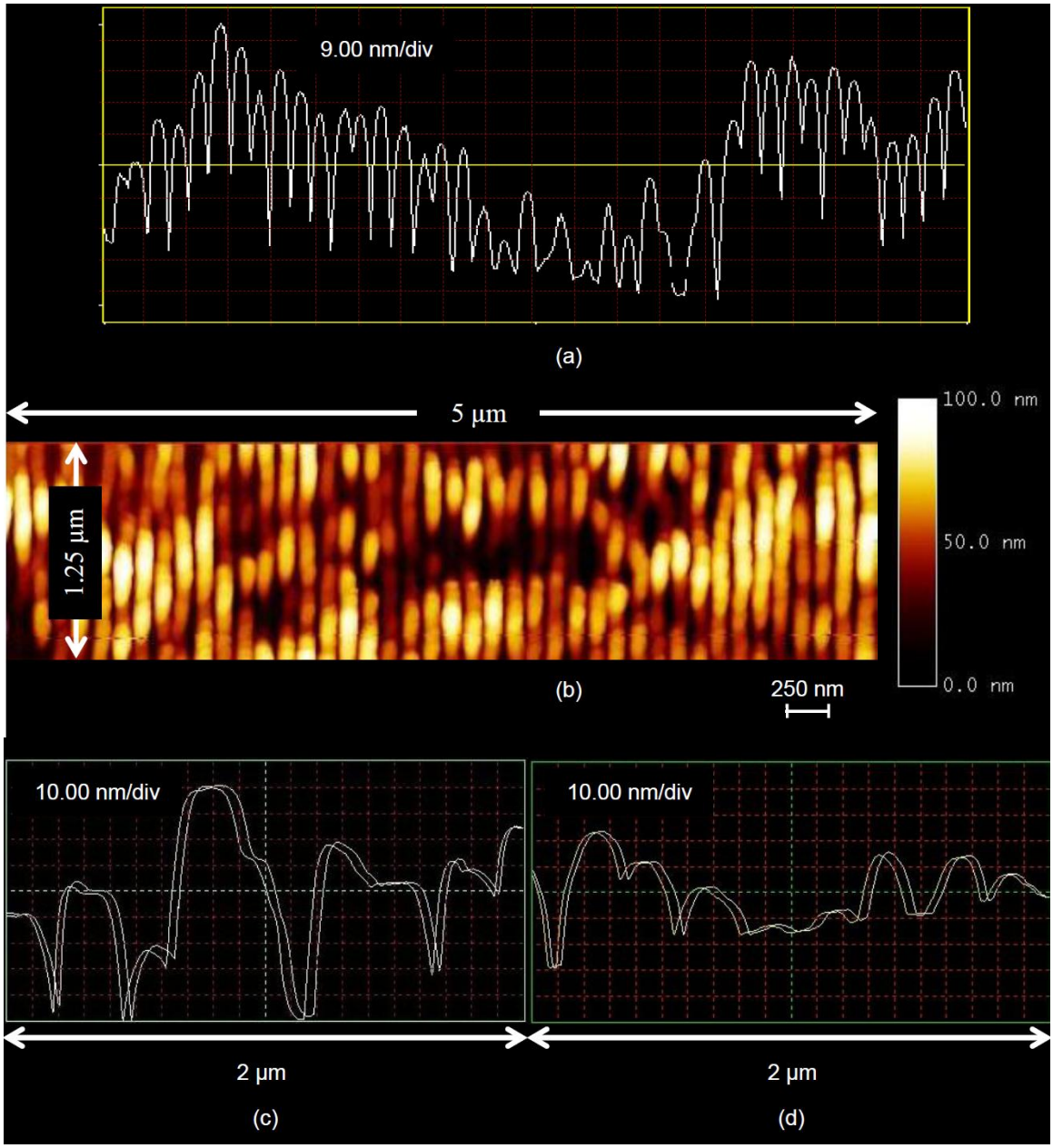

Figure 7-48 – EIL with SILMIL using the imaging stack of Figure 7-43. Pattern quality and depth demonstration for a PD of 8 mW-min only (a) 5 µm AFM scope plot showing chaotic pattern modulation (b) corresponding 5 µm by 1.25 µm AFM scan (c) and (d) separate 2 µm AFM scope plots. Overall most scans depicted resist collapse and some areas depicted chaotic modulation

The information regarding pattern depth and the amount of resist removed is summarized in Figure 7-49 for PDs 1 to 8. A short discussion is presented here to highlight the trends that have been noted. This plot may be compared with its analogous plot, Figure 3-28 in Chapter 3, as the same procedure was used to create this plot.

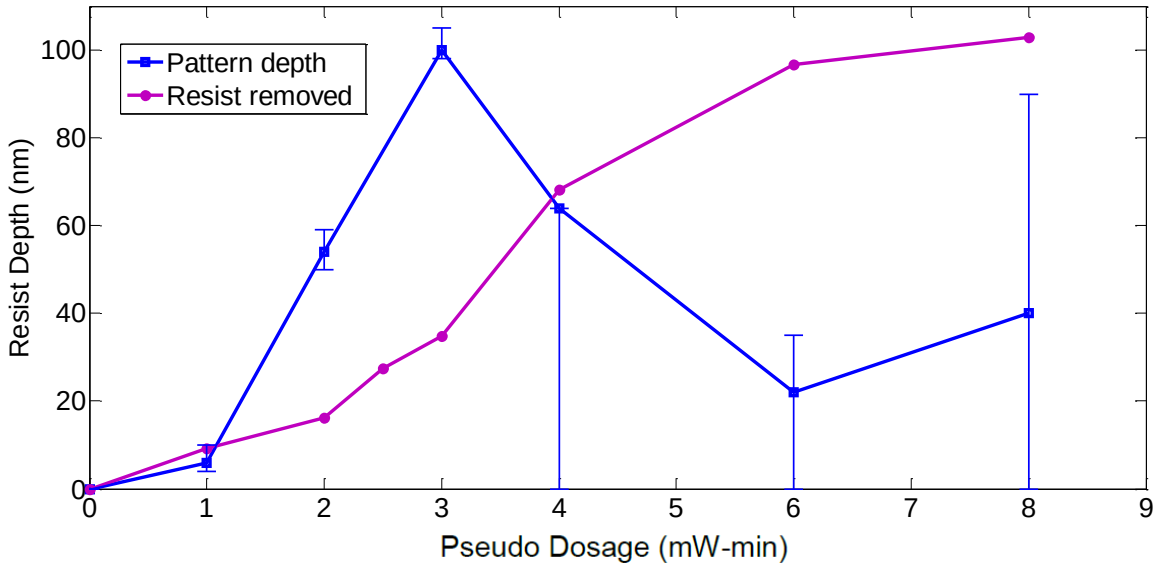

Figure 7-49 - Summary of Figure 7-44 - Figure 7-48, showing the depth of the grating patterned into the resist (square markers) with uncertainties as well as the depth of resist removed (circular markers) for EIL using SILMIL with the imaging stack from Figure 7-43 that utilizes a specially designed Effective Gain Medium (EGM) underlay

The pattern depth for the PD = 4 mW-min case (Figure 7-44 (d)) is much shallower than the PD = 3 mW-min case (Figure 7-44 (c)). This is due to the background exposure component (the result of imperfect minima, see the section 3.6.2, Critique 2 in Chapter 3 for an explanation as to why this is so) that is acting to develop away more resist from the top than it does at a PD of 3 mW-min Note also that the background exposure effects the pattern in two places now, namely the top and bottom of the resist. As this background exposure dosage increases, so does its amplification at the bottom of resist, and the system enters the onset of resist collapse. This phenomenon is noted here by us for the first time.

Hence, at PDs higher than 4 mW-min, there is no proper pattern modulation and the topography is largely dominated by rubble from resist collapse and any modulation patterns that exist due to under exposure locally in that region, i.e. due to system flaws (or noise as was described in Chapter 3) and possibly photoresist adhesion issues.

Since there is an undesired background exposure in the system, there will be a certain thickness of resist that is removed (or eaten away). As we now know, there will also be some null amplification in this system from the EGM underlay. Hence, for such a system a step-like response is expected with respect to the dosage i.e. no resist removed for PDs < 4 mW-min and all resist removed for PDs >= 4 mW-min. However, as the system is imperfect, not all areas are uniformly exposed. In addition, the method used to measure the resist removed, involves scratching away remaining resist and using a profilometer to scan the surface. Hence, this resist thickness measurement is also dominated by collapsed rubble at higher PDs

as will be evident in the plots of Figure 7-44 to Figure 7-48. This results in a sigmoid type response or approximate step like curve (resist-removed, see Figure 7-49) with respect to the dosage as expected. The pattern depth is seen to increase linearly from a PD of 1 mW-min to a PD of 3 mW-min, after which significant resist collapse occurs and there is significant uncertainty in the actual pattern depth (the ideal pattern depth for higher PD would be constant due to no background exposure component).

7.7 Summary

The primary goal of this chapter was to demonstrate the operation of a carefully tuned waveguide type effective gain medium (EGM) underlay in enhancing the depth of an image that has been created using evanescent interference lithography (EIL) by making use of the SILMIL system described in Chapter 3.

First the EGM was introduced; this is made up of a layer of HfO on SiO_2. An image qualification metric, figure of merit (FoM) was also introduced by making use of the imaging criteria from Chapter 6. A method was then introduced to characterize the optical properties of a particular EGM underlay; this was the attenuated total reflectance (ATR) method. The optical properties of the HfO layer in this particular underlay were measured using the ATR method and it was found that the use of this stack with ~105 nm of photoresist would result in a sufficiently high FoM of ~1.35 for imaging high aspect ratio structures at a *NA* of 1.824 at λ = 405 nm, the parameters of the case study that are also used for the rest of the experiments. This prediction was well supported and simulations were presented alongside AFM scans, scope plots and SEM scans. The experiments resulted in structures with aspect ratios as high as 1.84, i.e. 105 nm tall structures with a 55.5 nm half pitch using λ = 405 nm. While the maximal image depth in Chapter 3 was shown to be between 33-40 nm, here an image depth of 105 is obtained for the same dosage. This result boasts a clear, measurable and repeatable enhancement with the use of an effective gain medium surface state.

A method was then suggested to compensate for the resonance of an ill-designed EGM underlay. Resonance compensation was carried out by using a thin layer of PMMA, a low index spin on polymer. This fits well into the general idea of the thesis, where the amplitude and phase of the effective reflectivity of stack is adjusted so that the EGM surface state falls at the location that would allow maximal enhancement of the evanescent image created at a *NA* of 1.824. Multi-variable parametric searches were run and were used to define the optimum thickness of PMMA that would allow a maximal FoM to be attained. It was also shown that the allowable operating region was significantly widened using this approach. Experimental evidence of resonance compensation was also provided using the ATR method.

Another example was experimentally demonstrated to show reduced evanescent coupling when a non-ideal EGM was used. The results of this experiment showed that despite thinner resist being used, the resist did not develop all the way through to the bottom. However, enhancement over the non-EGM case was still clearly visible as the trench of the pattern was now measured using an AFM. This is owing to the fact that the use of an EGM considerably improves the ratio between the interference maxima to interference minima with the TE polarization and since the interference minima dosage lies below the development threshold, a wider trench forms than it would otherwise with conventional EIL.

Finally the effects of dosage variation on pattern modulation depth and resist depth were also analyzed. Beyond a pseudo-dosage (PD) of 4 mW-min, resist collapse took place owing to a previously discussed flaw in the SILMIL system that introduces imperfect interference minima (non-zero nulls). This electric fields contributing to the null are also amplified and redistributed by the EGM in the resist. As a result, beyond a particular PD (of 4 mW-min), the resist structure loses traction of the substrate and collapses. At the same time, the null also causes surface development of the resist (as is the case with conventional background exposure). Hence, to reiterate this, the uniqueness of the EGM enhanced imaging case is that, conventional background exposure (the result of imperfect nulls) now takes place both as a surface development and as a bottom development of the resist through energy redistribution in the resist cavity. Hence, one would expect that beyond a particular PD threshold, all of the resist lift away and that a plot of the *resist removed vs. PD* approximate a step function. This is in close accordance with the results, discrepancies with an actual step function may be attributed to several factors such as the presence of collapsed rubble on the substrate when the resist remaining measurement is made, the absence of a hard development threshold and the fact that there is a slight variation in the exposure dosage over the area of the sample due to a non-uniform thickness index matching liquid (IML) layer.

For a PD of 3 mW-min, clean tall standing structures were achieved, and some of these were at the onset of resist collapse, indicating that a PD of 2.5 mW-min might suffice. The pattern depths for PDs larger than 3 was difficult to measure and had a strong uncertainty associated with it. At higher PDs the pattern appears to be ‘noisy’. The source of this noise was pointed out as an in chapter discussion in Chapter 3 and it was noted that this is likely due to non-uniform thickness of the IML layer. Such a layer results in spatial variation of the intensity of the interference pattern, with the resulting noise being visible only at higher doses due to the increased sensitivity of the resist at such doses (point of operation on a contrast curve). It appears that this ‘noise’ has a stronger influence here due to the amplification provided by the EGM. This results in a large uncertainty of the pattern modulation at higher PDs. With this, the chapter is concluded and a final chapter follows and concludes the thesis highlighting and summarizing the novelties of the work carried out, the key results and its future scope.

Chapter 8. Conclusions & Future Work

In this thesis a novel near-field technique was developed to considerably enhance the depth of field of images created using evanescent interferometric lithography, a high resolution interferometric lithography technique. The work carried out was presented in four sections.

The first of these was largely experimental and described in Chapter 3. Chapter 3 detailed the design, development and experimental demonstration of a novel solid immersion interference lithography test-bed to allow evanescent interference lithography (EIL). This test-bed is titled solid immersion Lloyd's mirror interference lithography (SILMIL). SILMIL is a key result of this thesis. While EIL allows considerably high resolutions, the depth of field of the image in the resist and hence the aspect ratio (height to width ratio) of patterns is too low to allow for pattern transfer which is necessary for lithographic patterning. The subsequent chapters developed a solution to address this problem.

The second section, Chapter 4 introduced the modeling and simulation techniques that have been used throughout the thesis to study interference lithography in the evanescent regime. Chapter 4 detailed the development of the T-Matrix method and modifications that have been made to allow visualization of the field evolution in a 2D plane.

The third section comprised of Chapters 5 and 6 and these made up the theoretical sections of the thesis. Here new methods were presented to allow considerable depth of field enhancement for evanescent interferometric lithography by making use of a carefully designed reflective material underlay below the resist. They proposed key ideas regarding the physical mechanism behind evanescent image enhancement using material underlays, the use of the unique analysis of the Fresnel reflection equations that results not only in the known solution but also solutions that were previously unknown and derivation of the limits of EIL. One of these results was a novel solution, a hypothetical surface resonance resulting from a fictitious gain medium underlay as suggested by the equations to allow image depth enhancement for EIL. A further added novelty was showing how the behavior of this hypothetical medium may be mimicked and hence realized with the use of an effective gain medium constructed using several layers of naturally occurring materials. Stemming from this, a design proposal was also presented for an ultra-high *NA* of 1.85 imaging at the industry standard λ = 193 nm wavelength to allow imaging of super-resolved structures 26 nm half pitch at aspect ratios of ~3.2 or 83 nm image depth. It was shown that the design of

the requisite effective gain medium surface resonance may be realized using readily available materials such as aluminum oxide and silicon dioxide and standard thin-film deposition techniques.

The final section was Chapter 7. This combined aspects of all the three previous sections and experimentally demonstrated an image depth of field enhancement of > 2.5 times at an ultra-high *NA* of 1.824 imaging at λ = 405 nm wavelength by making use of hafnium oxide and silicon dioxide to construct the effective gain medium. Comparisons were made with the results of Chapter 3 and various parametric variations were used to demonstrate that the theory was sound. The results successfully demonstrated that the image depth limits of EIL may be considerably extended. The results are the first of their kind and demonstrate the necessary potential to make evanescent enhanced evanescent interferometric lithography attractive and of considerable interest to a wide audience of researchers. The remainder of this chapter details the work that has been carried out in the four sections and also presents their key results quantitatively.

8.1 SILMIL test-bed – Design, Construction and Experiments

A new solid immersion interference lithography test-bed called SILMIL was proposed. Successful demonstration of the design and operation of SILMIL was presented for λ = 405 nm using off-the-shelf equipment that is readily available to researchers. Patterns were imaged at a *NA* of 1.824 which was used as a case study. A pseudo-dosage (PD) of 2.5 mW-min was used and this resulted in line space patterns with a 111 nm pitch (55.5 nm half-pitch) with image depths of 33-40 nm or ~λ/10. This amounts to a maximum aspect ratio of only 0.72. Figure 8-1 illustrates a SEM plan view scan at a PD of 3 mW-min and Figure 8-2 illustrates a cross-sectional view for such a sample.

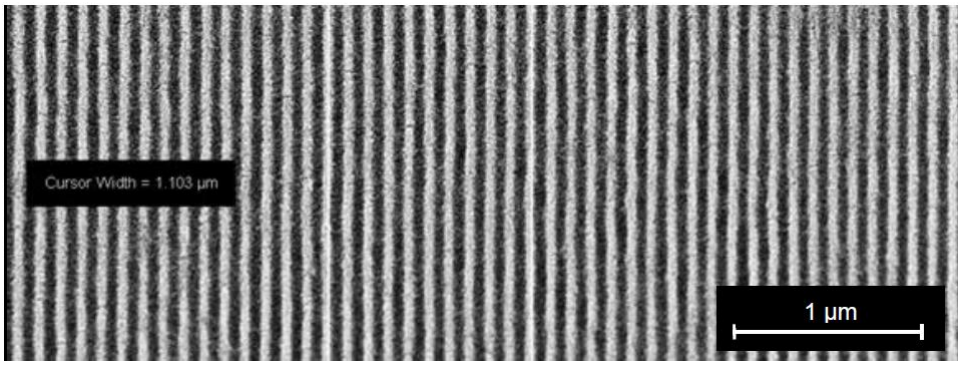

Figure 8-1 - SEM plan view at a PD of 3 mW-min, *NA* = 1.824, λ = 405 nm, conventional EIL using SILMIL, Resulting pitch ~111 nm (55.5 nm half-pitch)

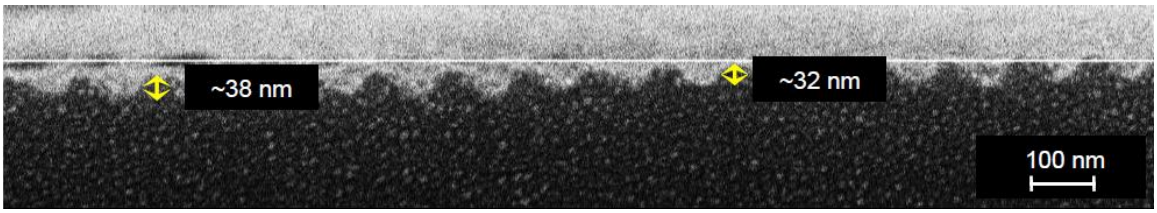

Figure 8-2 – SEM cross-sectional views at *NA* = 1.824, λ = 405 nm, conventional EIL using SILMIL, Resulting pitch ~111 nm (55.5 nm half-pitch) at PD of 3 mW-min, giving 30 – 40 nm image depths, i.e. a maximum aspect ratio of 0.72

At higher doses the image depth reached ~50 nm. Some limitations of the system include the introduction of background exposure and pattern degradation at higher doses. The former issue is believed to be the effect of unintentional focusing of the source beam that results in an intensity variation between the two beams that make up the interference pattern, thereby resulting in a background exposure. Pattern degradation at higher doses is believed to be the result of an improper layer of index matching liquid (IML) film. This introduces a spatial variation in the intensity of the interference pattern; this may be classified as added noise. At higher doses however, the resist sensitivity is much higher than it is at lower doses and hence the added noise contributes to pattern degradation. At lower doses, such problems were immeasurable and have allowed large area patterning of square areas of several 10s of microns.

8.2 Modeling & Simulation

The T-Matrix method was described in Chapter 4. Modifications were made to allow visualization of the full electric field intensity profile in the *x-z* plane. Evanescent interference lithography was modeled with considerable ease using such an implementation and the behavior of evanescent fields may then be studied at the interface of two media. MATLAB [179] was used to implement the technique, and this was successfully validated with implementations by other researchers and also with the use of a commercially available FEM program known as COMSOL Multiphysics [177]. Multi-variable parametric searches have been run using this implementation to optimize the result of image qualifying metrics and model the behavior of optical stacks comprising of real media and also of optical stacks consisting of artificial media primarily for the work carried out in Chapters 5, 6 and 7, but also in some amount for the work carried in Chapter 3.

8.3 Theory & Analytics

In Chapter 5, the motivation to understand the mathematical and physical basis for evanescent wave enhancements was introduced. This was done by showing how a material underlay beneath the photoresist may be used to enhance the field intensity before feeding it back into the photoresist medium.

It was then shown that further investigation requires the analysis of the Fresnel reflection equations to achieve a reflection much larger than unity.

It was found that this is possible in the evanescent regime when the material underlay is either a metal or a lossy dielectric; both of which support optical surfaces states known as the surface plasmon polariton (SPP) and the surface exciton polariton (SEP) onto which the evanescent waves couple. However this requires that the TM polarization of light be used. It was shown in Chapter 2 that TE is in fact the preferred polarization of light for lithography as TM contributes heavily to background exposure, especially when operating in the evanescent regime. However, the TE Fresnel reflection equations suggested that the underlying material would require a negative loss, i.e. a hypothetical gain medium to allow a reflection larger than unity in the photoresist. The result here is the occurrence of a new type of a hypothetical surface resonance and also the known result that no naturally occurring surface states actually exist when the choice of polarization is TE. Silver and molybdenum were investigated as SPP and SEP image enhancement candidates. It was found that while a silver underlayer has a negative impact on the image, there is some benefit to be gained from using molybdenum as it may allow an image depth of ~59 nm at a *NA* of 1.85. However, this did not seem like a very attractive improvement and still requires the use of the TM polarization of light. Clearly a better solution was needed.

The physical phenomenon that results in the said enhancement was detailed and examples were provided using the T-Matrix models involving fictitious metals. It was shown that the enhancement may be simply described as the extraction of the energy which is otherwise reflected away into free space and its redistribution into the photoresist cavity. Such extraction only takes place when the underlay is carefully chosen or designed to have an operating point near the surface state resonance and when there is a slight loss in the photoresist.

In Chapter 6, the limits of imaging were derived for both TE and TM polarized evanescent interferometric lithography for reflective material underlays. It was found that in theory TE imaging imposed no limits to the maximal *NA* that could be imaged as long as a limiting aspect ratio of 1.3 was acceptable. TE imaging also exhibits perfect nulls and hence does not contribute to background exposure. A similar analysis for TM limits indicated that the imperfect nulls considerably worsened the background exposure and efforts made to lower their relative intensity meant that the limiting aspect ratio was lower. If the lithographer is prepared to accept an interference maxima to minima ratio of 2, then this limit is 0.838. It should be noted that the ability to vary the maxima to minima ratio in a TM interference pattern is a privilege present only because of the presence of a reflecting substrate. Raising the maxima to minima ratio improves the pattern contrast; however it also reduces the achievable aspect ratio.

Of course the problem still remained that a reflection greater than unity would only be possible with the TE polarization if a hypothetical gain medium underlay was used. Since, the preferred choice of polarization by the industry is TE, a new approach was introduced and developed to mimic the reflectivity of a gain medium using a carefully designed multi-layered optical stack. This was called the equivalent reflectance approach (ERA) and its use was combined with the understanding gained in Chapter 5 regarding the physical mechanism of image depth enhancement.

Localization of electric fields at an interface and enhancement is characteristic of a surface state and hence an evanescent state couples onto a surface state. Using this knowledge and the ERA, it was then suggested that the *effective* gain medium (EGM) could be created. One way to do this would be to first use a high index medium. Then the evanescent state may be converted to a propagating one within the high index medium. The index and thickness of the high index medium would allow a particular evanescent state to be resonated. Stacking a thin layer of this high index medium upon a lower index medium would then also allow the wave to be confined within the high index medium. It was noted that this is very similar to an actual surface state where the fields are evanescent in the bulk of the media, such as a metal or a lossy dielectric and enhanced at the interface (in this case a pseudo-interface). This is illustrated by Figure 8-3.

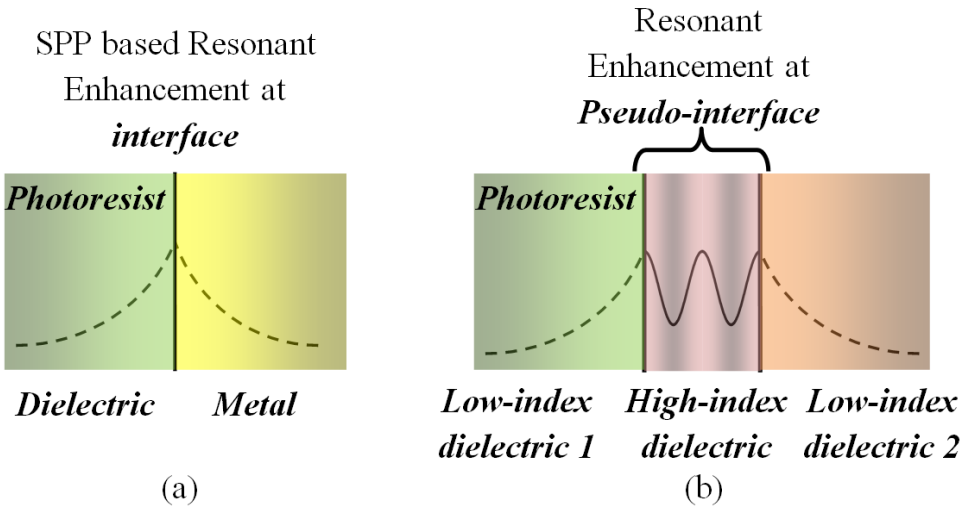

Figure 8-3 - Evanescent wave enhancement (a) at a metal-dielectric interface through SPP resonance, and (b) at a pseudo-interface formed by sandwiching a high index dielectric between two low-index dielectrics.

Note that while a wave-guide type approach is described in this thesis, there are other methods that exist to create an EGM surface state. In Chapter 5, an example was mentioned that used a thin layer of molybdenum upon silicon and the composite surface state that formed was in fact capable of providing an enhancement that would also be achieved using a homogenous semi-infinite gain medium. Similarly,

stacks of multiple materials may also be used. Upon careful tuning of such a stack, the desired effective gain medium could also be constructed.

By making use of the analysis as of yet, a feasible design was proposed that could utilize aluminum oxide (Al_2O_3, sapphire) as the high index medium and silicon dioxide as the low index medium and make use of a commercially available solid immersion interference lithography system, such as the Amphibian™ to pattern super-resolved 26 nm half pitch structures (*NA* = 1.85, λ = 193 nm) at an image depth of 82.5 nm, i.e. an aspect ratio of ~3.2. The design would use TE polarized light and be constructed using readily available materials and standard thin-film deposition techniques. Figure 8-4 (b) depicts the design and its performance alongside the conventional EIL method in Figure 8-4 (a).

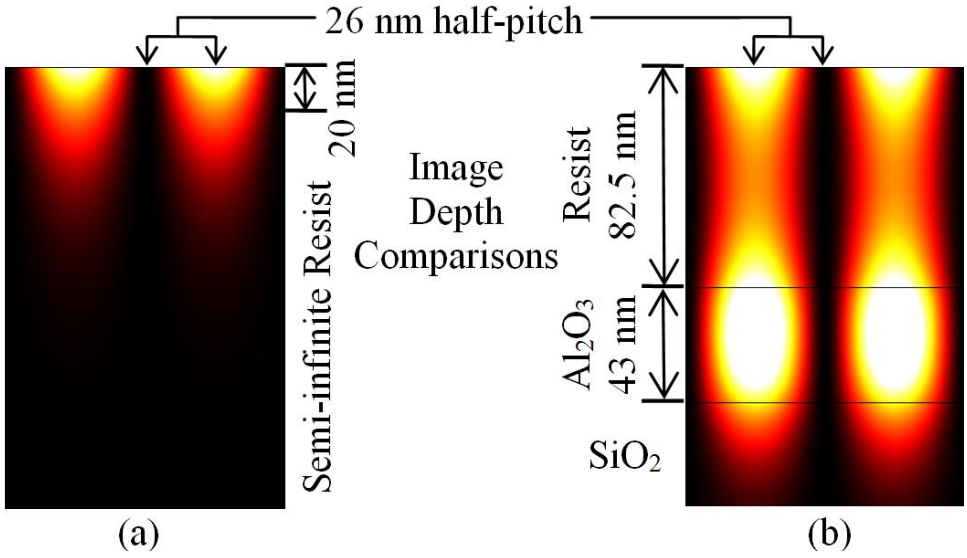

Figure 8-4 - Imaging of 26-nm (half-pitch) evanescent features into (a) semi-infinite lossy resist giving 20-nm image depth, and (b) 82.5 nm thick lossy resist on an effective gain medium made up of 43 nm of Al_2O_3 (Sapphire) on SiO_2, giving an image depth of 82.5 nm.

8.4 Experimental demonstration of image depth enhancement with EIL

In Chapter 7, experimental demonstration of the theory is provided. The primary goal here was to demonstrate the use of the waveguide type EGM to considerably enhance the image depths that were achieved in Chapter 3 under all other conditions constant. Here hafnium oxide (HfO) was used as the high index dielectric and silicon dioxide (SiO_2) as the low index dielectric for operation at λ = 405 nm.

An image qualification metric, namely the Figure of Merit (FoM) was defined. Optical stacks were qualified using this metric based on the results of an attenuated total reflectance (ATR) experiment, which was used to compute their optical properties. An optical stack with a FoM of 1.35 was used to

successfully demonstrate imaging of line and space patterns with a 111 nm pitch (55.5 nm half-pitch) at a *NA* of 1.824, λ = 405 nm and PD of 2.5 mW-min (as in Chapter 3). The resulting image depths were seen to be ~100 nm with good reproducibility and in some cases up to 105 nm, resulting in aspect ratios of ~1.8 (compare this with an aspect ratio of < 0.72 in Chapter 3). This was well supported by the modeling and simulations that were also carried out. This in comparison with the 33-40 nm image depths encountered in Chapter 3 is a considerable enhancement giving an image depth that is more than 2.5 times larger. These results are illustrated using AFM and SEM scans in Figure 8-5 and Figure 8-6 respectively.

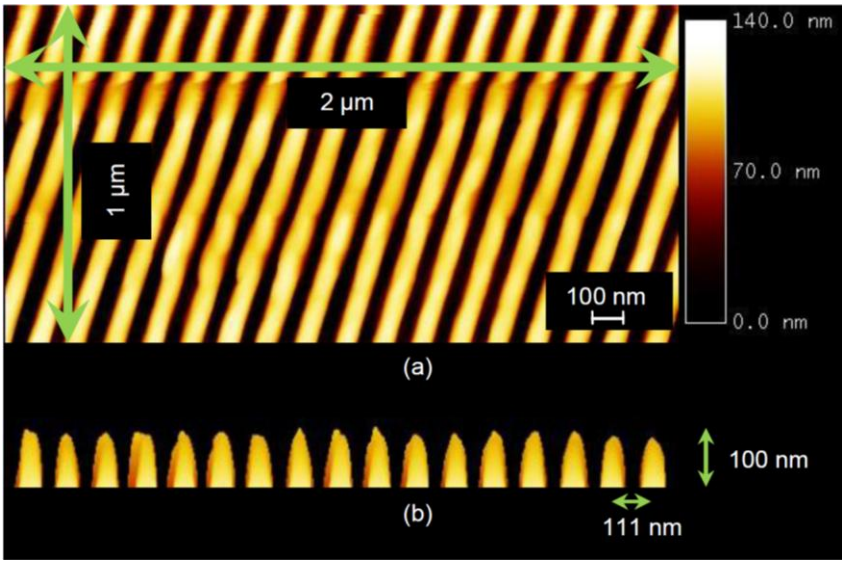

Figure 8-5 - AFM Scan demonstrating EIL using SILMIL using the imaging stack of Figure 7-26 (b), high aspect ratio (~1.8) structure imaged at a *NA* of 1.824 at λ = 405 nm with pattern half-pitch ~ 55.5 nm and average depth measured using AFM software to be 100 nm. (a) A 2 µm by 1 µm AFM scan (b) A corresponding 3D like perspective view to depict the tall standing structures

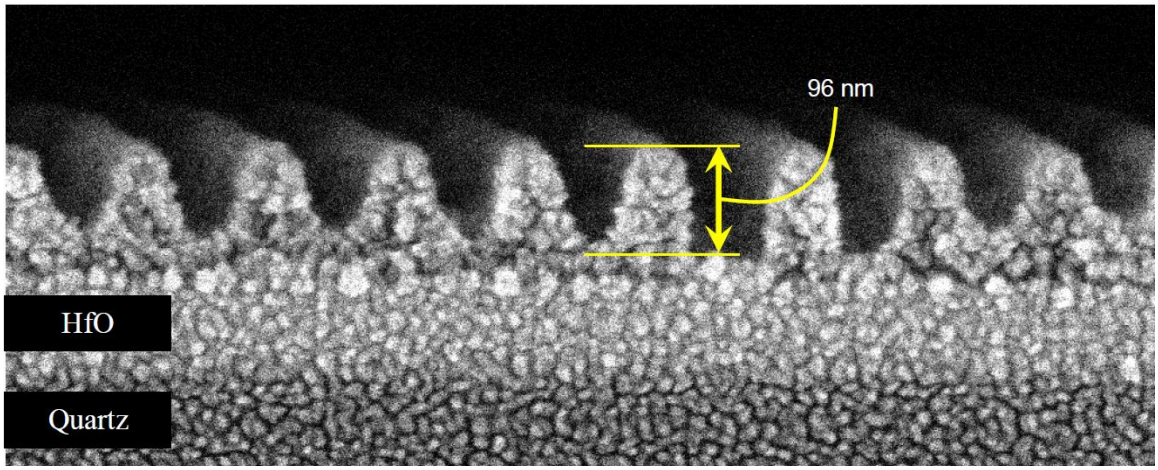

Figure 8-6 - SEM cross-sectional views showing tall standing structures, at PD of 2.5 mW-min, *NA* = 1.824, λ = 405 nm, EIL using SILMIL using the imaging stack of Figure 7-26 (b), Resulting half-pitch ~55.5 nm, with pattern depth ~96 nm (High Aspect Ratio of ~1.72).

A method was also proposed to 'repair' the performance of an ill-designed EGM underlay, i.e. one that would result in a low FoM. This was done by spinning on a thin layer of PMMA, a low index spin on polymer on the HfO layer. The right thickness allowed for resonance compensation, by tuning the amplitude and phase of the reflectivity from the stack. It was also shown that the right thickness of such a low index dielectric will in several instances considerably widen the allowable operating region, in addition to maximizing the FoM in that region. This was achieved by running a multi-variable parametric search routine on the optical stack using the T-Matrix method. The method picked the optimal PMMA thickness values that maximized the FoM.

Another example was also presented to demonstrate reduced evanescent coupling when a non-ideal EGM was used, i.e. one that provides a mediocre FoM. Thinner resist was used but the image depth was still limited. However, enhancement over the non-EGM case was still clearly visible as the trench of the pattern was now easily measured using an AFM. This is due to the fact that an EGM considerably improves the interference maxima to minima ratio for TE light. In addition to this, the dosage experienced by the interference minima may lie below the development threshold allowing a wider trench to form than it would otherwise with conventional EIL.

Finally effects of dosage variation on pattern modulation and resist depth were analyzed. It was found that there was resist collapse beyond a particular dosage. This is a very interesting phenomena, reported here for the first time with EIL and was attributed to the fact that a background exposure exists in the system, and the presence of EGM further amplifies this, causing the photoresist to develop from the surface (as it normally would) as well as lose traction from the substrate. At a low dosage, resist collapse was minimal

and clean features were imaged over large areas resulting in high aspect ratio line space structures. The results were reproducible. The effects of dosage variation were plotted and in general it was found that the theory was in accordance with what was demonstrated.

8.5 Scope, Summary & Future work

The interest in patterning a regular line and space structure is of considerable use to space applications, data storage [130-132]. A project titled, gratings of regular arrays and trimmed exposures (GRATE) was also funded by DARPA to initiate a low-cost circuit manufacturing technique IL [133]. A lot of these applications would benefit further if higher resolution structures could be patterned over large areas. It is believed that the techniques presented in this thesis are likely to be attractive to researchers requiring to produce such high resolution repeating patterns as it greatly alleviates one of the primary hindrances that communities have thus far faced with EIL, that of reduced depth of focus. It is hoped that the ideas and proposals laid down in this thesis act to encourage the use of solid-immersion systems and pave the way for feasible ultra-high *NA* imaging and patterning.

The development of the scanning interference evanescent wave lithography system [150] presents promise that EIL may be used to easily pattern large areas as easily as a scanning beam electron lithography tool but at a considerably lower cost. One can see how a combination of such a scheme with the one that has been proposed in this thesis might considerably extend the scope of solid immersion interference lithography.

As the analysis on TE imaging limits has suggested, any NA may be used for patterning at a tolerable aspect ratio of 1.3 by using the methods proposed. Hence, if a suitable prism material is available for evanescent interferometric imaging, it may also be deposited as a thin film on a low loss dielectric to resonate the image. We believe this finding has the potential to motivate further research in the development of higher index prism materials and immersion liquids for lithographic imaging.

Finally, other future work that could potentially benefit from the proposals in this thesis would be by using higher evanescent orders that cannot as of yet be created via prism coupling due to refractive index limitations. This could be carried out for instance using a carefully designed multilayered diffraction grating that reallocates the momentum of an incident beam into the desired evanescent order. This is somewhat analogous to the design of a narrow band RF filter. Hence, a quality factor would be associated with this reallocation. Such an evanescent order may then be used in interference lithography. Evanescent enhancement could be carried out using effective gain medium states using either TM or TE polarizations dependent upon the availability of real materials.

Appendix

As an interesting exercise, let us determine the conditions required for an infinite reflection. The approach involves analysis of the Fresnel reflections equations, followed by a graphic interpretation of results and a solution summary.

TE Infinite Reflector

To achieve an infinite reflection, we begin by setting the denominator of the TE Fresnel equation to zero.

$$r_{TE} = \frac{k_{z2} - k_{z3}}{k_{z2} + k_{z3}} \tag{0.1}$$

This would require,

$$k_{z2} = -k_{z3} \text{ for } r_{TE} = \infty \tag{0.2}$$

We rewrite this as,

$$k_{z3} = k_0\sqrt{\varepsilon_3 - (NA)^2} = -k_{z2} = -k_0\sqrt{\varepsilon_2 - (NA)^2} \tag{0.3}$$

Omitting the scaling factor and assuming a lossless resist (implying $k_{z2} = ik''_{z2}$,$\varepsilon_2 = \varepsilon'_2 = n_2^{'2}$) we have,

$$\sqrt{\varepsilon_3 - (NA)^2} = -\sqrt{n_2^{'2} - (NA)^2} \tag{0.4}$$

If we let,

$$\varepsilon_3 = n_2^{'2} \tag{0.5}$$

Then the magnitudes of the left and right hand sides of (0.4) are made equal, but (0.4) is still not valid.

If however we let,

$$\varepsilon_3 = n_2^{'2} - i\delta \tag{0.6}$$

We can ensure the validity of (0.4), when δ is an infinitesimal constant value tending to zero that acts to introduce a negative loss (i.e. gain) into the optical properties of medium 3. We will discuss the gain medium in a later chapter. We also illustrate this idea in the complex plane of Figure 0-1, the vector

lengths are not drawn to scale, as emphasis is placed on their relative locations and phases and once again the caption aids the reader in understanding the diagram.

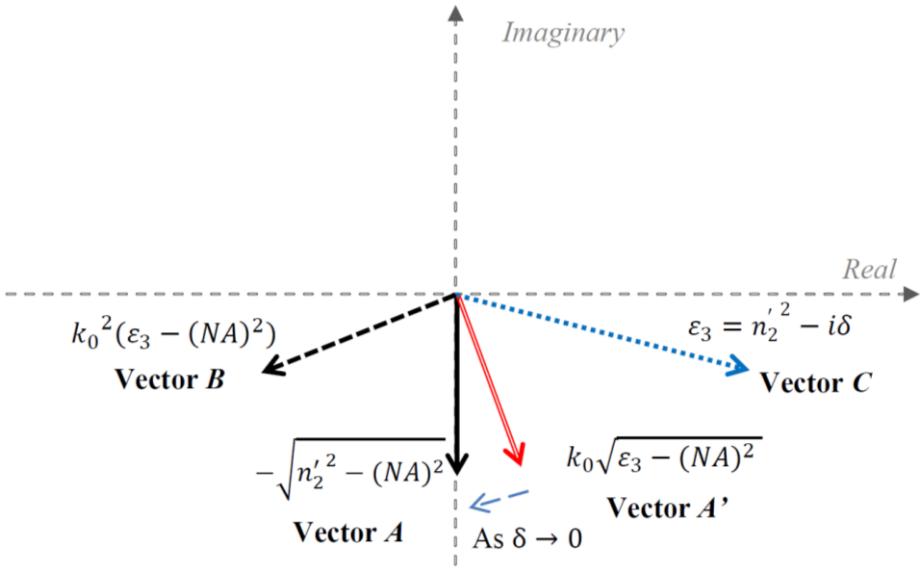

Figure 0-1 – If we set the substrate's electrical permittivity $\boldsymbol{\varepsilon_3}$ to the resist permittivity $\boldsymbol{\varepsilon_2 = n_2'^2}$, then at least the magnitudes of both sides of (0.4) are equal. For obvious reasons this will result in a zero reflection. We need to find a Vector *B* (the argument) which has a square root equal to Vector *A*, this will wholly satisfy (0.4) and result in a ∞ reflection. The only way to ensure that Vector *A* ~ $\sqrt{\boldsymbol{Vector\ B}}$ is by adding a negative infinitesimal loss into $\boldsymbol{\varepsilon_3}$ to make $\boldsymbol{n_2'^2 - i\delta}$ (Vector *C*). The square root of Vector *B* is now Vector *A'* and this approaches Vector *A* as δ tends to zero.

This is interesting because; the lack of presence of the δ in (0.5) results in a zero reflection corresponding to the impedance matched case, while the infinite reflector we have considered in (0.6) results in the maximal impedance mis-matched case. Hence, by the inclusion of an infinitesimal value, we are able to consider the two extremes of reflectivities.

TM Infinite Reflector

In a similar fashion, we analyze the TM Fresnel reflection equations and deduce conditions for an infinite reflection. Let us begin by once again setting the denominator of the TM Fresnel equation to zero.

$$r_{TM} = \frac{\varepsilon_3 k_{z2} - \varepsilon_2 k_{z3}}{\varepsilon_3 k_{z2} + \varepsilon_2 k_{z3}} \tag{0.7}$$

$$\varepsilon_3 k_{z2} = -\varepsilon_2 k_{z3} \text{ for } r_{TM} = \infty \tag{0.8}$$

Let us once again assume lossless resist (implying $k_{z2} = ik''_{z2}$,$\varepsilon_2 = \varepsilon'_2 = n_2^{'2}$)) and rewrite (0.8) as,

$$(\varepsilon'_3 + i\varepsilon''_3)ik''_{z2} = -\varepsilon'_2(k'_{z3} + ik''_{z3}) \tag{0.9}$$

If we let,

$$c = \frac{\varepsilon'_2}{k''_{z2}} \tag{0.10}$$

Then since c is a real constant, we may rewrite (0.9) as,

$$(\varepsilon'_3 + i\varepsilon''_3) = ic(k'_{z3} + ik''_{z3}) \; or \; e^{i\frac{\pi}{2}}c(k'_{z3} + ik''_{z3}) \tag{0.11}$$

This informs us that ε_3 and k_{z3} depicted in Figure 0-2 as vectors *C* and *A* respectively differ only by a constant real scaling factor and that ε_3 is 90° ahead of $k_{z,3}$ in phase angle. However, by definition we also have,

$$k_{z3} = k'_{z3} + ik''_{z3} = k_0\sqrt{(\varepsilon'_3 + i\varepsilon''_3) - (NA)^2} = k_0\sqrt{\varepsilon'_3 - (NA)^2 + i\varepsilon''_3} \tag{0.12}$$

The right hand side of (0.12) is depicted in Figure 0-2 as vector *A'*. Hence, a primary requirement here is that Vector *A* must be equivalent to Vector *A'*.

CASE 1: $k''_{z3} > 0$

We limit our analysis to positively refracting media (implying $k'_{z3} > 0$) and first consider the case with $k''_{z3} > 0$ while observing the relevant vectors depicted on the complex plane in Figure 0-2,

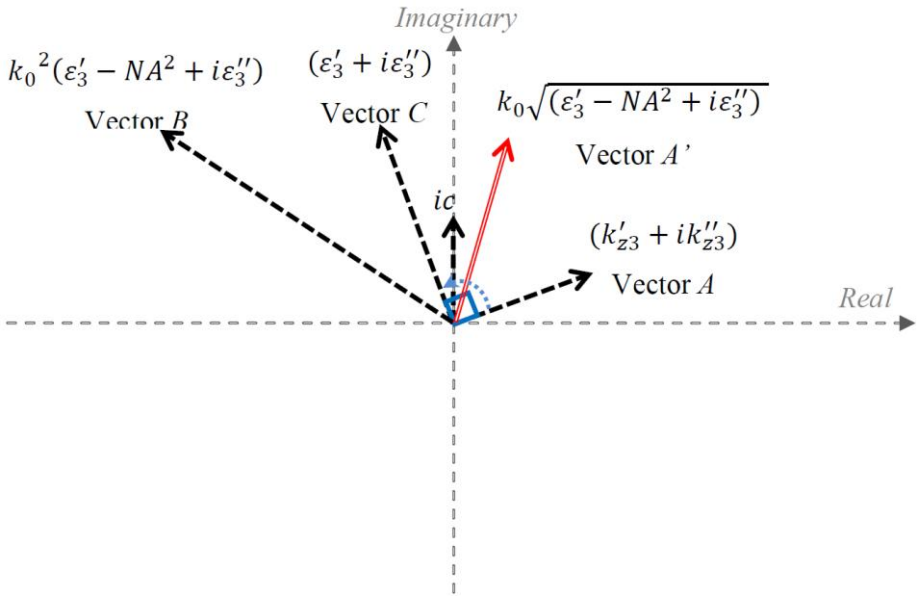

Figure 0-2 – To find an ∞ reflector for the TM case, we have to consider the $\boldsymbol{k''_{z3}} > 0$ and $\boldsymbol{k''_{z3}} < 0$ cases separately. This is the $\boldsymbol{k''_{z3}} > 0$ case. Equation (0.11) imposes the requirement that Vector *A* and Vector *C* differ in their relative positioning by exactly 90°. Then the argument Vector *B* must have a square root equal to Vector *A* (to satisfy (0.12)), however as the figure suggests, the square root is in fact Vector *A'* and not Vector *A*. It turns out that for Vector *A* to be equal to Vector *A'*, we need to satisfy the following requirements $\boldsymbol{\varepsilon'_3} < 0$, $\boldsymbol{\varepsilon''_3} = \mathbf{0}$, resulting in $\boldsymbol{k'_{z3}} = \mathbf{0}$ and of course allowing $\boldsymbol{k''_{z3}} > 0$ as is focus of this case. This is a lossless metal solution and is depicted in Figure 0-3

There is an obvious problem with the configuration of Figure 0-2. Vectors *A* and *A'* must denote the same vector as (0.12) suggests. The only scenario that allows this is when $k'_{z3} = 0$, requiring $\varepsilon'_3 < 0$ and $\varepsilon''_3 = 0$ to satisfy (0.11). Hence, it seems that ε_3 is required to be a lossless metal. This scenario is perhaps better depicted in Figure 0-3.

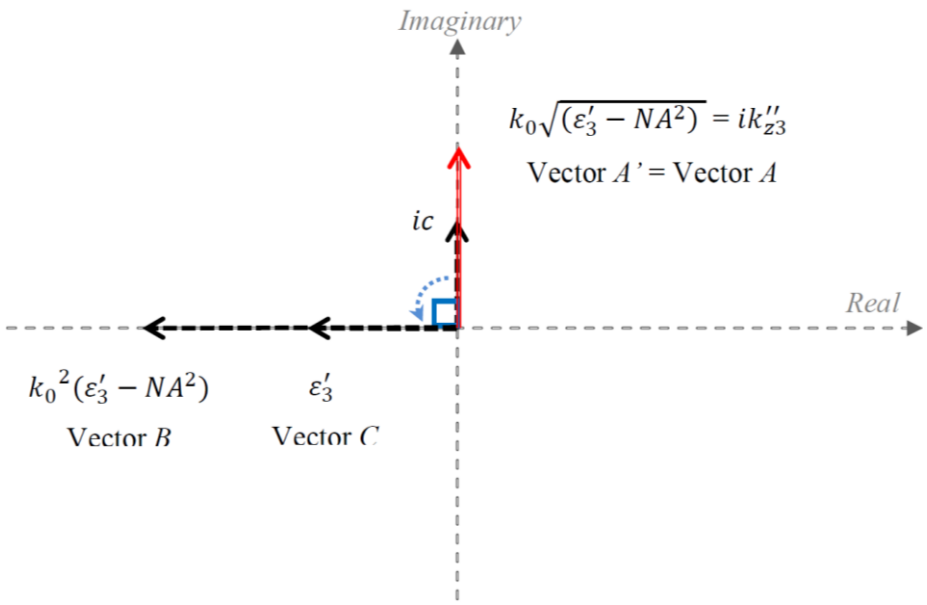

Figure 0-3 – Lossless metal solution. Following on from Figure 0-2, we see how both (0.11) and (0.12) are satisfied by making $\boldsymbol{\varepsilon_3}$ a lossless metal (*i.e.* $\boldsymbol{\varepsilon_3'} < 0$ and $\boldsymbol{\varepsilon_3''} = \mathbf{0}$). Vector A' and Vector A now denote the same vector, which is the square root of Vector *B*

Making use of this new information, we derive an expression for the electrical permittivity of the metal that will result in an infinite reflection. We can rewrite (0.9) as

$$\varepsilon_3' * ik_{z2}'' = -\varepsilon_2' ik_{z3}'' \tag{0.13}$$

$$\varepsilon_3' = -\frac{\varepsilon_2' k_{z3}''}{k_{z2}''} \tag{0.14}$$

And (0.12) as

$$k_{z3} = ik_{z3}'' = k_0\sqrt{\varepsilon_3' - (NA)^2} \tag{0.15}$$

Then (0.14) becomes,

$$\varepsilon_3' = i\frac{\varepsilon_2' k_0\sqrt{\varepsilon_3' - (NA)^2}}{k_{z2}''} \tag{0.16}$$

Squaring both sides of (0.16) and rearranging, we generate a quadratic in ε_3',

$$(\varepsilon_3')^2 + k_0^2\left(\frac{\varepsilon_2'}{k_{z2}''}\right)^2 \varepsilon_3' - k_0^2\left(\frac{\varepsilon_2'}{k_{z2}''}\right)^2 (NA)^2 = 0 \tag{0.17}$$

We solve this quadratic to derive the desired expression,

$$\varepsilon_3' = \frac{-k_0^2\left(\frac{\varepsilon_2'}{k_{z2}''}\right)^2 \pm \sqrt{k_0^4\left(\frac{\varepsilon_2'}{k_{z2}''}\right)^4 + 4\left(\frac{\varepsilon_2'}{k_{z2}''}\right)^2 k_0^2(NA)^2}}{2} \tag{0.18}$$

There are two roots to every quadratic, however we are aware of the fact that the solution is a lossless metal, i.e. has a negative real electrical permittivity only. Upon examination of (0.18), we see that the expression inside the square root is always greater than the expression outside of the quadratic. Hence, to achieve the negative electrical permittivity we must choose the negative sign of the square root resulting in (0.19).

$$\varepsilon_3' = \frac{-k_0^2\left(\frac{\varepsilon_2'}{k_{z2}''}\right)^2 - \sqrt{k_0^4\left(\frac{\varepsilon_2'}{k_{z2}''}\right)^4 + 4\left(\frac{\varepsilon_2'}{k_{z2}''}\right)^2 k_0^2(NA)^2}}{2} \tag{0.19}$$

CASE 2: $k_{z3}'' < 0$

Finally, let us consider the case where $k_{z3}'' < 0$. Once again we aim to satisfy the relationships imposed by (0.11) and (0.12). In fact, let us briefly refer back to Figure 0-2, where we made note that for vectors *A* and *A'* to be equal, k_{z3}' must be 0. Since, this requirement was made clear in Figure 0-2, we will not present the invalid scenario again. The previous result required $\varepsilon_3'' = 0$ and $\varepsilon_3' - (NA)^2 < 0$ allowing $k_{z3}'' > 0$, we found that a lossless metal with $\varepsilon_3' < 0$ satisfies this.

However, we now want to consider the $k_{z3}'' < 0$ case. To ensure this, in addition to satisfying (0.11) which states that ε_3 is 90° ahead of $k_{z,3}$ in phase angle, we know to put ε_3 in the right half of the complex plane and make sure that $\varepsilon_3' < (NA)^2$ so that the argument (see Vector *B*, Figure 0-4) falls in the left half of the complex plane. As before, we find the need to introduce δ as the infinitesimal imaginary component of ε_3 such that,

$$\varepsilon_3 = \varepsilon_3' - i\delta \tag{0.20}$$

Introducing δ allows us to ensure that $k''_{z3} < 0$ (and not $k''_{z3} > 0$). As δ→ 0, $k'_{z3} \to 0$, and the new solution of (0.20) comes into existence. This is depicted in Figure 0-4.

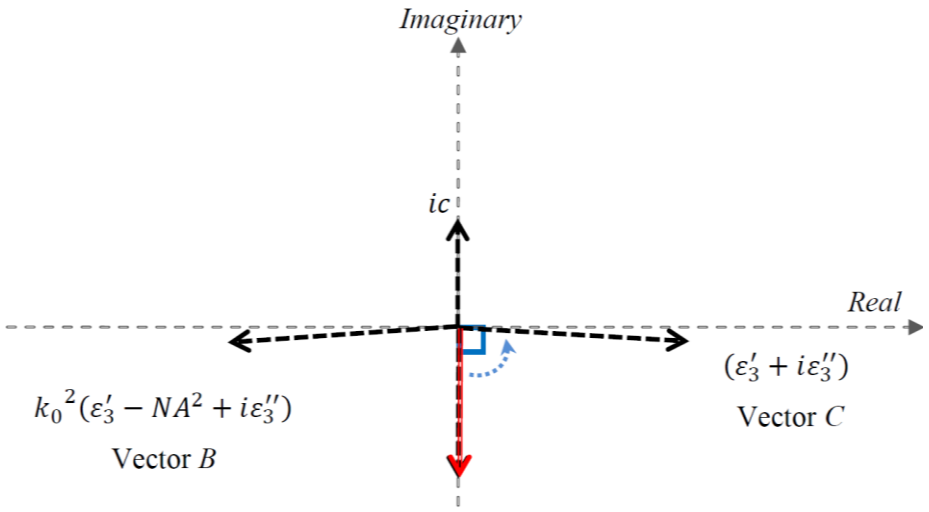

Figure 0-4 – For an ∞ reflection in the TM case, we have already considered the $\boldsymbol{k''_{z3} > 0}$ case in Figure 0-2 and Figure 0-3. This is the second case where $\boldsymbol{k''_{z3} < 0}$. As before, we require that $\boldsymbol{k'_{z3} = 0}$ (see caption of Figure 0-2). From prior analysis, this may be achieved with the presence of a negative loss in the substrate's permittivity (*i.e.* $\boldsymbol{\varepsilon''_3 < 0}$). The requirement of (0.11) that $\boldsymbol{\varepsilon_3}$ be 90° ahead of $\boldsymbol{k_{z,3}}$ in phase angle is satisfied if we put $\boldsymbol{\varepsilon_3}$ in the right half of the complex plane (Vector *C*). To ensure $\boldsymbol{k''_{z3} < 0}$ and not $\boldsymbol{k''_{z3} > 0}$, we make $\boldsymbol{\varepsilon'_3 < (NA)^2}$ so that the argument (Vector *B*) lies in the left half of the complex plane. We let $\boldsymbol{\varepsilon''_3 = -\delta \to 0}$, this allows Vector *A* → Vector *A'* resulting in the solution of (0.20) to come into existence

It turns out that the value of ε'_3 that allows an infinite reflection may then simply be computed using (0.18), where we now choose the positive square root in the expression inside the square root brackets. The reason we may utilize (0.18) is because the assumption of a lossless material still holds as $\delta \to 0$. Hence,

$$\varepsilon_3 = \frac{-k_0^2\left(\frac{\varepsilon'_2}{k''_{z2}}\right)^2 + \sqrt{k_0^4\left(\frac{\varepsilon'_2}{k''_{z2}}\right)^4 + 4\left(\frac{\varepsilon'_2}{k''_{z2}}\right)^2 k_0^2(NA)^2}}{2} - i\delta, \delta \to 0 \qquad (0.21)$$

This is our second and final solution for the TM infinite reflector and with this we conclude the analysis of infinite reflectors.

References

[1] Nobelprize.org. *"The Nobel Prize in Physics 1956"*. (2010). [Online] Available: http://www.nobelprize.org/nobel_prizes/physics/laureates/1956/ [26 April 2012].

[2] ScienCentral. *The Invention of the First Transistor, November 17-December 23, 1947 - The Miracle Month*. (1999). [Online] Available: http://www.pbs.org/transistor/background1/events/miraclemo.html [26 April 2012].

[3] J. Vardalas. *Twists and Turns in the Development of the Transistor*. (2003). [Online] Available: www.todaysengineer.org/2003/May/history.asp [26 April 2012].

[4] L. Berlin, *The man behind the microchip: Robert Noyce and the invention of Silicon Valley*. New York, USA: Oxford University Press, Inc., 2005.

[5] C. Lécuyer, *Making Silicon Valley: Innovation and the Growth of High Tech, 1930-1970*. Cambridge, Massachusetts, USA: The MIT Press, 2006.

[6] C. A. Mack, *Fundamental Principles of Optical Lithography: The Science of Microfabrication*. London, England, UK: John Wiley & Sons, 2007.

[7] G. Moore. (1965, April 19) Cramming More Components onto Integrated Circuits. *Electronics Magazine*.vol. 38, no. 8, pp. 82-85, *IEEE*.

[8] Lucent. *Replica of first transistor*. (1997). [Online] Available: http://clinton4.nara.gov/media/jpg/replica-of-first-transistor.jpg [3 May 2012].

[9] B. Hammack. *Does the first transistor ever built still work ?* (2010). [Online] Available: http://www.youtube.com/watch?v=xvrjIJw3OSU [3 May 2012].

[10] U. A. G. Bakshi, A. P., *Electronic Circuits*, 1st ed. Pune, India: Technical Publications Pune, 2008.

[11] Y. Cheng and H. Chenming, *Mosfet Modeling and Bsim3 User's Guide*. New York, USA: Kluwer Academic Publishers, 1999.

[12] J. E. Lilienfeld, "Method and apparatus for controlling electric current," United States Patent and Trademark Office Patent 1745175, 28 Jan 1930.

[13] J. E. Lilienfeld, "Amplifier For Electric Currents," United States Patent and Trademark Office Patent 1877140, 13 Sept 1932.

[14] J. E. Lilienfeld, "Device For Controlling Electric Current," United States Patent and Trademark Office Patent 1900018, 7 Mar 1933.

[15] Wgsimon. *CPU Transistor Counts 1971-2011 & Moore's Law*. (2008). [Online] Available: http://en.wikipedia.org/wiki/File:Transistor_Count_and_Moore%27s_Law_-_2008.svg [3 May 2012].

[16] A. Gonsalves. *Intel Debuts 32-nm Westmere Desktop Processors*. (2010). [Online] Available: http://www.informationweek.com/news/222200708 [30 May 2012].

[17] D. Perry. *Report: Intel Scheduling 22 nm Ivy Bridge for April 2012*. (2011). [Online] Available: http://www.tomshardware.com/news/intel-ivy-bridge-22nm-cpu-3d-transistor,14093.html [31 March 2012].

[18] L. Kelion. *Intel's Ivy Bridge chip launch using '3D transistors'*. (2012). [Online] Available: http://www.bbc.co.uk/news/technology-17785464 [31 March 2012].

[19] J. Hruska. *Despite economic slowdown, Intel on track with 32nm of win*. (2008). [Online] Available: http://arstechnica.com/hardware/news/2008/12/despite-economic-slowdown-intel-on-track-with-32nm-of-win.ars [3 May 2012].

[20] J. Ng. *IDF09: Intel Demonstrates First 22nm Chips, Discusses Die Shrink Roadmap*. (2009). [Online] Available: http://www.dailytech.com/IDF09+Intel+Demonstrates+First+22nm+Chips+Discusses+Die+Shrink+Roadmap/article16312.htm [3 May 2012].

[21] B. Crothers. *How Intel's 3D tech redefines the transistor (FAQ)*. (2011). [Online] Available: http://news.cnet.com/8301-13924_3-20059431-64.html [3 May 2012].

[22] SPIE-Newsroom. *Chris Mack on next-generation lithography and the future of Moore's law*. (2012). [Online] Available: http://spie.org/x86784.xml [3 May 2012].

[23] D. J. Michalak, *et al.*, "Nanopatterning Si(111) surfaces as a selective surface-chemistry route," *Nature Materials*, vol. 9, no. 3, pp. 266-271, Mar 2010.

[24] K. Qi, *et al.*, "Nano-patterned and layered synthetic-biological materials assembled upon polymer brushes via biotin/streptavidin recognition," *Abstracts of Papers of the American Chemical Society*, vol. 228, pp. 74-PMSE, Aug 2004.

[25] E. Kim, *et al.*, "Cell culture over nanopatterned surface fabricated by holographic lithography and nanoimprint lithography," in *3rd IEEE International Conference on Nano/Micro Engineered and Molecular Systems*, Sanya, China, 2008, pp. 725-728. 6-9 January 2008.

[26] W. Arden, *et al. "More-than-Moore" White Paper* [White Paper]. [Online] Available: http://www.itrs.net/Links/2010ITRS/IRC-ITRS-MtM-v2%203.pdf

[27] ITRS. *ITRS International Technology Roadmap for Semiconductors*. (2010). [Online]

[28] E. Hecht, *Optics*, 4th ed.: Addison Wesley, 2001.

[29] M. Born and W. Emil, *Principles of Optics*: Cambridge University Press, 1997.

[30] R. H. French and H. V. Tran, "Immersion Lithography: Photomask and Wafer-Level Materials," presented at the *Annual Review of Materials Research*, 2009, vol. 39, pp. 93-126,

[31] ASML. *ASML: Products - TWINSCAN NXT:1950i*. [Online] Available: http://www.asml.com/asml/show.do?ctx=6720&rid=36951 [3 May 2012].

[32] I. Newton, "Opticks: OR, A TREATISE OF THE REFLEXIONS, REFRACTIONS, INFLEXIONS and COLOURS OF LIGHT. ALSO Two TREATISES OF THE MAGNITUDE OF Curvilinear Figures," 1st ed. London, UK: Printed for Sam. Smith, and Benj. Walford, Printers to the Royal Society, at the Prince's Arms in St. Paul's Church-yard. MDCCIV., 1704.

[33] F. d. Fornel, *Evanescent Waves: From Newtonian Optics to Atomic Optics*. New York, USA: Springer, 2001.

[34] J. M. Zhou, *et al.*, "Immersion lithography with numerical apertures above 2.0 using high index optical materials - art. no. 65204T," presented at the *Optical Microlithography XX, Pts 1-3*, February 2007, vol. 65204T, pp. T5204-T5204, San Jose, CA, USA

[35] P. Mehrotra, *et al.*, "Solid-immersion Lloyd's mirror as a testbed for plasmon-enhanced ultrahigh numerical aperture lithography," *Journal of Micro-Nanolithography MEMS and MOEMS*, vol. 10, no. 3, p. 033012, Jul-Sep 2011.

[36] M. D. Smith, *et al.*, "A comprehensive EUV lithography model," *Solid State Technology*, vol. 55, no. 1, pp. 14-18, Jan 2012.

[37] H. Aoyama, *et al.*, "CD correction for half pitch 2x-nm on extreme ultraviolet lithography," presented at the *Extreme Ultraviolet (EUV) Lithography II*, 28 February - 3 March 2011, vol. 7969, p. 79691J, San Jose, CA, USA

[38] J. V. Hermans, *et al.*, "Overlay Progress in EUV Lithography Towards Adoption for Manufacturing," presented at the *Extreme Ultraviolet Lithography II*, 8 April 2011, vol. 7969, p. 79691M,

[39] H. W. Kim, *et al.*, "Status of EUV Resist and Process Development at IC Manufacture to Implement EUV Lithography to 2X DRAM and Beyond," *Journal of Photopolymer Science and Technology*, vol. 24, no. 2, pp. 119-125, 2011.

[40] M. Shibuya, *et al.*, "Evaluating the performance of DP and EUVL by using analytical equations for resolution of optical lithography with considering required DOF," presented at the *Optical Microlithography XXIV*, 1 March 2011, vol. 7973, p. 79732Y, San Jose, CA, USA

[41] P. Y. Yan, *et al.*, "EUVL Alternating Phase Shift Mask," presented at the *Extreme Ultraviolet Lithography II*, April 2011, vol. 7969, p. 79690G, San Jose, CA, USA
[42] M. J. Wieland, *et al.*, "Throughput enhancement technique for MAPPER maskless lithography," presented at the *Alternative Lithographic Technologies II*, 2010, vol. 7637, p. 76371Z, San Jose, CA, USA
[43] M. J. Wieland, *et al.*, "MAPPER: High throughput maskless lithography," presented at the *Alternative Lithographic Technologies II*, 2010, vol. 7637, p. 76370F, San Jose, CA, USA
[44] C. van den Berg, *et al.*, "Scanning exposures with a MAPPER multibeam system," presented at the *Alternative Lithographic Technologies III*, March 2011, vol. 7970, p. 79700D, San Jose, CA, USA
[45] L. Pain, *et al.*, "IMAGINE: an open consortium to boost maskless lithography take off First assessment results on MAPPER technology," presented at the *Alternative Lithographic Technologies III*, March 2011, vol. 7970, p. 79700Y, San Jose, CA, USA
[46] P. Kruit, "The role of MEMS in maskless lithography," *Microelectronic Engineering*, vol. 84, no. 5-8, pp. 1027-1032, May-Aug 2007.
[47] B. J. Kampherbeek, *et al.*, "An experimental setup to test the MAPPER electron lithography concept," *Microelectronic Engineering*, vol. 53, no. 1-4, pp. 279-282, Jun 2000.
[48] J. E. Poelma and C. J. Hawker, "BLOCK COPOLYMERS With a little help from above," *Nature Nanotechnology*, vol. 5, no. 4, pp. 243-244, Apr 2010.
[49] M. P. Stoykovich, *et al.*, "Directed self-assembly of block copolymers for nanolithography: Fabrication of isolated features and essential integrated circuit geometries," *ACS Nano*, vol. 1, no. 3, pp. 168-175, Oct 2007.
[50] H. Arora, *et al.*, "Block Copolymer Self-Assembly-Directed Single-Crystal Homo- and Heteroepitaxial Nanostructures," *Science*, vol. 330, no. 6001, pp. 214-219, Oct 2010.
[51] S. M. Park, *et al.*, "Sub-10 nm Nanofabrication via Nanoimprint Directed Self-Assembly of Block Copolymers," *ACS Nano*, vol. 5, no. 11, pp. 8523-8531, Nov 2011.
[52] J. Y. Cheng, *et al.*, "Nanostructure engineering by templated self-assembly of block copolymers," *Nature Materials*, vol. 3, no. 11, pp. 823-828, Nov 2004.
[53] R. Menon and H. I. Smith, "Absorbance-modulation optical lithography," *Journal of the Optical Society of America a-Optics Image Science and Vision*, vol. 23, no. 9, pp. 2290-2294, Sep 2006.
[54] R. Menon, *et al.*, "Far-field generation of localized light fields using absorbance modulation," *Physical Review Letters*, vol. 98, no. 4, p. 043905, Jan 2007.
[55] H. Y. S. Tsai, *et al.*, "Spatial-frequency multiplication via absorbance modulation," *Applied Physics Letters*, vol. 91, no. 9, p. 094103, 2007.
[56] H. Y. S. Tsai, "Absorbance Modulation Optical Lithography," Masters Thesis, Massachusetts Institute of Technology, Cambridge, MA, 2007.
[57] T. L. Andrew, *et al.*, "Confining Light to Deep Subwavelength Dimensions to Enable Optical Nanopatterning," *Science*, vol. 324, no. 5929, pp. 917-921, 2009.
[58] J. E. Foulkes and R. J. Blaikie, "Influence of polarization on absorbance modulated subwavelength grating structures," *Journal of Vacuum Science & Technology B*, vol. 27, no. 6, pp. 2941-2946, Nov 2009.
[59] C. W. Holzwarth, *et al.*, "Increased process latitude in absorbance-modulated lithography via a plasmonic reflector," *Optics Express*, vol. 19, no. 18, pp. 17790-17798, Aug 2011.
[60] T. Grotjohann, *et al.*, "Diffraction-unlimited all-optical imaging and writing with a photochromic GFP," *Nature*, vol. 478, no. 7368, pp. 204-208, Oct 2011.
[61] E. Rittweger, *et al.*, "STED microscopy reveals crystal colour centres with nanometric resolution," *Nature Photonics*, vol. 3, no. 3, pp. 144-147, Mar 2009.
[62] J. Foulkes, "Absorbance Modulation Optical Lithography: Simulating the Performance of an Adaptable Absorbance Mask in the Near-Field," Doctoral Thesis, Electrical and Computer Engineering, University of Canterbury, Christchurch, 2010.

[63] M. M. Alkaisi, *et al.*, "70 nm features on 140 nm period using Evanescent Near Field Optical Lithography," *Microelectronic Engineering,* vol. 53, no. 1-4, pp. 237-240, Jun 2000.
[64] M. M. Alkaisi, *et al.*, "Nanolithography in the evanescent near field," *Advanced Materials,* vol. 13, no. 12-13, p. 877, Jul 2001.
[65] S. J. McNab, *et al.*, "Analytic study of gratings patterned by evanescent near field optical lithography," *Journal of Vacuum Science & Technology B,* vol. 18, no. 6, pp. 2900-2904, Nov-Dec 2000.
[66] J. B. Pendry, "Negative refraction makes a perfect lens," *Physical Review Letters,* vol. 85, no. 18, pp. 3966-3969, Oct 2000.
[67] N. Fang, *et al.*, "Sub-diffraction-limited optical imaging with a silver superlens," *Science,* vol. 308, no. 5721, pp. 534-537, Apr 2005.
[68] S. Durant, *et al.*, "Theory of optical imaging beyond the diffraction limit with a far-field superlens - art. no. 63231H," presented at the *Plasmonics: Metallic Nanostructures and their Optical Properties IV,* August 2006, vol. 6323, pp. H3231-H3231, San Diego, CA, USA
[69] H. Lee, *et al.*, "Realization of optical superlens imaging below the diffraction limit," *New Journal of Physics,* vol. 7, no. 1, p. 255, Dec 2005.
[70] Z. W. Liu, *et al.*, "Rapid growth of evanescent wave by a silver superlens," *Applied Physics Letters,* vol. 83, no. 25, pp. 5184-5186, Dec 2003.
[71] R. J. Blaikie, *et al.*, "Near-field imaging through plasmonic superlenses - art. no. 680102," presented at the *Photonics: Design, Technology, and Packaging III*, December 2007, vol. 6801, pp. 80102-80102, Canberra, Australia
[72] R. J. Blaikie and D. O. S. Melville, "Imaging through planar silver lenses in the optical near field," *Journal of Optics A - Pure and Applied Optics,* vol. 7, no. 2, pp. S176-S183, Feb 2005.
[73] R. J. Blaikie, *et al.*, "Super-resolution near-field lithography using planar silver lenses: A review of recent developments," *Microelectronic Engineering,* vol. 83, no. 4-9, pp. 723-729, Apr-Sep 2006.
[74] D. O. S. Melville and R. J. Blaikie, "Near-field optical lithography using a planar silver lens," *Journal of Vacuum Science & Technology B,* vol. 22, no. 6, pp. 3470-3474, Nov-Dec 2004.
[75] D. O. S. Melville and R. J. Blaikie, "Response to "Comment on 'Submicron imaging with a planar silver lens' "," *Applied Physics Letters,* vol. 86, no. 12, p. 126101, Mar 2005.
[76] D. O. S. Melville and R. J. Blaikie, "Super-resolution imaging through a planar silver layer," *Optics Express,* vol. 13, no. 6, pp. 2127-2134, Mar 2005.
[77] D. O. S. Melville and R. J. Blaikie, "Experimental comparison of resolution and pattern fidelity in single- and double-layer planar lens lithography," *Journal of the Optical Society of America B-Optical Physics,* vol. 23, no. 3, pp. 461-467, Mar 2006.
[78] D. O. S. Melville and R. J. Blaikie, "Analysis and optimization of multilayer silver superlenses for near-field optical lithography," *Physica B-Condensed Matter,* vol. 394, no. 2, pp. 197-202, May 2007.
[79] D. O. S. Melville, *et al.*, "A comparison of near-field lithography and planar lens lithography," *Current Applied Physics,* vol. 6, no. 3, pp. 415-418, Jun 2006.
[80] D. O. S. Melville, *et al.*, "Submicron imaging with a planar silver lens," *Applied Physics Letters,* vol. 84, no. 22, pp. 4403-4405, May 2004.
[81] B. Sefa-Ntiri and P. D. Prewett, "Embedded metal mask enhanced evanescent near field optical lithography," *Microelectronic Engineering,* vol. 84, no. 5-8, pp. 729-732, May-Aug 2007.
[82] D. O. S. Melville, "Planar Lensing Lithography: Enhancing the Optical Near Field," Doctoral Thesis, Electrical and Computer Engineering, University of Canterbury, Christchurch, 2006.
[83] T. Ito, *et al.*, "Fabrication of sub-100 nm patterns using near-field mask lithography with ultra-thin resist process," *Journal of Photopolymer Science and Technology,* vol. 18, no. 3, pp. 435-441, 2005.
[84] V. G. Veselago, "Electrodynamics of substances with simultaneously negative values of sigma and mu," *Soviet Physics Uspekhi-Ussr,* vol. 10, no. 4, p. 509, 1968.

[85] ICL. *The Perfect Lens*. [Online] Available: http://www.cmth.ph.ic.ac.uk/photonics/Newphotonics/PerfectLens.html [3 May 2012].
[86] D. F. Sievenpiper, *et al.*, "3D wire mesh photonic crystals," *Physical Review Letters*, vol. 76, no. 14, pp. 2480-2483, Apr 1996.
[87] J. B. Pendry, *et al.*, "Extremely low frequency plasmons in metallic mesostructures," *Physical Review Letters*, vol. 76, no. 25, pp. 4773-4776, Jun 1996.
[88] J. B. Pendry, *et al.*, "Low frequency plasmons in thin-wire structures," *Journal of Physics-Condensed Matter*, vol. 10, no. 22, pp. 4785-4809, Jun 1998.
[89] D. R. Smith, *et al.*, "Composite medium with simultaneously negative permeability and permittivity," *Physical Review Letters*, vol. 84, no. 18, pp. 4184-4187, May 2000.
[90] R. A. Shelby, *et al.*, "Microwave transmission through a two-dimensional, isotropic, left-handed metamaterial," *Applied Physics Letters*, vol. 78, no. 4, pp. 489-491, Jan 2001.
[91] J. B. Pendry. (2001) New electromagnetic materials emphasize the negative. *Physics World* pp. 1-5,
[92] D. R. Smith and N. Kroll, "Negative refractive index in left-handed materials," *Physical Review Letters*, vol. 85, no. 14, pp. 2933-2936, Oct 2000.
[93] R. Srivastava, *et al.*, "Negative refraction by Photonic Crystal," *Progress in Electromagnetics Research B (PIER B)*, vol. 2, pp. 15-26, 2008.
[94] G. Tremblay and Y. L. Sheng, "Improving imaging performance of a metallic superlens using the long-range surface plasmon polariton mode cutoff technique," *Applied Optics*, vol. 49, no. 7, pp. A36-A41, Mar 2010.
[95] G. Tremblay and Y. L. Sheng, "Metallic superlens design using the long-range SPP mode cutoff technique," presented at the *Plasmonics: Metallic Nanostructures and Their Optical Properties VIII*, August 2010, vol. 7757, p. 77570W, San Diego, CA, USA
[96] S. A. Maier, *Plasmonics: Fundamentals and Applications*. New York, USA: Springer Science+Business Media LLC, 2007.
[97] R. J. Blaikie, *et al.*, "Nanoscale optical patterning using evanescent fields and surface plasmons," *International Journal of Nanoscience*, vol. 3, no. 4-5, pp. 405-417, 2004.
[98] M. D. Arnold and R. J. Blaikie, "Subwavelength optical imaging of evanescent fields using reflections from plasmonic slabs," *Optics Express*, vol. 15, no. 18, pp. 11542-11552, 2007.
[99] Wikipedia. *Surface States*. [Online] Available: http://en.wikipedia.org/wiki/Surface_states [28 May 2012].
[100] A. A. Maradudin, "Surface Waves," *Festkoperprobleme, Advances in Solid State Physics*, vol. 21, pp. 25-116, 1981.
[101] H. Raether, *Surface plasmons on smooth and rough surfaces and on gratings*. Berlin; New York: Springer-Verlag, 1988.
[102] A. R. Zakharian, *et al.*, "Surface plasmon polaritons on metallic surfaces," *Optics Express*, vol. 15, no. 1, pp. 183-197, 2007.
[103] T. W. Ebbesen, *et al.*, "Extraordinary optical transmission through sub-wavelength hole arrays," *Nature*, vol. 391, no. 6668, pp. 667-669, Feb 12 1998.
[104] A. Drezet, *et al.*, "Miniature plasmonic wave plates," *Physical Review Letters*, vol. 101, no. 4, p. 043902, Jul 25 2008.
[105] F. J. Garcia-Vidal, *et al.*, "Light passing through subwavelength apertures," *Reviews of Modern Physics*, vol. 82, no. 1, pp. 729-787, Jan-Mar 2010.
[106] C. Genet and T. W. Ebbesen, "Light in tiny holes," *Nature*, vol. 445, no. 7123, pp. 39-46, Jan 4 2007.
[107] A. Degiron, *et al.*, "Effects of hole depth on enhanced light transmission through subwavelength hole arrays," *Applied Physics Letters*, vol. 81, no. 23, pp. 4327-4329, Dec 2 2002.
[108] H. J. Lezec, *et al.*, "Beaming light from a subwavelength aperture," *Science*, vol. 297, no. 5582, pp. 820-822, Aug 2 2002.

[109] L. Martin-Moreno, *et al.*, "Theory of extraordinary optical transmission through subwavelength hole arrays," *Physical Review Letters*, vol. 86, no. 6, pp. 1114-1117, Feb 5 2001.
[110] J. B. Pendry, *et al.*, "Mimicking surface plasmons with structured surfaces," *Science*, vol. 305, no. 5685, pp. 847-848, Aug 6 2004.
[111] F. Z. Yang, *et al.*, "Experimental-Observation Of Surface Exciton-Polaritons On Vanadium Using Infrared Radiation," *Journal of Modern Optics*, vol. 37, no. 9, pp. 1545-1553, Sep 1990.
[112] Wikipedia. *Surface plasmon resonance*. [Online] Available: http://en.wikipedia.org/wiki/Surface_plasmon_resonance [28 May 2012].
[113] L. Lagois and B. Fischer, "Introduction to Surface Exciton Polaritons," *Festkorperprobleme, Advances in solid state physics*, vol. 18, pp. 197-216, 1978.
[114] J. Lagois and B. Fischer, "Experimental Observation Of Surface Exciton Polaritons," *Physical Review Letters*, vol. 36, no. 12, pp. 680-683, 1976.
[115] F. Yang, *et al.*, "Long-Range Coupled Surface Exciton Polaritons," *Physical Review Letters*, vol. 64, no. 5, pp. 559-562, Jan 1990.
[116] F. Z. Yang, *et al.*, "Long-Range Surface-Mode Supported By Very Thin Silver Films," *Physical Review Letters*, vol. 66, no. 15, pp. 2030-2032, Apr 1991.
[117] F. Z. Yang, *et al.*, "Long-Range Surface-Modes Supported By Thin-Films," *Physical Review B*, vol. 44, no. 11, pp. 5855-5872, Sep 1991.
[118] G. P. Bryanbrown, *et al.*, "Prism and Grating Coupling to Long-Range Coupled-Surface Exciton Polaritons," *Journal of the Optical Society of America B-Optical Physics*, vol. 8, no. 4, pp. 765-769, Apr 1991.
[119] S. R. J. Brueck, "Optical and interferometric lithography - Nanotechnology enablers," *Proceedings of the IEEE*, vol. 93, no. 10, pp. 1704-1721, Oct 2005.
[120] T. A. Savas, *et al.*, "Large-area achromatic interferometric lithography for 100 nm period gratings and grids," *Journal of Vacuum Science & Technology B*, vol. 14, no. 6, pp. 4167-4170, Nov-Dec 1996.
[121] E. A. Thomson. *Nanoruler a promising line of work*. (2004). [Online] Available: http://web.mit.edu/newsoffice/2004/nanoruler-0128.html [3 May 2012].
[122] C. P. Fucetola, *et al.*, "Low-cost interference lithography," *Journal of Vacuum Science & Technology B*, vol. 27, no. 6, pp. 2958-2961, Nov 2009.
[123] A. D. Apostol, *et al.*, "2D multiple beam interference lithography," presented at the *International Semiconductor Conference*, September 2006, vol. 1, pp. 151-154, Sinaia, Romania
[124] N. D. Lai, *et al.*, "Fabrication of two- and three-dimensional periodic structures by multi-exposure of two-beam interference technique," *Optics Express*, vol. 13, no. 23, pp. 9605-9611, Nov 2005.
[125] C. H. Chang, *et al.*, "Fabrication of 50 nm period gratings with multilevel interference lithography," *Optics Letters*, vol. 33, no. 14, pp. 1572-1574, Jul 2008.
[126] S. Lee, *et al.*, "An analysis of double exposure lithography options - art. no. 69242A," presented at the *Optical Microlithography XXI, Pts 1-3*, February 2008, vol. 6924, pp. A9242-A9242, San Jose, CA, USA
[127] A. K. Raub, *et al.*, "Fabrication of 22 nm half-pitch silicon lines by single-exposure self-aligned spatial-frequency doubling," *Journal of Vacuum Science & Technology B*, vol. 25, no. 6, pp. 2224-2227, Nov 2007.
[128] C.-H. Chang, "Multilevel Interference Lithography-Fabricating Sub-wavelenth Periodic Nanostructures," Doctoral Thesis, Department of Mechanical Engineering, Massachusetts Institute of Technology, 2008.
[129] A. Feigel, *et al.*, "Interference lithography for 3D photonic band gap crystal layer by layer fabrication," presented at the *Progress in Semiconductor Materials for Optoelectronic Applications*, November 2001, vol. 692, pp. 675-678, Boston, MA, USA

[130] M. Farhoud, *et al.*, "Fabrication of 200 nm period nanomagnet arrays using interference lithography and a negative resist," *Journal of Vacuum Science & Technology B,* vol. 17, no. 6, pp. 3182-3185, Nov-Dec 1999.
[131] B. D. Terris and T. Thomson, "Nanofabricated and self-assembled magnetic structures as data storage media," *Journal of Physics D-Applied Physics,* vol. 38, no. 12, pp. R199-R222, Jun 2005.
[132] W. Wu, *et al.*, "Large area high density quantized magnetic disks fabricated using nanoimprint lithography," *Journal of Vacuum Science & Technology B,* vol. 16, no. 6, pp. 3825-3829, Nov-Dec 1998.
[133] M. Fritze, *et al.*, "Gratings of regular arrays and trim exposures for ultralarge scale integrated circuit phase-shift lithography," *Journal of Vacuum Science & Technology B,* vol. 19, no. 6, pp. 2366-2370, Nov-Dec 2001.
[134] T. B. Greenslade. *Fresnel's and Lloyd's Mirrors*. [Online] Available: http://physics.kenyon.edu/EarlyApparatus/Optics/Fresnel_Mirrors/Fresnel_Mirrors.html [3 May 2012].
[135] C. H. Chang, *et al. The MIT Nanoruler: A Tool for Patterning Nano-Accurate Gratings.* [Annual Report]. [Online] Available: http://nanoweb.mit.edu/Annual%20Reports%202005/sec.10.ms.pdf [3 May 2012].
[136] J. M. Carter, *et al. Interference Lithography*. [Online] Available: http://snl.mit.edu/project_document/SNL-8.pdf [3 May 2012].
[137] K. Ronse, *et al.*, "Lithography Options for the 32 nm Half Pitch Node and Beyond," *IEEE Transactions on Circuits and Systems I-Regular Papers,* vol. 56, no. 8, pp. 1884-1891, Aug 2009.
[138] D. Bratton, *et al.*, "Recent progress in high resolution lithography," *Polymers for Advanced Technologies,* vol. 17, no. 2, pp. 94-103, Feb 2006.
[139] B. W. Smith, *et al.*, "Evanescent wave imaging in optical lithography - art. no. 61540A," presented at the *Optical Microlithography XIX, Pts 1-3*, February 2006, vol. 6154, pp. U200-U208, San Jose, CA, USA
[140] E. A. Bezus, *et al.*, "Evanescent-wave interferometric nanoscale photolithography using guided-mode resonant gratings," *Microelectronic Engineering,* vol. 88, no. 2, pp. 170-174, Feb 2011.
[141] E. A. Bezus, *et al.*, "Interference pattern generation in evanescent electromagnetic waves for nanoscale lithography using waveguide diffraction gratings," *Quantum Electronics,* vol. 41, no. 8, pp. 759-764, 2011.
[142] K. V. Sreekanth, *et al.*, "Interferometric lithography for nanoscale feature patterning: a comparative analysis between laser interference, evanescent wave interference, and surface plasmon interference," *Applied Optics,* vol. 49, no. 35, pp. 6710-6717, Dec 2010.
[143] B. Wang, *et al.*, "Subwavelength lithography by waveguide mode interference," *Applied Physics Letters,* vol. 99, no. 15, p. 151106, Oct 2011.
[144] X. P. Li, *et al.*, "Experimental analysis of solid immersion interference lithography based on backside exposure technique," *Microelectronic Engineering,* vol. 88, no. 8, pp. 2509-2512, Aug 2011.
[145] J. H. Burnett, *et al.*, "High-index materials for 193 nm immersion lithography," presented at the *Optical Microlithography XVIII, Pts 1-3*, March 2005, vol. 5754, pp. 611-621, San Jose, CA, USA
[146] B. W. Smith and J. Cashmore, "Challenges in high NA, polarization, and photoresists," presented at the *Optical Microlithography XV, Pts 1 and 2*, March 2002, vol. 4691, pp. 11-24, Santa Clara, CA, USA
[147] B. W. Smith and Z. J., "Snell or Fresnel - The influence of material index on hyper NA lithography," presented at the *Optical Microlithography XX*, March 2007, vol. 6520, p. 6520AA, San Jose, CA, USA

[148] B. W. Smith, *et al.*, "Amphibian XIS: An immersion lithography microstepper platform," presented at the *Optical Microlithography XVIII, Pts 1-3*, March 2005, vol. 5754, pp. 751-759, San Jose, CA, USA
[149] IBM. *A Testbed for 193 nm Interferometric Immersion Lithography*. [Online] Available: http://www.almaden.ibm.com/st/chemistry/lithography/immersion/NEMO/ [3 May 2012].
[150] P. Xie and B. W. Smith, "Scanning interference evanescent wave lithography for sub-22nm generations," presented at the *Optical Microlithography XXV*, February 2012, vol. 8326, p. 83260Y, San Jose, CA
[151] B. J. Lin, "Immersion lithography and its impact on semiconductor manufacturing," presented at the *Optical Microlithography XVII, Pts 1-3*, Santa Clara, CA, USA 2004, vol. 5377, pp. 46-67, Santa Clara, CA, USA
[152] E. C. Piscani, *et al.*, "Continuing 193nm optical lithography for 32nm imaging and beyond - art. no. 69242l," presented at the *Optical Microlithography XXI, Pts 1-3*, February 2008, vol. 6924, pp. L9242-L9242, San Jose, CA, USA
[153] B. J. Rice, "High-index materials research key to extending immersion lithography," *Solid State Technology*, vol. 51, no. 2, pp. 28-34, Feb 2008.
[154] P. A. Zimmenrman, *et al.*, "Development of an operational high refractive index resist for 193nm immersion lithography - art. no. 692306," presented at the *Advances in Resist Materials and Processing Technology Xxv, Pts 1 and 2*, February 2008, vol. 6923, pp. 92306-92306, San Jose, CA, USA
[155] P. A. Zimmerman, *et al.*, "Development and evaluation of a 193nm immersion generation-three fluid candidates - art. no. 69230A," presented at the *Advances in Resist Materials and Processing Technology XXV, Pts 1 and 2*, February 2008, vol. 6923, pp. A9230-A9230, San Jose, CA, USA
[156] P. A. Zimmerman, *et al.*, "Status of high-index materials for Generation-three 193nm immersion lithography," *Journal of Photopolymer Science and Technology*, vol. 20, no. 5, pp. 643-650, 2007.
[157] T. M. Bloomstein, *et al.*, "Immersion patterning down to 27 nm half pitch," *Journal of Vacuum Science & Technology B*, vol. 24, no. 6, pp. 2789-2797, Nov-Dec 2006.
[158] T. M. Bloomstein, *et al.*, "22-nm immersion interference lithography," *Optics Express*, vol. 14, no. 14, pp. 6434-6443, Jul 2006.
[159] M. Fritze, *et al.*, "Hybrid optical maskless lithography: Scaling beyond the 45 nm node," *Journal of Vacuum Science & Technology B*, vol. 23, no. 6, pp. 2743-2748, Nov-Dec 2005.
[160] M. Fritze, *et al.*, "Extending 193nm immersion with hybrid optical maskless lithography," *Solid State Technology*, vol. 49, no. 9, pp. 41-43, Sep 2006.
[161] M. Rothschild, *et al.*, "Nanopatterning with UV optical lithography," *Mrs Bulletin*, vol. 30, no. 12, pp. 942-946, Dec 2005.
[162] M. Switkes, *et al.*, "A 157nm immersion microstepper," presented at the *Optical Microlithography XVIII, Pts 1-3*, March 2005, vol. 5754, pp. 237-242, San Jose, CA, USA
[163] T. Itani, *et al.*, "Effect of high numerical aperture lens on lithographic performance in 157 nm lithography," *Journal of Vacuum Science & Technology B*, vol. 20, no. 6, pp. 2562-2566, Nov-Dec 2002.
[164] R. H. French, *et al.*, "Imaging of 32-nm 1 : 1 lines and spaces using 193-nm immersion interference lithography with second-generation immersion fluids to achieve a numerical aperture of 1.5 and a k(1) of 0.25," *Journal of Microlithography Microfabrication and Microsystems*, vol. 4, no. 3, p. 031103, Jul-Sep 2005.
[165] T. Miyamatsu, *et al.*, "Material design for immersion lithography with high refractive index fluid (HIF)," presented at the *Advances in Resist Technology and Processing XXII, Pt 1 and 2*, 28 February - 2 March 2005, vol. 5753, pp. 10-19, San Jose, CA, USA
[166] J. C. Taylor, *et al.*, "Fluids and resists for hyper NA immersion lithography," presented at the *Advances in Resist Technology and Processing XXII, Pt 1 and 2*, 28 February - 2 March 2005, vol. 5753, pp. 836-846, San Jose, CA, USA

[167] P. Mehrotra, *et al.*, "Solid-immersion Lloyd's Mirror as a Testbed for Plasmon-enhanced High-NA Lithography," presented at the *SPIE Advanced Lithography, Alternative Lithographic Technologies III*, 3rd March 2011 2011, vol. 7970, San Jose Marriott and San Jose Convention Center, San Jose, California, United States
[168] J. de Boor, *et al.*, "Sub-50 nm patterning by immersion interference lithography using a Littrow prism as a Lloyd's interferometer," *Optics Letters*, vol. 35, no. 20, pp. 3450-3452, Oct 2010.
[169] K. Zhang and D. Li, *Electromagnetic Theory for Microwaves and Optoelectronics*, 2nd ed., 2008.
[170] VLOC. *YAG Yttrium Aluminum Garnet Laser Materials*. [Online] Available: http://www.vloc.com/PDFs/YAGBrochure.pdf [28 May 2012].
[171] Cargille. *Cargille Laboratories*. [Online] Available: http://www.cargille.com/ [30 May 2012].
[172] R. Kumar, *et al.*, "Fabrication and characterization of polyvinyl-alcohol-based thin-film optical waveguides," *Optical Engineering*, vol. 43, no. 9, pp. 2134-2142, Sep 2004.
[173] AZ-Electronic-Materials. *(Germany) GmbH*. [Online] Available: http://www.azem.com/ [May 2012].
[174] E. D. Palik, *Handbook of Optical Constants of Solids*. Orlando, Florida, USA: Academic Press, Inc, 1985.
[175] S. Z. Shang, *et al.*, "High-reflectance 193 nm Al2O3/MgF2 mirrors," *Applied Surface Science*, vol. 249, no. 1-4, pp. 157-161, Aug 2005.
[176] S. N. Kasarova, *et al.*, "Analysis of the dispersion of optical plastic materials," *Optical Materials*, vol. 29, no. 11, pp. 1481-1490, Jul 2007.
[177] *COMSOL Multiphysics*, [Software] More info. available at: http://www.comsol.com
[178] C. A. Mack, "Analytical Expression for the standing wave intensity in photoresist," *Applied Optics*, vol. 25, no. 12, pp. 1958-1961, Jun 1986.
[179] *MATLAB - The Language of Technical Computing*, [Software] More info. available at: http://www.mathworks.com/products/matlab/
[180] N. Fang and X. Zhang, "Imaging properties of a metamaterial superlens," *Applied Physics Letters*, vol. 82, no. 2, pp. 161-163, Jan 2003.
[181] D. R. Smith, *et al.*, "Limitations on subdiffraction imaging with a negative refractive index slab," *Applied Physics Letters*, vol. 82, no. 10, pp. 1506-1508, Mar 2003.
[182] H. A. Macleod, *Thin-Film Optical Filters*. New York, USA: American Elsevier Publishing, 1969.
[183] G. Ghosh, "Dispersion-equation coefficients for the refractive index and birefringence of calcite and quartz crystals," *Optics Communications*, vol. 163, no. 1-3, pp. 95-102, May 1999.
[184] Umicore. *Special materials for Precision Optics & Laser Coatings* [Technical data]. [Online] Available: http://www.thinfilmproducts.umicore.com/Products/TechnicalData/show_precision_laser_e.pdf [28 May 2012].